



**UCGE Reports
Number 20200**

Department of Geomatics Engineering

Medium Accuracy INS/GPS Integration in Various GPS Environments

(URL: <http://www.geomatics.ucalgary.ca/links/GradTheses.html>)

by

Anastasia Olegovna Salytcheva

September 2004



UNIVERSITY OF
CALGARY

UNIVERSITY OF CALGARY

Medium Accuracy INS/GPS Integration in Various GPS Environments

by

Anastasia O. Salytcheva

A THESIS

SUBMITTED TO THE FACULTY OF GRADUATE STUDIES

IN PARTIAL FULFILMENT OF THE REQUIREMENTS FOR THE

DEGREE OF MASTER OF SCIENCE

DEPARTMENT OF GEOMATICS ENGINEERING

CALGARY, ALBERTA

SEPTEMBER, 2004

© Anastasia O. Salytcheva 2004

Abstract

The demand for a system capable of providing reliable navigation solutions regardless of operational environment prompted investigations into the use of medium accuracy inertial systems aided by GPS measurements. An algorithm for integration of a tactical-grade IMU (Honeywell 1700) with a conventional high performance receiver (NovAtel OEM4) for open sky areas, and a high sensitivity receiver (SiRF Star II Xtrac) for downtown canyons, is developed and tested. This research is focused on obtaining metre-level positional accuracies for automobile applications. A loosely-coupled integration scheme with estimation algorithms for two GPS environments is implemented: 1) a conventional Kalman filter for INS error estimation that includes a special procedure for in-motion estimation of INS azimuth error using GPS velocities; and 2) use of multiple Kalman filters with fixed and adaptive measurement covariances. The filter's operational mode criteria account for vehicle dynamics and the quality of GPS measurements. In open sky conditions, an attitude accuracy of 0.2° - 0.6° for azimuth and 0.05° - 0.1° for roll and pitch is achieved. System positional and velocity accuracy is tested in prediction mode using simulated GPS outages. For data gaps of 30 to 60 s in duration, the system accuracy in position and velocity domains ranges from 5 to 15 m and from 0.2 to 0.6 m/s respectively depending upon vehicle dynamics. In downtown canyons, the accuracies are tested in position domain only; positional error ranges from 10 to 50 m with occasional outliers reaching 70 m.

Acknowledgements

I would like to express my appreciation to my supervisor, Dr. M. Elizabeth Cannon, for her support, guidance and encouragement throughout my studies and for giving me the opportunity to come to Canada and to gain invaluable experience in a world-class research group. I am grateful to many at my adopted university: the staff and instructors at the Department of Geometrics Engineering for providing high quality education; and to the members of my examining committee for reading this thesis and for providing useful feedback. Thanks also go to the members of the PLAN group for their assistance in data collection, pre-processing and for interesting discussions; thanks to Andrew Huang, Wojciech Kubacki, Junjie Liu, Salman Syed, Glenn MacGougan and Mark Petovello. I would especially like to acknowledge my officemates, Diep Dao and Heidi Kuusniemi, for their unwavering support and for simply being there whenever I needed help. Thanks to my friends, particularly Bruce Wright, Rossen Grebenitcharsky and Rebecca Quinonez-Pinon for the encouragement and trust they have shown me. Special thanks to Leonid Gushtorov for his overall support and for helping me to develop my programming skills.

Most of all, I would like to thank my parents. Thanks, Mom for your love, encouragement and understanding over the years, and my darling Dad for your love, patience and belief in me as well as interesting ideas and creative suggestions. Spacibo, guys. I would not have made it this far without you.

Table Of Contents

Abstract	ii
Acknowledgements	iii
Table Of Contents	iv
List Of Figures	vii
List Of Tables	ix
Abbreviations and Acronyms	x
List of Symbols	xiii
1 Introduction	1
1.1 Background.....	2
1.1.1 Global Positioning System	2
1.1.2 Inertial Navigation System	4
1.1.3 INS/GPS Integration.....	7
1.2 Literature Review	10
1.3 Research Objectives and Motivation.....	12
1.4 Thesis Outline.....	14
2 Overview of Global Positioning System	16
2.1 GPS Concept	16
2.1.1 Pseudorange Measurements	18
2.1.2 Doppler Measurements.....	19
2.2 GPS Errors.....	21
2.2.1 Orbital Errors.....	21
2.2.2 Satellite Clock Errors	21
2.2.3 Receiver Clock Errors	22
2.2.4 Ionospheric Errors	22
2.2.5 Tropospheric Errors.....	23
2.2.6 Multipath Errors	24
2.2.7 Receiver Noise.....	28
2.3 High Sensitivity GPS.....	30
2.3.1 GPS Signal Power	30
2.3.2 Signal Power Reaching GPS Receiver	32
2.3.3 Carrier-To-Noise Density Ratio	33
2.3.4 Main Concept of High Sensitivity GPS.....	33
2.3.5 Other GPS Errors and High Sensitivity Applications	37
2.3.6 GPS Environments in Application to High Sensitivity GPS.....	40
3 Overview of Inertial Navigation System	43
3.1 Coordinate Frames.....	43

3.1.1	Inertial Navigation Frame.....	43
3.1.2	Earth – fixed Frame.....	44
3.1.3	Local – level Frame.....	45
3.1.4	Body Frame.....	47
3.1.5	Navigation Frame.....	48
3.1.6	Platform frame.....	48
3.1.7	Coordinate Transformations.....	49
3.2	Principle of Inertial Navigation.....	50
3.2.1	Poisson equation.....	50
3.2.2	Quaternion Transformation.....	51
3.2.3	Main Concept of Inertial Navigation.....	54
3.2.4	Mechanization Equations.....	55
3.3	Principle of INS Alignment.....	58
3.3.1	Horizontal Alignment.....	59
3.3.2	Azimuth Alignment.....	60
3.4	INS Errors.....	62
3.4.1	Schuler Loop.....	65
4	INS/GPS Integration.....	68
4.1	Integration Schemes.....	68
4.1.1	Loosely Coupled Integration.....	70
4.1.2	Tightly Coupled Integration.....	72
4.1.3	Centralized and Decentralized Integration Filters.....	73
4.2	Kalman Filter.....	74
4.2.1	State Space Model.....	74
4.2.2	Filter Algorithm.....	76
4.2.3	Main Filter Characteristics.....	79
4.2.4	Kalman Filter with Control Signal.....	83
4.2.5	Kalman Filter with Adaptive Measurement Covariance R.....	84
4.3	Estimation Concepts.....	85
4.3.1	Kalman Filter in Prediction Mode.....	86
5	System Realization and Methodology.....	88
5.1	INS/GPS Cascaded Integration Scheme.....	88
5.2	Error Estimation and Compensation for Open Area Applications.....	92
5.2.1	Observability Analysis of INS Errors.....	94
5.2.2	In-motion Azimuth Estimation Using Cascaded Kalman Filter.....	98
5.2.3	Heading Correction.....	101
5.2.4	Roll and Pitch Correction.....	103
5.2.5	Gyro Drift Compensation.....	104
5.2.6	Position and Velocity Correction.....	104
5.3	Error Estimation and Compensation for Downtown Applications.....	105
5.3.1	Velocity Filters.....	107
5.3.2	Coordinate filters.....	110
5.3.3	Azimuth Correction.....	112

5.3.4	Output of Estimation Block.....	112
6	Open Area Results	114
6.1	Test Description.....	114
6.2	Experimental Results.....	120
6.2.1	Results Using Clean GPS Data.....	121
6.2.2	Results Using GPS Data with Simulated Gaps	139
7	Results in Suburban and Urban Areas	153
7.1	Test Description.....	153
7.2	GPS Solution	156
7.3	Downtown Results.....	158
7.3.1	Conclusions	192
7.4	Residential Area Results.....	194
8	Conclusions and Recommendations.....	200
8.1	Summary.....	200
8.2	Conclusions	203
8.2.1	Open Area Applications	204
8.2.2	Urban and Suburban Area Applications.....	205
8.3	Recommendations	209
	References.....	212
	Appendix A: Strapdown INS Algorithm	220

List Of Figures

Figure 2-1: Multipath Delay on Code Measurements	26
Figure 2-2: Multipath Envelope.....	28
Figure 3-1: Inertial Frame.....	44
Figure 3-2: Earth-fixed Frame	45
Figure 3-3: Local-level Frame	46
Figure 3-4: Rotation Vector Transformation	52
Figure 3-5: Principle of INS Alignment	60
Figure 3-6: Schuler Loop.....	67
Figure 4-1: Calculation Algorithm for A Kalman Filter.....	78
Figure 4-2: Calculation Algorithm for An Adaptive Kalman Filter	85
Figure 4-3: Estimation Modes	86
Figure 5-1: Cascaded Scheme of INS/GPS Integration.....	91
Figure 5-2: Estimation Algorithm for Open Area Applications	93
Figure 5-3: GPS Heading.....	102
Figure 5-4: Estimation Algorithm for Downtown Applications.....	106
Figure 6-1: Test Set-up for Open Area Tests.....	115
Figure 6-2: Remote Station Set-up	116
Figure 6-3: Reference Trajectories for Tests 1 and 2	118
Figure 6-4: Test Area.....	119
Figure 6-5: Typical Urban Open Area Environment	120
Figure 6-6: North Position Component Using Clean GPS data, Test 1	122
Figure 6-7: Influence of Vehicle Dynamics on Velocity Accuracy, Test 1.....	124
Figure 6-8: Influence of Vehicle Dynamics on Velocity Accuracy, Test 2.....	125
Figure 6-9: North Velocity INS Error, Test 1	128
Figure 6-10: North Velocity INS Error, Test 2.....	129
Figure 6-11: Estimated by CKF INS Azimuth Misalignment	130
Figure 6-12: Influence of Vehicle Dynamics on INS Velocity Error, Test 1	131
Figure 6-13: Influence of Vehicle Dynamics on INS Velocity Error, Test 2	132
Figure 6-14: Impact of Gyro Drifts on INS Velocity Error, Test 1	133
Figure 6-15: Gyro Drift Estimates	134
Figure 6-16: Roll and Pitch, Test 1	135
Figure 6-17: Roll and Pitch, Test 2.....	136
Figure 6-18: Azimuth, Test 1.....	137
Figure 6-19: Azimuth, Test 2.....	138
Figure 6-20: North Position Using Data with Simulated GPS Outages, Test 1	140
Figure 6-21: North Position Using Data with Simulated GPS Outages, Test 2	141
Figure 6-22: Trajectory for Data with Simulated GPS Outages, Test 1	143
Figure 6-23: Trajectory for Data with Simulated GPS Outages, Test 2	144
Figure 6-24: RMS of Positional Errors in Prediction	145
Figure 6-25: North Velocity Using Data with Simulated Outages, Test 1	147
Figure 6-26: North Velocity Using Data with Simulated Outages, Test 2	148

Figure 6-27: RMS of Velocity Errors in Prediction.....	150
Figure 7-1: Test Set-up for Urban Areas	154
Figure 7-2: Typical Test Environment in Downtown Calgary	155
Figure 7-3: Typical Test Environment in Residential Area of Calgary.....	156
Figure 7-4: Reference Trajectory 1	160
Figure 7-5: Position of Integrated System Using The SiRF Internal Solution, Run #1..	162
Figure 7-6: C/N ₀ and Elevation Angles for All Satellites Tracked, Run #1	163
Figure 7-7: Position of Integrated System Using The C ³ NAVIG ² ™ Solution, Run #1 ..	164
Figure 7-8: PDOP and Number of Satellites Used in Solution for Run #1	166
Figure 7-9: Across-track Error, Run #1 on Trajectory 1	167
Figure 7-10: Position of Integrated System Using The SiRF Internal Solution, Run #2	170
Figure 7-11: C/N ₀ and Elevation Angles for All Satellites Tracked, Run #2	171
Figure 7-12: Filter Mode for Run #2, The INS/SiRF-Internal Solution	172
Figure 7-13: Position of Integrated System Using The C ³ NAVIG ² ™ Solution, Run #2	173
Figure 7-14: PDOP and Number of Satellites Used in Solution for Run #2	174
Figure 7-15: Filter Mode for Run #2, The INS/SiRF-C ³ NAVIG ² ™ Solution	175
Figure 7-16: Across-track Error, Run #2 on Trajectory #1	176
Figure 7-17: Position of Integrated System Using The SiRF Internal Solution, Run #3	177
Figure 7-18: Filter Modes of Integrated System and SiRF Internal Solution, Run #3 ...	178
Figure 7-19: C/N ₀ and Elevation Angles for All Satellites Tracked, Run #3	179
Figure 7-20: Position of Integrated System Using The C ³ NAVIG ² ™ Solution, Run #3	180
Figure 7-21: PDOP and Number of Satellites Used in Solution for Run #3	181
Figure 7-22: Across-track Error, Run #3 on Trajectory #1	182
Figure 7-23: Reference Trajectory #2.....	184
Figure 7-24: Position of Integrated System Using The SiRF Internal Solution, Run #4	185
Figure 7-25: C/N ₀ and Elevation Angles for All Satellites Tracked, Run #4.....	186
Figure 7-26: Position of Integrated System Using The C ³ NAVIG ² ™ Solution, Run #4	187
Figure 7-27: PDOP and Number of Satellites Used in Solution for Run #4	188
Figure 7-28: Across-track Error for Run #4 on Trajectory 2.....	189
Figure 7-29: C/N ₀ and Elevation Angles for All Satellites Tracked, Residential Test...	196
Figure 7-30: Position of Integrated System, Residential Test	197
Figure 7-31: PDOP and Number of Satellites Used in Solution, Residential Test.....	198
Figure A-1: SINS Calculation Algorithm.....	228

List Of Tables

Table 2-1: Signal Power Budget.....	32
Table 6-1: HG1700 IMU Specifications (Honeywell, 1997).....	115
Table 6-2: Coordinates of Base Stations.....	117
Table 6-3: Positional Errors for Clean GPS Data.....	123
Table 6-4: Velocity Errors for Clean GPS Data.....	127
Table 6-5: Positional Accuracy in Prediction.....	146
Table 6-6: Velocity Errors in Prediction.....	149
Table 7-1: Technical Characteristics of GPS Receivers Used for Testing.....	155
Table 7-2: Across-track Error.....	190
Table 7-3: Filter Mode: Percentage of Test Time in Prediction.....	191
Table 7-4: Longest Gap in GPS Measurements.....	191
Table 7-5: Statistics of Position Errors of Integrated System for Two Runs.....	199
Table 7-6: Filter Mode: Percentage of Test Time in Prediction.....	199

Abbreviations and Acronyms

2D- and 3D-	2-dimensional / 3-dimensional
AGPS	Assisted Global Positioning System
BDS	Black Diamond System
b-frame	Body frame
C/A	Coarse Acquisition
CKF	Cascaded Kalman Filter
C/N ₀	Carrier To Noise Density Ratio
CDMA	Code Division Multiple Access
CCIT	Calgary Centre for Innovative Technology
C ³ NAVIG ² ™	Combined Code and Carrier for NAVigation with GPS and GLONASS software
CW	Continuous Wave
DLL	Delay Lock Loop
DGPS	Differential GPS
DOP	Dilution of Precision
GDOP	Geometrical Dilution of Precision
PDOP	Position Dilution of Precision
e-frame	Earth-fixed frame
FD	Fixed Density
FM	Frequency Modulated

GPS	Global Positioning System
GLONASS	GLobal Orbiting Navigation Satellite System
HS	High Sensitivity
INS	Inertial Navigation System
i-frame	Inertial frame
IMU	Inertial Measurement Unit
KF	Kalman Filter
LOS	Line-Of-Sight
ll-frame	Local-level frame
MEDLL	Multipath Estimation Delay Lock Loop
MET	Multipath Elimination Technique
n-frame	Navigation frame
P-code	Precise code
p-frame	Platform frame
PRN	Pseudo Random Noise
ppm	Part-Per-Million
RF	Radio Frequency
RMS	Root Mean Square
SINS	Strapdown INS
SNR	Signal-To-Noise Ratio
SV	Space Vehicle
TOA	Time Of Arrival

UGPS	Unaided GPS
uv	Ultraviolet
ZUPT	Zero velocity UPdaTe

List of Symbols

β	Parameter of correlation function
ρ	Geometric range
φ	Geodetic latitude
λ	Geodetic longitude
$\dot{\phi}$	Doppler observable
Φ	Rotation vector / Transition matrix
Φ_N, Φ_E	Horizontal misalignment angles
Φ_{up}	Azimuth misalignment
μ	Accelerometer scale factor
v	Innovation sequence
ω	Raw gyro measurement
δ	Acceleration threshold
δM	Error of arbitrary value M
ω_m	Absolute angular velocity of arbitrary m-frame
ω_{m-n}	Relative angular velocity between m- and n-frames
$\tilde{\omega}_m$	Absolute angular velocity of arbitrary m-frame in matrix form
ω_m^{dr}	Gyro drift in arbitrary m-frame
Ω_m	Absolute angular velocity of arbitrary m-frame in matrix form
ε_ϕ	Phase noise

ε_p	Code noise
$\Delta\lambda$	Quaternion of slow motion (between the b- and n-frames)
Δa	Raw angle increment / acceleration increment
Δm	Quaternion of fast motion (between the b- and n-frames)
Δm^*	Conjugate of quaternion Δm
ΔW	Raw velocity increment
A	Azimuth/ Parameter of correlation function
a	Raw accelerometer measurement / acceleration / semi-major axis of reference ellipsoid
B	Accelerometer bias
$b_{11} \dots b_{33}$	Elements of the matrix R_e^{\parallel}
c	Speed of light
C	Covariance matrix of innovation sequence
$c_{11} \dots c_{33}$	Elements of the matrix R_b^{\parallel}
$d\rho$	Orbital error
d_{ion}	Ionospheric delay
dt	Satellite clock error
dT	Receiver clock error
d_{trop}	Tropospheric delay
E	Easting
e	Eccentricity of reference ellipsoid
f	Specific force

g	Gravity
G	Input matrix
H	Design matrix / Heading
h	Altitude above the reference ellipsoid
I	Identity matrix
K	Kalman gain matrix
k_1, k_2	Damping parameters for INS alignment
L	Control matrix
N	Northing
P	Pseudorange observable
P	Covariance matrix of estimation errors
P_r	Received power
P_t	Transmitted power
p	Pitch
Q	Covariance matrix of input noise
$q_{1..4}$	Quaternion coordinates
R	Covariance matrix of measurement noise
R_φ	Radius of curvature of the reference ellipsoid in north-south direction
R_λ	Radius of curvature of the reference ellipsoid in east-west direction
R_m^n	Rotation matrix from m- to n- frame
r	Roll / Covariance of measurement noise
T	Sampling interval

t	Time
U	Angular velocity of the Earth
Up	Coordinate in vertical direction in the ll-frame
u	Vector of control signal
V	Velocity
v	Measurement noise
w	White noise
x	State vector
z	Measurement vector

Chapter 1

Introduction

The demand for positioning services in recent years has driven extensive research towards the development of navigation systems. Beyond the value of scientific inquiry, the market also forces requirements in terms of quality, size and price. In the navigation marketplace, the Global Positioning System (GPS) and an Inertial Navigation System (INS) experience the highest level of demand. However, both systems have a number of limitations which challenge their use in many land-based applications. Inertial sensor errors, for example, can be large in magnitude and grow over time, while navigation data from another unit such as GPS can be used for the INS error compensation. On one hand, widespread use of a very accurate INS is constrained by their high cost. On the other hand, the operational capability of GPS degrades in harsh environments such as urban and forest areas, where GPS signals may be partially or completely blocked by buildings and dense foliage. Besides, a GPS receiver does not provide attitude data. The combination of an INS and GPS is well suited to the development of a range of applications as each system compensates for the other's shortcomings. An extended research in the field of INS/GPS integration has focused on the use of high accuracy inertial systems providing attitude data, augmented by GPS for precise positional and velocity information (Grejner-Brzezinska et al., 1998; Cannon et al., 1999; Kumagai et al., 2000, Asaoka et al., 2003). In such a configuration, very accurate GPS measurements are needed to correct INS errors, which is possible in open sky conditions only. In harsh

GPS environments, the accuracy of the GPS solution degrades due to effects such as signal masking, signal cross-correlation and multipath. This thesis investigates the use of a medium accuracy inertial system aided by GPS measurements in a range of different 'quality' levels depending on the operational environments. Two types of GPS receivers are used: a conventional high performance NovAtel OEM4 for open area applications and a high sensitivity SiRF receiver for downtown canyons.

1.1 Background

1.1.1 Global Positioning System

Global Positioning System provides accurate and continuous, three-dimensional position and velocity information via the satellite constellation to users worldwide. Designed by the United States Department of Defense in the 1960s for military purposes (Kaplan, 1996), GPS is also available to civilian users and it is capable of providing positions ranging from metres to centimetres depending on the type of measurements, methods implemented for the navigation solution, and operational environments (Misra and Enge, 2001; Lachapelle, 2002). With GPS, accurate positions have become available for a variety of applications. The falling cost of GPS receivers over the past twenty years has rendered the system attractive for automotive applications, where cost is a major factor in product acceptance (Misra and Enge, 2001).

GPS accuracy is constrained by its susceptibility to many types of systematic and random errors. Some GPS errors, such as atmospheric errors, orbit errors and clock drifts are independent of local surroundings of the receiver, i.e. operational environment. The differential GPS technique (DGPS) reduces or even eliminates several errors of this type (Enge, 1996). Other errors such as multipath, jamming, signal masking and consequently poor geometry are environmentally dependent and can cause significant accuracy degradation in harsh GPS conditions. Multipath is generally one of the largest error sources for land applications, especially in kinematic mode, when the magnitude of this error quickly changes in a manner that is difficult to anticipate or to model mathematically. When the receiver is moving, as in automobile applications, the positions of various multipath sources change rapidly based on vehicle speed and the resulting reflected signals cannot be reliably predicted (Cannon and Lachapelle, 1992). The accuracy degradation caused by signal masking and poor geometry can be mitigated by the use of innovative High Sensitivity (HS) GPS technology (Enge et al., 2001; MacGougan et al, 2002).

Unlike conventional GPS receivers, HS GPS receivers make measurements in signal conditions where conventional sensitivity receivers fail. HS receivers are capable of tracking and acquiring signals in challenging environments, which often include the interior of buildings, under heavy foliage and in urban canyons. HS receiver technology is a very powerful tool in terms of the range and quality of solutions available; however, its stand-alone operation is limited to significant errors caused by effects such as multipath, jamming, signal cross-correlation and high noise. MacGougan (2003)

investigated the impact of degraded GPS environments on measurement availability and usability which, in turn, are affected by pseudorange measurement errors, and signal power degradation. In such environments, position errors ranging from 150 metres to the kilometre level were observed. He also showed that a high sensitivity GPS receiver in stand-alone mode could not provide reliable, robust position solutions in certain severely degraded GPS signal conditions.

Thus, in urban canyons or under heavy foliage, it is advisable and feasible to use an external source for position and velocity information, such as an INS, to improve GPS reliability and integrity. GPS integrity is defined as the ability to protect the user from inaccurate information in a timely manner, e.g. during GPS outages ([Lachapelle, 2002](#)).

1.1.2 Inertial Navigation System

An Inertial Navigation System is a system of sensors designed to measure specific force and angular rates with respect to an inertial frame which, when integrated, provide velocity, position and attitude. Unlike GPS, an INS is a self-contained system, so it is autonomous regardless of the operational environment. However, the accuracy of an INS is diminished by systemic errors such as inertial alignment errors and inertial sensor errors ([Titterton and Weston, 1997](#)).

Unlike GPS-type errors, inertial errors are large in magnitude, low frequency in nature and grow over time (e.g. position errors). These error qualities stem from the solution of

the second order differential mechanization equation. INS errors can be divided into two parts. The first is the stationary component (e.g. gyroscope drifts, horizontal attitude errors), which is independent of motion parameters and yields those INS errors oscillating over time with a very small Schuler frequency corresponding to a period of 84.4 minutes. Therefore, this large component is quite predictable from an estimation point of view and, thus, the major part of the Schuler error can be compensated in the output. Its estimation accuracy is defined by knowledge of the system parameters and the nature of the associated errors (such as the level of gyro drifts and accelerometer biases). The second non-stationary class of errors (e.g. sensor scale factors and their nonlinearities, installation errors, and azimuth misalignment) is defined by motion parameters (vehicle accelerations and velocities, traveled distance), which makes it difficult to predict.

High performance INSs (gimballed systems in particular) experience less accuracy degradation. Due to restrictions such as price (over US\$100,000) and government regulations, high performance inertial systems are usually used in military applications and commercial airliners, and are not affordable for general-purpose application areas such as car navigation. Therefore, recent research efforts have focused on the use of a medium accuracy INS and Inertial Measurement Units (IMU) in particular. An IMU is the core hardware of any INS, which contains three accelerometers and three rate gyroscopes configured along three orthogonal axes. Unlike an INS, an IMU provides only raw data, which is already compensated for errors such as scale factors and biases. Consequently, the navigation algorithm has to be developed by users themselves, so that

velocity, position and attitude information can be evaluated. Due to the relatively lower cost of inertial sensors in comparison to high performance INSs, IMUs are characterized by their poor accuracy and run-to-run stability, which can result in large errors over short time intervals. For example, for a medium accuracy IMU with gyroscope (hereinafter gyro) drifts in the range of 1° to 2° per hour, the errors accumulated within an hour can be in the order of 50 to 80 m/s for velocity; up to 30 km in position; from 6° to 8° in azimuth; and 1° to 2° in roll and pitch.

An IMU-based on low cost inertial sensors cannot operate in stand-alone mode but, augmented by an external device such as GPS, it is capable of providing a relatively high accuracy of navigation solution. [Salychev et al. \(2000\)](#) and [Sukkarieh \(2000\)](#) discussed the integration of a Systron Donner MotionpakTM IMU with one or more GPS antennas. Salychev used external heading information to align the IMU, while Sukkarieh proposed the use of non-holonomic constraints, which describe the characteristics of land vehicle dynamics. In elementary terms, the motion of a wheeled vehicle on a surface is governed by two non-holonomic constraints; i.e. vehicles do not move in an upward/downward direction and lateral velocity is almost zero. In summary, it becomes necessary to provide an IMU with regular updates by using external information from other sensors such as a GPS and/or from Zero Velocity Updates (ZUPTs) as described in [Jekeli \(2001\)](#); [El-Sheimy \(2003\)](#). Both methods can be combined to obtain more precise information about the magnitude of the IMU errors ([Grejner-Brzezinska et al., 2002](#)). The complementary nature of IMU and GPS systems in principle and operation, specifically in the sense that

each system compensates for the other's shortcomings, demonstrate the prospective benefits of GPS and INS integration.

1.1.3 INS/GPS Integration

The combination of GPS and INS can deliver superior system performance in comparison to the performance of either system in stand-alone mode. Unlike a GPS receiver, an INS is capable of delivering navigation information at a relatively high rate. The data rate of GPS measurements is typically 1 to 20 Hz depending on the receiver type, while the INS data rate is 60 to 100 Hz on average. Another important advantage of an INS is the ability to provide attitude data in addition to position and velocity information. Despite the above advantages, system inaccuracies due to gyro drifts and accelerometer biases cause a rapid degradation in position quality, while GPS errors are generally smaller and are not time-dependent. Moreover, a GPS receiver has high frequency errors while an INS typically does not. The differences in the nature of errors associated with the two systems benefits their integration through the use of a Kalman filter, which is a linear estimator that uses knowledge of the system dynamics and external measurements to obtain an optimal estimate of the state variables at the current epoch (Gelb, 1974). It follows, therefore, that these two units combined in a common system will provide superior operation in terms of accuracy, integrity and availability (the ability to be used whenever it is needed (Lachapelle, 2002)) than each system in stand-alone operation.

The problem of achieving better performance in terms of accuracy of INS/GPS systems can be divided into two distinct problems: modeling and estimation. The modeling problem is concerned with the development of error models that describe more accurately the INS/GPS system. The estimation issue is devoted to achieving more accurate error estimates, which are used for error compensation, through the proper use of the available process and measurement information. However, there is a contradiction between the two issues, since excessive complication of a system model degrades the estimation accuracy of the state vector components. To achieve optimal results, a balance of the two approaches should be attained. The size of the state vector defines the length of the transition period for the last error component, when all estimates of the state vector converge to actual values. For high dimensions of the system model, this interval can be significantly long, ranging from 100 to 800 seconds. During this time, the estimation accuracy of the other state vector components (directly measured and close to directly measured) is degraded in comparison to the steady state accuracy. Moreover, the estimation accuracy is generally limited to the level of uncertainty of the system model as defined by input noise. The accurate modeling of the random part of INS errors is a very problematic task.

Although recently a wide variety of different estimation algorithms have been investigated for INS/GPS integration (for instance, the neural network technique ([Chiang and El-Sheimy, 2002](#))), Kalman filter techniques are still more commonly applied for many applications ([Shin and El-Sheimy, 2002](#)). From the estimation viewpoint, the optimality of a conventional Kalman filter requires, in principle, good *a priori* knowledge

about the process (the system model) and noise statistics (measurement noise) as well as a sufficiently long estimation time or data length. If the above information is inaccurate or varies in a manner that is not readily predictable, the estimation accuracy degrades from the theoretical prediction. These criteria have limited the applicability of the traditional Kalman filter in the case of INS/GPS systems, both conceptually and practically. Adaptive filters sense the properties of the environments in which they operate and adjust the filter parameters accordingly. Therefore, when the properties of the operating environments are not known, or when they change with time in a previously unknown manner, these filters become very useful. Thus, such estimation methods are beneficial for INS/GPS integration in changing GPS conditions.

Several different integration schemes have been developed in recent years. They can be divided into two types: loosely coupled (sometimes referred to as decentralized) and tightly coupled (referred as centralized) strategies. In tightly coupled schemes all measurements from GPS and INS are processed together in the same filter. The main advantage of this technique is in preserving data availability. When there are less than three satellites observable and the GPS receiver does not provide any navigation solution, the pseudoranges of the remaining satellites can be used for a measurement update. Another benefit of this type of integration comes from the fact, that poor GPS measurements can be detected and rejected from the solution. However, tightly coupled algorithms are computationally less efficient in comparison to loosely coupled schemes and usually have a complex system and measurement models (i.e. the measurement model contains partial derivatives of pseudorange errors, expressed via geodetic

coordinates; the colored measurement noise is introduced to the system model as additional error state). The larger dimension of the state vector in this integration scheme increases the elapsed time to filter convergence. Therefore, the loosely coupled integration has become popular for many applications. This method is based on the independence of the GPS and INS navigation functions. It is a simple and flexible scheme of integration, since the filter size is relatively small in comparison to the tightly-coupled approach. The only limitation of the loosely coupled scheme comes from the fact that at least four satellites are necessary to provide GPS updates for the INS filter (Jekeli, 2001; El-Sheimy, 2003).

Since there is a lack of research devoted to the integration of an IMU with GPS in different surroundings, the intent of this research is to develop a flexible, universal approach to integration of a medium accuracy IMU with two different types of GPS receivers: conventional high performance and high sensitivity. For harsh GPS conditions, the algorithm takes into account the challenge of using HS GPS measurements, which are characterized by high level of noise and exposed to large errors such as tracking of multipath or echo-only signals.

1.2 Literature Review

The idea of INS/GPS integration is not new. A sizeable amount of work has been done to investigate the potential benefits of such a navigation system for land applications (Wolf et al., 1997; Nayak, 2000; Shin, 2001; Petovello, 2003). However, these investigations

evaluate only system performance over short GPS data gaps (i.e. up to 20 seconds) (Nayak 2000), require special GPS attitude equipment for in-run calibration (Wolf et al., 1997) or focused on centimetre-level accuracy positioning (Petovello, 2003).

Some research has been dedicated to the usage of HS GPS receivers for land applications in challenging GPS environments. The operational characteristics of a high sensitivity receiver SiRF Star II Xtrac were investigated by MacGougan (2002). The results indicated that high sensitivity GPS receivers in unaided stand-alone mode provided a higher availability of observations in residential and urban areas as compared to standard receivers, as they were capable of a 3D fix over 92% to 94% of the test duration. However, the filtered position errors were in the order of 25 metres with occasional jumps of 100 metres and more. Mesenzev et al. (2002) used a HS receiver augmented with a low cost rate gyro. In downtown areas with heavily filtered stand-alone GPS solutions, across-track position errors occasionally reached 100 metres. Integration of an HS GPS receiver with a rate gyro improved the position accuracy, resulting in an average position error of below 20 metres.

Land applications, such as car or pedestrian navigation, have been constrained by the cost factor, and this has prevented the use of high performance INS units in these applications. Therefore, in the last few years, many new techniques have been developed using GPS integrated with lower cost IMUs. An IMU affords reduced performance accuracies and it cannot be used as a stand-alone navigation system; but, when augmented by GPS, it can provide acceptable performance. Recent developments demonstrated the reliability of

such systems. [Shin \(2001\)](#) tested a NovAtel Black Diamond System (BDS), which contains a medium accuracy IMU Honeywell 1700 and a NovAtel OEM4 receiver. Using field calibration, a velocity-matching alignment as well as non-holonomic constraints, the INS measurements were used to bridge GPS gaps. [Mohamed \(1999\)](#) investigated an INS/GPS system and developed an adaptive algorithm based on the use of an innovation sequence to estimate the system noise matrix, Q , and the measurement noise covariance matrix, R , in a Kalman filter algorithm for INS error estimation. This information was used for GPS ambiguity resolution technique by applying an On-The-Fly (OTF) Integer Whitening Filter. [Skaloud \(1999\)](#) proposed an adaptive algorithm for INS error estimation by defining the sensor noise using wavelets. This information was further used for GPS ambiguity resolution.

Many new approaches in the field of INS/GPS integration have appeared in recent years in navigation and geodetic applications. Inertial data was used to assist ambiguity resolution by reducing the search space ([Skaloud, 1998](#); [Scherzinger, 2000](#); [Petovello, 2003](#)) as well as for cycle slip detection ([Cannon, 1991](#); [Schwarz et al., 1994](#)). However, in automotive applications, a navigation system is assumed to operate and provide an acceptable solution in weak environments (e.g. urban or suburban areas), where only pseudorange measurements are available for use in the navigation solution.

1.3 Research Objectives and Motivation

Since there is a lack of research towards the integration of an IMU with different GPS receivers depending on the application environments, this thesis is devoted to the

combination of a medium accuracy IMU (Honeywell 1700) with two types of GPS receivers, namely a conventional high performance NovAtel OEM4 and a HS SiRF Star II Xtrac. This research examines the loosely coupled scheme of integration as a flexible method for augmenting an IMU with GPS measurements of different qualities (in other words, the level of errors). The intent of the study is to develop and investigate the operational capability of such a system in terms of accuracy, integrity and availability.

To implement the proposed integration algorithm, this work considers the following tasks:

1. Calculation of the navigation solution for a strapdown INS (SINS) using as an input raw IMU data;
2. Loosely-coupled scheme for INS/GPS integration, which includes estimation of IMU errors, their prediction during GPS outages and finally error compensation in the system output and in the SINS calculation scheme;
3. Investigation of different estimation approaches of the INS/GPS integration for applications in open sky conditions and in urban environments.

The programming is performed in the C++ language using object-oriented programming and is intended for use as a post-processing package utilizing estimation techniques that could be adapted for real-time applications.

The following tests were conducted to assess the quality of the integrated solution under a variety of operational environments:

1. Open areas with simulated GPS data gaps for verification of prediction accuracy;
2. Residential areas with partial short-term satellite blockage due to one- and two-level houses and roadside foliage;
3. Urban canyons with heavy masking effects due to high buildings.

1.4 Thesis Outline

The thesis consists of seven additional chapters. Chapter 2 provides an overview of GPS, namely the main concepts, error budget and high sensitivity theory. Chapter 3 describes the principle of inertial navigation, the mechanization equations for calculation of the navigation solution, as well as the INS error sources and their nature. Chapter 4 discusses the main algorithms of INS/GPS integration and the estimation methods, including the Kalman filter and its adaptive version for applications in harsh GPS environments. Chapter 5 describes in detail the INS/GPS method employed. The integrated scheme investigated in this thesis includes a cascaded technique for in-motion azimuth estimation, as well as gyro drift compensation. For downtown applications, the integrated scheme uses a simplified INS model and adaptive filtering for changing GPS measurement covariance; the algorithm also adjusts filter parameters depending on vehicle dynamics. Chapter 6 presents results of field testing in open areas. The analysis of the impact of different INS error components on the overall accuracy of the integrated system is given in this chapter. Chapter 7 presents the results of suburban and urban area testing. It describes the test conditions in terms of a profile of typical building heights and the nature of obstructions that may degrade GPS operation. The limitations in the system

accuracy due to long-term operation in prediction mode and error-corrupted GPS measurements are also discussed. Chapter 8 summarizes the major results of the integrated system operation in different GPS environments and makes recommendations for future work.

Chapter 2

Overview of Global Positioning System

This chapter presents an overview of the GPS concept and an introduction to high sensitivity GPS theory; the various GPS error sources, their nature. Methods of error mitigation are also discussed. GPS environments are briefly characterized and the main challenges that should be considered in degraded GPS mode are described.

2.1 GPS Concept

The Global Positioning System is a satellite-based navigation system, which provides accurate position and velocity information worldwide. It is well described in standard textbooks such as [Kaplan \(1996\)](#), [Parkinson \(1996\)](#), [Hofmann-Wellenhof et al. \(1997\)](#), [Misra and Enge \(2001\)](#) and is not discussed in detail here. Currently, the GPS constellation contains 28 operating satellites located in six orbital planes. GPS is based on the time-of-arrival (TOA) ranging principle of determining receiver position ([Kaplan, 1996](#)). The crux of the TOA concept lies in measuring the time it takes for a radio frequency (RF) signal broadcast from a GPS satellite with a previously determined position to a receiver. The pseudorange measurement, which incorporates distortions due to errors, can thus be obtained from knowledge of the signal propagation speed, i.e. the speed of light.

GPS satellites transmit two carrier frequencies: the primary L1 (1575.42 MHz) and secondary L2 (1227.60 MHz). These frequencies are modulated by the navigation message and by spread spectrum codes with a unique Pseudo-Random Noise (PRN) sequence for each satellite (Ward, 1996a). Therefore, a signal coming from each satellite of the GPS constellation can be distinguished and separated from others by the Code Division Multiple Access (CDMA) technique. Currently, GPS signals are modulated by two codes, namely, the Coarse-Acquisition (C/A) code on L1 and the Precise (P) code on L1 and L2. The P-code is restricted to military use via its encryption by the Y code, a practice known as anti-spoofing. To decode Y-code encrypted signals, codeless and semi-codeless cross-correlation tracking techniques are used (Lachapelle, 2002), however these methods diminish the signal-to-noise ratio (SNR) by 14 dB or more and thus increase the noise level in the observations. This thesis deals only with L1 C/A-code measurements, of which a more detailed description follows.

The C/A-code is generated by two 10-bit shift registers, where the outputs of the two registers are again added to produce the new code (Misra and Enge, 2001; Cannon, 2001). The C/A-code is a relatively short code with a period of 1 ms (1023 bits) for fast acquisition at a rate of 1023 Mbps. To provide good multiple access properties, the C/A-codes are designed from a family of codes referred as Gold codes, which are obtained from the product of two equal period 1023 bit codes to form a code with the same period (Spilker, 1996a).

In general, the GPS signal contains pseudorange, carrier phase and Doppler measurements. The L1 C/A-code pseudorange and Doppler measurements can be utilized for position and velocity calculation; these measurements are used typically in high sensitivity receiver applications.

2.1.1 Pseudorange Measurements

Pseudorange observations are obtained by measuring the transit time of the signal as it travels from the GPS satellite to the receiving antenna. Due to non-synchronized receiver and satellite clocks, the measured range (pseudorange) is biased. Therefore, the receiver's clock difference with respect to the satellite's GPS time must be taken into account. This leads to a system of equations with four unknown parameters (three coordinates and clock drift); thus at least four satellite observations are necessary for position calculation.

The code observable P for a single satellite can be expressed as (Misra and Enge, 2001; Lachapelle, 2002):

$$P = \rho + d\rho + c(dt - dT) + d_{ion} + d_{trop} + \varepsilon_p \quad (2-1)$$

where: ρ is the geometric range between the GPS satellite and receiver antenna (m);

$d\rho$ is the orbital error (m);

dt is the satellite clock error (s);

dT is the receiver clock error (s);

d_{ion} is the ionospheric delay (m);

d_{trop}	is the tropospheric delay (m);
ϵ_p	is the code noise (receiver noise + multipath) (m); and
c	is the speed of electromagnetic wave in vacuum (m/s).

A brief overview of each of these errors is given below; a more detailed treatment is given in works such as Kaplan (1996), Parkinson (1996), Hofmann-Wellenhof et al. (1997), Misra and Enge (2001). Orbital, satellite clock, and atmospheric errors can be reduced or even eliminated by differencing pseudorange measurements with a receiver at a known location (herein referred as DGPS) or by applying algorithms designed to model their effects. Some models are based on the parameters broadcast from the GPS constellation. The receiver clock error is usually included as an unknown parameter in single point and single difference GPS methods. Noise depends on the received signal strength and on the correlation method employed in the receiver, so that it cannot be decreased without access to the hardware. Multipath is caused by multiple reflections of GPS signals interfering with the line-of-sight signal (LOS). It is environmentally dependent and thus cannot be mitigated by DGPS. This error is also difficult to model and therefore to satisfactorily compensate for. More extended investigations concerning atmospheric and multipath errors can be found in Skone (1998), Ray (2000) and MacGougan (2003).

2.1.2 Doppler Measurements

Doppler measurements are based on an established physical principle that is readily observed in nature. For a moving emitter (namely a satellite) or a moving receiver, the

received frequency is Doppler shifted with respect to the emitted source. This means that the received frequency differs from the emitted one by a certain amount, which is velocity-dependent (Hofmann-Wellenhof et al., 1997). By measuring this frequency shift and knowing the emitter's velocity, one can determine the receiver's velocity. In the case of GPS, the Doppler is a measurement of the instantaneous phase rate of a tracked satellite's signal; as a result, the velocity of the user with respect to the GPS satellites can be determined. Doppler measurements are also error-corrupted (Misra and Enge, 2001; Lachapelle, 2002):

$$\dot{\phi} = \dot{\rho} + d\dot{\rho} + c(dt - dT) - \dot{d}_{ion} + \dot{d}_{trop} + \dot{\epsilon}_{\phi} \quad (2-2)$$

where: $\dot{\phi}$ is the Doppler observable (m/s);
 $\dot{\rho}$ is the geometric range rate (m/s);
 $d\dot{\rho}$ is the orbital error drift (m/s);
 dt is the satellite clock drift;
 dT is the receiver clock drift;
 d_{ion} is the ionospheric delay drift (m/s);
 d_{trop} is the tropospheric delay drift (m/s);
 $\dot{\epsilon}_{\phi}$ is the receiver noise and the rate of change of multipath (m/s).

Similarly to pseudorange errors, the atmospheric effects and satellite clock drift are reduced by DGPS, where the receiver clock drift is considered in the velocity calculation scheme as an unknown parameter, so that a minimum of four Doppler observables is needed to solve for the user's velocity.

2.2 GPS Errors

2.2.1 Orbital Errors

Orbital errors occur due to the differences in the actual and modeled positions of the satellites. Three types of data, of non-uniform accuracy levels, are accessible for position and velocity determination of the GPS satellites: almanac, broadcast ephemerides, and precise ephemerides (Hofmann-Wellenhof et al., 1997). Broadcast ephemerides are available in real time and orbital parameters are uploaded for each interval of two hours. Currently, this type of satellite orbit has an RMS accuracy of about 3 m. More accurate orbit information of about 5 cm can be obtained from the International GPS Service (IGS); however, it is available only from a few days, up to a week, after the observations (Rothacher and Beutler, 2002). Fortunately, orbital errors are correlated for two receivers simultaneously tracking the same satellite and thus can be diminished by differencing observations between the receivers. The remaining errors are generally in the range of much less than 0.5 parts per million (ppm) (Misra and Enge, 2001; Cannon, 2001). PPM is the measure of residual errors in GPS measurements, when differential GPS is used. One ppm means that one cm of position error is introduced per ten km baseline.

2.2.2 Satellite Clock Errors

These errors are due to the offsets in the clock frequency of each satellite with respect to the reference clock, which is monitored by the Master Control Station. The satellite errors are modeled via a polynomial, the coefficients of which are transmitted as a part of the

navigation message (Parkinson, 1996; Lachapelle, 2002). The satellite error is usually less than 1 ms and, after implementing the broadcast correction, the remaining error is in the order of 8 to 10 ns (2 to 3 m). This error can be eliminated by the DGPS (difference in between the receivers), since it is the same for all receivers in the proximity, subject to essentially identical signal paths, simultaneously tracking the same satellite.

2.2.3 Receiver Clock Errors

This error is the offset of the receiver clock with respect to the reference GPS time. The error magnitude is a function of the receiver's internal firmware. It can range from 200 ns up to a few ms, and changes over time due to the clock drift, the magnitude of which is a function of the type of oscillator used in the receiver. It can be estimated along with receiver coordinates or removed by single differencing between two satellites (*ibid*).

2.2.4 Ionospheric Errors

Signal propagation through the ionosphere produces one of the most significant sources of GPS error. It extends from roughly 50 to 1000 km above the Earth's surface (while the GPS orbits are 20000 km above the Earth). The ionosphere is formed by ultraviolet (uv) ionizing radiation from the Sun and is characterized by a significant amount of free electrons, which in turn affects electromagnetic wave propagation and thus GPS signals. The group delay of the ionosphere produces range errors, which typically vary from 1 to 50 ns or equivalently 0.3 to 15 m in vertical (Misra and Enge, 2001; Lachapelle, 2002). Ionospheric effects show diurnal and seasonal variations; they depend on the solar cycle

and the geographic location of the RF receiver. The ionospheric delay is a function of frequency. Dual frequency GPS users can utilize this property to correct the error in range and Doppler measurements. Single frequency users can compensate for ionospheric error using the approximate model (e.g. the Klobuchar model), which is based on broadcast parameters included in the GPS navigation message (Klobuchar, 1996). As the ionospheric error is spatially correlated, it can also be reduced by single differences between receivers. The degree of improvement in error mitigation depends on the baseline length between the two stations, typically resulting in a residual error of about 2 ppm.

During periods of heightened solar and geomagnetic activity, other effects - namely, ionospheric scintillation and magnetic storms - have a crucial influence on GPS signals. Irregularities in the ionosphere produce diffraction and refraction of RF signals, causing short-term signal fading and enhancements which, in turn, can significantly stress the tracking capabilities of a GPS receiver and can lead to complete loss of lock. Under extremely high ionospheric conditions, the error can reach 100 m and more for single point positioning and 20 ppm for differential GPS solutions (*ibid*).

2.2.5 Tropospheric Errors

The troposphere is a part of the Earth's atmosphere, which affects GPS signals at altitudes up to 50-70 km above the surface. The troposphere causes delays in GPS ranges due to the slowing and bending of GPS signals. Tropospheric errors can be on the order

of 2 m at the zenith and can reach 25 m for low elevation GPS signals. Tropospheric delay is subdivided into dry and wet components due to distinct influences on RF signal propagation. The dry portion typically contributes 80-90% of the entire effect; however, it can be modeled with an accuracy of about 1% at the zenith using meteorological data. By contrast, the wet term constitutes the remaining 10-20% of the total error, but it can be predicted with an accuracy of only 10–20% (Misra and Enge, 2001; Lachapelle, 2002). Several models are available to estimate the tropospheric delay such as the Hopfield, Saastamoinen and Black and Eisner (B&E) models (Spilker, 1996b). Due to the spatial correlation of the tropospheric error, it can be significantly mitigated by the differential technique (difference between receivers) producing a residual error in the order of about 1 ppm or less (Lachapelle, 2002).

2.2.6 Multipath Errors

This effect is well described by its name: a satellite-emitted signal arrives at the receiver via more than one path (Hofmann-Wellenhof et al., 1997). It is caused by reflected signals that interfere with the direct signal coming to the GPS antenna. Multipath is one of the largest GPS error sources, especially in weak signal environments. It is difficult to predict and to compensate for, since it is environmentally dependent and thus cannot be mitigated via the differential technique (Ray, 2000). Multipath occurs mainly due to reflecting surfaces near a GPS receiver, such as buildings, tree foliage, water bodies and even the ground surface. These surroundings are very typical for high sensitivity users, where LOS signals may be weak with respect to the strength of the multipath signal.

During signal transmission, secondary effects occur due to reflections at the satellite; however, multipath effects at the receiver are a main object of concern in published works on the subject.

Multipath signals are always delayed, since they travel longer distances than direct (LOS) satellite signals. When they arrive at the RF front end, reflected signals have relative phase offsets, and these phase differences are proportional to the differences of the path lengths (Hofmann-Wellenhof et al., 1997). The phase of the reflected signal defines the sign of the multipath error, which can be either negative or positive. There is no general model of the multipath effect because of the arbitrary nature of unique geometric situations. Based on the signal path geometry, it is understandable that signals received from low elevation satellites are more liable to be affected by multipath compared to signals close to the zenith. Multipath is classified by the properties of the reflecting sources: 1) diffuse forward-scattering from a widely distributed area (e.g. rough surfaces); or, 2) specular reflection from smooth surfaces (e.g. water bodies, metal surfaces).

Pseudorange multipath is limited by the chipping rate. The higher the chipping rate, the lower the maximum multipath (Leick, 1995; Misra and Enge, 2001). Code multipath errors are related to the GPS code. The maximum multipath error for the C/A-code and the wide correlator is 0.5 chip, which corresponds to 150 m since the C/A chip length is 300 m. The C/A-code is affected by a maximum delay of 1.5 code chips; in other words, signals delayed more than 450 m do not introduce an error to the C/A-code. Code

multipath errors are usually in the order of 10 m to 100 m depending on environmental conditions. The direct and reflected signals superimpose to produce the composite received signal and, in turn, affect the correlation property of the C/A-code. This is illustrated by Figure 2-1. In static applications, multipath introduces a systematic error that contains low frequency fluctuations. It can be measured and compensated via extended observation periods and statistical analysis, since multipath is correlated day-to-day due to the repeated satellite-receiver geometry (Ray, 2000; Lachapelle, 2002). Multipath decorrelates rapidly as a function of distance between the reflecting surface and the GPS antenna. In kinematic mode, due to the changing environments, the positions of various reflectors change rapidly based on vehicle speed; as a consequence, the resulting reflected signal is almost impossible to model and predict (Cannon and Lachapelle, 1992). Therefore, external navigation information from an independent device is needed to smooth GPS measurements that have been corrupted by multipath.

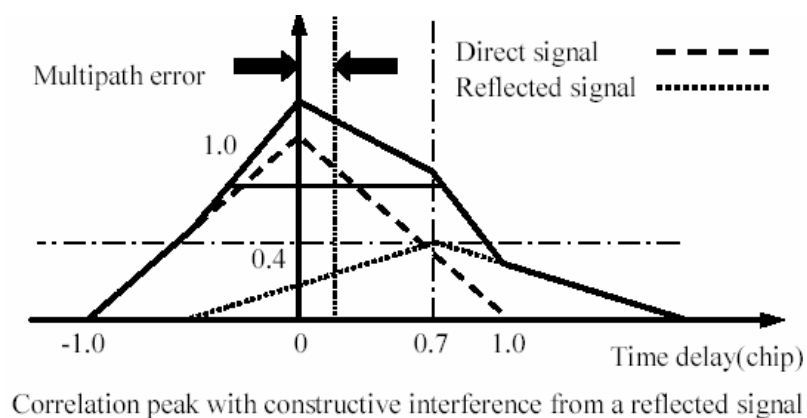


Figure 2-1: Multipath Delay on Code Measurements (GCTE, 2004)

Most multipath mitigation techniques are based on the design of suitable receiver architectures for multipath minimization. There are also special antenna designs such as

choke rings, groundplanes and other multipath-limiting technologies - namely antenna gain patterns, where the received signal strength is elevation-dependent. As was discussed in the above, multipath error depends on the distance between the refractor and the GPS antenna. It is also defined by correlator spacing and the pre-correlation bandwidth (Braasch, 1995; Braasch, 1996). This phenomenon is exploited in the Narrow Correlator technique, where the spacing between the early and the late correlators is decreased from the standard 1 chip, with a pre-correlation bandwidth of 2 MHz, to 0.1 chip with a pre-correlation bandwidth of 8 MHz. (van Dierendonck et al., 1992). The standard correlators are susceptible to multipath errors for C/A-code chip delays of up to 1.5 chips (450 m), with the most significant C/A-code multipath errors occurring at about 0.25 and 0.75 chips (75 and 225 m respectively). For narrow correlators, multipath susceptibility peaks are at about 0.2 chips (60 m) and maximum multipath error occurs at about 1.1 chip (330 m). More advanced methods have been developed recently, such as METTM (Multipath Elimination Technique) (Townsend and Fenton, 1994) and the MEDLLTM Multipath Estimation Delay Lock Loop, (van Nee et al., 1994). Multipath delays for different types of receiver correlators are illustrated in Figure 2-2. A detailed description of multipath error as well as methods of its mitigation can be found in Ray (2000), Misra and Enge (2001), and MacGougan (2003).

It must be mentioned that multipath becomes a large source of error especially for HS applications in downtown environments. In highly urbanized areas, LOS satellite signals can be completely blocked, while echo signals have enough power to be tracked by a HS GPS receiver. For echo-only signals, the maximum threshold for multipath does not

apply, since this error is generally unlimited. This can cause large blunders in GPS measurements, which develops into a challenge for estimation algorithms because this type of error is difficult to model or isolate.

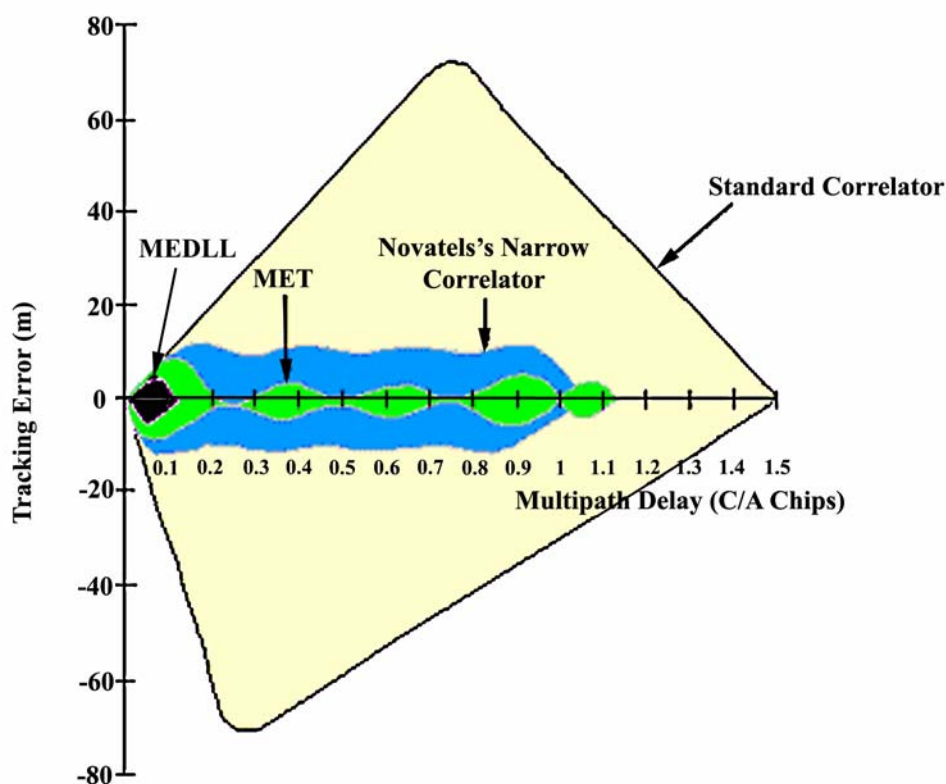


Figure 2-2: Multipath Envelope (Spencer, 2004)

2.2.7 Receiver Noise

Code noise is generated by the receiver itself in the process of taking a measurement. It may be considered as white noise and is typically caused by the high frequency thermal noise along with the effects of dynamic stresses on the tracking loops (Ward, 1996b). Also, because of the use of independent signal tracking loops for individual parallel

channels, there is no correlation due to noise between the channels for measurements taken at the same time. The noise level is a function of the code correlation method, receiver dynamics, and satellite elevation due to the antenna gain pattern (Ward, 1996b; Lachapelle, 2002). Code measurement noise is usually about 5-10 cm but, for GPS signals at low elevations, it can approach several decimetres. The receiver noise increases by a factor of $\sqrt{2}$ for differential measurements.

Noise on pseudorange and Doppler measurements increases as signal power decreases due to growing thermal noise jitter in the carrier tracking loop and the code tracking loop. Pseudorange measurement noise depends on correlation spacing and associated pre-correlation bandwidth, as well as the bandwidth of the delay lock loop (DLL) used in code tracking. Pseudorange noise can be reduced by the carrier-aided DLL (Ward, 1996b) as well as narrow correlation techniques. Doppler measurement noise depends on the thermal noise of the carrier tracking loop and thus depends on the correlation bandwidth. Weaker signals will have higher associated measurement noise in general, which becomes a big issue for HS GPS users. MacGougan (2003) tested the relationship between the signal power and Estimated Relative Pseudorange Error (ERPE) using a hardware signal simulator. ERPE is a relative measure of unmodelled error effects embedded in the measurements. In simulated free-of-error GPS measurements, the main source of ERPE is receiver noise. MacGougan (2003) showed that ERPE could increase up to 25 m for GPS signals faded by 20 to 25 dB. Fading is a measure of signal attenuation, and is defined as the difference between C/N_0 values measured by nearby

identical remote and reference receivers, where the reference station has LOS signal reception.

2.3 High Sensitivity GPS

High Sensitivity (HS) receivers are capable of tracking low power GPS signals, when conventional receivers typically experience frequent loss of lock or signal acquisition failure. HS receivers are generally used in challenging environments with heavy signal masking such as forests, urban areas and even indoors. In these conditions, weak signals usually contain attenuated LOS signals, diffracted signals, multipath and echo-only signals. Use of these measurements degrades the GPS solution significantly, since low power signals are generally noisy and can have large outliers due to reflection effects such as multipath and echo.

2.3.1 GPS Signal Power

Degraded GPS signals are frequently associated with the term, attenuation. Attenuation of a LOS GPS signal is defined as the decrease in its power with increasing distance from a transmitting source (satellite), due to geometrical spreading (free space loss) and absorption in the atmosphere (Misra and Enge, 2001; Lachapelle, 2002). Attenuation is usually expressed in decibels (dB): $\text{dB} = 10 \log(\text{ratio})$. In GPS applications, the following ratio is used:

$$\text{dB} = 10 \log \frac{P_t}{P_r} \quad (2-3)$$

where: P_t is transmitted power; and
 P_r is received power.

The signal power is expressed via dB-W (dB-Watt); that is the ratio, which is referenced to one Watt of power; nevertheless dB-W is still unitless:

$$\text{dB} - \text{W} = 10 \log_{10} \frac{X}{1\text{W}} \quad (2-4)$$

where X is the ratio P_t/P_r .

Due to attenuation, received GPS signals are generally weak. Table 2-1 presents the GPS signal power budget for a C/A-code L1 LOS signal. As shown in the table, free space loss accounts for the largest component of the signal power budget. It is frequency-dependent and increases with the distance traveled by the signal (i.e. the distance between a satellite and a receiver) and thus changes with elevation. The received minimum signal strength for the L1 C/A-code is -160 dB-W; however, the signal power received by a GPS antenna is typically about -158 to -156 dB-W, since GPS satellites emit signals that are on average 5.4 dB higher than the specified minimum (Spilker, 1996a).

The above discussion of signal budget does not account for attenuation due to propagation through various materials and signal reflection. These effects can significantly degrade signal power; thus, HS GPS receivers are designed to sense signals having a power level in the range of -182 dB-W to -188 dB-W (Ray, 2002; MacGougan, 2003). This facilitates receiver function at attenuations of 27 to 33 dB with respect to the typical average received power of -154.6 dB-W.

Table 2-1: Signal Power Budget (Lachapelle, 2001)

Signal Power Budget	Power (dB-W)
SV antenna power	13.4
SV antenna gain	13.4
Effective isotropically radiated power	+26.8
User antenna gain (hemispherical)	3.0
Free space loss for L1	-184.4
Atmospheric attenuation	-2.0
Depolarization loss	-3.4
Total loss reduced by antenna gain	-186.8
User receiver power	-160.0

2.3.2 Signal Power Reaching GPS Receiver

The received GPS L1 C/A-code signal power is specified to be at least -160 dB-W while, in reality, it is 2 dB greater at higher elevation angles due to the shaped transmit beam pattern on the satellite antenna arrays (Ward, 1996a). However, the received power also depends on the gain pattern of the GPS antenna, which is typically at its maximum at the zenith, and minimum at lower than 5° elevation angles.

2.3.3 Carrier-To-Noise Density Ratio

Carrier-to-noise density ratio (C/N_0) is one of the most commonly used estimates of GPS signal quality. C/N_0 is an instantaneous measure of the ratio of the carrier power with respect to noise power density measured per Hertz of bandwidth (and similarly for dB-W/Hz). With a nominal noise floor spectral density of about -204 dB-Hz and minimum guaranteed signal power at -160 dB-W/Hz, the nominal C/N_0 magnitude is around 44 dB-Hz (Ward, 1996a). In theory, C/N_0 is unrelated to the type of receiver; however, each receiver computes this value based on the measured signal (using the automatic gain control measurement or the signal-to-noise measurement). C/N_0 also depends upon the antenna gain pattern, and the correlation process used by the receiver.

2.3.4 Main Concept of High Sensitivity GPS

As mentioned in Chapter 1, HS receivers are specially designed to track low power GPS signals. The L1 C/A-code repeats every millisecond. This can be used by the GPS receiver, so that the signal can be integrated for extended periods of time in order to obtain a higher Signal-to-Noise Ratio SNR (Peterson et al., 1997). Prior investigations into the use of low power GPS signals using long dwell times (which is defined as signal integration time per frequency-time cell) have been performed by Peterson et al. (1997), Moeglein and Krasner (1998) and Chansarkar and Garin (2000).

If a receiver is already tracking a GPS signal, the task of maintaining signal tracking under weak signal conditions is much easier than acquisition of weak GPS signals. Signal

acquisition is generally difficult, while signal tracking is easier; signal reacquisition presents a challenge midway between these operations in terms of difficulty. The ability to acquire and track weak GPS signals depends on the capability of the receiver to maximize the coherent integration interval prior to non-coherent accumulation, while minimizing residual frequency during coherent integration (MacGougan, 2003). Coherent integration is the algebraic sum of the signal and noise over the integration period, while non-coherent integration uses the squared output of coherent integration. The ability to predict the sign of the bits and the timing of the navigation message signal modulation directly affects the ability to perform long coherent integration.

Unlike tracking mode operation, signal acquisition mode is characterized by unknown navigation data bits, which has the effect of limiting integration time. Signal acquisition is an initial search process in two dimensions (range and frequency), a situation that requires replication of both the code and carrier of a satellite to acquire the signal. If a GPS receiver is supplied with aiding data by means of an almanac, rough estimates of a user's velocity, position and GPS time, then SV's positions and LOS Doppler are computed; the most favorable constellation, in terms of lowest dilution of precision (DOP), is determined; thus, the search process time is relatively short, in the order of 30 seconds to first fix. Otherwise, a GPS receiver works in "sky search" mode; because of this, the search pattern is large and the expected search time is long, possibly approaching several minutes. During signal reacquisition, due to known Doppler uncertainty and almanac information, the search process time is reduced significantly (Ward 1996b; Ray, 2002).

Chansarkar and Garin (2000) described the use of GPS signals at very low power levels using long dwell times. In a coherent type of discriminator for the code, the local carrier frequency and phase are assumed to be the same as the incoming carrier frequency and phase (Ray, 2002). In this case, the correlation values of the quadrature-arm correlators are zero, and they are not implemented. Only the in-phase arm correlators are used for the coherent type of code tracking loops. The nominal maximum coherent integration time is limited to the navigation bit boundaries, thus the integration can be performed coherently for up to 20 ms (Ward, 1996b; Ray, 2002). Longer coherent integration is possible, if the navigation bits are known *a priori*, but this process is still restricted by the residual errors due to receiver and satellite movements during the integration interval. Non-coherent integration, which is defined as integration of the squared in-phase and quadrature-phase signal components, can be performed for longer periods of time relative to the coherent integration, since it is unrelated to navigation data bits. In addition, it is insensitive to residual frequency errors due to the recovery of the satellite movement during the accumulation period. However, squaring of the signal in non-coherent accumulation also results in squaring of the noise and thus leads to a squaring loss (van Diggelen, 2001a; Ray, 2002; MacGougan, 2003). Using the full coherent and non-coherent integration times, weak signal tracking in degraded GPS environments becomes possible.

To combat against the difficulty in working with weak signals, a new technique referred to as Assisted-GPS (AGPS) has been developed in recent years (Moeglein and Krasner, 1998; van Diggelen, 2001b). Unlike conventional GPS, the receiver does not extract the ephemeris or any other data from the GPS satellite data message. Information about

ephemeris - an approximate time and position - is instead provided over a wireless phone communication channel. Having information about in-view satellites and time, the receiver can make a pseudorange measurement, using a long integration interval, even when the signal power is much lower than the C/N_0 , normally needed to read the ephemeris data from the navigation message without an error.

An Unaided High Sensitivity (UHS) GPS receiver, hereinafter in this thesis referred to as an HS GPS receiver, differs from an AGPS receiver in that it must be provided once with time, position, and satellite ephemeris in order to use longer dwell times. Instead of telephone communication, the receiver should be initialized in open-sky conditions before being used in weak signal environments. Its use in such environments is limited in time and, thus, it is practical only for testing purposes and is not very suitable for the general user market.

Weak signal processing techniques as well as factors affecting them are well described by Peterson et al. (1997), Chansarkar and Garin (2000), van Diggelen (2001a) and MacGougan (2003), and are therefore not discussed here in detail. Low power signals are associated with high levels of noise. MacGougan (2003) investigated the relationship between noise level (ERPE) and signal fading. He showed that pseudorange noise could increase by up to 10–25 m for signals degraded by 20-25 dB. The amount of tolerable frequency error during the total dwell time depends on the length of coherent integration and the type of carrier tracking performed. Phase lock loops and frequency lock loops cannot tolerate phase errors greater than 15° and 30° respectively during the total dwell

time (Ward, 1996b). The dominant sources of phase error are phase jitter (mostly thermal noise) and dynamic stress error. The first component is mostly dependent on the noise bandwidth, C/N_0 and predetection integration time. The second component depends upon the loop bandwidth and its order. For information about the major error sources for signal acquisition, which become especially important for low power signals, the reader is referred to Ward (1996b).

2.3.5 Other GPS Errors and High Sensitivity Applications

In HS applications, GPS accuracy is limited not only by standard error sources such as clock drifts, orbit and atmospheric errors, but also by interference effects. High sensitivity GPS measurements are particularly vulnerable to tracking of false correlation peaks due to signal self-interference and echo-only signals. This section discusses signal masking and interference phenomena in the context of weak signal usage.

Due to receiver design and application areas, HS receivers are exposed to track echo-only signals. This condition occurs in urban canyons; for example, when a skyscraper blocks a direct GPS signal, while a strong glassy reflection from another building is tracked. The attenuated LOS signal may still reach the antenna but, if the power of the reflected signal is much greater, the receiver will most likely track the echo-only signal (Chansarkar and Garin, 2000; MacGougan, 2003). This situation can cause very large measurement errors much greater than the maximum multipath error of ± 150 m for wide correlator receivers.

In harsh GPS environments, such as downtown canyons and forests, signal masking frequently occurs due to obstacles, such as buildings and trees. It can cause severe degradation in geometry and consequently accuracy degradation. This situation may lead to a complete loss of signal tracking and may visibly induce direct signal attenuation. The direct signals may be weaker than the reflected ones (multipath or echo only) reaching the antenna. Such signal masking could also cause large tracking errors.

Due to the *C/A*-code properties, its cross-correlation and autocorrelation features are not ideal, such as small autocorrelation peaks in the periods between maximum autocorrelation peaks as well as the sensitivity of the code to continuous wave (CW) and broadband interference (Ward, 1996c; MacGougan, 2003; Deshpande and Cannon, 2004). These *C/A*-code properties can be especially problematic during search and acquisition modes. Acquisition of a false correlation peak due to cross-correlation signals, jamming or sidelobe tracking leads to large measurement errors. The cross-correlation peaks and the true correlation peak could have comparable power levels under some conditions, which makes false correlation peak phenomena quite frequent occurrences for HS receivers.

Interference effects from different jammers or unintentional in-band sources can have a significant influence on the resultant GPS accuracy, especially for HS users. Continuous wave and broadband interference effects are the most harmful kinds of interference for civilian applications. CW interference generally consists of signals with very narrow bandwidths, occupying less than 100 kHz (Rash, 1997; MacGougan, 2003). It can be

centered around L1, and may effectively avoid filtering techniques due to the fact that all of the interfering power is located within its narrow bandwidth (MacGougan, 2003). Besides intentional jamming, CW interference can be produced by the transmitter harmonics of FM radio stations. Deshpande and Cannon (2004) showed that narrow in-band CW interference could jam the GPS signal with 15dB more power than the GPS signal power. Wideband jammers effectively lower the C/N_0 ratio by increasing the noise level. The effect of such jamming varies from increase of the noise level to loss of signal tracking and the inability of the receiver to reacquire the GPS signals. Apart from intentional jammers, typical sources of wideband interference in the GPS spectrum are television transmitter's harmonics or overpowered pseudolites. Broadband interference is a Gaussian wideband interference signal that is usually generated by an intentional noise jammer (Spilker and Natali, 1996). Broadband interference signal being close to the GPS signal noise, adds to the GPS correlation noise to increase it in the bandwidth of the broadband signal (Deshpande and Cannon, 2004). A broadband interference signal is potentially more dangerous than the CW interference signal since it is more difficult to predict. Deshpande and Cannon (2004) demonstrated that broadband interference could jam the GPS signal with 30 dB more interference power than the GPS signal.

Weaker signals will have higher associated measurement noise in general; therefore, it also becomes an issue for HS GPS. For more details on error sources affecting HS users, see Ward (1996c), MacGougan (2003).

2.3.6 GPS Environments in Application to High Sensitivity GPS

Open Sky Areas

Open areas present ideal conditions for GPS use and in this case GPS receiver typically tracks up to 10-12 satellites. Thus, at least 7 or 8 satellites above the elevation cut-off (usually it is above 10°) are used in an ideal navigation solution. It provides good geometry and redundancy for error analysis. In this case, only standard GPS errors, such as clock, orbital and atmosphere errors, have to be considered in the calculation algorithm. By implementing error modeling and/or the differential technique, one can achieve a positional accuracy in the range of metres to centimetres depending on the measurements used (i.e., code or carrier phase).

Harsh GPS Environments

High sensitivity GPS receivers are capable of operating in environments that have traditionally challenged conventional GPS receivers. Degraded (harsh) environments include forests, suburban residential areas, urban canyons and even enclosed artificial structures. This thesis is devoted to navigation applications in an urban environment, including residential and urban areas; a brief discussion of these environments is, therefore, given below.

In suburban environments, signal masking is observed only at low elevations due to trees and one to two-storey buildings. Multipath sources are also located at low elevation angles. Environmental variables include the surrounding foliage, the height of buildings, and the proximity of obstacles to the GPS receiver. Generally, interference effects can be significantly reduced by an increase in elevation cut-off.

In urban canyons, signal masking occurs due to skyscrapers and other high buildings. Thus, signal attenuation and strong glassy reflections become frequent sources of signal degradation. In some downtown areas, signal masking occurs from two directions only. For example, when driving in a city with streets running East-West and North-South, there will often be open sky perpendicular to the direction of motion. Environmental variables in urban canyons include the height of buildings, the reflective ability of building walls, and street orientation. Such environments are characterized by severe masking and interference effects, which are difficult to model and mitigate.

Measurement Availability

Measurement availability is a measure of the number of available measurements within each epoch. Another characteristic of availability is a fix density (FD), which is defined as the percentage of time during the test when the navigation solution can be computed (MacGougan, 2003). The assumption is that, if less than four satellites are available, then the receiver cannot provide a three-dimensional (3D) position solution at that epoch. With three measurements, a height-constrained solution can provide 2-dimensional (2D)

position. In this thesis the term 4D fix density (4D FD) is defined as percentage of test time when at least four measurements are available, and similarly a 3D fix density (3D FD) is percentage of time when at least three measurements are available.

Chapter 3

Overview of Inertial Navigation System

This chapter gives a brief introduction to inertial navigation in general, including a description of the coordinate frames usually utilized in inertial data processing, and a classification of inertial navigation systems and mechanization equations. The principle of INS alignment is also presented, followed by a discussion of INS errors and their estimation.

3.1 Coordinate Frames

To proceed with the basic concept of inertial navigation, the definitions of coordinate frames usually utilized are below.

3.1.1 Inertial Navigation Frame

According to the Newtonian definition, an inertial frame (i-frame) is considered as non-rotating and non-accelerating relative to distant stars. However, in practice this is impossible to achieve. The best approximation of such frame characteristics is the right ascension system. Thus, the definition of an inertial frame may be re-stated as the following (Schwarz, 1996; Salychev, 1998):

Origin Earth's centre of mass;

- X_i – axis towards mean vernal equinox;
 Y_i – axis complete a right-handed system; and
 Z_i – axis parallel to the spin axis of the Earth.

The inertial frame is presented in Figure 3-1. It should be mentioned that the inertial frame is an abstract definition, since the realistic inertial frame is constrained to the accuracy of gyros of an inertial system.

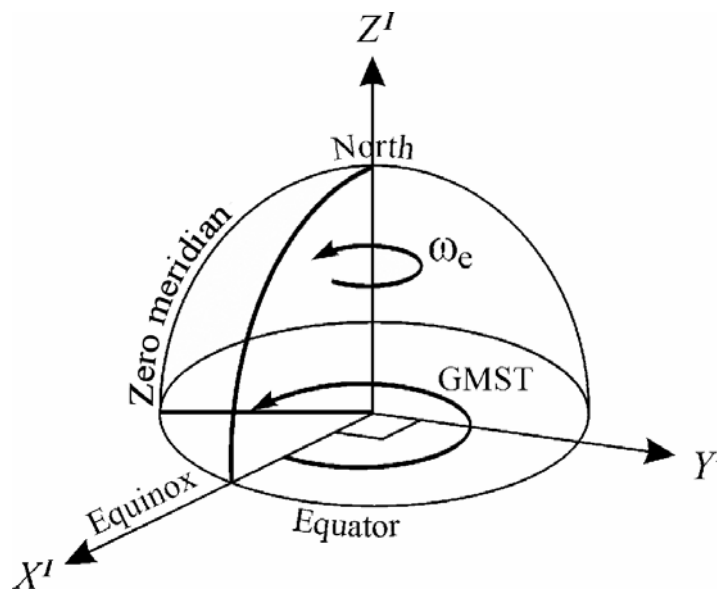


Figure 3-1: Inertial Frame (ibid)

3.1.2 Earth – fixed Frame

By comparison, an Earth-centered, or Earth-fixed, frame is defined as follows:

- Origin Earth's centre of mass;
 X_e – axis towards the mean Zero meridian;
 Y_e – axis complete a right-handed system; and
 Z_e – axis parallel to the spin axis of the Earth.

The coordinates in the Earth-Fixed frame (e-frame) can be transformed to the i-frame by a negative rotation of the Z – axis by the amount of the Greenwich Mean Time (GMST).

A geometrical representation of the e-frame is given in Figure 3-2.

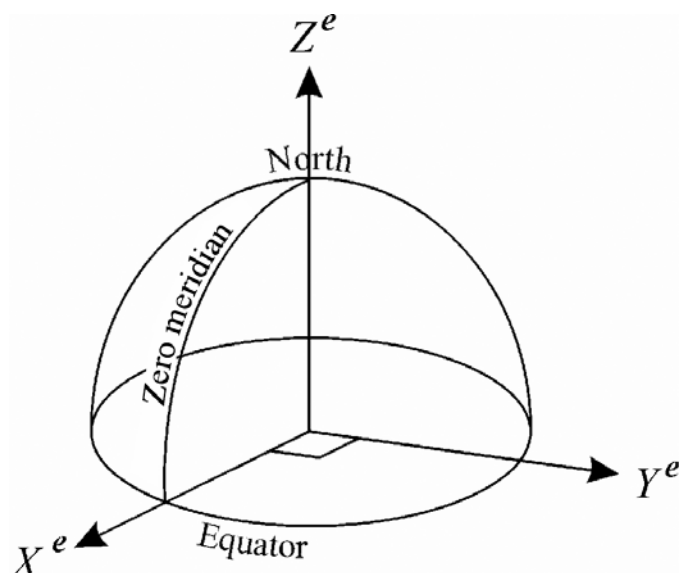


Figure 3-2: Earth-fixed Frame (ibid)

3.1.3 Local – level Frame

A Local-Level frame of reference differs from the Inertial frame and the Earth-fixed frame in location of its origin and axes orientation:

Origin	the centre of an inertial system (its sensitive axes);
X_{ll} – axis	ellipsoidal east (E);
Y_{ll} – axis	ellipsoidal north (N); and
Z_{ll} – axis	upward direction along ellipsoidal normal (Up).

The velocity calculations of an INS are typically performed in the local-level frame (ll-frame). Figure 3-3 gives a graphical interpretation of this coordinate frame.

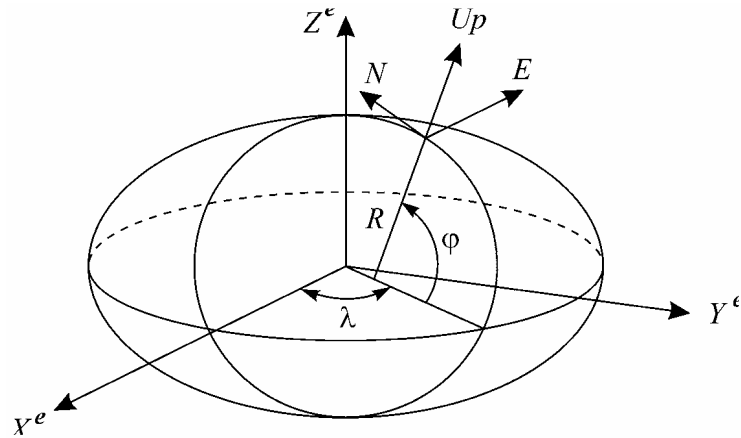


Figure 3-3: Local-level Frame (ibid)

The transformation between the local-level and Earth-fixed frames can be obtained by two consecutive rotations around the X^e and Z^e axes of the e-frame by magnitudes of geodetic latitude, φ , and longitude, λ . It has the following form:

$$\begin{bmatrix} x^e \\ y^e \\ z^e \end{bmatrix} = \begin{bmatrix} -\sin \lambda & -\sin \cos \lambda & \cos \cos \lambda \\ \cos \lambda & -\sin \sin \lambda & \cos \sin \lambda \\ 0 & \cos & \sin \end{bmatrix} \begin{bmatrix} E \\ N \\ Up \end{bmatrix} \quad (3-1)$$

where: φ, λ are geodetic latitude and longitude respectively;

x^e, y^e, z^e are coordinates in the e-frame; and

E, N, Up are coordinates in the local-level frame;

The angular velocity of the ll- frame ($\omega_N, \omega_E, \omega_{up}$) is defined as a sum of two types of rotations: rotation of the Earth and rotation caused by linear motion of the ll-frame:

$$\begin{aligned} \omega_E &= -\frac{V_N}{R_\varphi + h} = \Omega_E \\ \omega_N &= \frac{V_E}{R_\lambda + h} + U \cos \varphi = \Omega_N + U_N \\ \omega_{up} &= \frac{V_E}{R_\lambda + h} \operatorname{tg} \varphi + U \sin \varphi = \Omega_{up} + U_{up} \end{aligned} \quad (3-2)$$

where: U_N, U_{up} are the projections of Earth's rate on the ll-frame;

$\Omega_E, \Omega_N, \Omega_{up}$ are the projections of the relative angular velocity of the ll-frame with respect to the e-frame;

R_φ, R_λ are the radii of curvature of the reference ellipsoid in North-South and East-West directions, respectively; and

h is the altitude above the reference ellipsoid.

Note, that the second components in the right hand side of equation (3-2) are the projections of the Earth's rate of rotation onto the local-level frame.

For a moving vehicle, the change in curvilinear coordinates has the form:

$$\begin{aligned}\dot{\varphi} &= \frac{V_N}{R_\varphi + h} \\ \dot{\lambda} &= \frac{V_E}{(R_\lambda + h) \cos \varphi}\end{aligned}\tag{3-3}$$

3.1.4 Body Frame

A body frame (b-frame) is an orthogonal frame, in which the axes coincide with the axes of an IMU. In gimballed systems, the IMU can be kept aligned to a particular navigation frame of interest (e.g. the local-level frame) using external torques derived from the measured angular rates (Jekeli, 2001). However, in a strapdown inertial system such as that used herein, the IMU is rigidly mounted to the test vehicle and thus can have arbitrary orientation. The ll-frame can be rotated to the b-frame by three consecutive right-handed rotations about its three axes. The first rotation is about its Z-axis with an angle called the heading. The second rotation is about the rotated X-axis by an angle referred to as the pitch. The third rotation about the rotated Y-axis, through an angle

denoted as the roll, completes the total rotation in three dimensions between the two frames. The body frame can thus be defined by the following parameters:

Origin	centre of an IMU;
X_b – axis	towards the right side of an IMU;
Y_b – axis	towards the front of an IMU; and
Z_b – axis	upwards and perpendicular to the XY plane.

In automotive applications, an INS is usually installed in a vehicle in such a way that the Y_b axis coincides with the vehicle's longitudinal axis; the Z_b axis coincides with the vertical axis of the vehicle; and the X_b axis completes a right handed system.

3.1.5 Navigation Frame

The axes of a navigation frame (n-frame) can coincide with any arbitrarily chosen frame such as the local-level or wander frames, where navigation computations are made.

3.1.6 Platform frame

The platform frame (p-frame) is an image of the navigation frame, which is obtained from sensor data. Theoretically, for ideal sensors, the p-frame coincides with the n-frame. In reality the platform frame incorporates small deviations (attitude errors) from the navigation frame due to the IMU sensor errors. The definition of the p-frame is as follows:

Origin	the IMU centre;
X_p – axis	slightly misaligned due to attitude errors with the IMU's X axis;

Y_p – axis slightly misaligned with the Y axis of the IMU;
 Z_p – axis completes an orthogonal right-handed system.

3.1.7 Coordinate Transformations

In order to transform an arbitrary vector from one coordinate frame to another, the transformation (direction cosine) matrix between the two frames is needed. The transformation matrix is based on the computation of the direction cosines between each pair of axes of the two respective frames. The commonly used transformation contains three consecutive right-handed rotations. Each rotation can be represented by a direction cosine matrix R (rotation angle). The angles of rotation, called Euler angles, are three independent quantities, which define the position of one coordinate frame with respect to another. For example, the transformation matrix between the local-level and body frames R_b^l can be obtained from three direction cosine matrices $R_3(A)R_2(r)R_1(p)$ and has the final form (see for example Jekeli, 2001; El-Sheimy, 2003):

$$R_b^l = \begin{bmatrix} \cos(A) \cos(r) - \sin(A) \sin(p) \sin(r) & -\sin(A) \cos(p) & \cos(A) \sin(r) + \sin(A) \sin(p) \cos(r) \\ \sin(A) \cos(r) + \cos(A) \sin(p) \sin(r) & \cos(A) \cos(p) & \sin(A) \sin(r) - \cos(A) \sin(p) \cos(r) \\ -\cos(p) \sin(r) & \sin(p) & \cos(p) \cos(r) \end{bmatrix}$$

(3-4)

3.2 Principle of Inertial Navigation

3.2.1 Poisson equation

The differentiation of any vector with respect to the inertial space has the form (given by the Coriolis formula) as follows:

$$\left. \frac{d\bar{r}}{dt} \right|_I = \left. \frac{d\bar{r}}{dt} \right|_m + \bar{\omega}_m \times \bar{r} \quad (3-5)$$

where: $\left. \frac{d\bar{r}}{dt} \right|_I$ is the derivative of vector \bar{r} with respect to the i-frame;

$\left. \frac{d\bar{r}}{dt} \right|_m$ is the derivative of vector \bar{r} with respect to an arbitrary m-frame;

$\bar{\omega}_m$ is the absolute angular velocity of an m-frame.

After a number of derivations (Salychev, 1998), the relationship between transformation matrices of an inertial frame and a non-inertial arbitrary m-frame can be defined as:

$$\dot{R}_m^i = R_m^i \tilde{\omega}_m \quad (3-6)$$

where: R_m^i, \dot{R}_m^i are transformation matrix from the m-frame to the inertial frame and its derivative, respectively;

$$\tilde{\omega}_m = \begin{bmatrix} 0 & -\omega_z & \omega_y \\ \omega_z & 0 & -\omega_x \\ -\omega_y & \omega_x & 0 \end{bmatrix} \quad (3-7)$$

is the absolute (with respect to the i-frame) angular velocity of the m-frame in matrix form.

The behaviour of the direction cosine matrix between two arbitrary non-inertial frames, m and n , can be described in the form of a Poisson equation:

$$\dot{R}_m^n = R_m^n \tilde{\omega}_{m-n} = R_m^n \tilde{\omega}_m - \tilde{\omega}_n R_m^n \quad (3-8)$$

where: R_m^n, \dot{R}_m^n are the transformation matrix from the m - to n - frame and its derivative, respectively;

$\tilde{\omega}_{m-n}$ is the relative angular velocity between the m - and n - frames in matrix form as in equation (3-7); and

$\tilde{\omega}_m, \tilde{\omega}_n$ is the absolute angular velocities of the m - and n - frames (see equation (3-5)).

3.2.2 Quaternion Transformation

Instead of the three ordered rotations to transform a vector from one frame to another using a direction cosine matrix, the transformation can be performed by one rotation around a single fixed axis. The rotation vector defining this operation can be represented as follows (see Figure 3-4) (*ibid*):

$$\bar{\Phi} = \begin{bmatrix} \Phi_x \\ \Phi_y \\ \Phi_z \end{bmatrix} = |\Phi| \begin{bmatrix} \cos \alpha \\ \cos \beta \\ \cos \gamma \end{bmatrix} \quad (3-9)$$

where: $|\Phi|$ is the magnitude of the rotation vector; and

α, β, γ are the angles between the axis of rotation and a coordinate frame.

Usually Hamilton quaternion algebra, which implements the rotation vector idea, is used (El-Sheimy, 2003). Hamilton's quaternion is defined as a hyper-complex number of the form:

$$Q = q_0 + q_1\bar{i} + q_2\bar{j} + q_3\bar{k} \quad (3-10)$$

where: q_0, q_1, q_2, q_3 are real numbers; and

set $\{1, i, j, k\}$ forms the vector basis for a quaternion vector space.

Quaternion elements can be represented through the parameters of the rotation vector $\bar{\Phi}$ (Salychev, 1998):

$$\begin{aligned} q_0 &= \cos \frac{|\Phi|}{2} \\ q_1 &= \frac{\Phi_x}{|\Phi|} \sin \frac{|\Phi|}{2} \\ q_2 &= \frac{\Phi_y}{|\Phi|} \sin \frac{|\Phi|}{2} \\ q_3 &= \frac{\Phi_z}{|\Phi|} \sin \frac{|\Phi|}{2} \end{aligned} \quad (3-11)$$

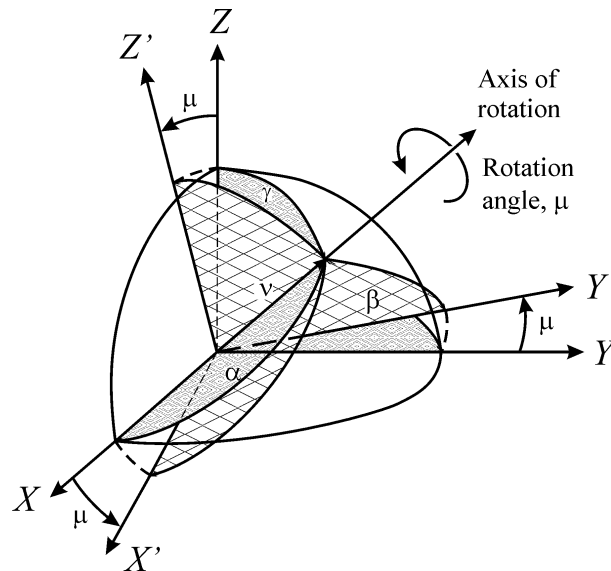


Figure 3-4: Rotation Vector Transformation (ibid)

The norm of quaternion $|Q| = q_0^2 + q_1^2 + q_2^2 + q_3^2 = 1$ is usually used to normalize the quaternion operations in SINS algorithms. The relationship between a direction cosine matrix and a quaternion is the following:

$$R = \begin{bmatrix} q_0^2 + q_1^2 - q_2^2 - q_3^2 & 2(q_1q_2 - q_3q_0) & 2(q_1q_3 + q_0q_2) \\ 2(q_1q_2 + q_0q_3) & q_0^2 - q_1^2 + q_2^2 - q_3^2 & 2(q_2q_3 - q_0q_1) \\ 2(q_1q_3 - q_0q_2) & 2(q_2q_3 + q_0q_1) & q_0^2 - q_1^2 - q_2^2 + q_3^2 \end{bmatrix} \quad (3-12)$$

The Poisson expression in quaternion form is:

$$\dot{Q} = \frac{1}{2} Q \cdot \bar{\omega} \quad (3-13)$$

where $Q = \begin{bmatrix} q_0 & q_1 & q_2 & q_3 \\ -q_1 & q_0 & -q_3 & q_2 \\ -q_2 & q_3 & q_0 & -q_1 \\ -q_3 & -q_2 & q_1 & q_0 \end{bmatrix}$ is the quaternion of rotation in matrix form.

Quaternion transformations are usually used in SINS algorithms since only four unknowns are necessary for calculation of an updated transformation matrix, while the direction cosine method requires nine. Moreover, the direction cosine method entails implementation of the six constraints under which the Poisson equation has to be solved (because of the main properties of the direction cosine matrix: its symmetry and orthogonality). Like the direction cosine method, quaternion transformation also avoids singularity issues (which is a main disadvantage of any three-parameter set such as Euler angle transformation or Rodrigues parameter transformation (El-Sheimy, 2003)).

3.2.3 Main Concept of Inertial Navigation

Inertial navigation is an autonomous process of computing position by doubly integrating the acceleration of a point, whose position is to be determined (Jekeli, 2001). Consequently, it has to be initialized with an initial velocity and position; therefore, based on this principle, any INS is a relative positioning system (unlike GPS, which is an absolute system).

There are two classifications of inertial systems: gimbaled and strapdown. A gimbaled INS deals with the physical realization of the navigation frame using a free axis gyrostabilizer platform with three orthogonally placed accelerometers. The isolation of the inertial platform from rotations of the host vehicle can be exploited to eliminate many sensor error sources and to achieve very high system accuracy (Titterton and Weston, 1997). However, gimbals are very sophisticated electromechanical assemblies that are delicate and expensive to manufacture. As a consequence, gimbaled systems tend to be more expensive than strapdown systems. A strapdown inertial system, such as that used herein, provides the analytical image of the navigation frame in the on-board computer, using the measurements from accelerometers and gyros installed directly on the vehicle body. In other words, strapdown gyroscopes are not used to keep the accelerometer input axes stabilized, but they are used to maintain a coordinate transformation between the two frames. Therefore, the inertial sensors for strapdown systems experience much higher rotation rates than gimbaled systems and, consequently, they deliver poorer accuracy than their gimbaled counterparts (ibid).

3.2.4 Mechanization Equations

The mechanization equations convert the output of the IMU, which includes rotation rates and specific force measurements, into position, velocity and attitude information. Once the angular rates and accelerations are obtained, the calculation algorithm can be executed. Firstly, having the initial navigation information with respect to the navigation frame, the angular rates are integrated to obtain the new orientation of the IMU. Secondly, using this information, the accelerations are rotated into the n-frame, where they are twice integrated to obtain velocity and position increments ([ibid](#)).

The specific force, f , measured by accelerometers, is related to the total vehicle acceleration, a , via the gravitational acceleration, g_m , as follows:

$$\bar{f} = \bar{a} - \bar{g}_m \quad (3-14)$$

The equation of the absolute acceleration (with respect to the i-frame) can be defined using the well-known Coriolis formula ([Salychev, 1998](#)):

$$\bar{a} = \frac{d}{dt} \left[\frac{d\bar{r}}{dt} \Big|_I \right]_I = \left[\frac{d}{dt} \bar{V} + \bar{U} \times \bar{r} \right]_I \quad (3-15)$$

where: \bar{V} is the vehicle velocity with respect to the e-frame;

\bar{U} is the angular velocity of the Earth;

\bar{r} is the position vector in the i-frame; and

I represents differentiation with respect to the inertial frame.

By expanding equation (3-14), the general navigation equation can be derived:

$$\bar{f} = \left. \frac{d\bar{V}}{dt} \right|_N + \bar{\omega}_N \times \bar{V} + \bar{U} \times \bar{V} - \bar{g} \quad (3-16)$$

where: $\bar{\omega}_N$ is the absolute angular velocity of the n-frame;

$\bar{g} = \bar{g}_m - \bar{U} \times (\bar{U} \times \bar{r})$ is the apparent gravity, defined as a vector difference between the gravitational acceleration and centripetal acceleration due to the Earth's rotation; and

$\left. \frac{d}{dt} \right|_N$ represents differentiation with respect to the n-frame.

Usually, the modeling of motion is performed in the local-level frame as the navigation frame, because in this case, the attitude angles as well as geodetic coordinates, can be obtained directly from the system (El-Sheimy, 2003). In addition, the computational errors in the navigational parameters on the horizontal (North-East) plane are bounded due to the Schuler effect, which will be discussed in the following section 3.4.

From equation (3-16), the projections of the specific force on the ll-frame can be derived (Salychev, 1998):

$$\begin{aligned} f_E &= \frac{dV_E}{dt} + \omega_N V_{up} - \omega_{up} V_N + U_N V_{up} - U_{up} V_N \\ f_N &= \frac{dV_N}{dt} - \omega_E V_{up} + \omega_{up} V_E - U_E V_{up} + U_{up} V_E \\ f_{up} &= \frac{dV_{up}}{dt} + \omega_E V_N - \omega_N V_E + U_E V_N - U_N V_E + g \end{aligned} \quad (3-17)$$

where: V_N, V_E, V_{up} are the projections of the linear velocity on the ll-frame;

$\omega_N, \omega_E, \omega_{up}$ are the projections of the absolute angular velocity on the ll-frame;

U_N, U_E, U_{up} are the projections of the Earth's rate on the ll-frame; and
 g is the apparent gravity.

Substituting the projections of the absolute angular velocity and the Earth's rate in the local-level frame from equation (3-2) into the above formula, the following set of equations can be obtained:

$$\begin{aligned}
 f_E &= \frac{dV_E}{dt} - \frac{V_E V_N}{R_\lambda + h} \operatorname{tg}\varphi - 2U \sin \varphi V_N + V_{up} \left(\frac{V_E}{R_\lambda + h} + 2U \cos \varphi \right) \\
 f_N &= \frac{dV_N}{dt} + \frac{V_E^2}{R_\lambda + h} \operatorname{tg}\varphi + 2U \sin \varphi V_E + V_{up} \frac{V_E}{R_\lambda + h} \\
 f_{up} &= \frac{dV_{up}}{dt} - \frac{V_N^2}{R_\lambda + h} \operatorname{tg}\varphi - \frac{V_E^2}{R_\lambda + h} - 2V_E U \cos \varphi + g
 \end{aligned} \tag{3-18}$$

In any strapdown INS, the IMU unit provides gyro and accelerometer measurements in the body frame, which are further recalculated into the navigation frame. The direction cosine matrix between the body and navigation frames, R_b^N , can be defined using the well-known Poisson equation (3-6). The absolute angular velocity of the body frame is directly measured by gyros, whereas the absolute angular velocity of the navigation frame is defined from accelerometer measurements. The procedure is as follows:

The INS system is first initialized with known matrix, R_b^N . Then the projections of specific force are transformed from the b-frame to the n-frame (in this case, the ll-frame), so that the absolute angular velocity and absolute linear velocity of the ll-frame are calculated, using formulas (3-17) or (3-18). Thus, the Poisson equation and, therefore, the direction cosine matrix, R_b^N , can be updated in preparation for the next step. The

positions are derived by integrating velocities using equation (3-3), while attitude information is defined directly from the elements of R_b^N .

For more details on the principles of INS operation refer to [Titterton and Weston, 1997](#); [Salychev \(1998\)](#); [Jekeli \(2001\)](#) and [El-Sheimy \(2003\)](#). In practice, a few calculation schemes have been developed to define navigation parameters. The algorithm of a SINS utilized in this thesis is described in Appendix A.

3.3 Principle of INS Alignment

The principle of inertial navigation assumes that initial information about the system is already known. While the starting position and velocity are usually easy to obtain using an external device such as GPS, the initial orientation of the system is not typically available. Therefore, the INS should perform an initial alignment, which produces coincidence between the sensor axes of the IMU with the navigation frame (e.g., the ll-frame). In a strapdown algorithm, the purpose of INS alignment is to establish the relationship between the b-frame and the ll-frame; thus, the initial parameters of the transformation matrix, R_b^{ll} (rotation matrix from the body frame to the local-level frame) are required. Two steps are needed in the alignment procedure; namely, horizontal alignment (accelerometer leveling) and azimuth alignment (gyro compassing) ([Jekeli, 2001](#); [El-Sheimy, 2003](#)). The essential operation involved in INS alignment is based on the sensor output in the local-level frame.

3.3.1 Horizontal Alignment

Horizontal alignment is the procedure for computing the initial misalignment angles in horizon $\theta_x(0)$ and $\theta_y(0)$. For ideal (error-free) accelerometers, the vertical accelerometer measures the apparent gravity, g , while the horizontal accelerometers have zero output in the ll-frame (see equation (3-4)):

$$\begin{bmatrix} f_E \\ f_N \\ f_{up} \end{bmatrix} = \begin{bmatrix} 0 \\ 0 \\ g \end{bmatrix} \quad (3-19)$$

Accelerometer axes coincide with the b-frame axes and consequently the specific force measurements, f_E , f_N , f_{up} , can be rewritten as:

$$\begin{bmatrix} f_{xb} \\ f_{yb} \\ f_{zb} \end{bmatrix} = R_{ll}^b \begin{bmatrix} 0 \\ 0 \\ g \end{bmatrix} \quad (3-20)$$

where: R_{ll}^b is the transformation matrix between the ll- and b- frames of the form (3-14).

In the-b-frame, accelerometer measurements, f_{xb} , f_{yb} , describe the tilt in the X and Y directions of the vertical accelerometer with respect to the vertical direction (see Figure 3-5):

$$\begin{aligned} f_{xb} &= -g \sin \theta_y(0) \\ f_{yb} &= g \sin \theta_x(0) \end{aligned} \quad (3-21)$$

For small angles, equation (3-21) can be rewritten:

$$\begin{aligned} f_{xb} &= -g\theta_y(0) \\ f_{yb} &= g\theta_x(0) \end{aligned} \quad (3-22)$$

Thus, using accelerometer measurements, the pair of initial horizontal misalignment angles, $\theta_x(0)$ and $\theta_y(0)$, can be defined. However, in reality, accelerometers measure these angles with their own errors, mainly biases B_{xb} , B_{yb} (Salychev, 1998):

$$\begin{aligned} z_{xb} &= -g\theta_y(0) + B_{xb} \\ z_{yb} &= g\theta_x(0) + B_{yb} \end{aligned} \quad (3-23)$$

Equation (3-23) indicates that the horizontal alignment is accurate to the level of horizontal accelerometer biases:

$$\begin{aligned} \tilde{\theta}_x(0) &= -\frac{B_{yb}}{g} \\ \tilde{\theta}_y(0) &= \frac{B_{xb}}{g} \end{aligned} \quad (3-24)$$

where $\tilde{\theta}_x(0), \tilde{\theta}_y(0)$ are the errors of horizontal alignment.

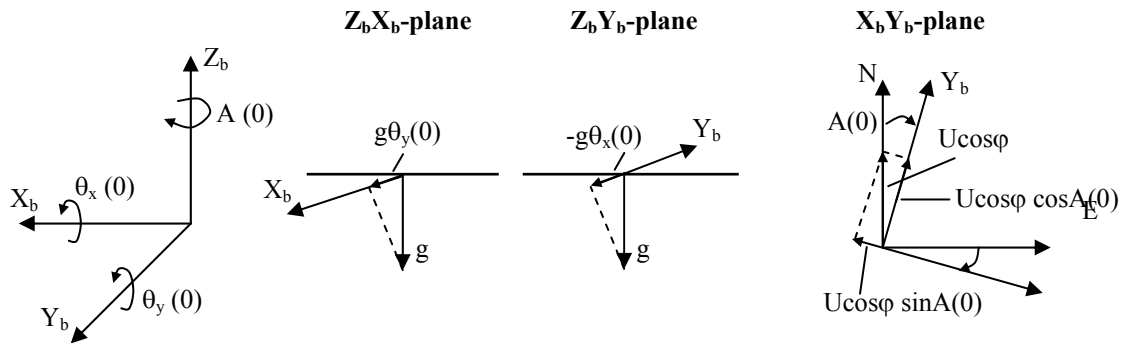


Figure 3-5: Principle of INS Alignment

3.3.2 Azimuth Alignment

Similar to the horizontal alignment problem, azimuth alignment utilizes measurements in the local-level frame. Basically, this procedure is the process of obtaining the azimuth

angle $A(0)$, which is defined as an angle between the North axis of the l -frame and the projection of the longitudinal axis of the b -frame (of the test vehicle) on the horizontal plane. Theoretically, in the l -frame, the north gyro measures the projection of the Earth's rotation rate, $U \cos \varphi$, while the east gyro has zero output. After accelerometer leveling, it is assumed that the plane $X_b Y_b$ (of the b -frame) is located on the horizon. Thus, gyro measurements, ω_{xb} , ω_{yb} , in the b -frame contain projections of $U \cos \varphi$ on their sensitive axes due to the tilt angle between horizontal axes X_b , Y_b of the b -frame with respect to the East and North axes of the l -frame (see Figure 3-5). This tilt, namely the azimuth angle, can therefore be defined using gyro measurements as:

$$\text{tg}A = -\frac{\omega_{xb}}{\omega_{yb}} \quad (3-25)$$

In reality, due to gyro errors, the azimuth alignment is limited to the level of the X-gyro drift bias ω_{xb}^{dr} (Salychev, 1998; El-Sheimy, 2003):

$$\tilde{A}(0) = \frac{\omega_{xb}^{\text{dr}}}{U \cos \varphi} \quad (3-26)$$

where $\tilde{A}(0)$ is the azimuth misalignment error.

Equation (3-26) shows that, for latitude $\varphi = 90$ (at the North Pole), the azimuth angle cannot be calculated. Therefore, at high latitudes, the local-level frame is not the optimal navigation frame for solving mechanization calculations. The Y-axis of the l -frame always points towards geodetic North. In the vicinity of the Poles, any East-West movement therefore results in large rotation rates about the Z-axis of the l -frame. To avoid latitude-dependent rotation rates, the wander frame can be used (for details see Salychev, 1998 and El-Sheimy, 2003).

Using the theoretical base given in this chapter, a navigation solution from raw sensor data can be obtained. The complete calculation scheme of a SINS algorithm, employed in this thesis, is described in Appendix A.

3.4 INS Errors

The INS error state vector for many applications includes coordinate, velocity and attitude errors. Since the errors are variable in time, they are usually described by a set of differential equations, which characterize the certain behaviour of different error components (Jekeli, 2001; El-Sheimy, 2003). A detailed discussion of INS errors is considered in the following.

For small misalignment angles, Φ_E , Φ_N and Φ_{up} , between the platform and local-level frames, the transformation matrix between these two coordinate frames can be described in matrix form, as derived from the standard direction cosine matrix, considering the assumption that, for small angles, $\cos \Phi = 1$ and $\sin \Phi = \Phi$.

$$\mathbf{R}_{ll}^p = \begin{bmatrix} 1 & \Phi_{up} & -\Phi_N \\ -\Phi_{up} & 1 & \Phi_E \\ \Phi_N & -\Phi_E & 1 \end{bmatrix} \quad (3-27)$$

From the Poisson equation, the gyro measurements in the p-frame can be expressed via the absolute angular velocity of the ll-frame and the derivatives of the attitude errors Φ_E , Φ_N , Φ_{up} (Salychev, 2003):

$$\begin{bmatrix} \omega_E \\ \omega_N \\ \omega_{up} \end{bmatrix}_p = \mathbf{R}_{ll}^p \begin{bmatrix} \omega_E \\ \omega_N \\ \omega_{up} \end{bmatrix}_{ll} + \begin{bmatrix} \dot{\Phi}_E \\ \dot{\Phi}_N \\ \dot{\Phi}_{up} \end{bmatrix} \quad (3-28)$$

Similarly, the accelerometer measurements in the p-frame contain specific force values as well as accelerometer errors:

$$\begin{bmatrix} \mathbf{a}_E \\ \mathbf{a}_N \\ \mathbf{a}_{up} \end{bmatrix}_p = \mathbf{R}_{II}^p \begin{bmatrix} \mathbf{a}_E \\ \mathbf{a}_N \\ \mathbf{a}_{up} \end{bmatrix}_{II} + \begin{bmatrix} \mathbf{a}_E \mu_E \\ \mathbf{a}_N \mu_N \\ \mathbf{a}_{up} \mu_{up} \end{bmatrix}_{II} + \begin{bmatrix} \mathbf{B}_E \\ \mathbf{B}_N \\ \mathbf{B}_{up} \end{bmatrix}_{II} \quad (3-29)$$

where: μ_E, μ_N, μ_{up} are the accelerometer scale factors; and
 $\mathbf{B}_N, \mathbf{B}_E, \mathbf{B}_{up}$ are the accelerometer biases.

The difference between the angular velocities of the platform and local-level frames is caused mainly by the platform gyro drifts and calculation errors from equation (3-2), while the acceleration difference comes mostly from accelerometer scale factors and biases as well as errors in the calculation of the Coriolis corrections. Neglecting high order terms and other sensor errors (e.g. non-linearities of scale factors, installation errors, etc.), a simplified INS error model can be obtained. Herein, the attitude errors can be derived from equation (3-28) and velocity errors from equation (3-29), while errors in position can be obtained from variation of parameters in equation (3-3). For short-term analysis, the following error model can be used (*ibid*):

$$\begin{cases} \delta \dot{\mathbf{E}} = \delta \mathbf{V}_E \\ \delta \dot{\mathbf{V}}_E = \mathbf{a}_N \Phi_{up} - \mathbf{g} \Phi_N + \mathbf{a}_E \mu_E + \mathbf{B}_E \\ \dot{\Phi}_N = \frac{\delta \mathbf{V}_E}{R} + \omega_N^{dr} \\ \dot{\omega}_N^{dr} = 0 \\ \dot{\mathbf{B}}_E = 0 \end{cases} \quad \begin{cases} \delta \dot{\mathbf{N}} = \delta \mathbf{V}_N \\ \delta \dot{\mathbf{V}}_N = \mathbf{g} \Phi_E - \mathbf{a}_E \Phi_{up} + \mathbf{a}_E \mu_E + \mathbf{B}_N \\ \dot{\Phi}_E = -\frac{\delta \mathbf{V}_N}{R} + \omega_E^{dr} \\ \dot{\omega}_E^{dr} = 0 \\ \dot{\mathbf{B}}_N = 0 \end{cases} \quad (3-30)$$

where: $\omega_N^{dr}, \omega_E^{dr}$ are the drifts of East and North gyros; and

$\mathbf{a}_{up} \approx \mathbf{g}$ is the vertical acceleration, which is equal to the gravity vector.

Due to the unique nature of INS error sources, the error model can be divided into two parts: Schuler (stationary) and non-stationary. The Schuler component does not depend on vehicle motion parameters and it is defined mainly by gyro drifts and accelerometer biases. The non-stationary component depends upon vehicle dynamics and it is characterized mostly by accelerometer scale factors and azimuth misalignment. The solution of such a decoupled model is the sum of the two component solutions. The portion of the simplified INS error model based on the Schuler component can be described as:

$$\left\{ \begin{array}{l} \delta \dot{E}^{\text{sh}} = \delta V_E^{\text{sh}} \\ \delta \dot{V}_E^{\text{sh}} = -g \Phi_N^{\text{sh}} + B_E \\ \dot{\Phi}_N^{\text{sh}} = \frac{\delta V_E^{\text{sh}}}{R} + \omega_N^{\text{dr}} \\ \dot{\omega}_N^{\text{dr}} = 0 \\ \dot{B}_E = 0 \end{array} \right. \quad \left\{ \begin{array}{l} \delta \dot{N}^{\text{sh}} = \delta V_N^{\text{sh}} \\ \delta \dot{V}_N^{\text{sh}} = g \Phi_E^{\text{sh}} + B_N \\ \dot{\Phi}_E^{\text{sh}} = -\frac{\delta V_N^{\text{sh}}}{R} + \omega_E^{\text{dr}} \\ \dot{\omega}_E^{\text{dr}} = 0 \\ \dot{B}_N = 0 \end{array} \right. \quad (3-31)$$

The non-stationary part, meanwhile, has the from:

$$\left\{ \begin{array}{l} \delta \dot{E} = \delta V_E^{\text{nst}} \\ \delta \dot{V}_E^{\text{nst}} = -g \Phi_N^{\text{nst}} + a_N \Phi_{\text{up}} + a_E \mu_E \\ \dot{\Phi}_N = \frac{\delta V_E^{\text{nst}}}{R} \end{array} \right. \quad \left\{ \begin{array}{l} \delta \dot{N} = \delta V_E^{\text{nst}} \\ \delta \dot{V}_N = g \Phi_E^{\text{nst}} - a_E \Phi_{\text{up}} + a_E \mu_E \\ \dot{\Phi}_E = -\frac{\delta V_N^{\text{nst}}}{R} \end{array} \right. \quad (3-32)$$

The solution of the differential equation of the Schuler part in equation (3-31) yields INS velocity errors oscillate with a very small frequency, called the Schuler:

$\nu = \sqrt{g/R_E} \cong 1/5000$ Hz, which corresponds to a long period of approximately 84 minutes. (Herein: R_e is the Earth's radius and g is a gravity vector.) In contrast, the solution of the second part in equation (3-32) provides noise-like high frequency behaviour of the INS non-stationary errors. Equation (3-32) shows that the azimuth misalignment error, Φ_{up} , and scale factors, μ_E and μ_N , are modulated by vehicle motion, a_E and a_N , which will be discussed in detail in Chapter 5.

Similarly to velocity errors, the attitude and position INS errors also contain the Schuler oscillations due to the solution of the second order differential equation. The position error equations can be obtained by integrating the velocity error formulas; these equations show that the INS position errors grow over time due to the Schuler part and increase with traveling distance due to the non-stationary part of the total INS error. Since the Schuler errors are much larger than the non-stationary ones, the magnitude of the gyro drift is one of the main indicators of the quality of an INS. For a SINS, the sensor errors, ω^{dr} , B and μ are represented in the error model not in the body- but in the local-level frame via the direction cosine matrix, R_b^{ll} . A more comprehensive discussion of INS errors in terms of their modeling and estimation will be given in Chapter 5.

3.4.1 Schuler Loop

The block-diagram based on equation (3-31), Figure 3-6, illustrates behaviour of the Schuler part of the INS error for a single channel (east component) (*ibid*). The analytical image of the gyro platform (p-frame) has a small digression from the local-level frame

due to the IMU sensor errors. As a consequence, the east accelerometer measures the projection of the apparent gravity, g , on its sensitivity axis with its own bias, B_E . The integration of this signal yields the INS east velocity error, δV_E . The second integration leads to the INS position error in the east direction, δE . In order to superpose the platform frame with the local-level frame, the torque of the absolute angular velocity of the ll-frame, V_E/R , is introduced to the gyroplatform (for a strapdown system to the quaternion block). The errors in linear velocity V_E in turn cause the misalignment angle, Φ_N , between the analytical gyroplatform and the true horizon (see Figure 3-6). This feedback is referred to as a Schuler loop. Due to the feedback from the first integrator, the INS velocity error, V_E , is bounded and it oscillates with the Schuler frequency and a constant magnitude. By contrast, the INS position error grows over time, since there is no feedback from the second integrator (*ibid*). The diagram in Figure 3-6 is based on the following differential equations derived from equation (3-31):

$$\begin{cases} \delta \dot{E}^{sh} = \delta V_E^{sh} \\ \delta \dot{V}_E^{sh} = -g\Phi_N^{sh} + B_E \\ \dot{\Phi}_N^{sh} = \frac{\delta V_E^{sh}}{R} + \omega_N^{dr} \end{cases} \quad (3-33)$$

A similar scheme can be drawn for the north component of the INS error. The well-known physical interpretation of the Schuler effect is a pendulum with an arm of the Earth's radius, so that the platform maintains the horizontal plane in any type of motion (*ibid*).

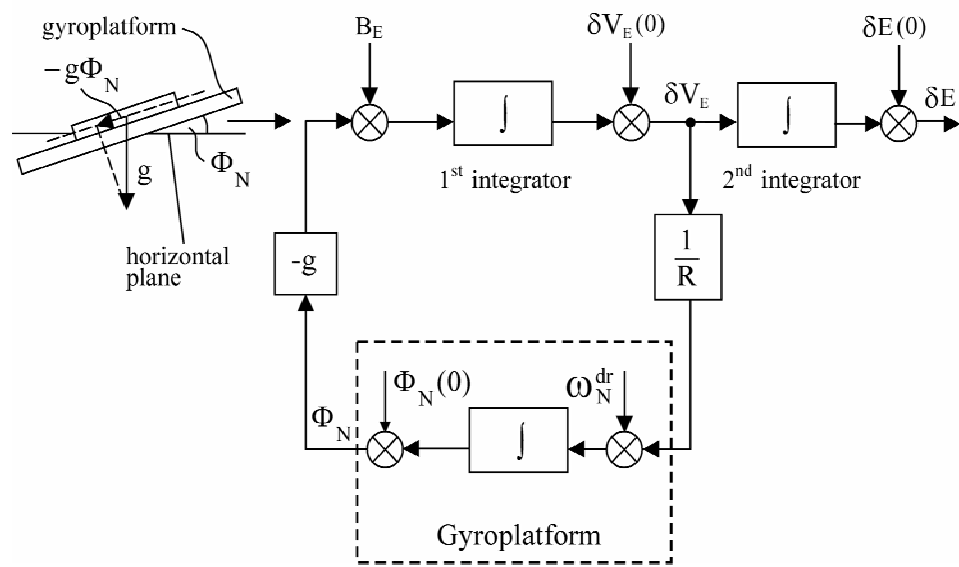


Figure 3-6: Schuler Loop (ibid)

Chapter 4

INS/GPS Integration

As discussed in Chapter 1 complementary characteristics of INS and GPS produce synergistic benefits in combined system, as each system compensates for the other's shortcomings. While the main aspects of GPS and INS were reviewed in Chapters 2 and 3, this chapter is devoted to the theoretical and practical aspects of integrating the two systems. First, a basic description of the most common INS/GPS integration techniques is presented with a focus on the cascaded method utilized in this thesis. Due to the combination of data types, the error estimation is a subject of concern. Traditionally an optimal Kalman filter is used for error estimation in integrated systems. Its calculation algorithm and main properties are also explored in this chapter, followed by a discussion of an adaptive estimation method. In this thesis, an adaptive Kalman filter with unknown measurement covariance is considered. Its calculation scheme based on an innovation sequence is also given below.

4.1 Integration Schemes

There are several integration strategies applied to INS/GPS integration and they are characterized by the type of information that is shared between the individual systems. The preferred integration strategy is typically defined by the quality of the INS used in the combined system.

In practice, four well-known integration approaches are implemented in the navigation field (Jekeli, 2001; Petovello, 2003): uncoupled, loosely coupled, tightly coupled and finally, ultra-tightly coupled integration. Uncoupled integration implies no data feedback from either instrument to the other to facilitate its performance improvement. By contrast, in the ultra-tightly coupled approach, the sensors are treated as a common system, which produces several types of data that are processed simultaneously to enhance the function of individual sensor components. In a loosely coupled system, data from one instrument is fed back to aid and improve the other's performance, but each retains its own individual data processing algorithm throughout the interchange process (Jekeli, 2001).

In an uncoupled INS/GPS scheme, GPS measurements are used to compensate INS errors in the output of the integrated system only; the GPS information does not contribute to decreasing the error rate (i.e. there is no feedback of estimated INS errors into the navigation algorithm). Therefore, during GPS outages, the INS works in stand-alone mode and the accuracy of the integrated system degrades rapidly; the magnitude, i.e. the speed, of such degradation depends on the INS sensor quality. The uncoupled and loosely coupled integration schemes are characterized by the same degree of observability due to their identical system structures and measurement models. Because of the complex relationship between the measurements and the error states, tightly coupled integration is distinguished by a weaker degree of observability. The ultra-tight algorithm for INS/GPS integration is preferable in terms of the system performance in general. In this case, the GPS receiver and the INS no longer work independently, but they operate as a common system. GPS updates are utilized to calibrate the INS, while the INS is used to aid the

GPS receiver tracking loops during interference or other degraded signal conditions (Sennott and Senffner, 1997; Petovello, 2003). However, this type of integration method requires access to a receiver's firmware; as a result, this scheme of integration is usually implemented only by equipment manufacturers, and is not currently available to the general user or academic communities.

4.1.1 Loosely Coupled Integration

Loosely and tightly coupled integration algorithms are the most commonly applied for many surveying applications. In both cases, the GPS receiver and the INS operate as independent systems, and differ only in the type of information shared between them. The cascaded scheme is a well known, and frequently implemented, type of loosely coupled integration; it is considered through a comprehensive discussion in the following subsection.

In the cascaded scheme of integration, GPS data is fed to an INS-only filter. Usually, the differences between the INS and GPS velocities and positions are utilized as measurements for the estimation block, in which the INS error equations are used as the system model. In this way, the INS filter provides estimates of all observable INS errors, which are applied to correct INS raw measurements and to compensate them in the system output. When GPS measurements are not available, INS errors must be predicted (Salychev, 2003).

The main advantage of the loosely coupled strategy lies in the relatively small dimensions of the state vectors in the filter, as compared to the tightly coupled case. This affects the filter convergence time, by shortening the transition period, so that the filter is more flexible for changes in operational environments. Another advantage of this approach is the computational simplicity of its implementation. However, the most important benefit comes from the flexibility and universality of the loosely coupled scheme for different types of INS and GPS units; e.g. herein for the two different types of GPS receivers deployed (conventional or HS GPS receivers) in distinct operational environments.

The disadvantage of loosely coupled integration is that, in general, a GPS receiver needs at least three satellites to compute the navigation solution (in height-constrained mode). Under harsh GPS conditions, GPS receivers experience frequent losses of lock due to severe satellite blockage. As a result of regular GPS outages, the integrated system therefore offers a diminished degree of overall accuracy owing to the prediction mode of the INS filter. Nevertheless, the severity of such shortages is questionable and can also be considered as an advantage. In challenging GPS applications (e.g. downtown canyons, forests), GPS measurements are corrupted significantly by many errors such as multipath, signal cross-correlation and echo-only signals. When GPS fails or provides an unreliable or erroneous solution, loose integration, operating essentially on two independent solutions, is more likely to detect these faults or consequent outliers and is better able to take appropriate remedial action (*ibid*). In consideration of the above, the loosely coupled

integration strategy (that is, the cascaded scheme) is considered as more suitable for INS/GPS integration in various operating conditions, i.e. urban or open sky areas.

4.1.2 Tightly Coupled Integration

Tightly coupled algorithm deals with the overall INS/GPS system, where data processing is performed in a single filter. This approach is similar to the loosely coupled one and differs mostly in terms of its diverse measurement model: instead of positions and velocities, pseudoranges calculated by the INS and measured by a GPS receiver are fed to the filter as observables. Clearly, tightly coupled integration is more forgiving for GPS data gaps (it permits the use of as few as one GPS pseudorange measurement in the estimation algorithm). However, the common filter in tight integration is more cumbersome than in the loosely coupled case due to a complex measurement model; the design matrix defines the relationship between pseudoranges and geodetic coordinates and the measurement noise in this case is coloured noise that must be introduced to the system model as an additional component. Moreover, the degree of the observability of the state vector is generally weaker than in the loosely coupled strategy due to the large dimension of the state vector as well as indirect measurements. This degree of observability, in turn, defines the longer convergence period for error estimates as compared to the loosely-coupled case; furthermore, it can result in accuracy degradation of INS error estimation during this interval. For HS applications, due to error-corrupted GPS measurements, the additional challenge lies in separation of GPS and INS errors.

4.1.3 Centralized and Decentralized Integration Filters

Processing algorithms fall into two basic categories: centralized and decentralized. The centralized approach is usually associated with any tight system integration, where the raw sensor data is combined optimally through the use of one sensor processor (e.g. a Kalman filter) to obtain the integrated solution (Jekeli, 2001). In INS/GPS integration applications, the centralized scheme considers that GPS and INS measurements are processed together in the same filter (e.g. in tightly coupled scheme differences between INS and GPS ranges are fed into the filter). The main advantages such as system availability, and disadvantages, such as weaker observability or sophistication in the system design, have been addressed, based on their association with the tightly coupled technique.

A decentralized method is associated with loosely coupled or uncoupled integration schemes; such methods are characterized by sequential processing where filters of individual instruments provide solutions that are ultimately combined in the system output or in a common filter called the master processor. Variations of decentralized integration, such as cascaded and federated integration, also occur in the literature (*ibid*). In the field of INS/GPS integration, a decentralized filter is based on the independence of the GPS and INS navigation functions. Its benefits and limitations have been addressed above in section 4.1.1 and 4.1.2 in reference to the cascaded scheme. In a summary, the implementation of a cascaded integrated scheme using a decentralized Kalman filter is

assumed to be appropriate to serve the requirements of integration and will be considered in more detail in Chapter 5.

4.2 Kalman Filter

The Kalman filter has been the subject of extensive research and application, particularly in the area of autonomous or assisted navigation, since it has many advantages over other estimators. A Kalman filter is a set of mathematical equations that provides an efficient recursive solution of the least-squares method (Gao and Sideris, 2002). The filter is very powerful in several respects: it supports estimations of past, present, and even future states; it can do so even when the precise nature of the modeled system is unknown and, finally, it is flexible enough to be used either in real-time or for post-mission analysis. Accordingly, the Kalman filtering technique has become a widely applied tool in INS/GPS integration owing to its applicability to the wide range of error types found in INS/GPS applications, as discussed in previous chapters. Details of the Kalman filter derivation will not be given here; however, there are numerous references available, such as Kalman (1960), Gelb (1974), Krakiwsky (1990) and Brown and Hwang (1992).

4.2.1 State Space Model

According to linear system theory, the dynamics of a linear system can be represented by a state space model (SSM), where an n-order system of differential equations is converted to a set of n-coupled first-order differential equations. In the field of INS/GPS integration, the differential equations of INS errors are represented in SSM form and used

as a system model in the Kalman filter. This model is linear, when the misalignment angles between the platform and the local-level frames, Φ_x , Φ_y , Φ_z , are small (i.e., they do not exceed 3° to 5°). In this case, the main assumption made for small angles in the INS error model (see equation 3-27: $\sin\Phi = \Phi$ and $\cos\Phi = 1$) is valid. For low-cost inertial systems, these angles can be much larger than the above threshold; therefore, in such applications, error damping should be implemented in order to confine the errors to a linear region. For medium accuracy inertial systems as employed herein, the horizontal errors do not exceed 1° to 3° , while azimuth misalignment can be reduced to 1° to 2° by applying a one-step correction using GPS heading. Therefore, in this research, the linearization problem does not have affect on estimation accuracy.

In discrete form, any linear system can be described using SSM as (Salychev, 1998):

$$\mathbf{x}_k = \Phi_{k,k-1} \mathbf{x}_{k-1} + \mathbf{G}_{k,k-1} \mathbf{w}_{k-1} \quad (4-1)$$

where: $\mathbf{x}_k, \mathbf{x}_{k-1}$ is a $(n \times 1)$ state vector at the current and previous epochs;

$\Phi_{k,k-1}$ is a $(n \times n)$ transition matrix between the two epochs in discrete form: $\Phi_{k,k-1} = I + \mathbf{A}_{k-1}T$, here: \mathbf{A}_{k-1} is a system matrix at the previous epoch in continuous time form and T is a sampling interval;

$\mathbf{G}_{k,k-1}$ is an $(n \times r)$ input matrix between the two epochs in discrete form: $\mathbf{G}_{k,k-1} = \mathbf{B}_{k-1}T$; here, \mathbf{B}_{k-1} is an input matrix in continuous time form;

w_{k-1} is $(r \times 1)$ input noise, assumed to be white, and possessing a zero mean with known covariance matrix $Q = M[w_{k-1}, w_{k-1}^T]$.

The appearance of input noise is caused by input disturbances since, in general, user knowledge about system behaviour is limited and some state vector components act randomly during the estimation process. These components are usually described by a shaping filter, which is defined as a differential equation with white noise input and output of a certain correlation function (*ibid*). Since the level of input white noise defines system uncertainties, it therefore characterizes the accuracy of the model representation.

Some part of the system state vector is physically measured according to the measurement model:

$$z_k = Hx_k + v_k \quad (4-2)$$

where: z_k is a $(m \times 1)$ measurement vector at the current epoch;

H is a $(m \times n)$ design matrix; and

v_k is $(m \times 1)$ measurement noise, assumed to be white and zero mean with known covariance matrix $R = M[v_{k-1}, v_{k-1}^T]$.

4.2.2 Filter Algorithm

To estimate the system vector optimally, the following condition should be satisfied:

$$\text{tr}M[(x_k - \hat{x}_k)(x_k - \hat{x}_k)^T] = \text{tr}M[\tilde{x}_k \tilde{x}_k^T] \equiv \min \quad (4-3)$$

where: \hat{x}_k is an estimate of a state vector x_k ; and

\tilde{x}_k is the estimation error.

An optimal Kalman filter provides minimization of criterion expressed in equation (4-3). Its algorithm is well-known and will be introduced without deduction (Kalman, 1960; Gelb, 1974; Krakiwsky, 1990 and Brown and Hwang, 1992).

The major equation of the Kalman filter is:

$$\hat{x}_k = \Phi_{k,k-1} \hat{x}_{k-1} + K_k (z_k - H \Phi_{k,k-1} \hat{x}_{k-1}) \quad (4-4)$$

where K_k is an optimal gain matrix. The first component on the right hand side of this formula expresses the solution of the deterministic part of the system model. The second component of equation (4-4) reflects the impact of input uncertainties on the system. This component is a weighted (gain K_k) difference between the actual (z_k) and the predicted measurements. The gain matrix, K_k , can be determined from the following equations:

$$P_{k/k-1} = \Phi_{k,k-1} P_{k-1} \Phi_{k,k-1}^T + G_{k,k-1} Q G_{k,k-1}^T \quad (4-5)$$

$$K_k = P_{k/k-1} H^T [H P_{k/k-1} H^T + R]^{-1} \quad (4-6)$$

$$P_k = (I - K_k H_k) P_{k/k-1} \quad (4-7)$$

where: $P_{k,k-1} = M[(x_k - \Phi_{k,k-1} \hat{x}_{k-1})(x_k - \Phi_{k,k-1} \hat{x}_{k-1})^T] = M[\tilde{x}_{k/k-1} \tilde{x}_{k/k-1}^T]$ is an *a priori* covariance matrix of estimation errors (errors in prediction); and

$P_{k,k-1} = M[(x_k - \hat{x}_k)(x_k - \hat{x}_k)^T] = M[\tilde{x}_k \tilde{x}_k^T]$ is the *a posteriori* covariance matrix of the estimation errors.

The recurrent calculation algorithm of the Kalman filter is presented in Figure 4-1.

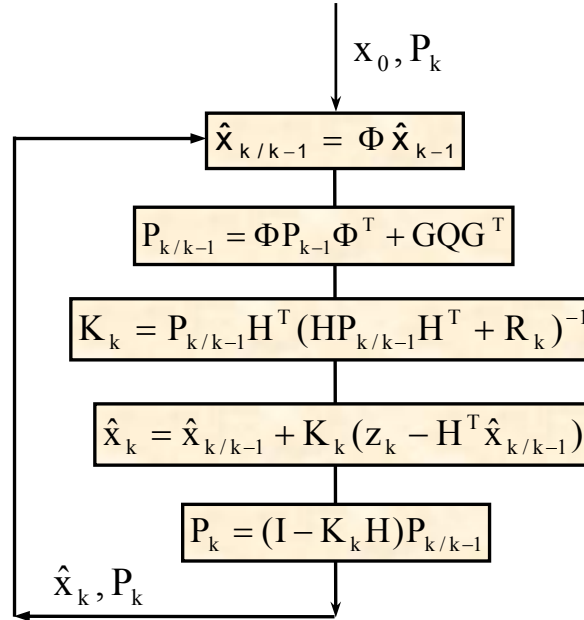


Figure 4-1: Calculation Algorithm for A Kalman Filter (Salychev, 1998)

First, the *a priori* state vector estimate, $\hat{x}_{k/k-1}$, is defined using the deterministic part of the system model (prediction of estimation errors). The next step illustrates the accuracy of this calculation via the *a priori* covariance matrix of estimation errors, $P_{k/k}$. Then, the optimal gain matrix, K_k , is computed, which defines the relationship between the level of the useful signal and the intensity of the measurement noise. In other words, for small noise in the measurements, the gain, K_k , tends to an identity matrix; and, conversely, for noisy error-corrupted measurements, it is close to zero. After the gain calculation, the *a priori* estimate, $\hat{x}_{k/k-1}$, is updated using current measurements, z_k , to obtain the final estimate of a state vector, \hat{x}_k . Its accuracy is then determined via calculation of the *a posteriori* covariance matrix of estimation errors, P_k .

The magnitude of the initial covariance matrix of estimation errors, P_0 , defines the length of the transition period; a larger magnitude of P_0 corresponds to a shorter transition period and vice versa. Thus, an exaggerated level of initial estimation errors is usually chosen.

4.2.3 Main Filter Characteristics

Observability

Observability of the state vector is an ability to obtain the initial state from current measurements (Gelb, 1974). For time-varying systems, observability can be classified as either complete, differential or instantaneous. Instantaneous observability means that the state of the system at any time may be determined instantaneously from the observation of the output and its derivatives. Differential observability requires that the state of the system be observable over a finite time interval, while complete observability implies that the initial state can be calculated any time during the estimation procedure (Rhee et al., 2002). In this thesis, only the notion of complete observability is used and is referred to herein simply as observability.

Since the design (measurement) matrix H links the measurements with the state vector, it characterizes observability. Theoretically, observability can be verified via an observability matrix (A), which is calculated using the transition (Φ) and design (H) matrices:

$$A = \begin{bmatrix} H \\ H\Phi \\ H\Phi^2 \\ \dots \\ H\Phi^{n-1} \end{bmatrix} \quad (4-8)$$

where n is the number of measurements.

If the observability matrix is non-singular, the state vector is observable (Gelb, 1974). The property of observability defines the possibility of state vector estimation. In practice, a certain vector component is considered observable if it can be derived from directly measured components via differentiation (and inversely, integration implies non-observability) (Salychev, 2003).

Convergence and Observability Degree

A Kalman filter operates in two modes: a transition process and a steady state. During the transition process, all estimates of the state vector components have to converge to true values. At steady state, the Kalman filter operates with a certain constant accuracy, which is limited by the accuracy of the system model. For stationary systems, the state vector components in the Kalman filter converge sequentially (Gelb, 1974). First, directly measured states converge; then, the components, which are closest to the directly measured ones, and so on. The position of a certain component in the state vector thus defines its degree of observability. Directly measured components are strongly observable; weakly observable estimates stand in the state vector further from the directly measured ones. Consequently, the duration of the transition process for a certain component is defined by its degree of observability (Salychev, 2003).

Divergence

A Kalman filter is designed to be stable; however, in practice, estimation accuracy differs from its theoretical prediction. This inconsistency, commonly referred as divergence, can be classified as either apparent or true divergence (Gelb, 1974). In apparent divergence, estimation errors are bounded, but they grow over time and are generally greater than theoretical values. In true divergence, true error estimates eventually become infinite (ibid). In general, divergence is caused by inaccurate system model representation. Commonly if wrong filter parameters are chosen, the filter has apparent divergence, which degrades estimation accuracy, while true divergence occurs with the adoption of the wrong system model. As was discussed in section 4.2.1, in regard to INS/GPS applications, the system model is linear when misalignment errors Φ_x , Φ_y , Φ_z , are small (i.e. less than 5°). Due to the linearization problem, true divergence can occur if the misalignment errors are in the order of 20° , which is not the case for medium accuracy INS's. An apparent divergence in the INS/GPS filter can occur when the azimuth correction is not implemented. In this thesis, due to the use of INS error compensation in the navigation algorithm, the linearization problem cannot cause filter divergence.

Innovation Sequence and Adaptive Filtering

An innovation sequence, v_k , can be defined as the difference between the actual measurement, z_k , and the predicted measurement, $H\Phi\hat{x}_{k-1}$ (Teunissen and Salzmann, 1998):

$$v_k = z_k - H\Phi\hat{x}_{k-1} \quad (4-9)$$

The main properties of the innovation sequence are the following (Salychev, 1998):

1. It is white noise for an optimal Kalman filter;
2. The covariance matrix of the innovation sequence v_k can be defined as:

$$C_k = M[v_k v_k^T] = HP_{k,k-1}H^T + R \quad (4-10)$$

$$3. M[\tilde{x}_k v_l] = 0 \text{ for } l \leq k \quad (4-11)$$

The innovation sequence is frequently used in adaptive filtering, since it is one of the major indicators of real estimation errors. Adaptive filters sense the properties of the environments in which they operate and adjust the filter parameters accordingly. These filters are useful in cases where the properties of the operating environments are unknown, or when they change with time in a previously unknown manner. In other words, the implementation of adaptive estimation methods is preferable when the accuracy of *a priori* knowledge about the system model and noise statistics is insufficient. Adaptive Kalman filters can be classified in terms of parameters (matrices), which should be optimized during the estimation procedure, such as: filters that estimate the covariance matrix of measurement noise, R ; filters that estimate the covariance matrix of input (process) noise, Q ; and, finally, algorithms that estimate the matrices of input noise and measurement noise simultaneously.

In this thesis, an adaptive Kalman filter of unknown measurement covariance, R , is used for estimation and filtering of GPS errors in challenging environments. For INS/GPS applications such as those studied herein, the measurement noise is defined by GPS

noise. In urban areas, HS GPS measurements are characterized by large errors induced by tracking of multipath or echo signals as well as by high code noise due to severe signal fading. Therefore, the level of measurement noise of the integrated algorithm frequently changes in a random manner, which benefits implementation of a filter with adaptive measurement covariance.

4.2.4 Kalman Filter with Control Signal

In a field of INS/GPS integration, the Kalman filter with control is frequently applied. For example, in this thesis the vector of control signal contains the estimates of gyro drifts and azimuth misalignment. In the presence of a control signal, a linear system in SSM can be described as:

$$\mathbf{x}_k = \Phi_{k,k-1}\mathbf{x}_{k-1} + \mathbf{L}u_{k-1} + \mathbf{G}_{k,k-1}\mathbf{w}_{k-1} \quad (4-12)$$

where u_{k-1} is a known control signal.

The main Kalman filter formula (4-4) transforms to:

$$\hat{\mathbf{x}}_k = \Phi_{k,k-1}\hat{\mathbf{x}}_{k-1} + \mathbf{L}u_{k-1} + \mathbf{K}_k(z_k - \mathbf{H}\Phi_{k,k-1}\hat{\mathbf{x}}_{k-1} - \mathbf{H}\mathbf{L}\mathbf{C}u_{k-1}) \quad (4-13)$$

The introduction of a known control signal, u_k , to the system, however, does not affect the gain matrix, \mathbf{K}_k , determination and the rest of the calculation scheme remains the same as in a conventional Kalman filter (Salychev, 2003).

4.2.5 Kalman Filter with Adaptive Measurement Covariance R

This algorithm is developed for the case of unknown precise information about the covariance matrix of the measurement noise, R (Salychev, 1998). The calculation algorithm is shown in Figure 4-2.

The covariance matrix of the innovation sequence can be derived by applying the condition of maximum probability density of the process v_1, v_2, \dots, v_n . For a stationary system, this matrix can be obtained by simple averaging in recurrent from:

$$\hat{C}_k = \frac{k-1}{k} \hat{C}_{k-1} + \frac{1}{k} v_k v_k^T \quad (4-14)$$

Let's prove that the above formula is an averaging procedure:

$$\text{For step 1, } k=1: \hat{C}_1 = v_1 v_1^T$$

$$\text{For step 2, } k=2: \hat{C}_2 = \frac{1}{2} \hat{C}_1 + \frac{1}{2} v_2 v_2^T = \frac{v_1 v_1^T + v_2 v_2^T}{2}$$

$$\text{For step 3, } k=3: \hat{C}_3 = \frac{2}{3} \hat{C}_2 + \frac{1}{3} v_3 v_3^T = \frac{v_1 v_1^T + v_2 v_2^T + v_3 v_3^T}{3}$$

And so on.

Substituting this estimate into (4-9), the formula for matrix R can be defined as:

$$\hat{R}_k = \hat{C}_k - H P_{k,k-1} H^T \quad (4-15)$$

At the beginning of estimation, the defined R_k can be negative definite; therefore, the following normalization procedure should be considered: If $\text{diag } \hat{R}_k < 0$, then diag

$$\hat{R}_k = 0$$

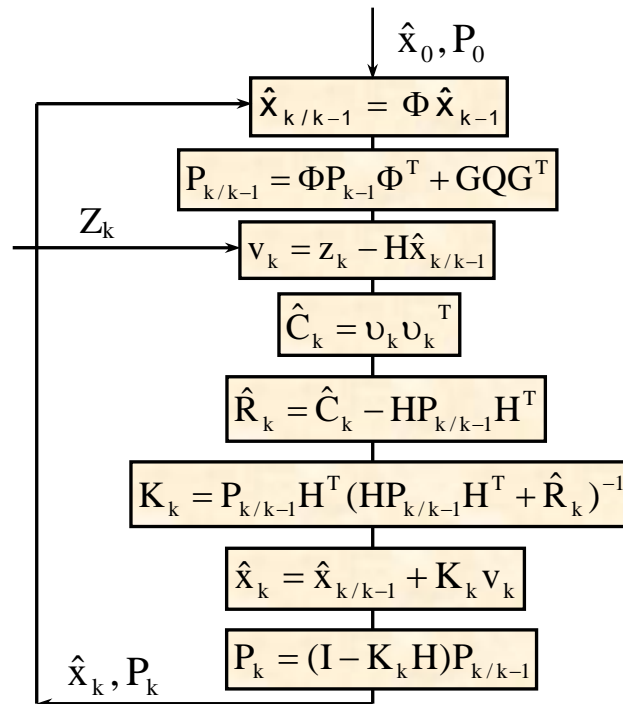


Figure 4-2: Calculation Algorithm for An Adaptive Kalman Filter (ibid)

4.3 Estimation Concepts

Figure 4-3 demonstrates the principal of different estimation approaches. The term, prediction, denotes estimation of the state vector x_k at the current epoch t_k using measurements made in the past z_{k-n} , where $t_k > t_{k-n}$. Filtering is estimation of the state vector x_k utilizing current measurement z_k . These two estimation procedures can be implemented in real time as well as in post-mission. Smoothing is estimation of the state vector x_k , taking into account the total number of measurements within the fixed time interval $t_{k-n} < t_k < t_{k+n}$. This procedure can be employed only in post-mission analysis.

Smoothing provides better estimation accuracy than filtering and filtering, in turn, is more accurate than prediction (Teunissen and Salzmann, 1998).

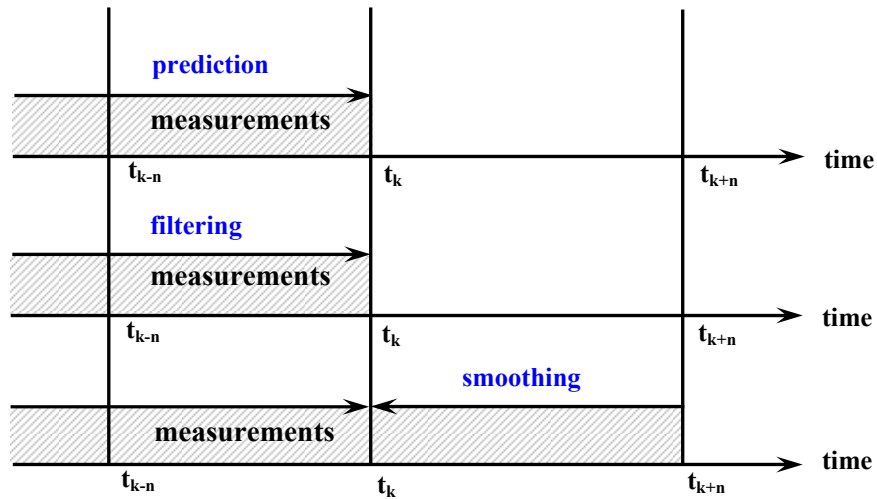


Figure 4-3: Estimation Modes

4.3.1 Kalman Filter in Prediction Mode

Prediction is usually performed during data gaps (herein, during GPS outages). In this case, the last estimate of the state vector is used to initialize the prediction procedure. When measurements are not available, the covariance matrix of measurement noise $R \rightarrow \infty$ and consequently, the Kalman gain $K \rightarrow 0$. It leads to the following transformation of the Kalman filter equations:

$$\begin{aligned}\hat{\mathbf{x}}_k &= \Phi \hat{\mathbf{x}}_{k-1} \\ \mathbf{P}_k &= \Phi \mathbf{P}_{k-1} \Phi^{-1} + \mathbf{G} \mathbf{Q} \mathbf{G}^T\end{aligned}\tag{4-16}$$

Prediction accuracy is mainly defined by the accuracy of the system model, and thus the level of input noise (the second component in the equation for \mathbf{P}_k contains covariance matrix of input noise, \mathbf{Q}), and by the accuracy of the last estimate obtained in filtering

mode (the first component in the same equation contains the covariance matrix of estimation errors, P_{k-1}); thus, it degrades over time (Gelb, 1974). For INS/GPS applications, the linearization problem is similar for filtering and prediction modes and does not have much impact on the estimation accuracy.

Chapter 5

System Realization and Methodology

The contribution of this thesis is development of a special scheme for INS/GPS integration that can be used in various GPS conditions. Based on the of the cascaded integration, which is flexible and compatible method for integration of different types of GPS receivers, two diverse estimation algorithms were developed and tested for implementation in areas with LOS signal reception and in challenging GPS environments. This chapter gives comprehensive analysis of the integration algorithm employed. Both estimation techniques used in the INS/GPS system is also presented. This discussion includes the system and measurement models utilized in a Kalman filter and in adaptive filtering, as well as mechanisms for INS error compensation via feedbacks of error corrections to the navigation block and in the system output.

5.1 INS/GPS Cascaded Integration Scheme

The integration algorithm is presented in Figure 5-1 and the process is described below. First, raw sensor data is processed in the Strapdown Inertial Navigation System (SINS) algorithm, where the INS navigation solution is obtained. The SINS algorithm works in two modes: alignment and navigation. The GPS position is used to initialize the INS alignment (the feedback of $X_{GPS}(0)$ in the Figure 5-1). In the next step, the differences between the INS and GPS positions, as well as the velocities, are formed and fed into the INS Kalman filter. The INS estimation block also works in two modes: filtering, when

GPS measurements are available; and prediction, e.g. during GPS data gaps or when the GPS solution is not reliable. Following this, the estimated INS errors are compensated in the system output and in the SINS algorithm. For open area applications, the estimates of INS errors in position and velocity, as well as the estimated horizontal misalignment angles, are utilized to correct the integrated navigation solution, while the estimates of gyro drifts and azimuth misalignment are fed back to the SINS calculation scheme. For highly urbanized environments such as downtown districts, in the SINS algorithm a feedback of only the estimated INS azimuth misalignment is arranged. Position and velocity compensation is performed similarly to open area applications.

The combination of INS and GPS improves total system performance, since GPS is used for in-motion correction of the INS errors, while the INS bridges GPS outages caused by satellite blockage and signal power degradation. In this latter case, the estimation algorithm works in prediction mode. As expected, prediction accuracy degrades rapidly with time. Analysis of the Kalman filter equations shows that prediction accuracy depends only on the estimation accuracy of the state vector components of the last epoch, in which GPS measurements were available, along with the accuracy of the system model (Salychev, 1998). Consequently, for INS/GPS integration, accurate estimation of the INS errors becomes critical in prediction (see section 4.3.1). In this case, the Kalman filter calculation algorithm is transformed to the form of equations (4-16).

In filtering mode, the accuracy of the integrated system is defined by the level of accuracy of the GPS solution, which depends upon the type of observables used (e.g.

pseudorange or carrier phase measurements) and the navigation methods employed (e.g. a Least Squares method, or a Kalman filter). In this thesis, a DGPS code solution is utilized to assist the INS. Thus, under line-of-sight GPS signal conditions, a positional accuracy at the sub-metre level can be achieved. In downtown canyons, GPS measurements are potentially corrupted by multipath, signal degradation and signal cross-correlation. In such cases, the implementation of traditional estimation tools such as a conventional Kalman filter becomes problematic due to challenges with fault detection. Under harsh GPS conditions, the measurement covariance is not always trustworthy, or may change in a manner that is not highly predictable. Therefore, a Kalman filter with an adaptive measurement covariance (see section 4.2.5) is used for error estimation. In degraded GPS signal environments, a GPS solution is not always reliable for correction of INS errors, such as gyro drifts. Thus, two different estimation schemes for INS/GPS integration are employed for open and urban area applications, respectively.

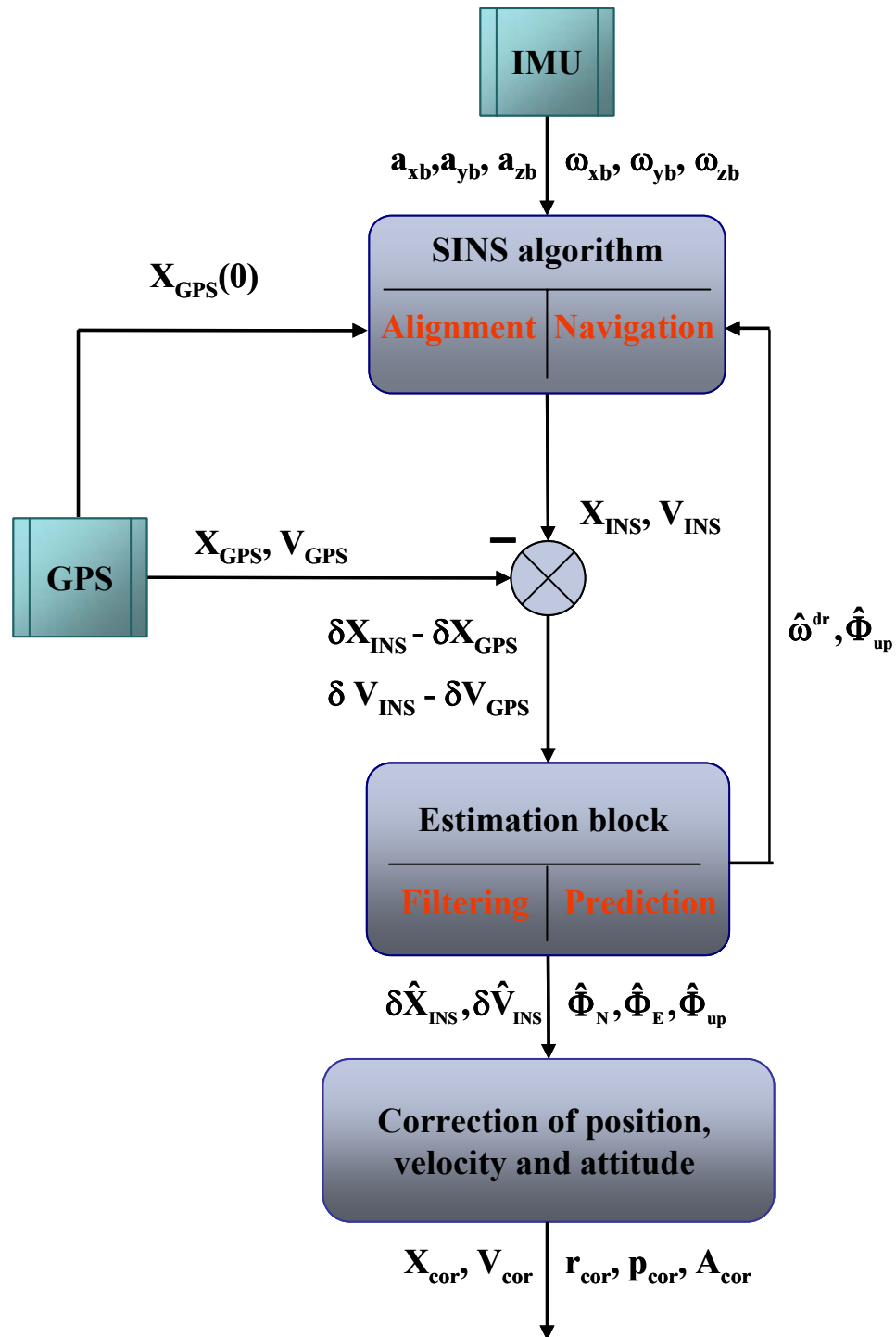


Figure 5-1: Cascaded Scheme of INS/GPS Integration

5.2 Error Estimation and Compensation for Open Area

Applications

The INS error estimation scheme is shown in Figure 5-2. As previously mentioned, a traditional Kalman filter is implemented. In this thesis, the INS error equations are used as a system model, and measurements that are fed to the filter are the differences between the INS and GPS positions and velocities. When GPS data is not available, the Kalman filter works in prediction mode. The estimation of INS positional errors is performed in an individual Kalman filter in order to improve estimation accuracy, since the estimates of position and velocity errors have different time lags with respect to actual values, which leads to different input noise covariances.

The INS filter output contains the following parameters: position, velocity and attitude errors as well as gyro drifts. Estimated INS position and velocity errors are compensated in the system output. INS horizontal errors are used to correct the elements of the transformation matrix between the body and navigation frames, R_b^N . The INS azimuth misalignment is compensated independently in the SINS algorithm as a one-step control signal introduced to the quaternion of a small rotation, Δm . Estimated gyro drifts are also taken into account in the SINS navigation scheme, in a similar fashion to azimuth error compensation.

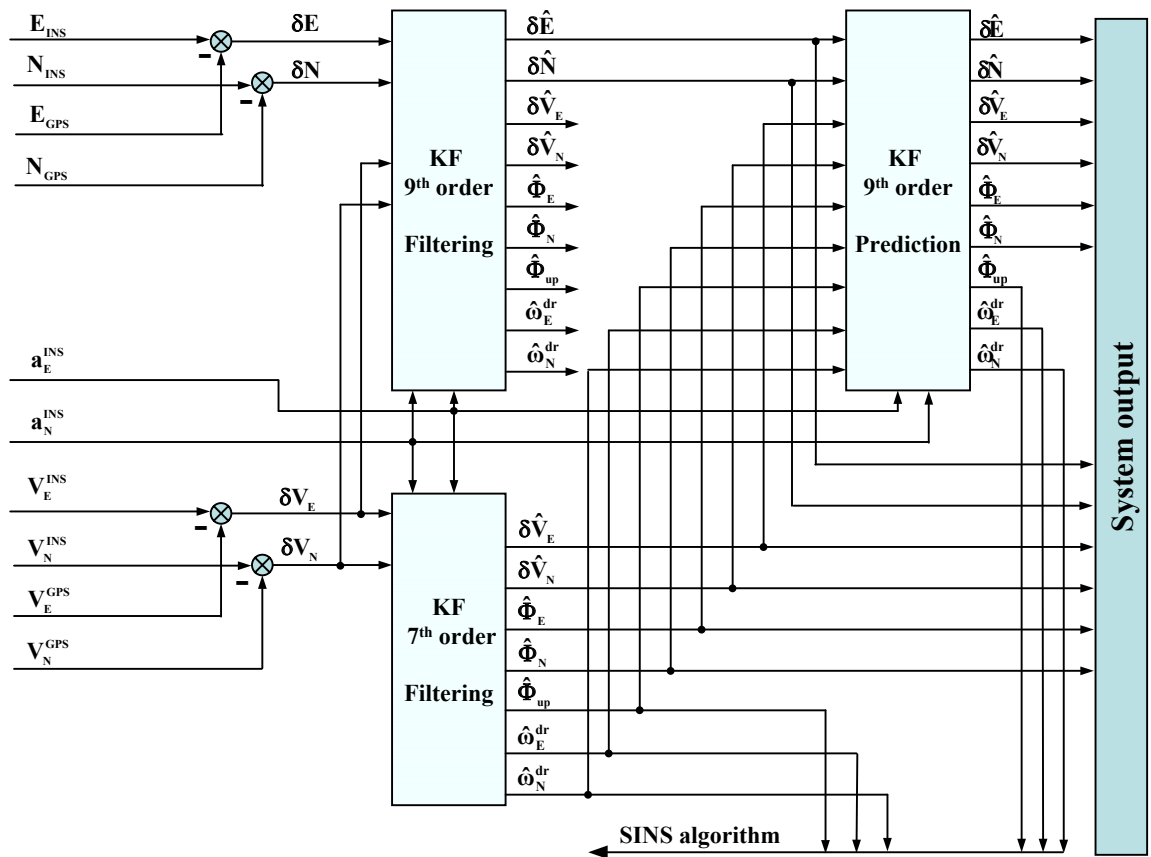


Figure 5-2: Estimation Algorithm for Open Area Applications

Chapter 3 discusses the main characteristics of INS errors in detail. Azimuth misalignment can have a significant impact on overall system performance during high vehicle dynamics, because it is motion-dependent. Due to the non-stationary property of this error, its accurate estimation can be problematic using traditional estimation approaches; therefore, a special estimation procedure is implemented to obtain an accurate estimate of azimuth error. Since the method takes into account the degree of observability of different INS error components, an observability analysis of the INS errors is presented below.

5.2.1 Observability Analysis of INS Errors

For INS error estimation, only the observable components of the INS error need to be considered in the system model. Equations (3-30) can be used for short-term analysis of half an hour – an hour and prediction intervals of several seconds only, since they do not describe INS error behavior with high accuracy. The following error equations are utilized for INS error estimation (Salychev, 2003):

$$\begin{aligned}
 \delta \dot{E} &= \delta V_E \\
 \delta \dot{N} &= \delta V_N \\
 \delta \dot{V}_E &= -g\Phi_N + a_N\Phi_{up} + u_E + w_1(t) \\
 \delta \dot{V}_N &= g\Phi_E - a_E\Phi_{up} + u_N + w_2(t) \\
 \dot{\Phi}_E &= -\frac{\delta V_N}{R} + \omega_E^{dr} + u_N + w_3(t) \\
 \dot{\Phi}_N &= \frac{\delta V_E}{R} + \omega_N^{dr} + u_E + w_4(t)
 \end{aligned} \tag{5-1}$$

where: $\delta E, \delta N$ are the position errors in the East and North directions, respectively;

$\delta V_E, \delta V_N$ are the velocity errors in the East and North directions, respectively;

Φ_E, Φ_N are the attitude errors of the horizontal channels, respectively;

Φ_{up} is the azimuth misalignment;

a_E, a_N are the vehicle accelerations;

g is the gravity vector;

$\omega_E^{dr}, \omega_N^{dr}$ are the gyro drifts projected into the local-level frame;

- $w_1(t), w_2(t)$ is input noise caused by accelerometer biases, accelerometer scale factors, their non-linearities and accelerometer installation errors;
- $w_3(t), w_4(t)$ is input noise caused by gyro scale factors, their non-linearities and gyro installation errors; and
- u_E, u_N vectors of control signal with error correction (feedback of gyro drifts and azimuth misalignment to the quaternion, Δm).

The gyro drifts, ω_E^{dr} and ω_N^{dr} , are estimated in projections onto the ll-frame. To consider these errors in the SINS algorithm, they have to be recalculated in the body frame (*ibid*). For automobile applications, a vehicle typically changes its attitude significantly in heading only; therefore, gyro drifts in the ll-frame can be represented via the projections of the drifts onto the b-frame, ω_{xb}^{dr} and ω_{yb}^{dr} :

$$\begin{aligned}\omega_E^{dr} &= \omega_{xb}^{dr} \cos H + \omega_{yb}^{dr} \sin H \\ \omega_N^{dr} &= -\omega_{xb}^{dr} \sin H + \omega_{yb}^{dr} \cos H\end{aligned}\tag{5-2}$$

where H is a heading angle.

The drifts, ω_{xb}^{dr} and ω_{yb}^{dr} , are usually represented by a shaping filter with a certain correlation function (here represented by a 1st Order Gauss-Markov process):

$$\begin{aligned}\dot{\omega}_{xb}^{dr} &= -\beta \omega_{xb}^{dr} + A \sqrt{2\beta} w_6(t) \\ \dot{\omega}_{yb}^{dr} &= -\beta \omega_{yb}^{dr} + A \sqrt{2\beta} w_7(t)\end{aligned}\tag{5-3}$$

where: A, β are parameters of the correlation function $R(\omega_{dr}) = A^2 \exp(\beta |\tau|)$;

$w_6(t), w_7(t)$ is input white noise of identity intensity (*ibid*).

Equations (5-1), (5-2) and (5-3) are utilized as a system model in a Kalman filter. Since the INS position and velocity errors are derived from the GPS data, these INS error components are considered to be directly measured. Due to the fact that separation of several nearly constant parameters is problematic, the separation of $g\Phi_N(0)$ and $g\Phi_E(0)$ from higher order terms in many cases can be a very difficult task (e.g. accelerometer biases, B_{xb} and B_{yb} , can be separated from horizontal errors, $\Phi_N(0)$ and $\Phi_E(0)$, only when vehicle azimuth changes significantly, i.e. more than 20°). Therefore, in this thesis, the accelerometer biases, scale factors and installation errors are selected as unobservable components and reduced to input noise, w_1 and w_2 . Similarly, the high order gyro errors are assumed to be not observable and reduced to input noise, w_3 and w_4 .

An observability analysis of the INS Schuler components can be performed by calculating the observability matrix (A) of the single channel model (see equations (5-15)). Because this matrix has a non-zero determinant, all Schuler components are generally observable. For example, the observability matrix for three measurements ($n = 3$ in equation (3-8)) has the following form:

$$A = \begin{bmatrix} H \\ H\Phi \\ H\Phi^2 \end{bmatrix} = \begin{bmatrix} 1 & 0 & 0 \\ 0 & -gT & 0 \\ 1-gT^2/R & -2gT & -gT^2 \end{bmatrix} \quad \text{and : } \det A = g^2T^3 \neq 0$$

Furthermore, it is clear that all INS errors, which take part in the above set of equations, are generally observable since they can be derived through differentiation of the directly measured INS error components (position and velocity errors) (*ibid*).

Analysis of the degree of observability of each state vector component shows that the strongly observable state vector components (Φ_E and Φ_N) are nearest to the directly measured ones (δV_E and δV_N). The remaining components are weakly observed (ω_E^{dr} and ω_E^{dr}). Consequently, the attitude errors and gyro drift rates have a greater degree of observability, when velocity error measurements are used instead of position error measurements (in this case, gyro drifts stand closer to the directly measured components in the state vector); therefore, the reduced system model, without the position errors, δE and δN , is considered. Moreover, the degree of observability corresponds to the duration of the estimation transition process (*ibid*).

Equations (5-1) show that Φ_{up} can be separated from Φ_E and Φ_N only when a vehicle has a substantial acceleration change during motion ($\Delta a_N, \Delta a_E > \text{threshold}$). It comes from the fact that two components $g\Phi_N$ and $a_N\Phi_{\text{up}}$ in the third formula of (5-1) as well as $g\Phi_E$ and $a_E\Phi_{\text{up}}$ in the forth formula of (5-1) are nearly constant, if a_N and a_E do not change, while the separation of two nearly constants is a very problematic task. Thus, the observability of Φ_{up} depends on vehicle dynamics, and precise estimation of the azimuth misalignment error is questionable for moderate (stationary) motion or in static mode (*Park et al., 2000; Salycheva and Cannon, 2004*). Hereinafter, stationary motion is defined as motion with nearly constant speed.

5.2.2 In-motion Azimuth Estimation Using Cascaded Kalman

Filter

The considered method is based on the above conventional Kalman filter (KF7 in Figure 5-2). The INS error model in equation (5-1) (without positions since they are estimated independently in the Kalman filter with nine error states, referred as KF9 in Figure 5-2) is used as a system model. In the SSM representation, it can be described as:

$$\begin{aligned}
 \begin{bmatrix} \delta \dot{V}_E \\ \delta \dot{V}_N \\ \dot{\Phi}_E \\ \dot{\Phi}_N \\ \dot{\Phi}_{up} \\ \dot{\omega}_{xb}^{dt} \\ \dot{\omega}_{yb}^{dr} \end{bmatrix} &= \begin{bmatrix} 0 & 0 & 0 & -g & a_N & 0 & 0 \\ 0 & 0 & g & 0 & -a_E & 0 & 0 \\ 0 & -1/R & 0 & 0 & 0 & \cos H & \sin H \\ 1/R & 0 & 0 & 0 & 0 & -\sin H & \cos H \\ 0 & 0 & 0 & 0 & 0 & 0 & 0 \\ 0 & 0 & 0 & 0 & 0 & -\beta & 0 \\ 0 & 0 & 0 & 0 & 0 & 0 & -\beta \end{bmatrix} \begin{bmatrix} \delta V_E \\ \delta V_N \\ \Phi_E \\ \Phi_N \\ \Phi_{up} \\ \omega_{xb} \\ \omega_{yb} \end{bmatrix} + \\
 &+ \begin{bmatrix} 0 & 0 & 0 \\ 0 & 0 & 0 \\ 0 & -1 & 0 \\ 0 & 0 & 1 \\ -1 & 0 & 0 \\ 0 & 0 & 0 \\ 0 & 0 & 0 \end{bmatrix} \begin{bmatrix} \hat{\Phi}_{up}/T_1 \\ \hat{\omega}_E^{dr} \\ \hat{\omega}_N^{dr} \end{bmatrix} + \begin{bmatrix} 1 & 0 & 0 & 0 & 0 & 0 & 0 \\ 0 & 1 & 0 & 0 & 0 & 0 & 0 \\ 0 & 0 & 1 & 0 & 0 & 0 & 0 \\ 0 & 0 & 0 & 1 & 0 & 0 & 0 \\ 0 & 0 & 0 & 0 & 1 & 0 & 0 \\ 0 & 0 & 0 & 0 & 0 & A\sqrt{2\beta} & 0 \\ 0 & 0 & 0 & 0 & 0 & 0 & A\sqrt{2\beta} \end{bmatrix} \begin{bmatrix} w_1 \\ w_2 \\ w_3 \\ w_4 \\ w_5 \\ w_6 \\ w_7 \end{bmatrix} \quad (5-4)
 \end{aligned}$$

The gyro drifts, $\hat{\omega}_N^{dr}$ and $\hat{\omega}_E^{dr}$, in equations for $\dot{\Phi}_E$ and $\dot{\Phi}_N$ are obtained from the estimates, $\hat{\omega}_{xb}^{dr}$ and $\hat{\omega}_{yb}^{dr}$, using formula (5-2). The azimuth misalignment is compensated once as an impulse signal $\hat{\Phi}_{up}/T_1$. Herein, $T_1 = 0.04$ seconds is the sampling time of the navigation solution calculation (inertial data rate is reduced from 100 Hz to 25 Hz).

The measurement model is based on the velocity difference between an INS and GPS. It has the form:

$$\begin{aligned} z_E &= V_E^{\text{INS}} - V_E^{\text{GPS}} = \delta V_E^{\text{INS}} - \underbrace{\delta V_E^{\text{GPS}}}_{\substack{V^E\text{-measurement} \\ \text{noise}}} \\ z_N &= V_N^{\text{INS}} - V_N^{\text{GPS}} = \delta V_N^{\text{INS}} - \underbrace{\delta V_N^{\text{GPS}}}_{\substack{V^N\text{-measurement} \\ \text{noise}}} \end{aligned} \quad (5-5)$$

or, in matrix form:

$$\underbrace{\begin{bmatrix} z_E \\ z_N \end{bmatrix}}_Z = \underbrace{\begin{bmatrix} 1 & 0 & 0 & 0 & 0 & 0 & 0 \\ 0 & 1 & 0 & 0 & 0 & 0 & 0 \end{bmatrix}}_H \underbrace{\begin{bmatrix} \delta V_E \\ \delta V_N \\ \Phi_E \\ \Phi_N \\ \Phi_{\text{up}} \\ \omega_E^{\text{dr}} \\ \omega_N^{\text{dr}} \end{bmatrix}}_X + \underbrace{\begin{bmatrix} V^E \\ V^N \end{bmatrix}}_V \quad (5-6)$$

Using the above system and measurement models, a Kalman filter that estimates the azimuth misalignment angle Φ_{up} along with the other INS error components can be applied. However, an analysis of the degree of observability proves that the transition process of the estimation of Φ_{up} may be significantly long. Because of the large size of the total state vector, the Kalman filter spends additional time for convergence of the components, which are closer to the directly measured ones (Φ_E and Φ_N). In order to reduce the convergence time for estimation of Φ_{up} , a direct approach is implemented.

Estimation of azimuth misalignment is initialized only when Φ_{up} is strongly observable, i.e. when the magnitude of the vehicle acceleration change reaches a certain threshold. In

this case, the estimation problem statement is reformulated so that Φ_{up} is directly measured. The estimation algorithm for Φ_{up} can be determined directly from the system model equations as follows (Salychev, 2003):

If $|\Delta a_N|$ or $|\Delta a_E| > \delta$, then

$$\hat{\Phi}_{up} = \frac{\delta \hat{V}_E a_N - \delta \hat{V}_N a_E + g \hat{\Phi}_N a_N + g \hat{\Phi}_E a_E}{a_N^2 + a_E^2} \quad (5-7)$$

where: $\delta \hat{V}_E, \delta \hat{V}_N$ are the estimates of the acceleration errors;

$\hat{\Phi}_E, \hat{\Phi}_N$ are the estimates of the horizontal attitude errors, obtained when $|\Delta a_N|, |\Delta a_E| < \delta$;

δ is the threshold of the vehicle acceleration change (here: $\delta \approx 0.2$ m/s²).

In this thesis, in order to additionally smooth the estimation errors, Φ_{up} is averaged over some time interval (a sliding window with a size of 100 seconds).

The above approach is applied in the beginning of the estimation of Φ_{up} , but after the termination of the transition process, the estimate of Φ_{up} is introduced into the extended Kalman filter. This method decreases the time for convergence of the azimuth misalignment significantly, because this error is treated as a directly measured value. Initially, the elements of the state vector are set to zero: $x_0 = 0$ (see section 4.2.2). The initial covariance matrix of estimation errors, P_0 , is the following:

$$P_0 = \begin{bmatrix} 10 & 0 & 0 & 0 & 0 & 0 & 0 & 0 & 0 \\ 0 & 100 & 0 & 0 & 0 & 0 & 0 & 0 & 0 \\ 0 & 0 & 0.01 & 0 & 0 & 0 & 0 & 0 & 0 \\ 0 & 0 & 0 & 0.01 & 0 & 0 & 0 & 0 & 0 \\ 0 & 0 & 0 & 0 & 0.0003 & 0 & 0 & 0 & 0 \\ 0 & 0 & 0 & 0 & 0 & 0.0003 & 0 & 0 & 0 \\ 0 & 0 & 0 & 0 & 0 & 0 & 0.03 & 0 & 0 \\ 0 & 0 & 0 & 0 & 0 & 0 & 0 & 1.9e^{-8} & 0 \\ 0 & 0 & 0 & 0 & 0 & 0 & 0 & 0 & 1.9e^{-8} \end{bmatrix}$$

The accuracy of the azimuth error estimation depends on an initial value of Φ_{up} after INS alignment. For medium accuracy INS units, such as the Honeywell's HG1700, it can be in the order of 6-15°. In this case, the assumed linear INS error model does not describe INS error behaviour properly (the assumption made about small angles is not appropriate). In order to achieve high accuracy in azimuth misalignment estimation, a heading correction is initially used (Salycheva and Cannon, 2004). After a one-step correction of the azimuth, the remaining azimuth misalignment of approximately 1 to 2° is estimated by a cascaded filter and is compensated in the navigation scheme. Finally, the estimation procedure is divided into two parts:

- (1) Coarse azimuth error compensation using external heading information; and
- (2) Fine azimuth error compensation using the cascaded filter.

5.2.3 Heading Correction

Another method of in-motion azimuth alignment is the application of a heading correction. Approximate heading information can be derived from GPS measurements,

see for instance (Shin and El-Sheimy, 2002). For a land vehicle, the heading angle H can be calculated using the GPS velocity components (see Figure 5-3). Heading from GPS velocities can be computed as follows:

$$H^{\text{GPS}} = \arctan^{-1} \frac{V_E^{\text{GPS}}}{V_N^{\text{GPS}}} \quad (5-8)$$

and the standard deviation of the heading error $\sigma(\delta H)$ is

$$\sigma(\delta H^{\text{GPS}}) = \frac{\sigma(\delta V^{\text{GPS}})}{V^{\text{GPS}}} \quad (5-9)$$

where: $\sigma(\delta H^{\text{GPS}})$ is the standard deviation of the GPS velocity error;

$V^{\text{GPS}} = \sqrt{(V_N^{\text{GPS}})^2 + (V_E^{\text{GPS}})^2}$ is the GPS velocity (nominal value of vehicle speed).

For example, for a typical value of $\sigma(\delta V^{\text{GPS}}) = 0.1-0.2$ m/s; and vehicle speed $V^{\text{GPS}} = 10$ m/s, $\sigma(\delta H^{\text{GPS}})$ according to equation (5-9) is $0.6^\circ-1^\circ$.

Using GPS measurements, the INS correction of the heading angle is

$$\delta \hat{H}^{\text{INS}} = H^{\text{INS}} - H^{\text{GPS}} \quad (5-10)$$

where H^{GPS} is calculated only when a vehicle has sufficient speed (more than 5 m/s, which is defined empirically). Before compensation of the INS heading error, it is averaged over a certain time interval (a sliding window with a size of 100 seconds).

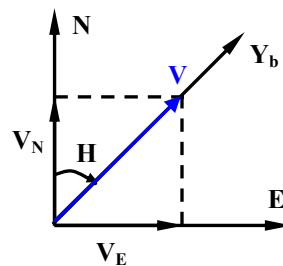


Figure 5-3: GPS Heading

For the heading correction, the one-step control signal to the gyro torque (quaternion of a small rotation) is arranged as follows:

$$\omega_z^c = \frac{\delta \hat{H}^{INS}}{T_1} \quad (5-11)$$

where T_1 is time sampling interval.

In this case, a Kalman filter with a control signal (vector u in equations (5-1)) is applied.

The conventional Kalman filter equations are changed to equations (4-12) and (4-13).

5.2.4 Roll and Pitch Correction

The Kalman filter estimates of the horizontal attitude errors, Φ_E and Φ_N , represent the fact that the platform frame has a small angular deviation from the navigation frame due to sensor errors. This means that in the SINS algorithm, the transformation matrix between the b-frame and p-frame R_b^p is calculated, instead of transformation matrix between the b-frame and the n-frame R_b^N . In order to compensate the attitude errors, the R_b^N is corrected using the estimates, $\hat{\Phi}_E$ and $\hat{\Phi}_N$ (Salychev, 2003):

$$R_b^N = R_p^N R_b^p \quad (5-12)$$

where R_p^N is the transformation matrix between the platform and navigation frames,

which has a form (see equation (3-27) without Φ_{up} correction):

$$R_p^N = \begin{bmatrix} 1 & 0 & \hat{\Phi}_N \\ 0 & 1 & -\hat{\Phi}_E \\ -\hat{\Phi}_N & \hat{\Phi}_E & 1 \end{bmatrix} \quad (5-13)$$

Using the new elements of R_b^N , roll and pitch angles are corrected (see equation (A-16) in Appendix A).

5.2.5 Gyro Drift Compensation

The gyro drifts in the projections on the b-frame, ω_{xb}^{dr} and ω_{yb}^{dr} , can be compensated in the raw output directly; however, in this thesis, the gyro drifts in the ll-frame, ω_E^{dr} and ω_N^{dr} , are compensated instead by applying the control signals to the quaternion of a slow motion Δm (in a manner similar to the treatment of the heading correction).

5.2.6 Position and Velocity Correction

The integrated position and velocities are obtained from the corrected INS output:

$$\begin{aligned} E^{INS/GPS} &= E^{INS} - \delta \hat{E}^{INS} \\ N^{INS/GPS} &= N^{INS} - \delta \hat{N}^{INS} \\ V_E^{INS/GPS} &= V_E^{INS} - \delta \hat{V}_E^{INS} \\ V_N^{INS/GPS} &= V_N^{INS} - \delta \hat{V}_N^{INS} \end{aligned} \tag{5-14}$$

where: $E^{INS/GPS}$, $N^{INS/GPS}$ are the position increments in the North and East directions, which are outputted by the integrated system;

E^{INS} , N^{INS} are the position increments, outputted from the SINS algorithm;

$\delta \hat{E}^{INS}$, $\delta \hat{N}^{INS}$ are the estimated INS position errors;

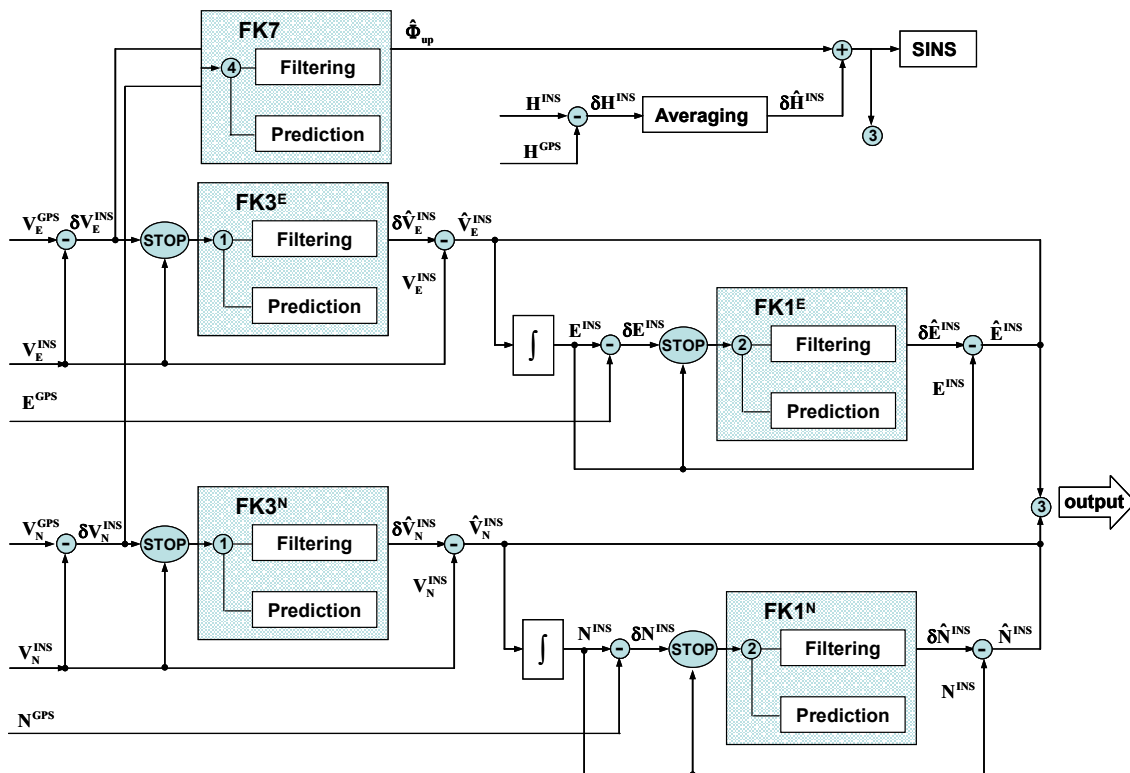
$V^{INS/GPS}$, $V^{INS/GPS}$ are the North and East velocities of the integrated system;

V^{INS}, V^{INS} are the INS velocities; and
 $\delta\hat{V}^{INS}, \delta\hat{V}^{INS}$ are the estimated INS velocity errors.

5.3 Error Estimation and Compensation for Downtown Applications

The scheme of integration is presented in Figure 5-4. As with the open area algorithm, Kalman filters are used for error estimation and prediction. In this case, the position and velocity estimation is performed independently for the east and north channels. The main reason for such separation lies in the relatively small dimensions of the filter state vectors which, in turn, decreases the filter convergence time.

For downtown applications, accurate estimation of the weakly observable INS errors becomes problematic due to error-corrupted GPS updates. Therefore, only the estimated azimuth misalignment error is compensated in the SINS scheme. The azimuth error estimate is obtained from an individual Kalman filter with the 7-th state system model analogously to the above strategy for open area applications. It is then combined with heading error correction, which is obtained from GPS heading, and introduced to the SINS scheme.



- ① **Prediction:** 1. PDOP > 7 or Num SV < 7
2. $\hat{V}^{INS} - V^{GPS} > 2\text{m/s}$
- ② **Prediction:** 1. PDOP > 7 or Num SV < 7
2. In stop
- ③ If Num SV > 7 or PDOP < 7 and $\hat{\phi}_{up} + \delta\hat{H}_{INS} > 3^0$: $\mathbf{X}^{output} = \mathbf{X}^{GPS}$
 $\mathbf{V}^{output} = \mathbf{V}^{GPS}$
Else: $\mathbf{X}^{output} = \hat{\mathbf{X}}^{INS}$
 $\mathbf{V}^{output} = \hat{\mathbf{V}}^{INS}$
- ④ **Prediction:** $\hat{V}^{INS} - V^{GPS} > 10\text{m/s}$
- ⊙ **STOP Filter inputs:** In stop: $E^{INS}, N^{INS}, V_E^{INS}, V_N^{INS}$
In motion: $\delta E^{INS}, \delta N^{INS}, \delta V_E^{INS}, \delta V_N^{INS}$

Figure 5-4: Estimation Algorithm for Downtown Applications

5.3.1 Velocity Filters

Conventional Kalman filters with a reduced system model are utilized for the INS velocity error estimation (boxes FK3^E and FK3^N in Figure 5-4). The system equations are (see equations (5-1)):

$$\begin{cases} \delta\dot{V}_E = -g\Phi_N + w_1(t) \\ \dot{\Phi}_N = \frac{\delta V_E}{R} + \omega_N^{dr} \\ \dot{\omega}_N^{dr} = -\beta\omega_N^{dr} + A\sqrt{2\beta}w_2(t) \end{cases} \quad \begin{cases} \delta\dot{V}_N = g\Phi_E + w_3(t) \\ \dot{\Phi}_E = -\frac{\delta V_N}{R} + \omega_E^{dr} \\ \dot{\omega}_E^{dr} = -\beta\omega_E^{dr} + A\sqrt{2\beta}w_4(t) \end{cases} \quad (5-15)$$

In the SSM representation, the system model thus has the following from:

$$\begin{bmatrix} \delta\dot{V}_E \\ \dot{\Phi}_N \\ \dot{\omega}_N^{dr} \end{bmatrix} = \begin{bmatrix} 0 & -g & 0 \\ 1/R & 0 & 1 \\ 0 & 0 & -\beta \end{bmatrix} \begin{bmatrix} \delta V_E \\ \Phi_N \\ \omega_N^{dr} \end{bmatrix} + \begin{bmatrix} 1 & 0 & 0 \\ 0 & 0 & 0 \\ 0 & 0 & A\sqrt{2\beta} \end{bmatrix} \begin{bmatrix} w_1 \\ 0 \\ w_2 \end{bmatrix} \quad (5-16)$$

$$\begin{bmatrix} \delta\dot{V}_N \\ \dot{\Phi}_E \\ \dot{\omega}_N^{dr} \end{bmatrix} = \begin{bmatrix} 0 & -g & 0 \\ 1/R & 0 & 1 \\ 0 & 0 & -\beta \end{bmatrix} \begin{bmatrix} \delta V_N \\ \Phi_E \\ \omega_N^{dr} \end{bmatrix} + \begin{bmatrix} 1 & 0 & 0 \\ 0 & 0 & 0 \\ 0 & 0 & A\sqrt{2\beta} \end{bmatrix} \begin{bmatrix} w_3 \\ 0 \\ w_4 \end{bmatrix}$$

The measurement model employed is similar to the open area algorithm:

$$z_E = \begin{bmatrix} 1 & 0 & 0 \end{bmatrix} \begin{bmatrix} \delta V_E \\ \Phi_N \\ \omega_N^{dr} \end{bmatrix} + V^E \quad (5-17)$$

$$z_E = \begin{bmatrix} 1 & 0 & 0 \end{bmatrix} \begin{bmatrix} \delta V_N \\ \Phi_E \\ \omega_E^{dr} \end{bmatrix} + V^N$$

Being driven in urban areas, an automobile must frequently come to a complete stop due to a high density of controlled intersections with traffic lights as well as periodic traffic jams. This type of vehicle motion can be used to update an inertial system. When a test vehicle stops and its linear velocity is equal to zero, the non-zero output of the INS

velocity indicates is a pure INS velocity error. In this case, the Schuler component of the INS error becomes directly measured, since the non-stationary INS error is negligible in static mode (see section 3.3). Measurements of this type are called Zero Velocity Updates (ZUPTs), in the case where a test vehicle routinely stops in order to obtain error updates (El-Sheimy, 2003). However, in this research a test vehicle is not forced to stop purposely to obtain measurement updates, and static measurements (i.e. during stop, which will be discussed in the following section) are used when available. Therefore, hereinafter, the term ‘stop’ is utilized instead.

The considered estimation scheme takes vehicle dynamics into account. When a test vehicle stops, the INS East and North velocities are fed into the filters while, in motion, the differences between the INS and GPS velocities are used as measurements analogously to the algorithm for open area applications. To accurately estimate the Schuler component of the INS error, static measurements should have larger gain than in-motion measurements, which is defined by the Kalman gain matrix. Therefore, different parameters of the measurement covariance are chosen for static and kinematic modes (see Kalman equations (4-5) and (4-6)):

$$\text{In motion: } Q = \begin{bmatrix} 1e^{-2} & 0 & 0 \\ 0 & 0 & 0 \\ 0 & 0 & 1e^{-13} \end{bmatrix}, R = 10m^2 / c^2$$

$$\text{In stop: } Q = \begin{bmatrix} 1e^{-2} & 0 & 0 \\ 0 & 0 & 0 \\ 0 & 0 & 1e^{-13} \end{bmatrix}, R = 1m^2 / c^2$$

In downtown areas, HS GPS measurements are characterized by high levels of noise due to signal attenuation and they are potentially corrupted by large errors such as those induced by the tracking of multipath or echo-only signals. Therefore, in this thesis, the value of measurement noise covariance is chosen to be significantly large and defined empirically.

The initial error state in the Kalman filter is set to zero ($x_0 = 0$) while the initial covariance matrix of estimation errors, P_0 , has the following form (see section 4.2.2):

$$P_0 = \begin{bmatrix} 1 & 0 & 0 \\ 0 & 0.0003 & 0 \\ 0 & 0 & 1.9e^{-8} \end{bmatrix}$$

During the transition process of the azimuth misalignment estimation (the independent Kalman filter with 7 states in the system model, box FK7 in Figure 5-4) velocity filters work as they do in static mode (the filter estimates are based mainly on the measurements rather than on the system model: $R=10 \text{ m/s}^2$). A complete stop of a test vehicle is determined from the filtered accelerometer output. Raw accelerometer data is averaged with a sliding window of one second. The stop criterion threshold equals to 0.05 m/s^2 .

The filters switch to prediction mode when the GPS measurements are not available or not reliable. In this case, the Kalman gain is set to zero and the Kalman equations are transformed to the form of equations (4-16). The reliability criterion is defined by the GPS Position DOP (PDOP), the number of satellites used in the solution and the difference between GPS velocity and predicted INS velocity.

5.3.2 Coordinate filters

The INS position increments in the East and North directions, E^{INS} and N^{INS} , are determined via integration of the East and North velocities, \hat{V}_E^{INS} and \hat{V}_N^{INS} , which are already corrected for major errors. The differences between the INS and GPS position increments are considered as the INS position error in the East and North directions. These measurements are fed into two independent coordinate filters (for the East and North channels respectively; see boxes $FK1^E$ and $FK1^N$ in Figure 5-4). Each coordinate filter is a Kalman filter with one state x and adaptive measurement covariance r . It is assumed that the INS position error does not vary significantly, since the INS positions are obtained from integration of the corrected INS velocities. Therefore, the system model is defined as:

$$\dot{x} = w(t) \quad (5-18)$$

Analogously to the velocity filters, a measurement model with random walk process is implemented in each coordinate filter:

$$z_k = x_k + v_k \quad (5-19)$$

where: z_k is the measurement of the INS-GPS position difference in the East or North directions;

x_k is the state of the INS error in the East or North positions; and

v_k is measurement noise assumed to be zero mean white noise with covariance r .

For this simple model, the Kalman filter equations are transformed to the following scalar formulas (see section 4.2.5):

$$\begin{aligned}
\hat{x}_k &= \hat{x}_{k-1} + \frac{P_{k-1} + G^2Q}{P_{k-1} + G^2Q + \hat{r}_k} (z_k - \hat{x}_{k-1}) \\
\hat{r}_k &= (z_k - \hat{x}_{k-1})^2 - P_{k-1} - G^2Q \\
P_k &= \frac{(P_{k-1} + G^2Q)\hat{r}_k}{P_{k-1} + G^2Q + \hat{r}_k}
\end{aligned} \tag{5-20}$$

where: $k = \frac{P_{k-1} + G^2Q}{P_{k-1} + G^2Q + \hat{r}_k}$ is the Kalman gain; and

\hat{r}_k is the adapted measurement covariance.

Similarly to the treatment of velocity filters, the coordinate filters switch to prediction mode in the case of GPS data gaps or error-corrupted GPS measurements. The reliability criterion is based on the PDOP and the number of satellites used in the solution (see Figure 5-4). The filter mode also depends upon vehicle dynamics. When a test vehicle stops, the position increments do not change and therefore the filters also work in prediction mode. In this case, the estimate is based on the system model and thus the Kalman gain is set to zero (the measurement covariance tends to infinity: $r \rightarrow \infty$). Equation (5-20) is thus modified to:

$$\begin{aligned}
\hat{x}_k &= \hat{x}_{k-1} \\
P_k &= P_{k-1} + G^2Q
\end{aligned} \tag{5-21}$$

The initial values for the Kalman filter are the following: initial position error, $x_0 = 0$; initial covariance of estimation errors, $P_0 = 10000 \text{ m}^2$.

5.3.3 Azimuth Correction

Since GPS measurements are not always available in downtown canyons, and the GPS solution is potentially corrupted by large errors, the estimation accuracy of the weakly observable INS error components degrades significantly due to long-term predictions of a few minutes. These rough estimates cannot be used for error compensation inside the SINS algorithm of a tactical grade (herein a medium accuracy) INS. Therefore, only the estimate of azimuth misalignment is fed back to the navigation algorithm.

The azimuth error correction is obtained from two independent sources, similarly to the method used for open area application. The first deterministic part $\delta\hat{H}^{\text{INS}}$ is the INS heading correction determined using the GPS heading (section 5.2.3). The second estimated part is the INS azimuth misalignment, $\hat{\Phi}_{\text{up}}$, acquired from a Kalman filter with seven states (box FK7 in Figure 5-4). The method of azimuth estimation and compensation is analogous to the open area method. The Kalman filter works in prediction, when the GPS velocities are not trustworthy or not available. The reliability criterion is based on the difference between the predicted INS velocity and GPS velocity.

5.3.4 Output of Estimation Block

The INS/GPS integrated system outputs the corrected INS velocities and positions in a similar manner to open area algorithm (equation (5-14)), if the estimate of the INS azimuth misalignment has already converged and if the GPS positions and velocities are

not reliable (defined by the PDOP threshold and number of satellites used in the solution, see Figure 5-4). Otherwise, the system output is defined by the GPS solution.

Chapter 6

Open Area Results

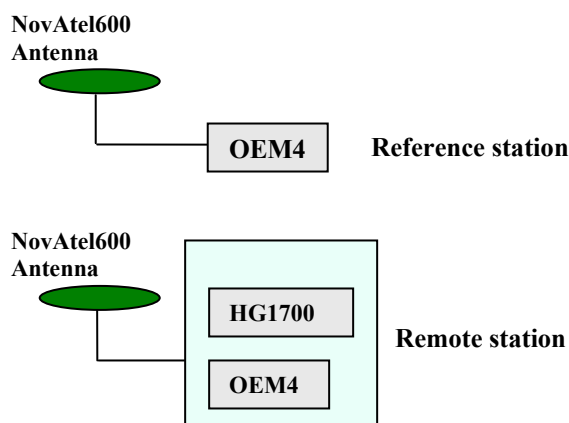
In this chapter, the performance of the integrated INS/GPS system is evaluated for open area applications. The details of data collection are presented first, followed by the results themselves. Results address the objectives listed in Chapter 1 and include position, velocity and attitude accuracy analysis during GPS signal acquisition as well as during GPS data outages, which are simulated to analyze system performance in prediction mode. This chapter also discusses the impact of INS azimuth misalignment error on overall system accuracy.

6.1 Test Description

Figure 6-1 shows the set-up scheme of the test system. The main piece of equipment used for testing was NovAtel's Black Diamond System (BDS). The BDS contains a medium accuracy Honeywell HG1700 AG11 IMU and a high performance NovAtel OEM4 dual-frequency GPS receiver. The technical characteristics of the test IMU are presented in Table 6-1. Because differential GPS measurements were utilized in the integration algorithm, two base stations and one remote station were established throughout the tests. NovAtel OEM4 receivers at the reference stations and a NovAtel BDS system at the remote station were each connected to a NovAtel 600 antenna.

Table 6-1: HG1700 IMU Specifications (Honeywell, 1997)

<i>Specification</i>	<i>Value</i>
Gyros	
Input Range	$\pm 1,000$ °/sec
Bias	1.0 - 10 °/h
Scale Factor Accuracy	150 ppm
Scale Factor Linearity	150 ppm
Axis Alignment Stability	500 μ rad
Angular Random Walk	0.125-0.3 °/ \sqrt{h}
Accelerometers	
Input Range	± 50 g
Bias	1.0 mg (980 mGal)
Scale Factor Accuracy	300 ppm
Scale Factor Linearity	500 ppm
Axis Alignment Stability	500 μ rad
Velocity Random Walk	0.0013 (m/s)/ \sqrt{h}

**Figure 6-1: Test Set-up for Open area Tests.**

The test set-up of the remote station is presented in Figure 6-2. Inertial data from the HG1700 was time tagged with the OEM4 GPS measurements providing synchronization of the data coming from the two units. The IMU was rigidly mounted to the floor of the University of Calgary's test van. The GPS antenna was mounted on the roof of the vehicle.



Figure 6-2: Remote Station Set-up

Two base stations were needed to ensure a short baseline between the base and remote receivers. In this way, the distance from the test vehicle to the base station ranged from a few metres during initialization to about 4 and 15 km. These relatively short distances were selected such that an accurate DGPS solution could be used as a reference for system evaluation. The first station, placed on a pillar on the roof of the CCIT Building at the University of Calgary, provided reference data for the second one, which was set up on a pre-existing pillar a few metres from the main road in the test area, midway along the test track. Equipment in the vehicle and at the field base station was powered either from the van itself or from additional car batteries. At the base station in the test area, a 12V battery powered the NovAtel receiver and data was logged on the receiver's memory card. In the test vehicle, splitting the DC power from the car's cigarette lighter provided the power for the GPS antenna and a laptop for data logging, while two 12V car batteries

powered the BDS system. GPS data was logged at a rate of 1 Hz; raw IMU measurements had a data rate of 100 Hz.

The coordinates of the field reference station, the reference trajectory for error analysis and reference velocity information were obtained from a double difference carrier phase solution. The FLYKIN+™ software, developed by the PLAN Group of the University of Calgary, was utilized for this purpose (FLYKIN+™, Liu et al., 2003). The coordinates of the base stations are presented in Table 6-2. The reference trajectories for the two tests, obtained from the GPS carrier phase solution, are presented in Figure 6-3.

Table 6-2: Coordinates of Base Stations

Station	Latitude (dms)	Longitude (dms)	Height (m)
Field Station	51 05 46.9138	-114 22 09.8795	1183.142
E2 Base station	51 04 47.9168	-114 08 01.3605	1118.504

Two tests were conducted in Calgary, on July 30, 2003. They were performed in open sky conditions, on a highway 250 running parallel to the Trans-Canada Highway towards Banff. The road has a stretch of about 12 km, which is illustrated in Figure 6-4. This area was selected because it provided excellent GPS satellite visibility as seen in Figure 6-5. The number of satellites tracked was varying from four to ten with an average number of seven. The average PDOP was two. Each test commenced with a ten-minute warm-up period for INS alignment.

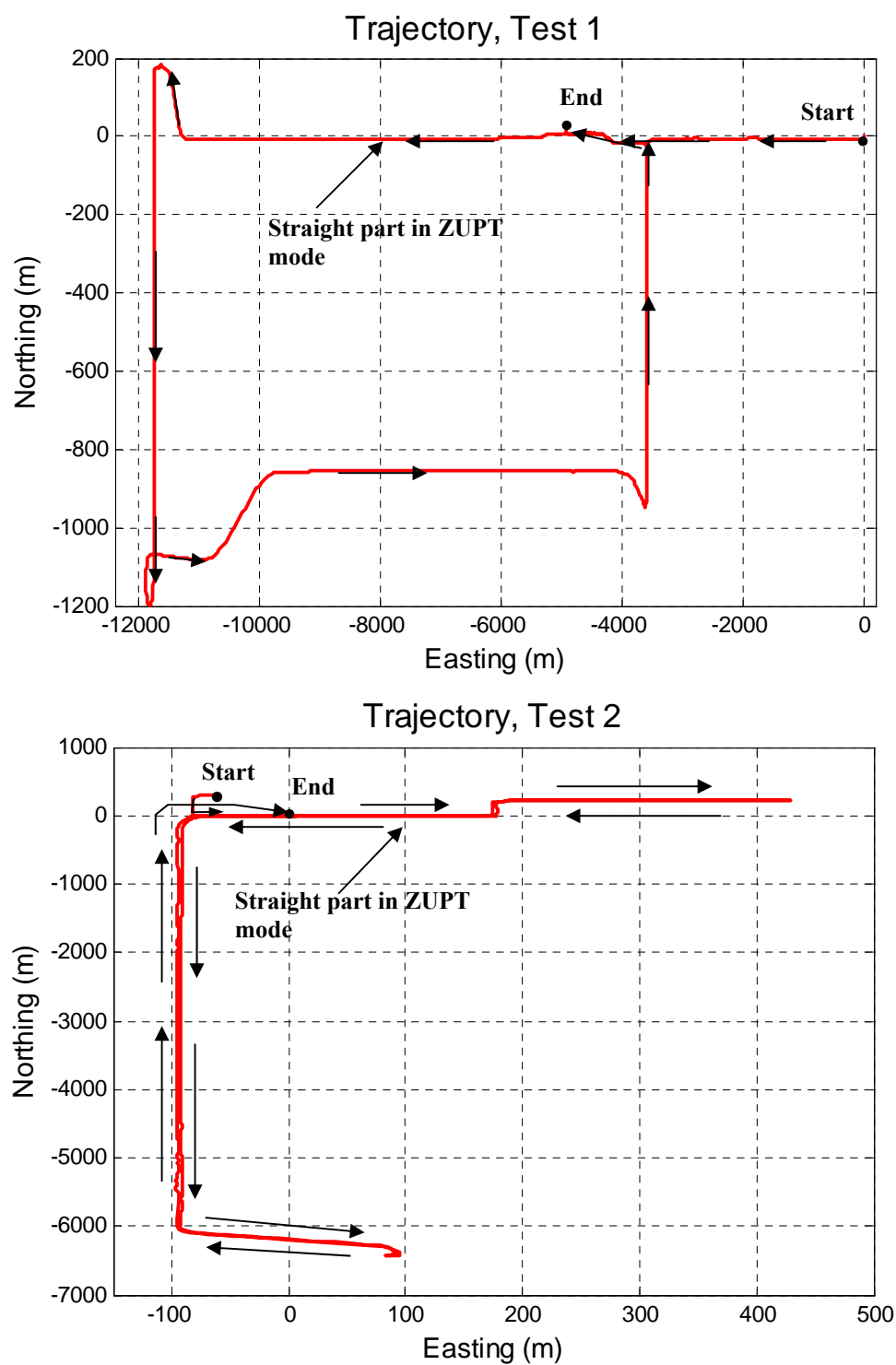


Figure 6-3: Reference Trajectories for Tests 1 and 2

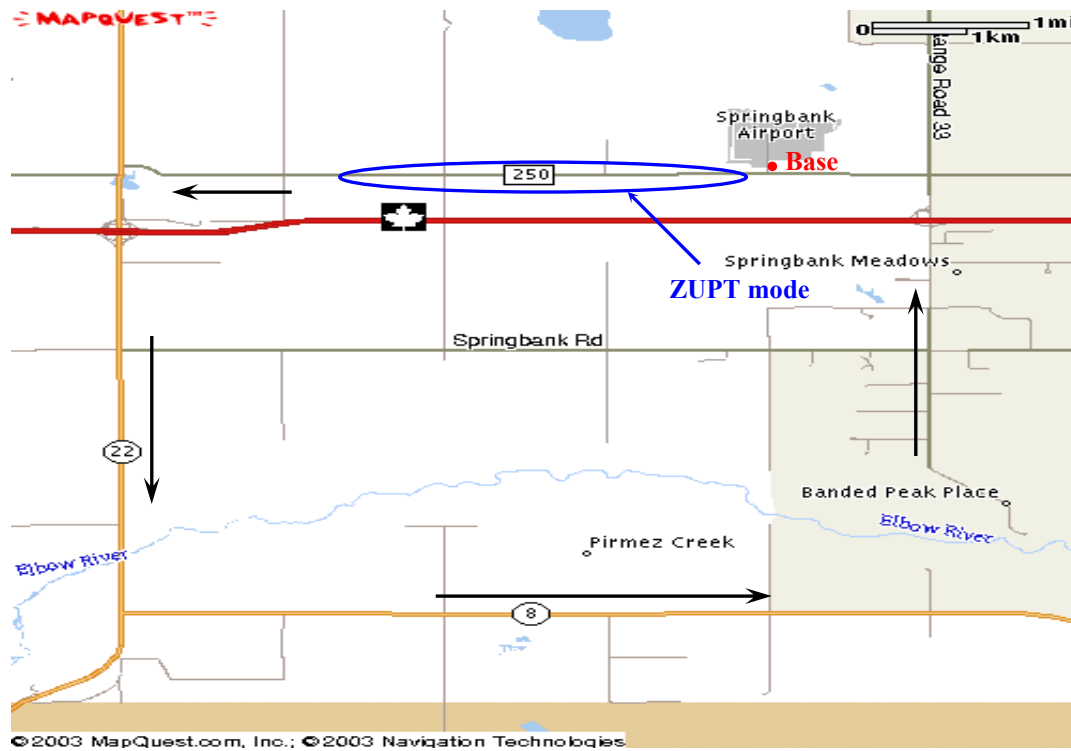


Figure 6-4: Test Area

After that, on the straight part of the trajectory, three or four consecutive ZUPTs were performed to validate the effect of the non-stationary errors on IMU accuracy. The duration of each ZUPT was about 10-15 seconds (defined empirically); and the time between consecutive ZUPTs was around two to four minutes. During that time, the test vehicle was experiencing accelerations of one to two m/s^2 (further, referred to as high dynamics), which provided good observability for the motion-dependent INS errors. Each test was approximately 20 to 30 minutes in duration.

GPS velocities and positions, which were fed into the integrated system, were obtained from the differential code solution with carrier phase smoothing using the $\text{C}^3\text{NAV}^2\text{TM}$

software, developed by the PLAN Group of the University of Calgary (C^3NAVG^{2TM} , Petovello et al. 2000). The elevation cut-off used for all data analysis was 10° .



Figure 6-5: Typical Urban Open Area Environment

6.2 Experimental Results

Three algorithms were tested to validate the improvement in performance of the INS/GPS system using the cascaded Kalman filter for accurate azimuth misalignment estimation:

- 1 Reduced Kalman filter (three states in a system model for each channel, referred to herein as FK3);
- 2 Conventional Kalman filter with a feedback of the estimated azimuth correction to the navigation scheme (nine states in a system model, further referred to as FK9);

- 3 Cascaded Kalman filter with combined estimated azimuth and heading corrections as a feedback into the navigation block (nine states in a system model, further referred to as CKF). This scheme was introduced in section 5.2.1 for open area applications.

It must be mentioned that, for the latter two cases, gyro drift compensation was also performed in accordance with the algorithm discussed in section 5.2.1. In this research, a third state Kalman filter was expected to show the impact of the non-stationary INS errors on INS accuracy in the position and velocity domains. In the following, the proposed approach is first tested for the ideal situation, when GPS data is constantly available (clean data). Next, it is applied to data with simulated gaps in the GPS measurements, so that system accuracy during prediction can be analyzed.

6.2.1 Results Using Clean GPS Data

Positional Accuracy

The positional accuracy of the integrated system is generally limited to the accuracy of the GPS code solution excluding a few short-term gaps of several seconds, when GPS measurements are not available. The positional accuracy for all three algorithms is demonstrated in Figure 6-6, which presents the north position component for Test 1. In the lower plot, the north position is shown on a larger scale.

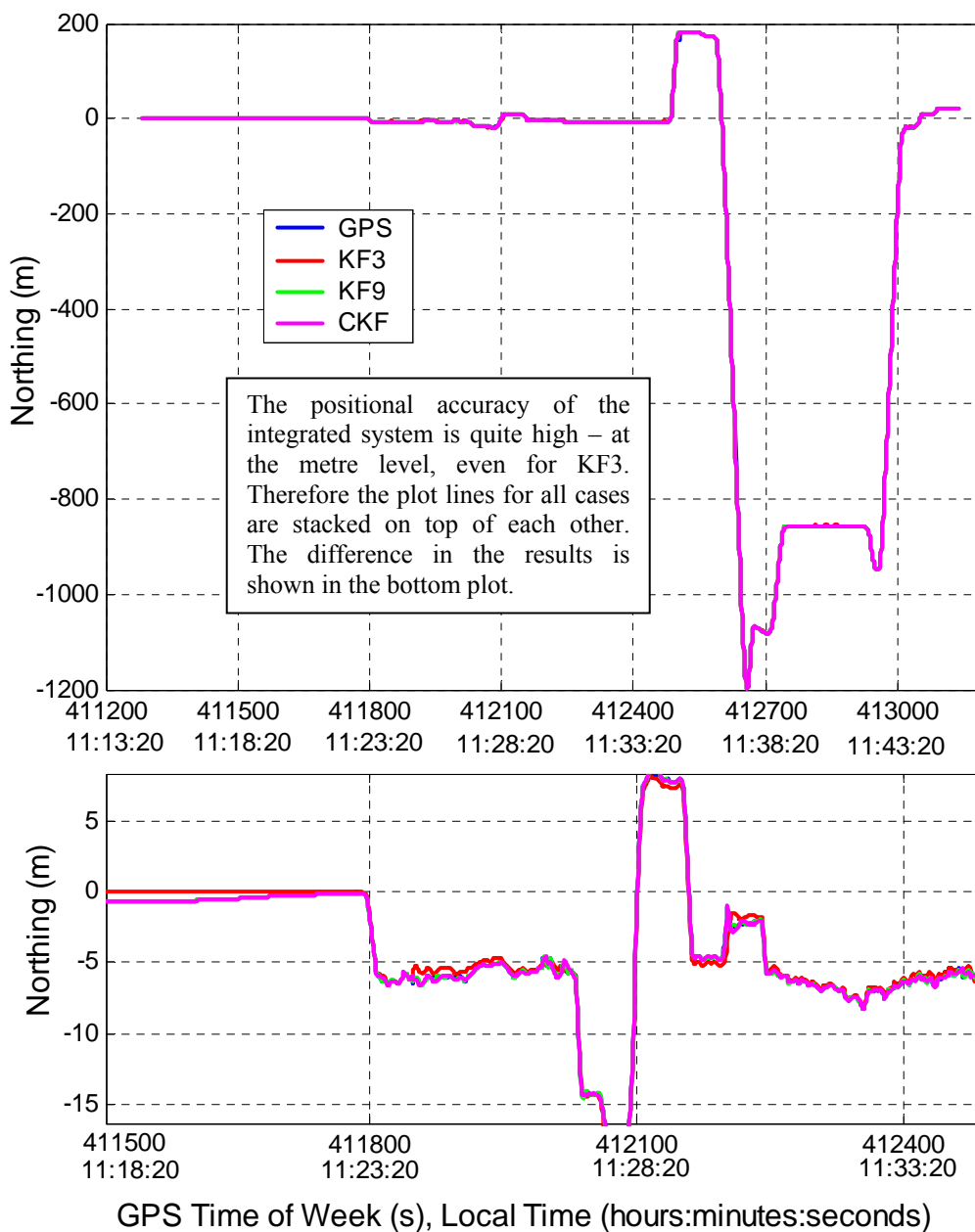


Figure 6-6: North Position Component Using Clean GPS data, Test 1

Both tests were performed under similar conditions and thus provided analogous results. Due to the continuous correction of the INS positional errors, even a traditional Kalman filter with the reduced model (FK3) provides relatively high accuracy at the sub-metre

level. Table 6-3 gives a statistical analysis of the positional errors of the integrated system based on data from both tests.

Table 6-3: Positional Errors for Clean GPS Data

Errors	RMS	Mean	Max
<i>FK 3</i>			
$\delta N (m)$	0.4	-0.1	1.7
$\delta E (m)$	0.2	-0.1	0.5
<i>FK 9</i>			
$\delta N (m)$	0.3	-0.1	1.5
$\delta E (m)$	0.2	-0.1	0.7
<i>CKF</i>			
$\delta N (m)$	0.3	-0.1	1.5
$\delta E (m)$	0.2	-0.1	0.7

Velocity Accuracy

In the velocity domain, the situation is slightly different. On one hand, the INS positions change smoothly in comparison to the INS velocities, since they are obtained by integration. On the other hand, the elements of covariance matrix of input noise are chosen to be the same (theoretically optimal) for both cases: KF3 and CKF. Therefore, when the Kalman filter with three states in the system model is used, the algorithm trusts the model more than the measurements and the impact of the uncompensated INS non-stationery errors is observed. Figure 6-7 and Figure 6-8 present north velocities of the integrated system using the above three algorithms for Test 1 and Test 2, respectively. The lower plots of Figure 6-7 and Figure 6-8 show enlargements of the plot areas, where several consecutive ZUPTs were conducted. These plots illustrate the influence of non-stationary INS errors on the velocity accuracy in one channel during high accelerations in

another one. Analysis of the results confirms correctness of the assumption that can be easily derived from the INS error model (equation (5-1)). At the beginning of each test, when the vehicle was experiencing acceleration changes in the east direction (ZUPT mode), several jumps due to the non-stationary INS error components occurred.

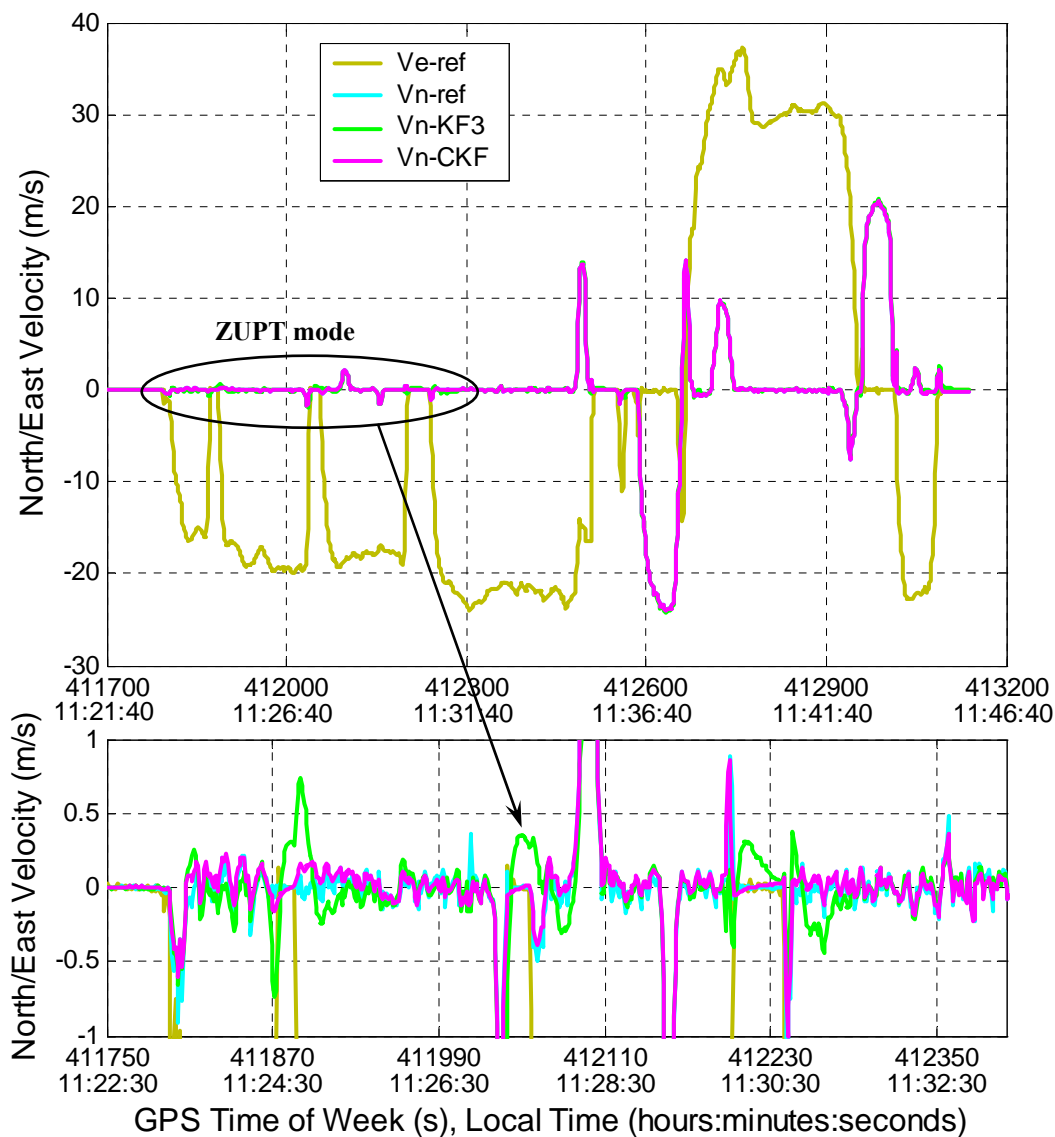


Figure 6-7: Inter-channel Influence of Vehicle Dynamics on Velocity Accuracy, Test 1

INS azimuth misalignment, being one of the largest non-stationary INS error components, is considered in the system model; therefore, it is assumed to have major impact (among other non-stationary errors such as accelerometer scale factors and their non-linearities) on the overall system accuracy.

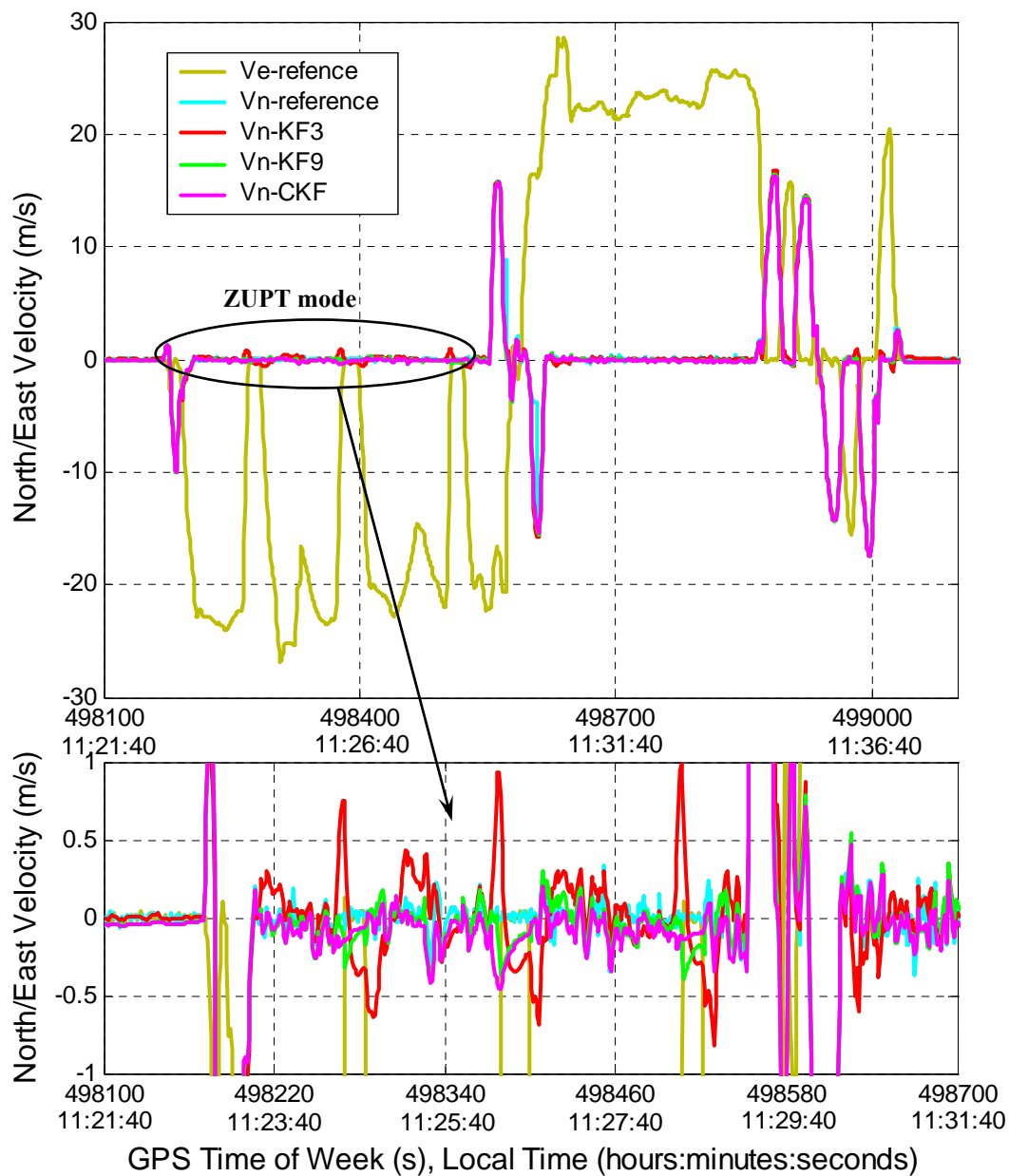


Figure 6-8: Inter-channel Influence of Vehicle Dynamics on Velocity Accuracy,

Test 2

At the beginning of the test, when the vehicle was experiencing acceleration changes in the east direction (ZUPT mode), several jumps in north velocity due to the azimuth error occurred. Using the traditional Kalman filter with three and nine state system models (red and green lines in the plots, respectively), these jumps are in the order of 0.5 to 1 m/s respectively; while, in the output of the Cascaded Kalman filter (magenta line), the jumps due to the azimuth error are absent.

It must be noted that the velocity errors were calculated using the FLYKIN+™ output as a reference. The FLYKIN+™ velocities cannot be considered as true values and they are highly correlated with the velocities obtained from C³NAVIG²™ software. The same Doppler measurements were utilized in the GPS solution, using the same GPS receiver; the observed slight improvement in GPS velocity accuracy is expected due to implementation of Kalman filtering in the FLIKIN+ software. The current analysis of velocity accuracy of the integrated system is performed to validate overall system performance in the velocity domain. As shown in Figure 6-7 and Figure 6-8, traditional Kalman filters with three and nine state system models (1st and 2nd methods) provide similar results; while the Cascaded Kalman filter (3rd method) offers better accuracy. Table 6-4 gives a statistical analysis of the velocity errors of the integrated system using clean GPS data from Tests 1 and 2.

Table 6-4: Velocity Errors for Clean GPS Data

Errors	RMS	Mean	Max
FK 3			
$\delta V_N (m/s)$	0.2	0.0	1.1
$\delta V_E (m/s)$	0.2	0.0	1.2
FK 9			
$\delta V_N (m/s)$	0.1	0.0	0.9
$\delta V_E (m/s)$	0.1	0.0	0.5
CKF			
$\delta V_N (m/s)$	0.1	0.0	0.5
$\delta V_E (m/s)$	0.1	0.0	0.3

Impact of INS Azimuth Misalignment on Accuracy of Integrated System

To analyze the impact of azimuth misalignment on system accuracy, the INS velocity error is considered. Figure 6-9 and Figure 6-10 present the north component of the INS velocity error for Tests 1 and 2, respectively. The raw INS velocity error (difference between the GPS and INS velocities) contains the low frequency INS Schuler component, while the jumps are due to the non-stationary part of the INS error and GPS noise. During ZUPTs or in moderate motion, the INS non-stationary part is negligible and, thus, a smooth behavior of the Schuler component is observed. During motion with high dynamics, the non-stationary errors become significant, which causes jumps in the INS velocity error output.

As seen in the plots, the traditional nine state Kalman filter does not estimate azimuth misalignment, Φ_{up} , very accurately; therefore, large jumps are observed so that the estimated velocity error almost repeats the raw signal, slightly smoothing the measurement noise from GPS. The main reason for this comes from the very large

magnitude of the initial azimuth misalignment, so that this error does not belong to the linear region any longer. In other words, after the initial INS alignment, the remaining azimuth error is still significant, so that the assumption for small angles made in the INS error model is no longer appropriate.

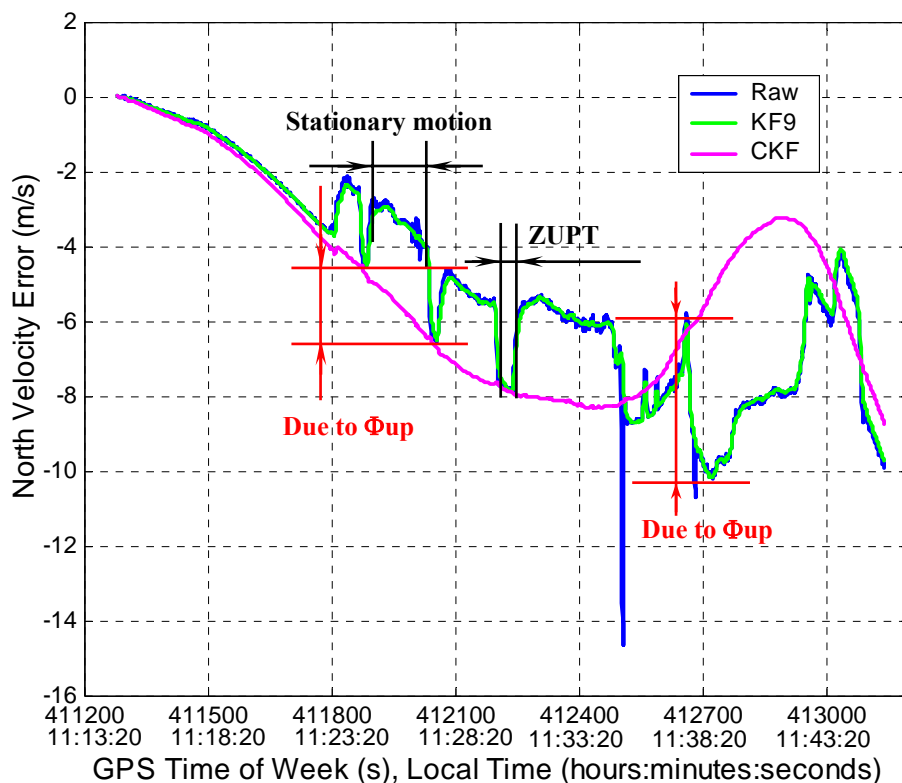


Figure 6-9: North Velocity INS Error, Test 1

Consequently, the estimate of Φ_{up} does not provide an acceptable level of accuracy. The large jumps in the raw signal in the plots are caused by actual outages in the GPS measurements. The combination of two algorithms - the Cascaded Kalman filter and heading correction - provides better results in terms of accuracy. By initially applying the heading correction, the remaining azimuth error is reduced to a level of one to two degrees. After that, the Cascaded Kalman filter provides a very accurate azimuth error

estimate, which is used for fine azimuth misalignment compensation in the SINS algorithm.

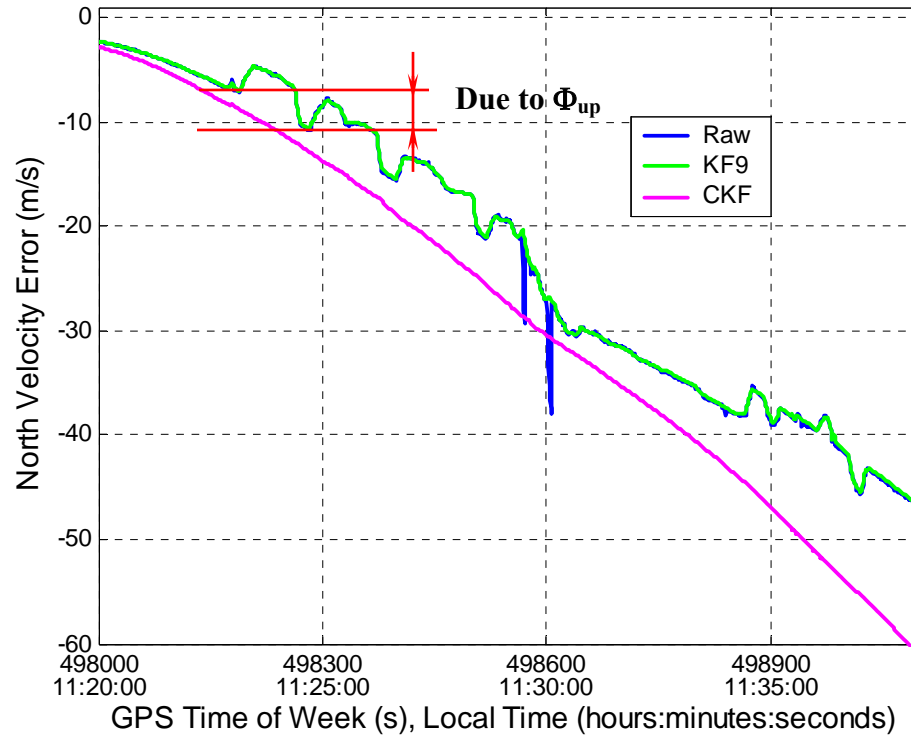


Figure 6-10: North Velocity INS Error, Test 2

The time taken for $\hat{\Phi}_{up}$ convergence is also reduced. In some stages of the tests, the magnitude of the INS velocity error for the Cascaded Kalman filter is larger than in the case of the traditional Kalman filter with nine states. This is due to the combined influence of the $\Phi_{up}U\cos\phi$ and ω_E^{dr} components on the velocity error that can have the same or opposite signs during the tests. The estimated $\hat{\Phi}_{up}$ for Tests 1 and 2 using the Cascaded Kalman filter is shown in Figure 6-11. The jumps in the azimuth error estimates at the beginning of the tests are due to the transition process; the initial covariance matrix of estimation errors, P_0 , is chosen to be large in order to hasten convergence (see section 4.2.2). As a result to the above, the filtered INS velocity error

has a smooth Schuler and, consequently, well-predicted behaviour, which is especially important for prediction. In order to check this, gaps are simulated in the GPS data. An analysis of the system accuracy in prediction mode is considered in the next section.

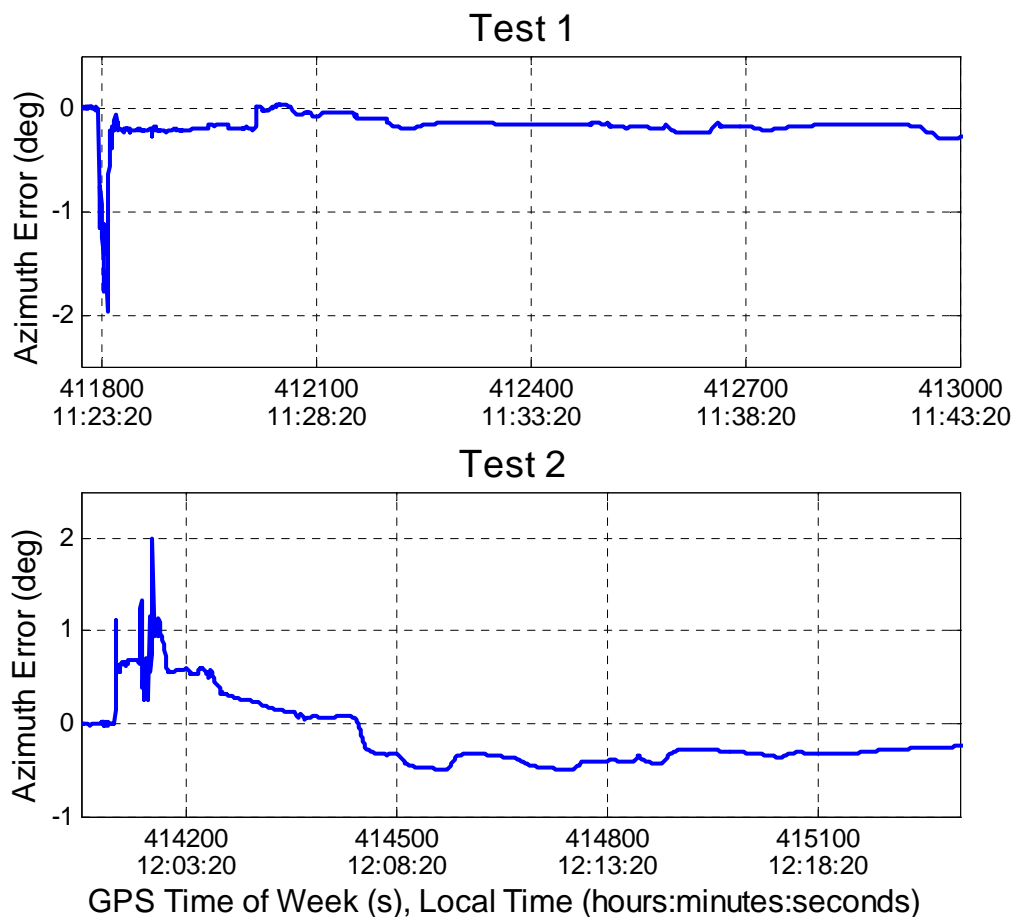


Figure 6-11: Estimated by CKF INS Azimuth Misalignment

The residual azimuth error can be determined by integration of equation (3-32). Assuming that the accelerometer scale factors have been previously calibrated and that the azimuth error is nearly constant, the non-stationary component of the north velocity error δv_N^{nst} can be approximately defined as:

$$\delta V_N^{nst} \approx -\Phi_{up} V_E \Rightarrow \Phi_{up} \approx -\frac{\delta V_N^{nst}}{V_E}$$

$$\delta V_E^{nst} \approx \Phi_{up} V_N \Rightarrow \Phi_{up} \approx \frac{\delta V_E^{nst}}{V_N}$$
(6-1)

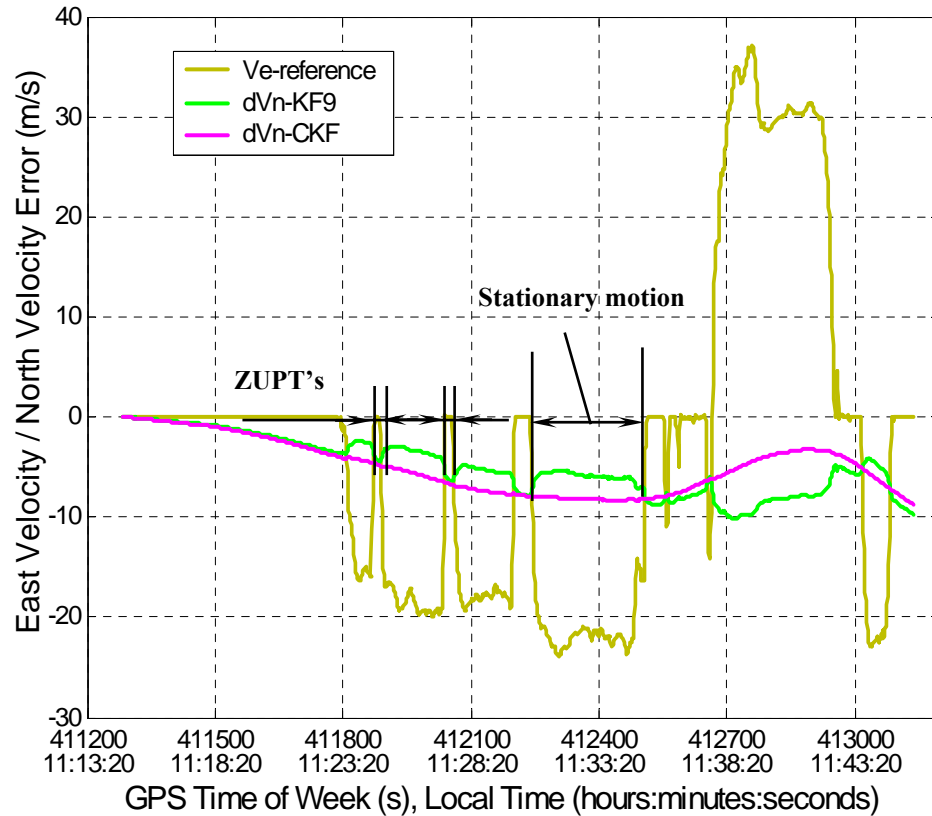


Figure 6-12: Inter-channel Influence of Vehicle Dynamics on INS Velocity Error, Test 1

Therefore, the remaining azimuth error is approximately:

$$\hat{\Phi}_{up} \approx -\frac{\delta \hat{V}_N - \delta \hat{V}_N^{Sch}}{\hat{V}_E} \cong \frac{\delta \hat{V}_N^{jump}}{\hat{V}_E} \cong \frac{\delta \hat{V}_E^{jump}}{\hat{V}_N}$$
(6-2)

If the 3rd state Kalman filter is applied, the unestimated azimuth misalignment reaches 8-10°. Using the traditional 9th state Kalman filter with an Φ_{up} correction, the remaining azimuth error is approximately 0.5°-2.5°, while the proposed combined method gives

0.2°-0.6°. The influence of high vehicle dynamics in one channel on the velocity accuracy of another channel is demonstrated in Figure 6-12 and Figure 6-13 for the two tests, respectively.

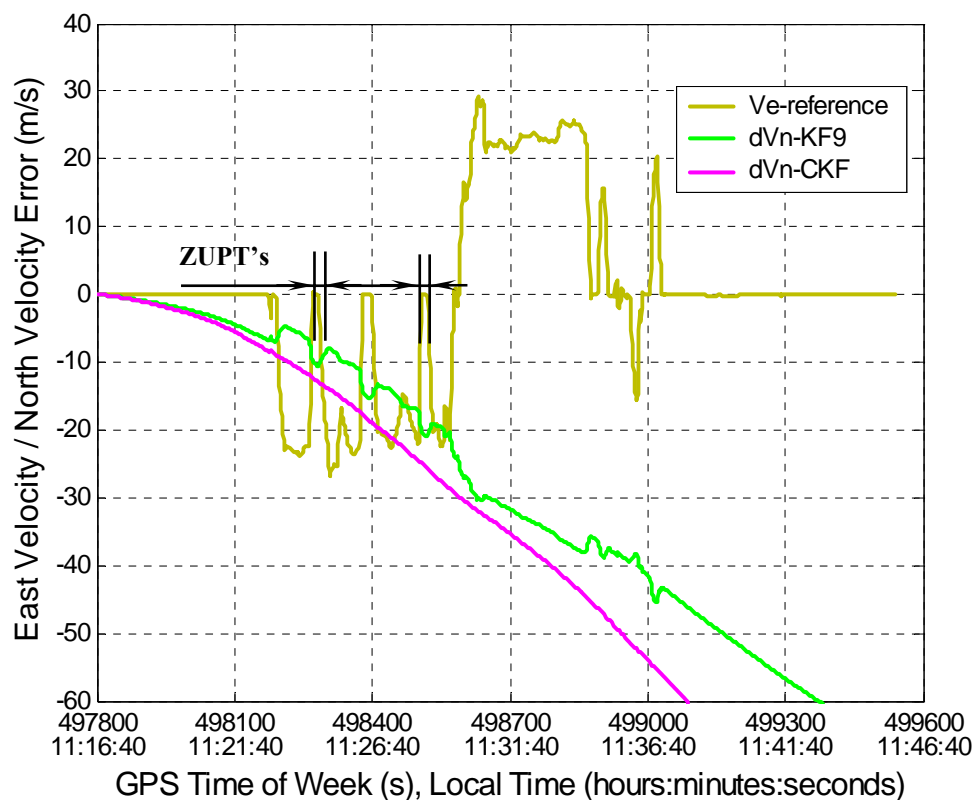


Figure 6-13: Inter-channel Influence of Vehicle Dynamics on INS Velocity Error, Test 2

Gyro Drift Compensation

Gyro drift, being one of the major Schuler error components, has a significant impact on the INS velocity error. Figure 6-14 presents the INS velocity North and East error components after azimuth correction for two cases: with and without compensation of gyro drifts ω_N^{dr} and ω_E^{dr} (see equations (3-31)).

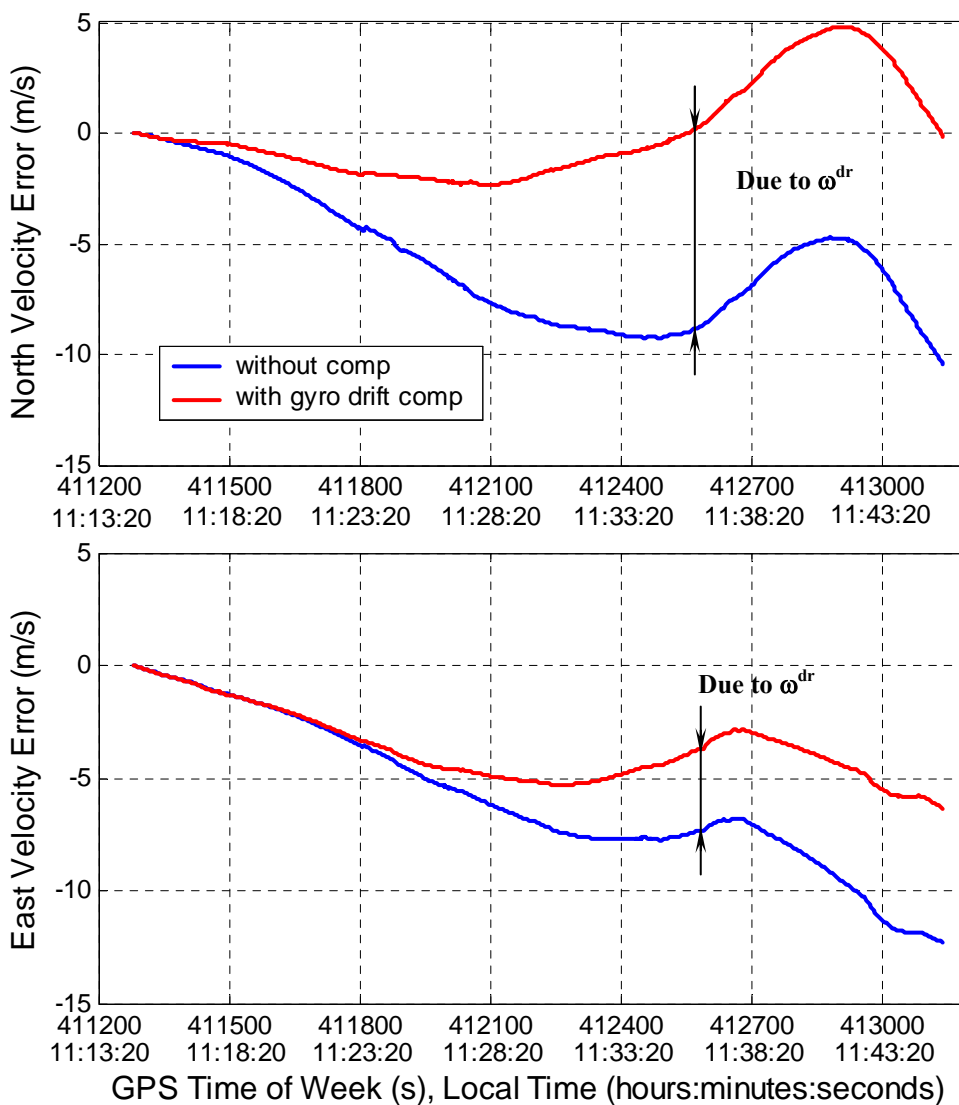


Figure 6-14: Impact of Gyro Drifts on INS Velocity Error, Test 1

As shown in the plots, if gyro drifts are compensated in the SINS algorithm, the amplitude of the Schuler component of the INS velocity error is reduced significantly, which improves its estimation accuracy. The estimates of gyro drifts ω_N^{dr} and ω_E^{dr} for the Tests 1 and 2 are presented in Figure 6-15. As seen from the plots, mutually distinct gyro drift behaviours were observed for the two tests. A possible explanation of this effect is the influence of temperature on the gyros' operational capabilities. Two runs were

performed sequentially on the same date. During Test 1, the gyro drifts were quite stable, not exceeding one degree, while during Test 2, they varied from 1° to 2° . The jumps at the outset of the tests are caused by the transition period of the estimation process.

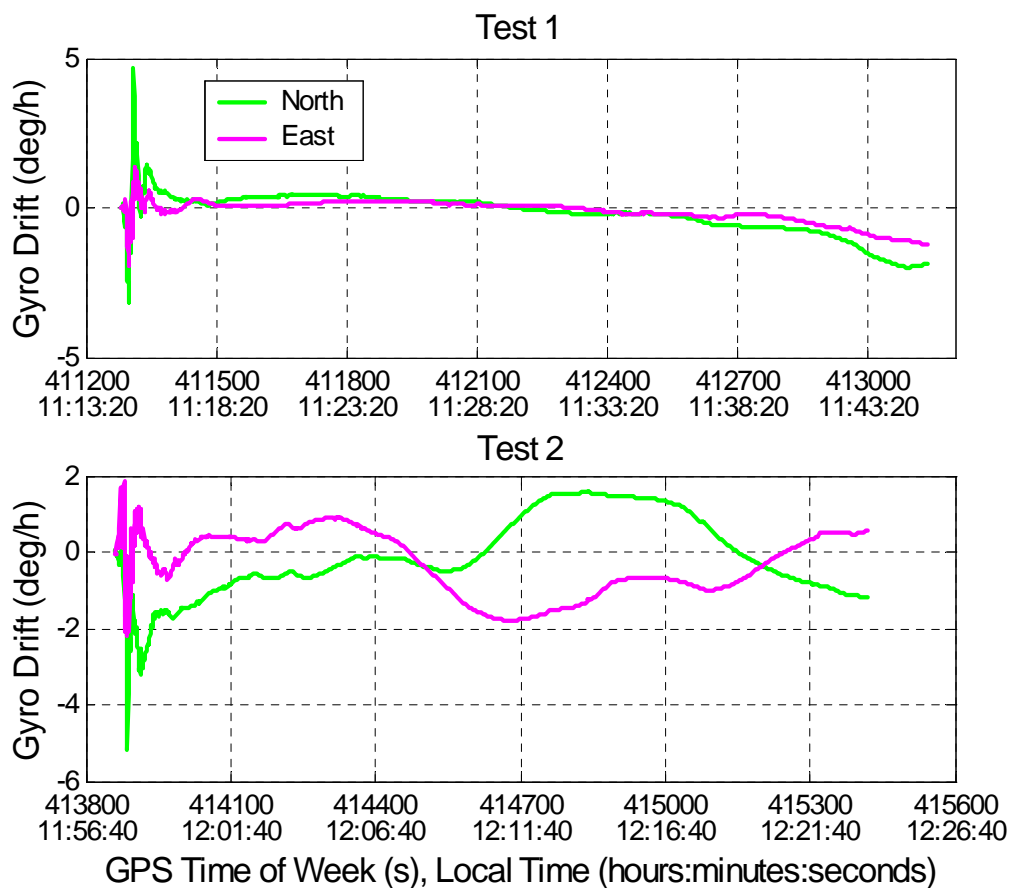


Figure 6-15: Gyro Drift Estimates

Attitude Accuracy

Since reference attitude information was not available for Tests 1 and 2, an analysis of the attitude accuracy could not be performed directly. Figure 6-16, Figure 6-17, Figure 6-18 and Figure 6-19 present the attitude angles for the two tests, obtained from the

integrated solution for two cases: (1) with INS error compensation in the SINS algorithm, and (2) without such compensation.

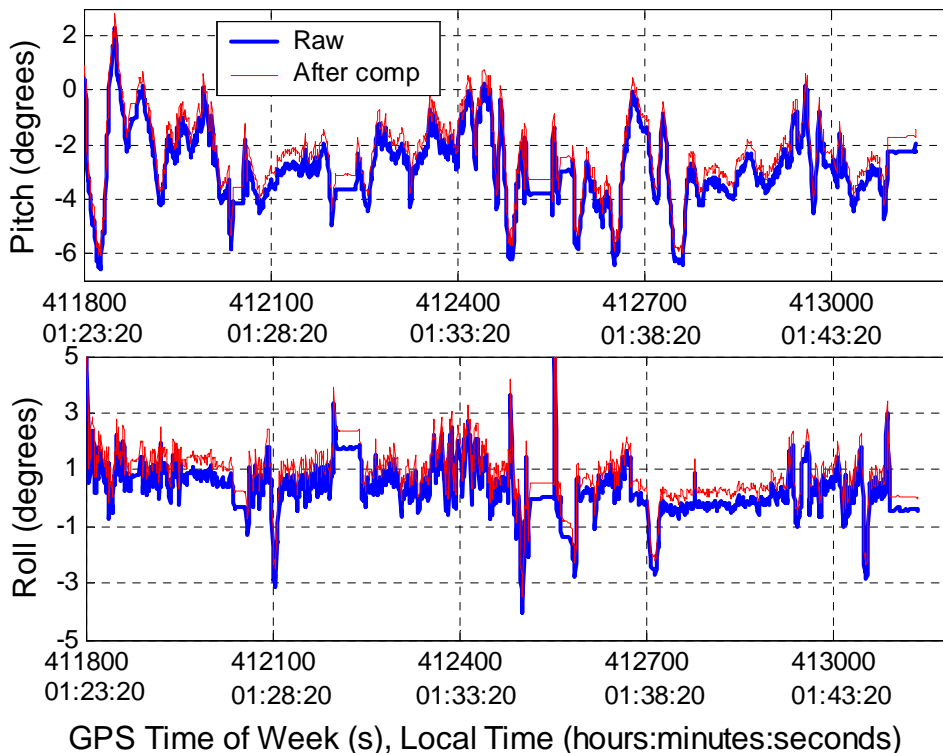


Figure 6-16: Roll and Pitch, Test 1

The difference in system output using the above two strategies illustrates the marginal improvement in the attitude accuracy of the integrated system. In roll and pitch, this difference ranges from 0.3° to 0.5° while, in azimuth, it varies from 7° to 10° for the two tests, respectively; this is shown at a larger scale in the lower plots of Figure 6-18 and Figure 6-19. These results confirm the assumption made in Chapter 5 about the accuracy of the initial INS alignment. Without azimuth compensation (FK3), the residual azimuth misalignment is large; so that it significantly degrades the estimation accuracy of the azimuth error. The approximate estimation accuracy of the horizontal errors can be obtained from an analysis of INS positional errors in stationary motion during prediction.

When the Cascaded Kalman filter is used, the estimation roll-pitch accuracy is better than 0.05° to 0.1° ; the estimation accuracy of azimuth error using the above approach, considered in the previous subsection, is better than 0.2° to 0.6° .

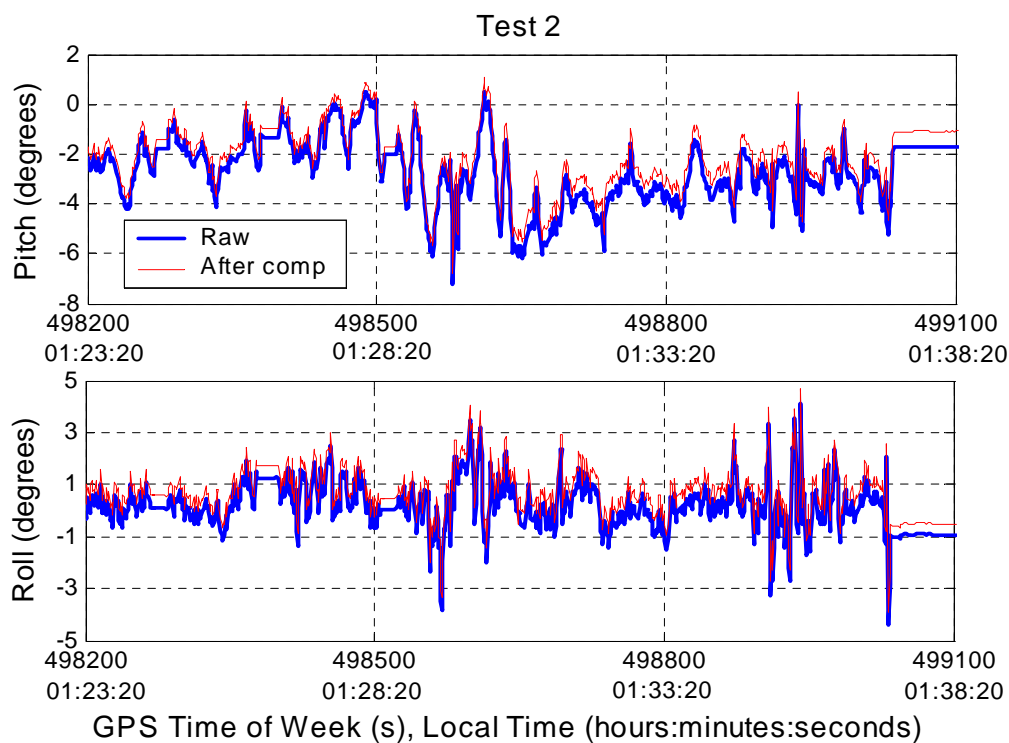


Figure 6-17: Roll and Pitch, Test 2

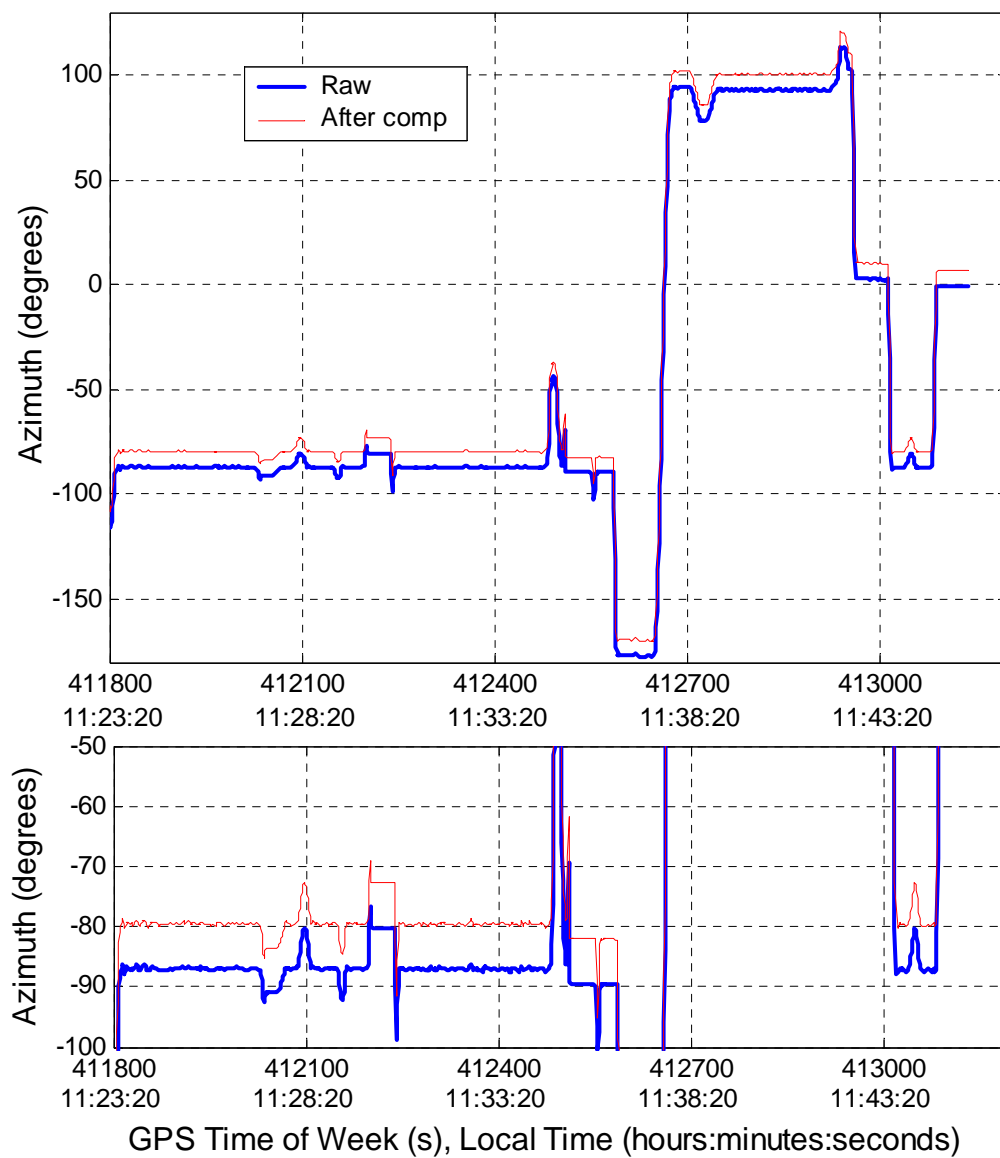


Figure 6-18: Azimuth, Test 1

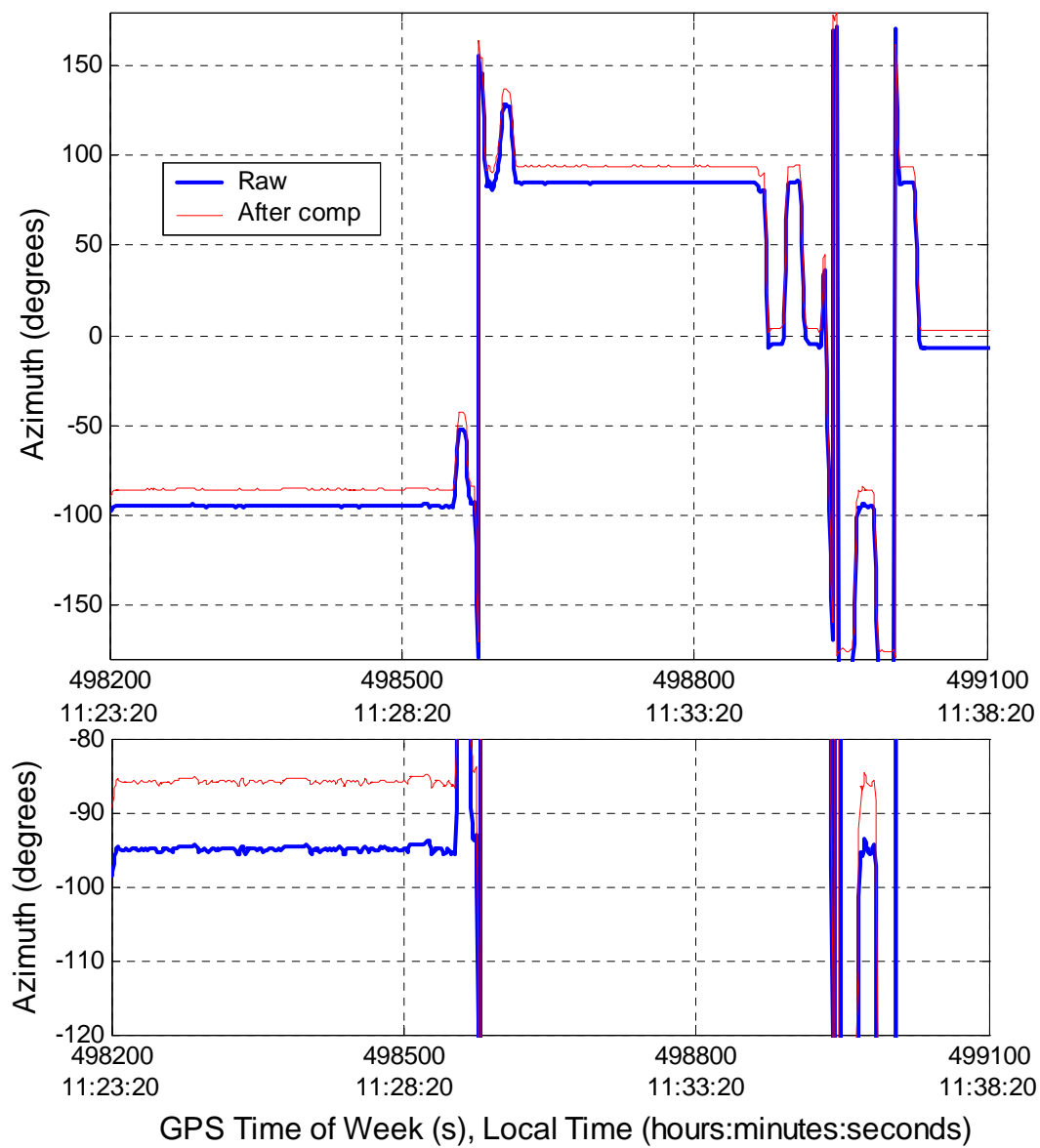


Figure 6-19: Azimuth, Test 2

6.2.2 Results Using GPS Data with Simulated Gaps

Positional Accuracy

Eight gaps in the GPS data for both tests were simulated, each with a duration of 10 to 60 seconds for parts of the tests with moderate (defined as motion with nearly constant speed: $a < 1 \text{ m/s}^2$) and high vehicle dynamics ($a > 2 \text{ m/s}^2$), to observe the influence of INS azimuth misalignment on prediction accuracy. Obviously, the accuracy in prediction depends mainly on vehicle dynamics as well as on the duration of a given gap. The lengths of simulated data gaps were chosen to be similar to the typical durations of the GPS outages in urban areas.

To illustrate the prediction accuracy in position, three cases are considered: (1) the reduced Kalman filter without error compensation in the SINS algorithm (1st method – FK3, represented by a red line in the following plots); (2) the traditional Kalman filter with azimuth correction (2nd method – FK9, represented by a green line in the plots); and (3) the proposed combined approach with azimuth and GPS heading corrections (3rd method – CKF, represented by a magenta line in the following plots). Figure 6-20 and Figure 6-21 present the north position component as an output of the integrated system for the two tests, respectively. In these figures, the lower plots show a prediction accuracy for the above three cases during a GPS outage with high vehicle dynamics. On the top of Figure 6-22 and Figure 6-23, simulated GPS data gaps are plotted on the test

trajectories for the two tests; the lower plots show the positional accuracies using the above three algorithms.

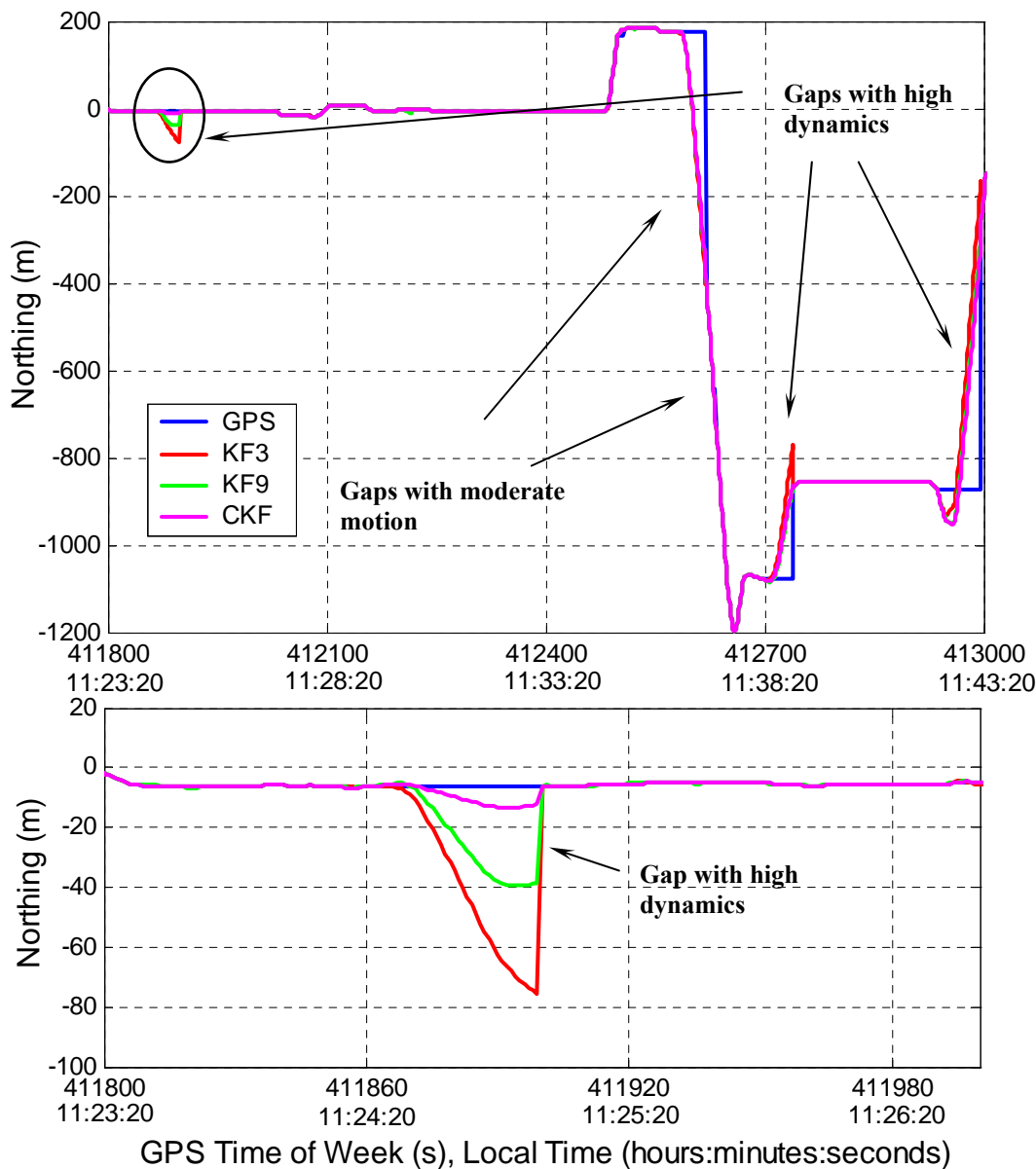


Figure 6-20: North Position Component Using Data with Simulated GPS Outages, Test 1

For five- to ten-second outages with stationary vehicle motion, even with use of the reduced Kalman filter, metre-level position accuracies are achieved. Firstly, the impact of

the azimuth misalignment for stationary motion is negligible. Secondly, INS velocity errors start to grow during GPS gaps and, being integrated, expand the INS positional error; however, for intervals on the order of several seconds, these errors do not have time to accumulate, making positional accuracy degradation inconsequential.

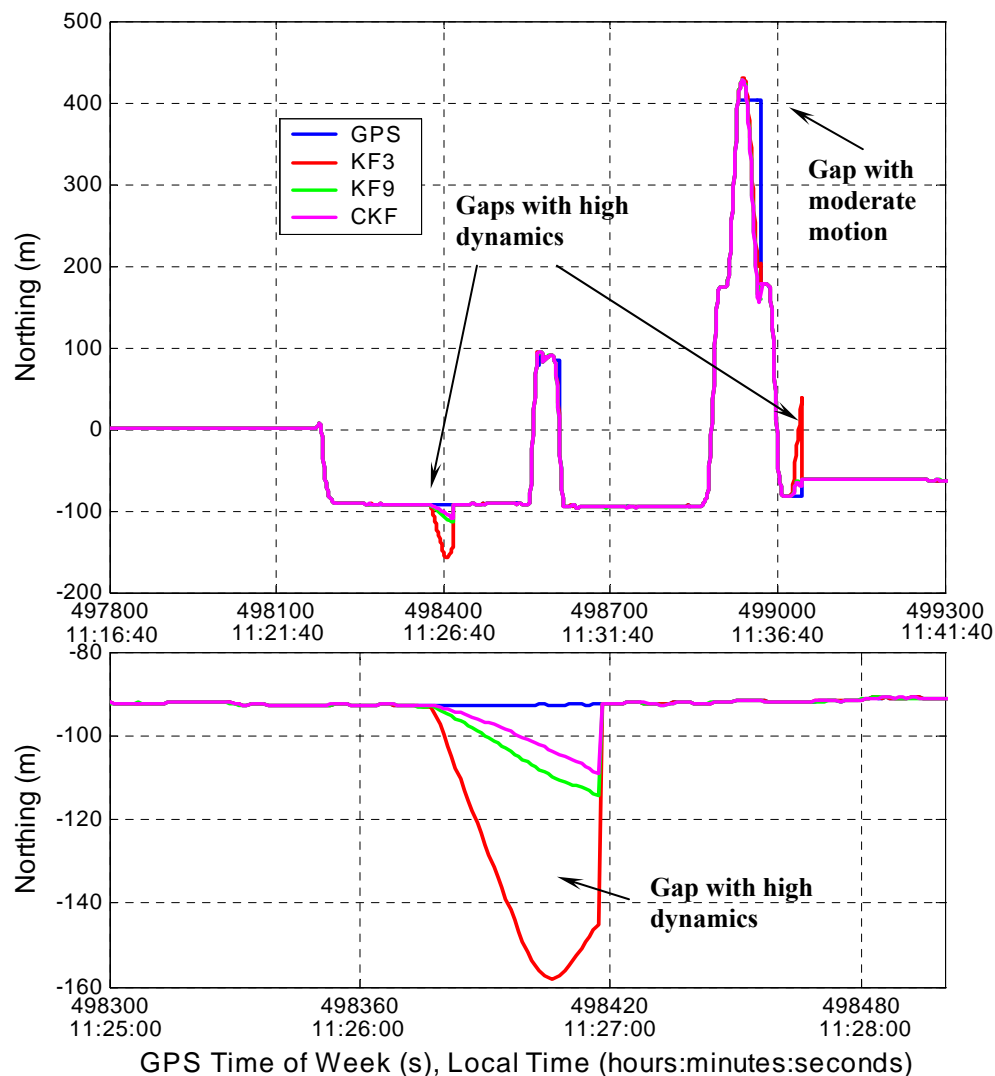


Figure 6-21: North Position Component Using Data with Simulated GPS Outages, Test 2

For long-term prediction, the influence of the azimuth misalignment becomes evident. During moderate motion - even for relatively long GPS gaps of 40 to 60 seconds - both

filters with azimuth error correction provide a high positional accuracy of 1 to 2 metres. However, during high vehicle dynamics with outages of the same duration, the azimuth misalignment error causes major accuracy degradation. This effect is well demonstrated in the lower plots of Figure 6-20 and Figure 6-21. For example, in Figure 6-20 during a 30-second GPS gap with relatively high vehicle dynamics, when the 3rd state Kalman filter is used, the positional errors grow over the prediction interval up to 70 metres; the 9th state Kalman filter provides a positional accuracy of about 30 metres, while the Cascaded Kalman filter improves the result to 5 metres. To summarize, for stationary vehicle motion, metre-level positional accuracy can be obtained even for relatively long prediction intervals (with duration of 30 to 60 seconds); nevertheless, for high vehicle accelerations, non-stationary INS errors (mostly azimuth misalignment) cause positional accuracy degradation in the order of tens of metres. In order to achieve better results, accurate estimation of the azimuth misalignment should be considered.

A statistical analysis of the positional errors during prediction using data from both tests is presented in Table 6-5. Diagrams in Figure 6-24 depict the RMS values of positional errors of the integrated system in prediction for all three cases. As seen in Table 6-5, there is a noticeable difference in the results for short-term and long-term data gaps. This stems mainly from the fact that the results are categorized by data gap durations, so that the results for outages on parts of the test trajectories with low and high vehicle dynamics are combined. The influence of high accelerations on system accuracy becomes evident during long prediction intervals of more than 20 seconds. By comparison, during outages in the order of a few seconds, system errors do not have enough time to accumulate.

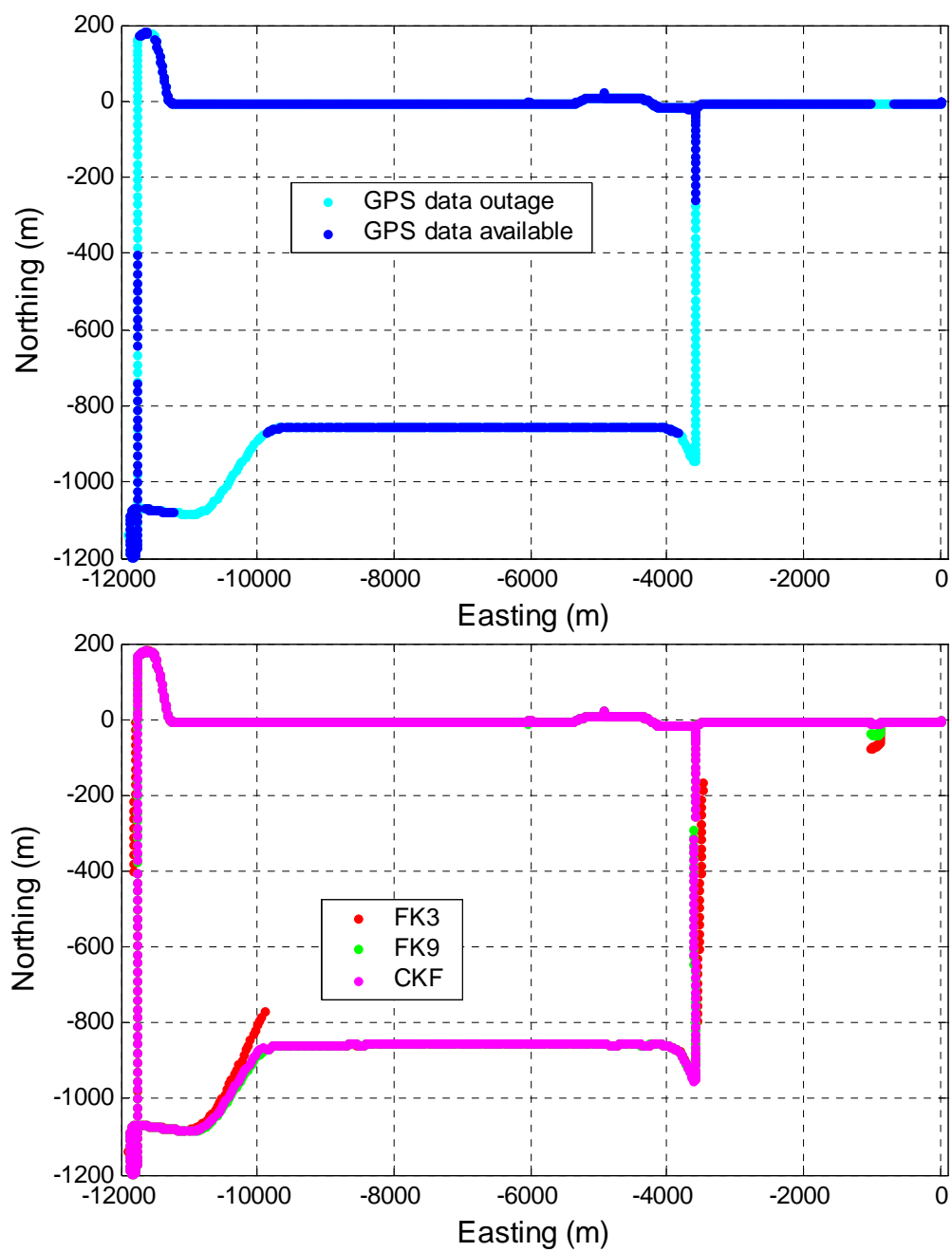


Figure 6-22: Trajectory for Data with Simulated GPS Outages, Test 1

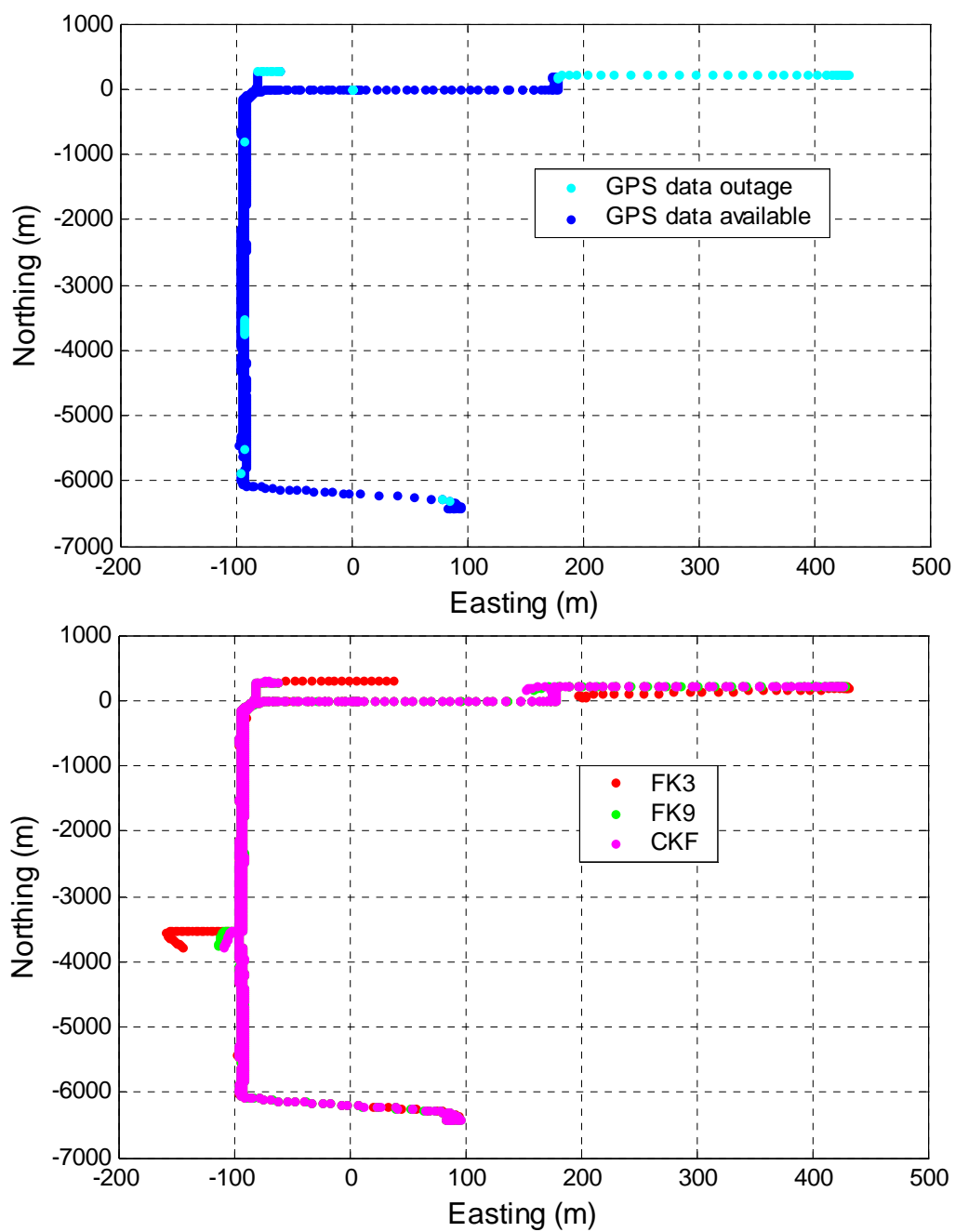


Figure 6-23: Trajectory for Data with Simulated GPS Outages, Test 2

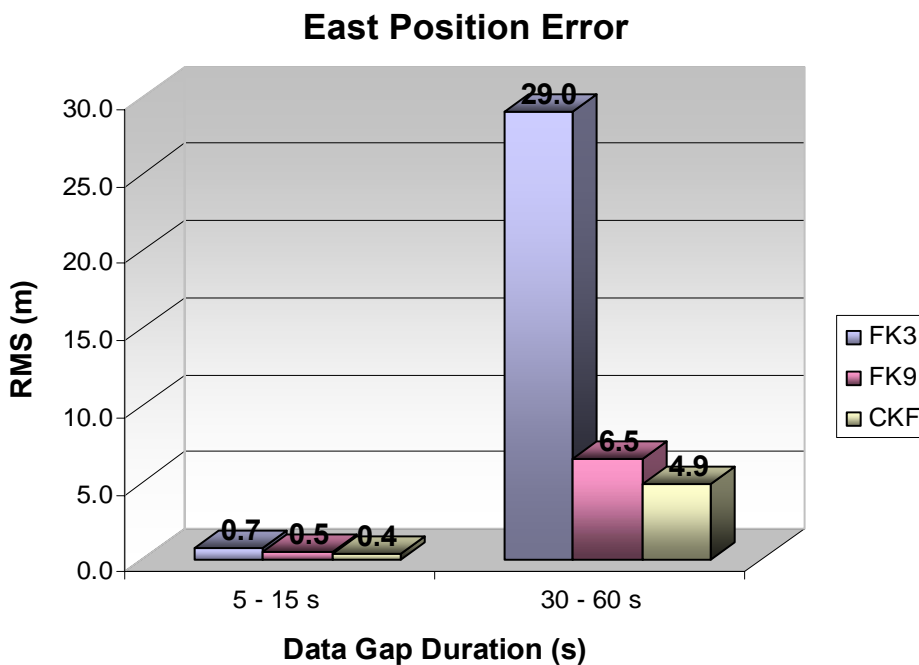
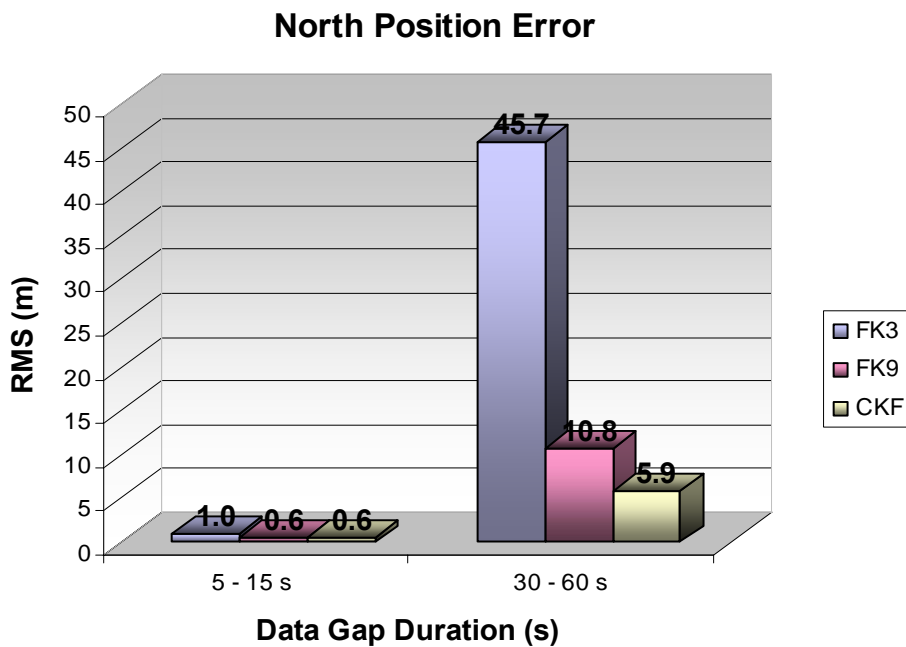


Figure 6-24: RMS of Positional Errors in Prediction

Table 6-5: Positional Accuracy in Prediction

<i>Errors</i>	Gaps (5-15 sec)			Gaps (30-60 sec)		
	RMS	Mean	 Max 	RMS	Mean	 Max
<i>FK3</i>						
δN (m)	1.0	-0.3	3.9	45.7	-5.6	109.7
δE (m)	0.7	-0.1	1.0	29.0	-2.6	106.2
<i>FK9</i>						
δN (m)	0.6	0.3	1.5	10.8	5.3	34.0
δE (m)	0.5	0.1	1.9	6.5	4.0	20.9
<i>CKF</i>						
δN (m)	0.6	0.1	1.9	5.9	2.0	18.5
δE (m)	0.4	0.0	1.0	4.9	1.1	11.1

Velocity Accuracy

In the velocity domain, a similar situation is observed. Actually velocity errors, being integrated over the prediction interval, yield the above errors in position. Figure 6-25 and Figure 6-26 present the north component of the system velocity for the two tests, respectively. In stationary periods, the two schemes with INS error compensation provide comparable velocity accuracies of 0.1 to 0.5 m/s; while, using the 3rd state Kalman filter, the achieved accuracy is in the order of 1 to 2 m/s. When the vehicle is experiencing high accelerations, the impact of azimuth misalignment becomes observable, which is demonstrated in the lower plots of Figure 6-25 and Figure 6-26. These plots represent the same gaps considered in the analysis of positional accuracy. By implementing a Kalman filter with the reduced model, a prediction accuracy of 2 to 3 m/s is obtained. A conventional Kalman filter with Φ_{up} correction improves the result to between 0.5 and 1.5 m/s. Finally, the Cascaded Kalman filter provides the best results, so that the velocity error in this case is between 0.2 m/s and 0.5 m/s.

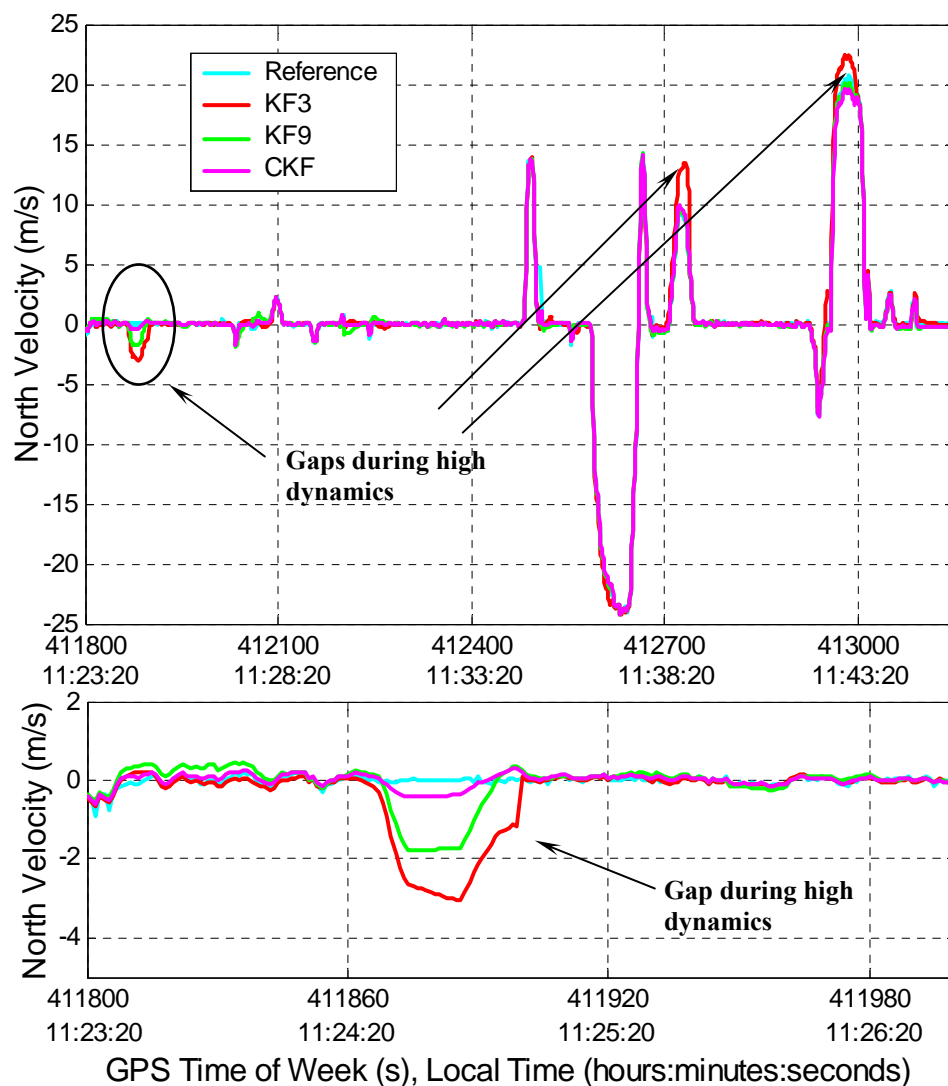


Figure 6-25: North Velocity Using Data with Simulated Outages, Test 1

A statistical analysis of the velocity errors during prediction, based on data from both tests, is presented in Table 6-6. In Figure 6-27 the diagrams show RMS values of velocity errors for the three strategies investigated. Similar to the position domain, a considerable degradation of the system accuracy is observed for long-term data gaps in the order of 30 to 60 seconds, while prediction intervals of 5 to 16 seconds do not produce such large errors even for the Kalman filter with the reduced model. This may be explained in the

following way: even during high vehicle accelerations, the system errors in prediction do not accumulate within 5 to 8 seconds; meanwhile, gaps of 10 to 15 seconds appeared to be associated mostly with those parts of the test trajectory with moderate dynamics.

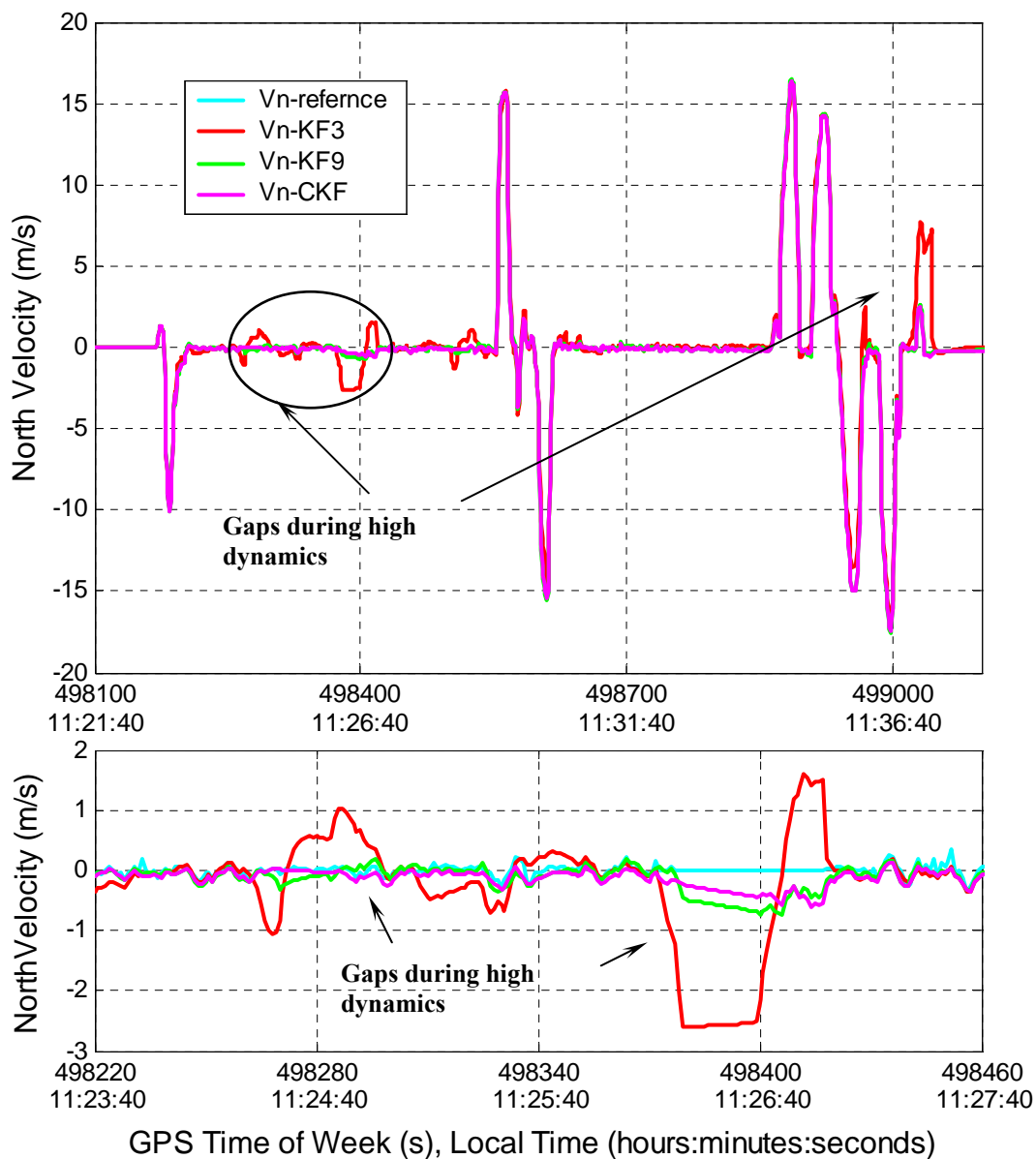


Figure 6-26: North Velocity Using Data with Simulated Outages, Test 2

It is important to note that the reference velocity information was obtained from the FLYKIN+™ software using GPS measurements from the same GPS unit; on this basis, the velocity errors of the integrated system cannot be considered as absolute but as relative only with respect to the stand-alone GPS solution during the simulated gaps.

Table 6-6: Velocity Errors in Prediction

Errors	Gaps (5-15 sec)			Gaps (30-60 sec)		
	RMS	Mean	Max	RMS	Mean	Max
FK3						
δV_N (m/s)	0.5	-0.3	1.3	2.1	-0.3	5.8
δV_E (m/s)	0.2	-0.1	0.6	3.6	-0.2	13.3
FK9						
δV_N (m/s)	0.2	0.1	0.6	0.6	0.3	1.8
δV_E (m/s)	0.2	0.1	0.5	3.5	0.2	8.7
CKF						
δV_N (m/s)	0.2	0.0	0.5	0.3	0.2	1.2
δV_E (m/s)	0.1	0.0	0.3	1.5	0.1	3.8

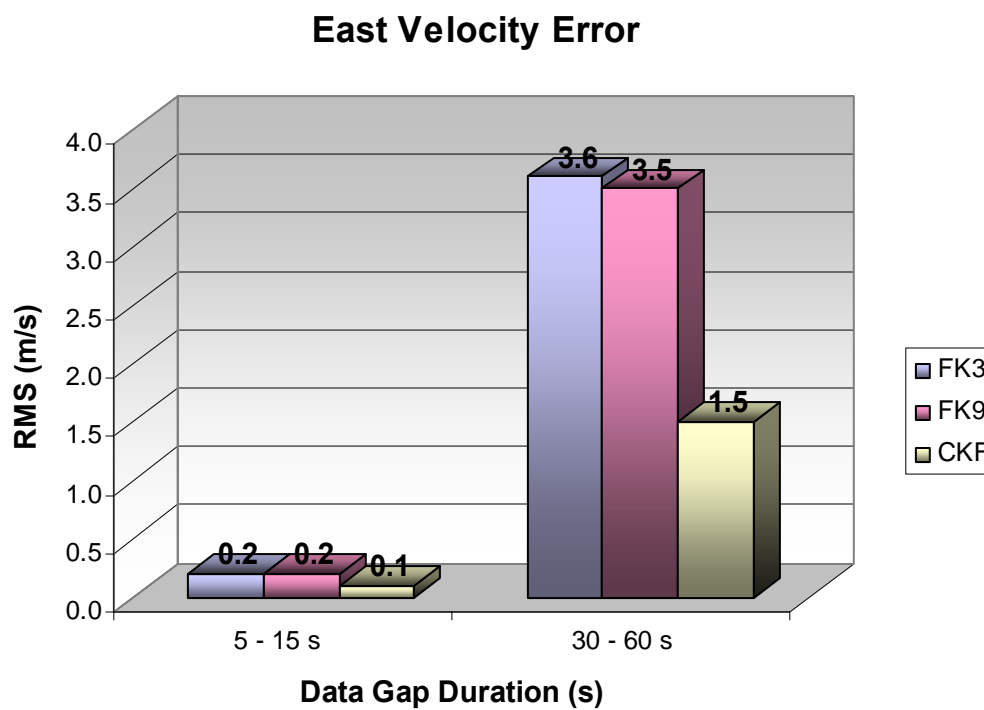
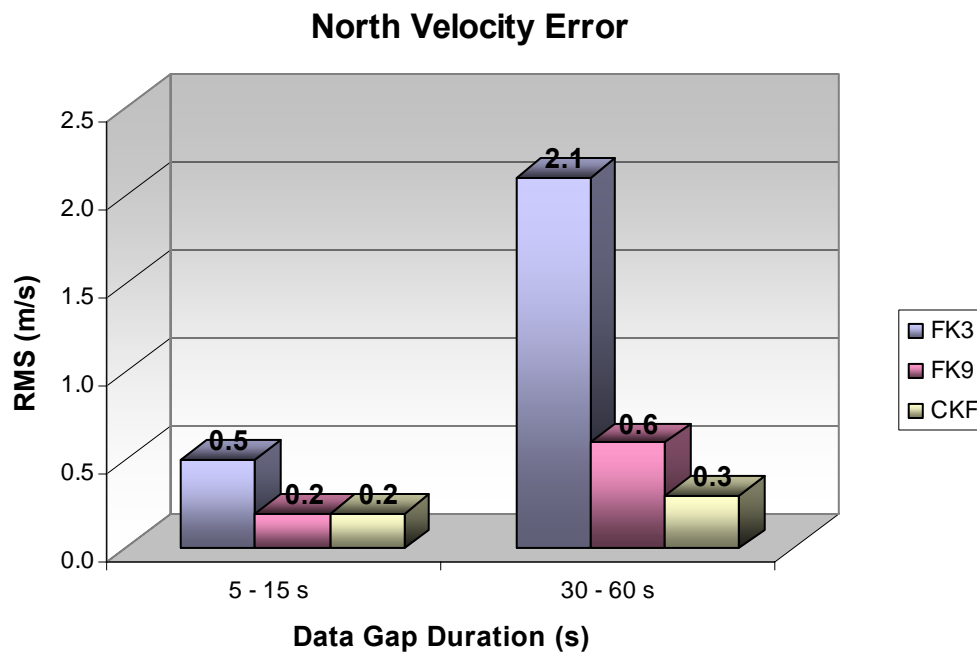


Figure 6-27: RMS of Velocity Errors in Prediction

6.3 Conclusions

The objective of this research was to develop and test the cascaded scheme of INS/GPS integration for open area applications. The integration strategy, which was described in detail in Chapter 5, includes the cascaded scheme of azimuth error estimation as well as compensation for the effects of the estimated azimuth misalignment and gyro drifts in the SINS algorithm. The influence of the above INS errors on system performance was evaluated. To analyse the prediction accuracy in position and velocity domains, GPS data gaps with different durations were simulated.

Test results illustrate the impact of azimuth misalignment on the system accuracy. In Chapter 5, an observability analysis showed that azimuth error could be accurately estimated during periods of high vehicle dynamics while, in stationary mode, accurate estimation became questionable. The test results show that the Cascaded Kalman filter decreases the time of the transition process and improves estimation accuracy of the azimuth error in general. The combined azimuth correction using the GPS heading and the filter's azimuth error estimate provides better results in comparison to the traditional approach. Azimuth compensation in the SINS algorithm also improves the attitude accuracy of integrated system; while gyro compensation contributes the improvement of estimation accuracy of INS errors in total.

The experimental results demonstrate that, in prediction mode, accurate estimation of the INS azimuth error becomes essential, especially for long-term GPS outages of 30-60 seconds with high vehicle dynamics. Crucial prediction accuracy degradation of 60 to 120 m in position and 3 to 6 m/s in velocity, on average, is observed, if the azimuth error is not considered in the estimation scheme. The extended Kalman filter provides better positional accuracy of approximately 10 to 30 m and velocity accuracy of 0.5 to 2 m/s for GPS outages of the same duration. The proposed method considered in this thesis improves upon the results expected from the traditional approach, so that an accuracy of between 5 and 15 m and 0.2-0.6 m/s in the position and velocity domains, respectively, is achieved.

Chapter 7

Results in Suburban and Urban Areas

Chapter 6 focused on the performance of the integrated system in open areas, using a conventional GPS receiver. This chapter presents the description and results of field tests of the integrated system in residential and downtown areas, when a high-sensitivity GPS receiver is used. The aim of the analysis is to assess overall system performance in terms of its positional accuracy. The limitations of system performance in challenging GPS environments - namely, long-term prediction accuracies as well as fault detection of HS GPS measurements – are also considered herein.

7.1 Test Description

Figure 7-1 shows the test set-up. Differential GPS measurements were utilized in the integration algorithm for residential area tests; this entailed observation at reference and remote stations, which were established throughout the testing. The equipment mounted in the test vehicle at the remote station included: a NovAtel's Black Diamond System (BDS) (the same unit used in open area tests) and a SiRF Star II Xtrac high sensitivity GPS receiver. Both GPS receivers were connected to a NovAtel 600 antenna via a signal splitter. Similar to the open area tests, the reference station was located on a pillar on the roof of the CCIT Building at the University of Calgary. Test equipment comprised a NovAtel OEM receiver connected to a NovAtel 600 antenna. The coordinates of the reference station were the same as given in Chapter 6. The IMU was rigidly affixed to the

floor of the test van, while the GPS antenna was mounted on the roof of the vehicle. Analogously to the open area tests, the HG1700 inertial data was time-tagged with GPS time. GPS data were collected at a rate of 1 Hz, while the raw IMU measurements were logged at a rate of 100 Hz. In the test vehicle, power for the NovAtel antenna, the SiRF receiver and a laptop for data logging was provided by splitting the DC power from the car's cigarette lighter; two 12V car batteries powered the BDS system. Table 7-1 presents several key characteristics of the GPS receivers used for testing.

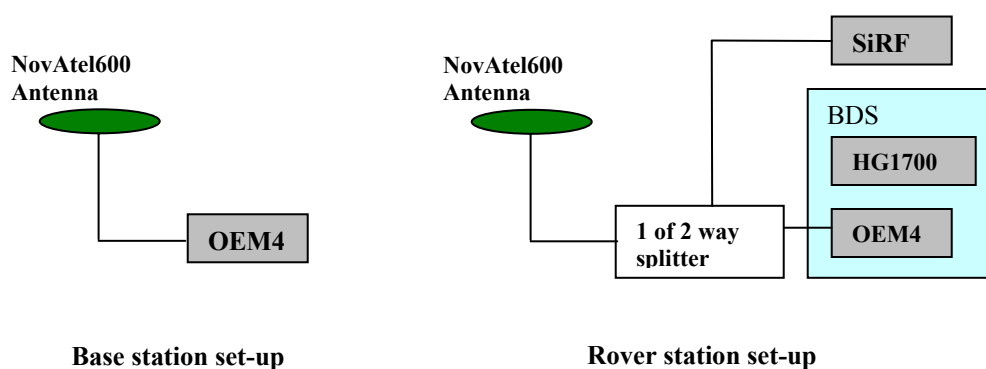


Figure 7-1: Test Set-up for Urban Areas

A series of tests were conducted in Calgary, on February, 19 and 20, 2004. Seven tests took place in an urban area, each test having a duration of about 20 to 30 minutes. The vehicle speed varied from 30 to 60 km/s and the test van frequently stopped on traffic lights during each run. The city's downtown has a variety of tall buildings ranging from 40 to 200 metres, as illustrated in Figure 7-2. This could cause GPS signal masking effects. Several underpasses are located on the test trajectories that could lead to complete satellite blockage and consequently loss of lock. Two additional tests were carried out in a residential district of Calgary. This area is characterized by one- and two-storey buildings and occasional roadside trees, as shown in Figure 7-3.

Table 7-1: Technical Characteristics of GPS Receivers Used for Testing

Type of receiver	Technical specifications
SiRF High Sensitivity (SiRFStarIIe chipset) (Rover Station)	<ul style="list-style-type: none"> • 12-Channel L1-only C/A • Code with carrier aiding • 340-800 ms dwell time • Wide correlator • Tracking Sensitivity -186.0 dB-W • Reacquisition Sensitivity - 177.9 dB-W*
NovAtel OEM4 (Rover Station)	<ul style="list-style-type: none"> • 24-Channel L1/L2 C/A code with full carrier tracking • Pulse Aperture Correlator™
NovAtel OEM4 (Rover Station)	<ul style="list-style-type: none"> • 24-Channel L1/L2 C/A code with full carrier tracking • Pulse Aperture Correlator™

* As determined by hardware simulation testing (MacGougan et al., 2002)

**Figure 7-2: Typical Test Environment in Downtown Calgary**



Figure 7-3: Typical Test Environment in Residential Area of Calgary

7.2 GPS Solution

GPS position and velocity information used in the integrated system was obtained from two sources: (1) the single point internal code solution of a SiRF receiver; and (2) the code solution using the $C^3\text{NAV}G^{2\text{TM}}$ software, developed by the PLAN Group of the University of Calgary ($C^3\text{NAV}G^{2\text{TM}}$, Petovello et al. 2000). The signal power cut-off was set to 0 dB-Hz. For post-processing analysis using the $C^3\text{NAV}G^{2\text{TM}}$ software, different parameters were chosen for tests in downtown and residential areas, respectively. In the case of the downtown data sets, these parameters were set to the following values:

- Solution mode: height-constrained single point;
- GDOP threshold: 10;
- elevation mask: 7° ;
- threshold for residual checking: 5 metres;
- carrier phase smoothing: not implemented; and

- atmosphere modeling: not implemented.

In urban conditions, large GPS positional errors in the order of the tens of metres were observed due to multipath and echo-only signals as well as signal cross-correlation. Atmospheric errors did not have a significant impact on the GPS solution as compared to the above effects; therefore, these errors were not taken into consideration in post-processing. Moreover, in downtown areas, the single-point GPS solution provided results similar to those of the differential GPS solution; thus, only the single point solution was utilized for data processing. To improve solution availability, which is weak due to signal masking, a height-constrained strategy was implemented. The average number of satellites used in the GPS solution ranged from three to seven, while the PDOP values varied from two to more than ten. Using a HS GPS receiver in downtown areas, reasonably high GPS measurement availability of 77% to 98% of total test time was observed.

The parameters for processing of data from residential areas using C³NAVIG²™ are as follows:

- Solution mode: differential;
- GDOP threshold: 10;
- elevation mask: 15°;
- threshold for residual checking: 5 metres;
- Standard deviation of height (for constraints): 10 metres;
- carrier phase smoothing: implemented; and

- tropospheric correction: implemented.

In contrast to urban canyons the major errors in position and velocity occurring in suburban areas were caused by multipath, signal cross-correlation and echo-only signals – all of which could be reduced significantly or even eliminated by increasing the elevation mask (set to 15°). As a result, the average number of satellites used in the solution was relatively low in comparison to open area environments and ranged from four to six; however this still provided a favourable value of the PDOP that did not exceed two during most of the testing. GPS measurement availability was very high - in the order of 98% to 100% of overall test time. Due to the above, the differential GPS solution utilized in these field tests was capable of providing better results than the single point approach.

7.3 Downtown Results

The reference information was available in the position domain only as supplied by a Digital Map of Calgary, which had an accuracy of 5 to 10 metres. The map provides the coordinates of a road centreline, so that the precise location of the test vehicle - in terms of which lane of the roadway was occupied - remains unknown. As a result, the analysis of position accuracy simply is considered herein.

In downtown conditions, the INS is updated by GPS positions and velocities. These quantities are potentially corruptible by large errors such as tracking of multipath and echo-only signals, and signal cross-correlation; they are also susceptible to degradation of

geometry as a result of satellite blockage, which in turn lowers the overall availability of a GPS solution. As a consequence of the above, the integrated algorithm is characterized by: (1) frequent prediction intervals with a duration varying from 10 seconds up to 1-3 minutes; and (2) erroneous GPS updates, when undetected. These factors combine to drastically degrade the overall system accuracy.

Figure 7-4 presents the reference trajectory for Run #1. It is about 3-4 kilometres long and contains several turns for heading accuracy evaluation. This trajectory is characterized by a high density of skyscrapers, which produce severe signal masking and attenuation along with strong glassy reflections. In a major part of the trajectory (5th and 6th Avenue) signal masking occurs from two directions only (north and south) due to the orientation of the grid pattern of Calgary's downtown core.

Figure 7-5 demonstrates the achieved system accuracy when the internal GPS solution is used. The GPS position and velocity information obtained from the internal solution does not contain data gaps of more than a few seconds. Presumably, when a GPS receiver loses lock, the positions and velocities are propagated through the duration of an outage. The receiver firmware utilizes filtering techniques, which explains the smooth low frequency behaviour of position errors (MacGougan et al., 2002 and Basnayake, 2004).

The time intervals, during which the GPS internal solution predicts its positions and velocities, are not provided by the receiver firmware. Therefore, measurement availability is determined by the number of satellites used in the solution. For this run, it

is quite high. The 3D- and 4D- fix density is 95% of the overall test time. As mentioned in Chapter 2, fix density is defined herein as the percentage of test time when at least three (3D FD) or four (4D FD) measurements are available.

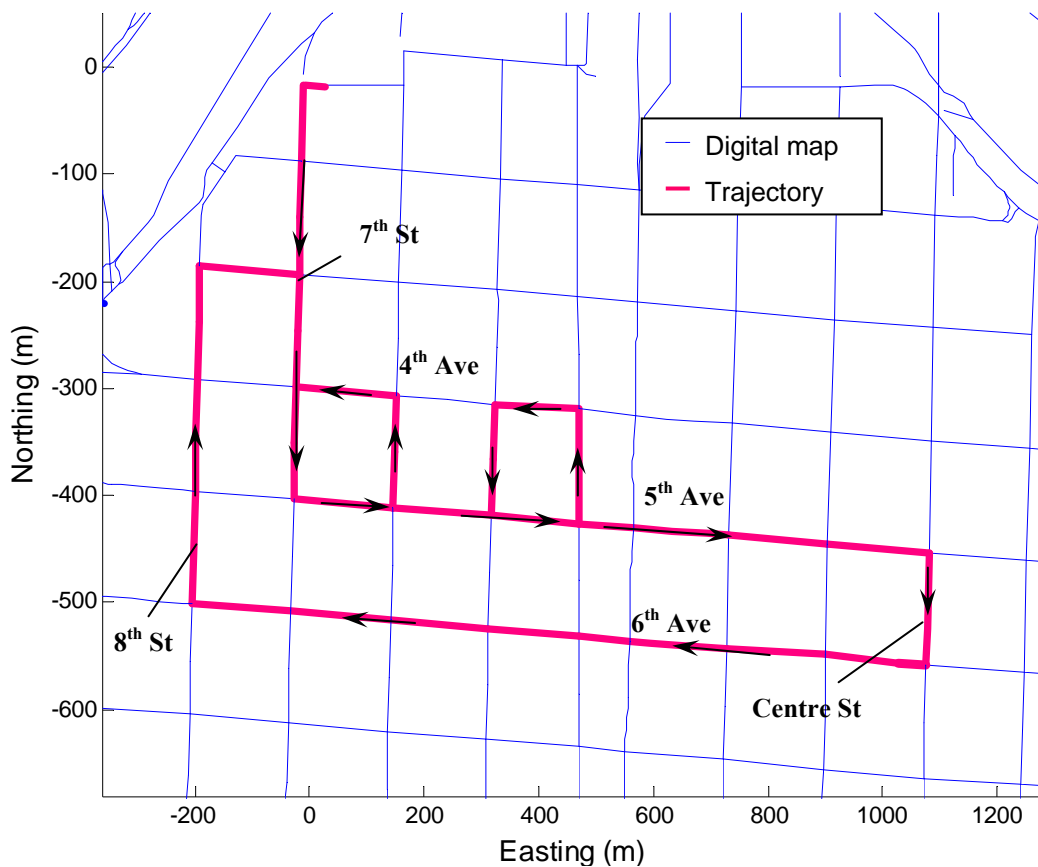


Figure 7-4: Reference Trajectory 1

Due to smooth behaviour of GPS velocities and positions, the estimation algorithm ‘trusts’ GPS measurements, and no dramatic improvement in accuracy is observed in the given example: the RMS of across-track error for stand-alone GPS solution is 14 metres, while the integrated solution improves the result to 12 metres. This is well illustrated in Table 7-3, which shows the percentage of time during the tests when the filters in the integrated scheme work in prediction mode. For Run #1, it is observed for only 4% of the

test duration for the velocity filters (only during GPS gaps as indicated by FD of 96%), and 19% of the test time for the coordinate filters. It must be mentioned that the coordinate filters work in prediction mode more frequently than velocity filters. This is due mainly to the operational mode criteria for the filters. Unlike velocity filters, the coordinate filters always switch to prediction mode, when the test vehicle stops due to traffic jams or lights at controlled intersections. Moreover, GPS velocity measurements are typically less noisy in comparison to GPS positions and do not contain large outliers due to tracking of multipath and echo-only signals.

Figure 7-6 shows the C/N_0 and elevation angles for all satellites tracked during Run #1. As seen from the plots, a HS GPS receiver is capable of tracking highly attenuated signals with power levels less than 16 to 18 dB-Hz, which is 25 dB-Hz lower than the nominal value of C/N_0 for LOS signals (by comparison, a conventional GPS receiver is able to track signals attenuated by 9 to 10 dB-Hz (MacGougan et al., 2002)). As expected, the signals from the satellites at lower elevations are more attenuated than the SVs, which are closer to zenith (due to longer signal paths and, consequently, larger space loss (Lachapelle, 2002)). The average C/N_0 value is approximately 35 dB-Hz, which is 10 dB-Hz lower than the average signal power in open sky areas. Due to the elevation cut-off, severely degraded GPS signals at low elevations (PRN 1 and 25) with C/N_0 less than 20 dB-Hz are not used in the solution. Meanwhile, the satellite signals with PRNs 4, 10 and 30, for example, can be attenuated LOS, multipath or even echo-only signals caused by strong glassy reflections. The C/N_0 values are characterized by medium and high frequency fluctuations. The medium frequency oscillations (herein in a range from 20 to

43 dB-Hz) are primarily due to multipath errors, while the high frequency components are due to receiver noise (Ray, 2000).

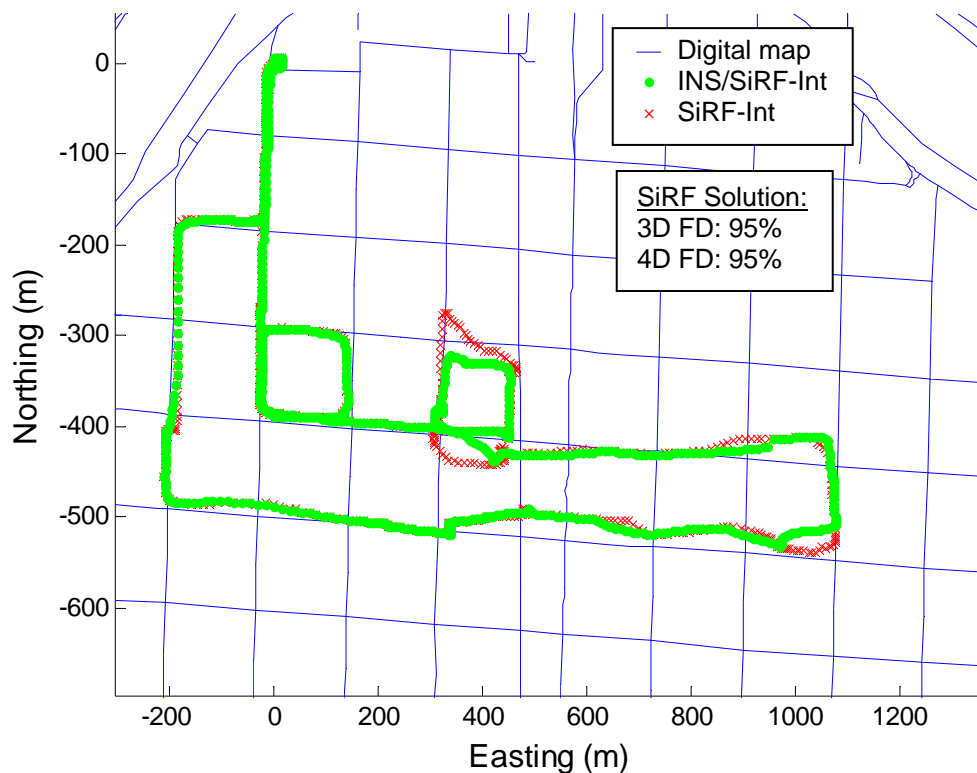


Figure 7-5: Position Output of Integrated System Using The SiRF Internal Solution, Run #1 on Trajectory #1

Figure 7-7 presents position output of the integrated system for Run #1, when the DGPS C³NAV²™ solution is used. By comparison to the previous case, considerable improvement in the system accuracy is observed: the RMS of across-track error of stand-alone GPS solution is 86 metres, while the integration with the INS improves the result almost in four times to 23 metres. The coordinate Kalman filter with adaptive measurement covariance works appropriately in this case due to the following:

C³NAV²™ positions are noisy and contain large errors of high frequency so that the GPS accuracy changes abruptly during the test.

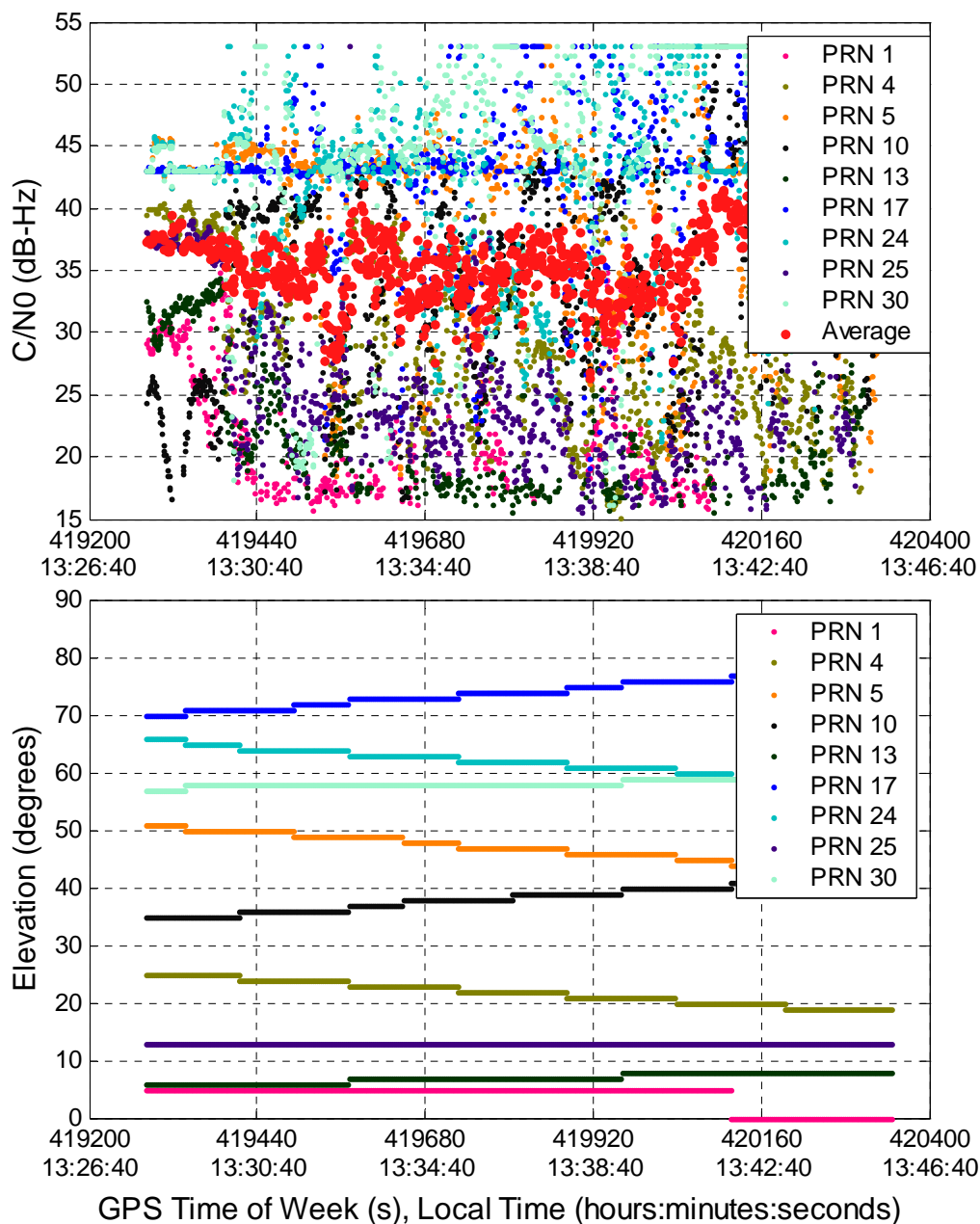


Figure 7-6: C/N_0 and Elevation Angles for All Satellites Tracked, Run #1

When the GPS solution is uncertain (i.e. magnitude of the innovation sequence is large), the measurement covariance increases, the Kalman gain tends towards zero and the estimation algorithm relies on the system model. Probable sources of large GPS errors include: false reacquisition or acquisition of the correlation peaks, namely signal cross-correlation, along with tracking of multipath or echo-only signals. (For example- as seen in Figure 7-6, signals transmitted by the satellites with PRNs 4, 10 and 30 can be multipath or echo-only due to large variations of the C/N_0 values).

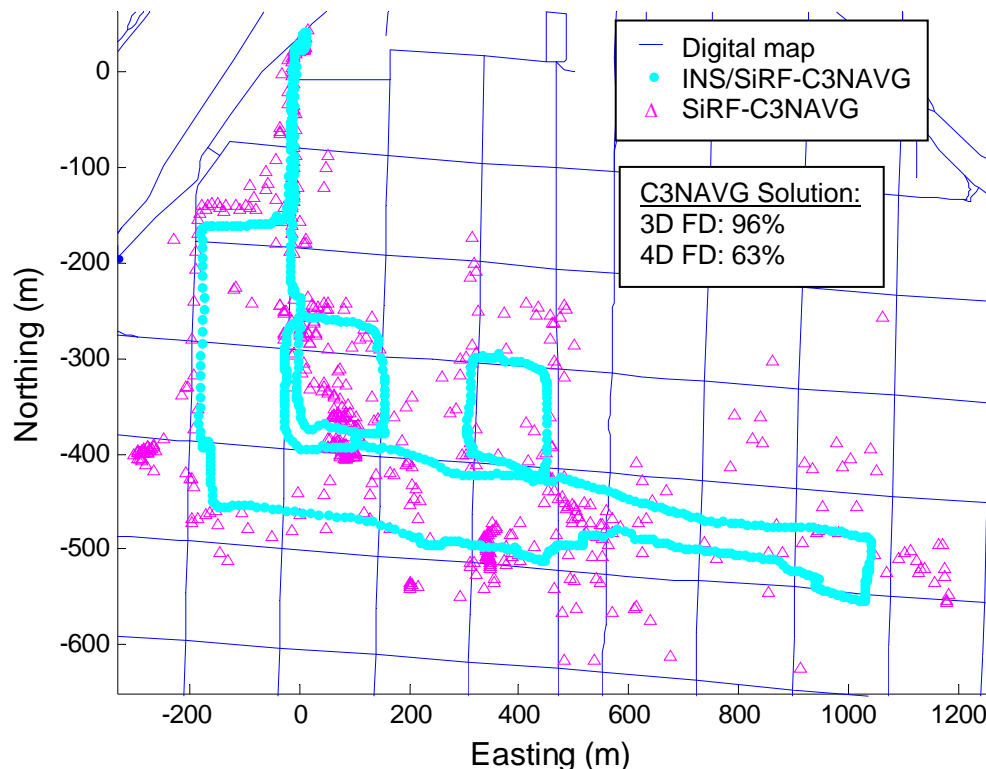


Figure 7-7: Position Output of Integrated System Using The C³NAVG²™ Solution, Run #1 on Trajectory #1

This is expected to some extent owing to two factors: (1) the probability of false detection at lower signal power levels is much higher; (2) echo-only and multipath

signals may have higher signal levels than line-of-sight signals (MacGougan, 2003). MacGougan investigated the influence of signal cross-correlation effects in the measurement domain. The cross-correlation functions have peak levels that reach -24 dB with respect to the autocorrelation peak. This is known to result in tracking of false correlation peaks at certain Doppler offsets and levels of strength differences between signals (Ward, 1996a). Therefore, signal cross-correlation is assumed to be one of the major sources of large outliers in GPS positions.

C³NAVIG²™ GPS measurements contain frequent data gaps of a few seconds caused by signal masking as well as the chosen post-processing parameters, such as residual checking and the DOP threshold. The reliability criteria based on the PDOP values, the number of satellites used in the solution, and the INS-GPS velocity difference also force the estimation algorithm to switch to prediction mode, so that the filters work in prediction mode more often and for longer time intervals than if this switch were motivated by actual gaps in GPS measurements. This situation is well illustrated in Figure 7-8, which shows the PDOP values along with the number of satellites used in the solution, as obtained from the C³NAVIG²™ software. The 3D- and 4D- fix density calculated from the number of measurements available, is 96% and 63% respectively. Meanwhile, the integrated solution for Run #1 is characterized by prediction intervals of 30 to 40 seconds, which degrades the position accuracy of the integrated system (see Table 7-4) As shown in Table 7-3 the Kalman filters in the estimation algorithm work in prediction mode for 41% (the velocity filters) and 54% (the position filters) of the total test duration.

Figure 7-9 presents the across-track errors for Run #1 for the above two cases: (1) using the GPS internal solution; and (2) using the C³NAV²™ solution. The across-track error for all tests was computed using the digital map of Calgary as a reference. As mentioned, the positional accuracy of a reference trajectory therefore is on the order of 10 to 15 metres (the digital map provides the coordinates of the road centreline only). Therefore, herein the measured position accuracy of less than 15 metres can be evaluated as relatively high. The stand-alone C³NAV²™ positions contain a few outliers in the range of 200 to 500 metres. In addition to signal cross-correlation, these large errors may be caused by tracking echo-only signals, since this type of error is basically unlimited in magnitude.

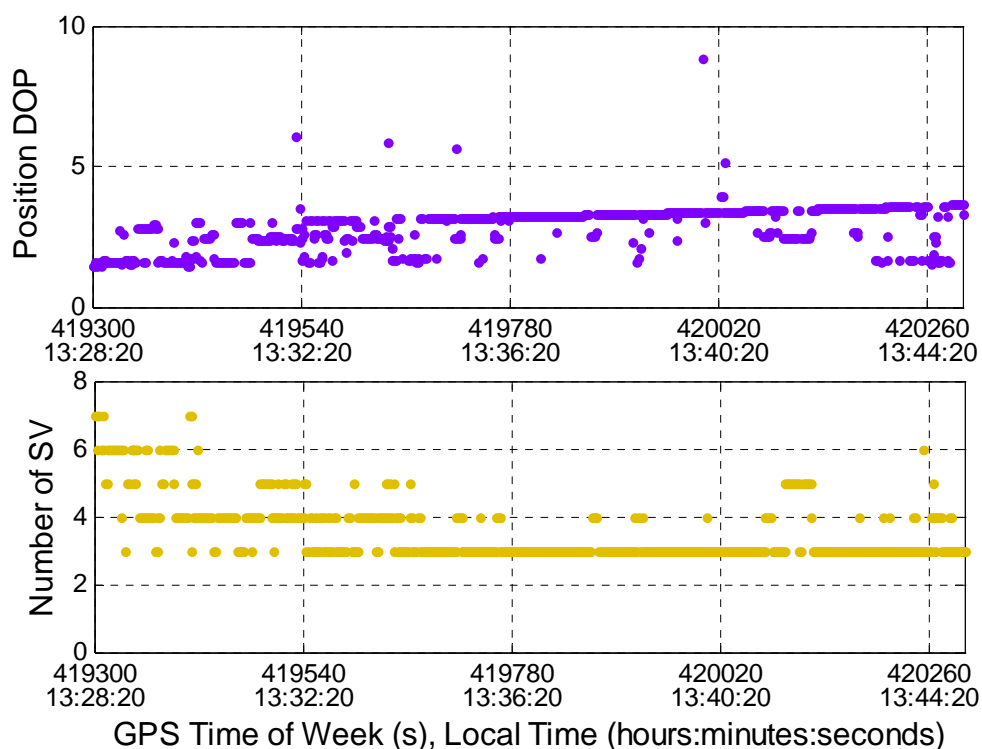


**Figure 7-8: PDOP and Number of Satellites Used in Solution for Run #1,
Based on The C³NAV²™ Output**

For Run #1, the stand-alone positional accuracy of the SiRF internal solution varies from 15 to 40 metres, while the integrated solution slightly improves the result to between 10 and 35 metres.

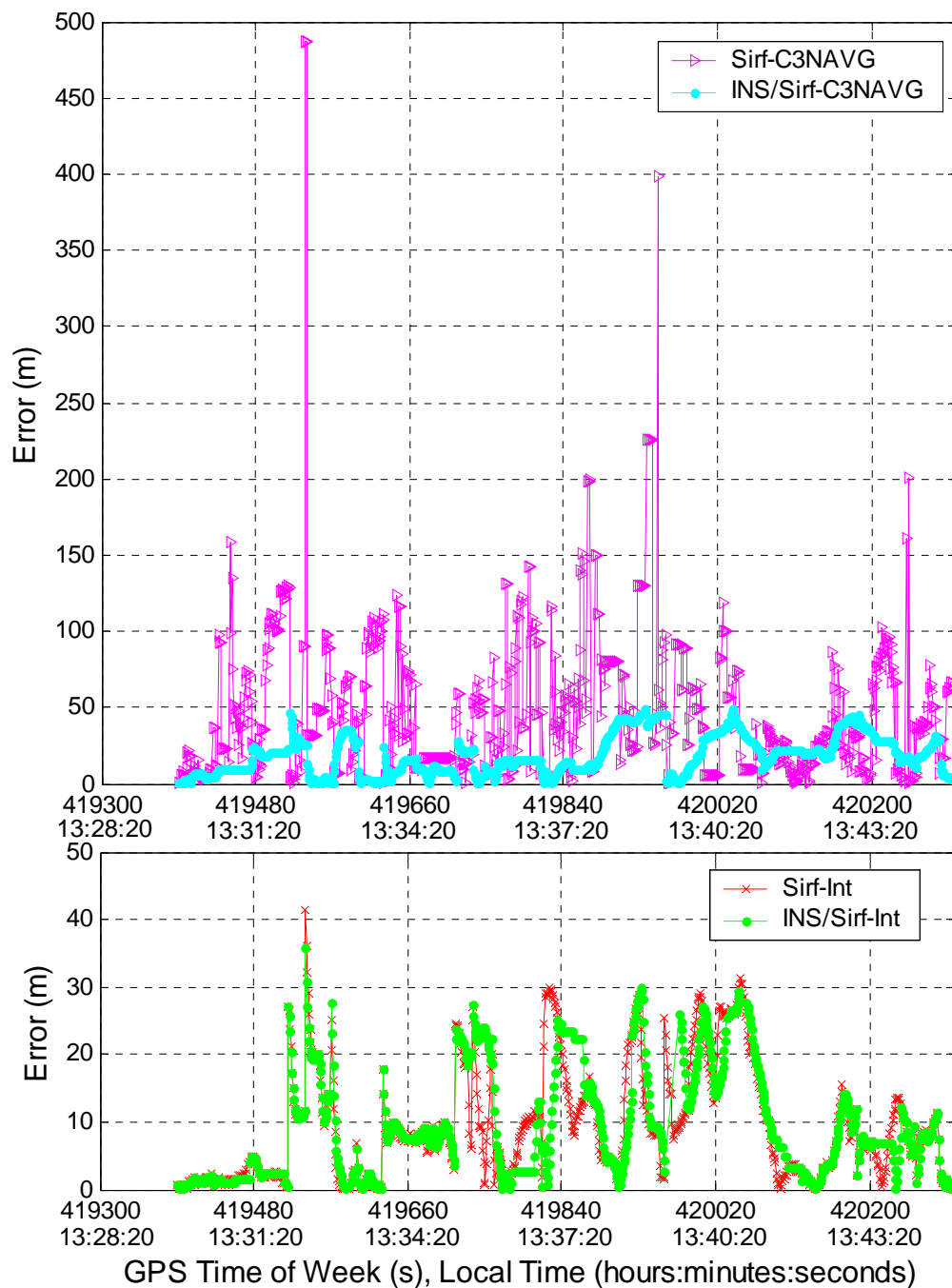


Figure 7-9: Across-track Error, Run #1 on Trajectory 1

The accuracy of the raw C³NAV²™ solution is in the order of 50 to 80 metres on average with occasional outliers of 200 to 500 metres. The integrated solution improves the results significantly, producing a position accuracy ranging from 10 to 50 metres. As seen in Figure 7-9, the integrated solution contains occasional jumps in the order of 10 to 50 metres. They are caused by implementation of the Kalman filter with adaptive measurement covariance. In some cases, the filter does not work optimally due to the challenge of separating the system errors from GPS measurement errors. Theoretically, when the filter is supported with erroneous GPS measurements over several consecutive epochs, it obliges the innovation sequence (as defined by the difference between predicted state and actual measurements) to grow and the Kalman gain to decrease. As a result, the algorithm works similarly to prediction mode and it smoothes the GPS blunders. However, in some cases, the innovation sequence remains relatively small, when the GPS positions are biased and change slowly over time. It leads to a large gain on measurements and causes jumps in the integrated solution. The same effect is observed in results for the other runs, described below.

Four more runs were conducted on the same trajectory. Very large across-track errors of up to 100-500 metres for the internal solution, and up to 500-2000 metres for the C³NAV²™ solution, were observed due to the effects listed above. Unlike the situation in Run #1, even the internal GPS solutions for Run #2 and Run #3 are characterized by long-term data gaps of more than one minute.

Figure 7-10 presents the position output of the stand-alone SiRF internal and integrated solutions for Run #2. As seen in the figure, at the end of the test the GPS positions are not available for over 400 metres of the test trajectory, which corresponds to the data gap of 40-80 seconds. The across-track error of the internal solution ranges from 60 to 300 metres, while the integrated system improves the result to between 10 and 20 metres. In Run #2, the internal solution loses its smoothing ability. The magnitude of the GPS position error changes rapidly, varying from tens of metres to over 100 metres. The possible cause of this behaviour is the tracking of one or more echo-only signals of high elevation which, being undetected, causes divergence of the GPS solution so that it becomes unreliable by the end of the test. For example, signals from the satellites with PRNs 9 (elevation angle $\sim 50^\circ$) and 20 (elevation angle $\sim 18^\circ$) can be multipath or echo-only, as shown in Figure 7-11, which depicts the C/N_0 values and elevation angles for all tracked satellites. The power levels of these SVs contain large variations from 15 to 45 dB-Hz. The average C/N_0 ranges from 30 to 35 dB-Hz. Signal cross-correlation also has the potential to cause divergence of the GPS solution.

The availability obtained from the receiver firmware is relatively high: 3D FD is 96% and 4D FD is 90%. The 10% loss in 4D FD is presumably due to the long gap at the end of the test. However, these values are assumed to be overly optimistic and do not reflect the quality of the actual GPS measurements. It can be illustrated by the fact that the filters in the integrated algorithm work in prediction for almost half of the overall test duration. The integrated system improves the SiRF internal solution significantly. Due to noisy-

like behaviour of the internal GPS solution, the reliability criteria works optimally, which allows successful fault detection of erroneous GPS measurements.

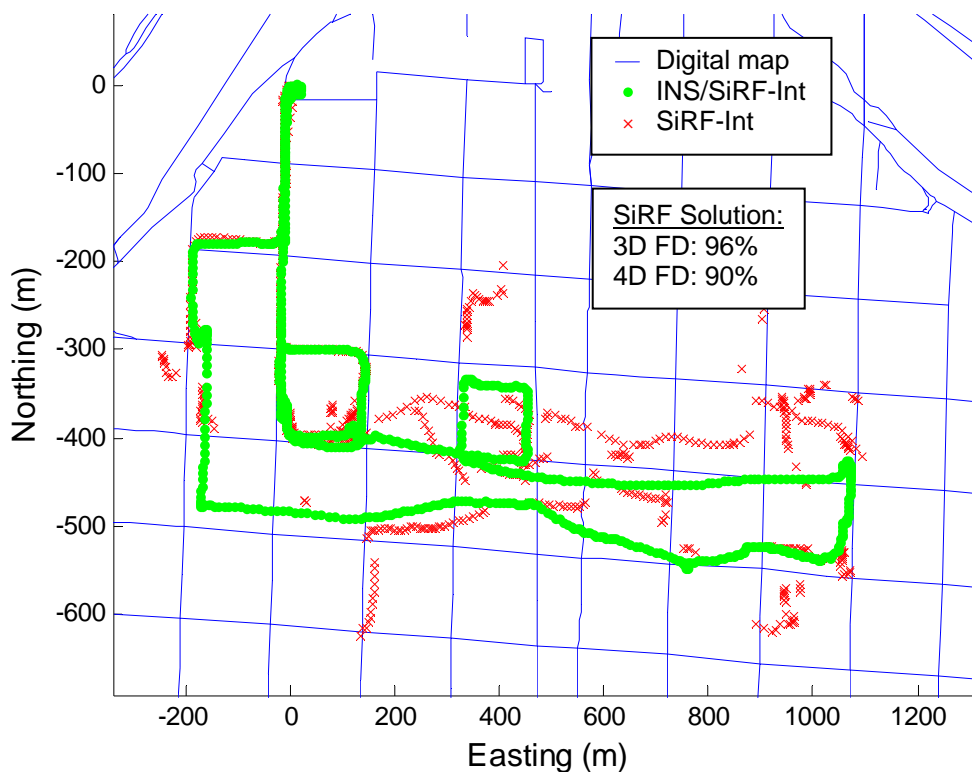


Figure 7-10: Position Output of Integrated System Using The SiRF Internal Solution, Run #2 on Trajectory #1

Figure 7-12 depicts the parts of the test trajectory, when velocity and coordinate filters switch operation to prediction mode. This happens when GPS data contains outliers larger than 40 to 50 metres. As demonstrated in Table 7-3, the velocity and coordinate filters work in prediction mode 23% and 50% of elapsed test time respectively.

Figure 7-13 presents the position output of the integrated system using the C³NAV²™ GPS solution for Run #2. A similar situation to the case of Run #1 is observed.

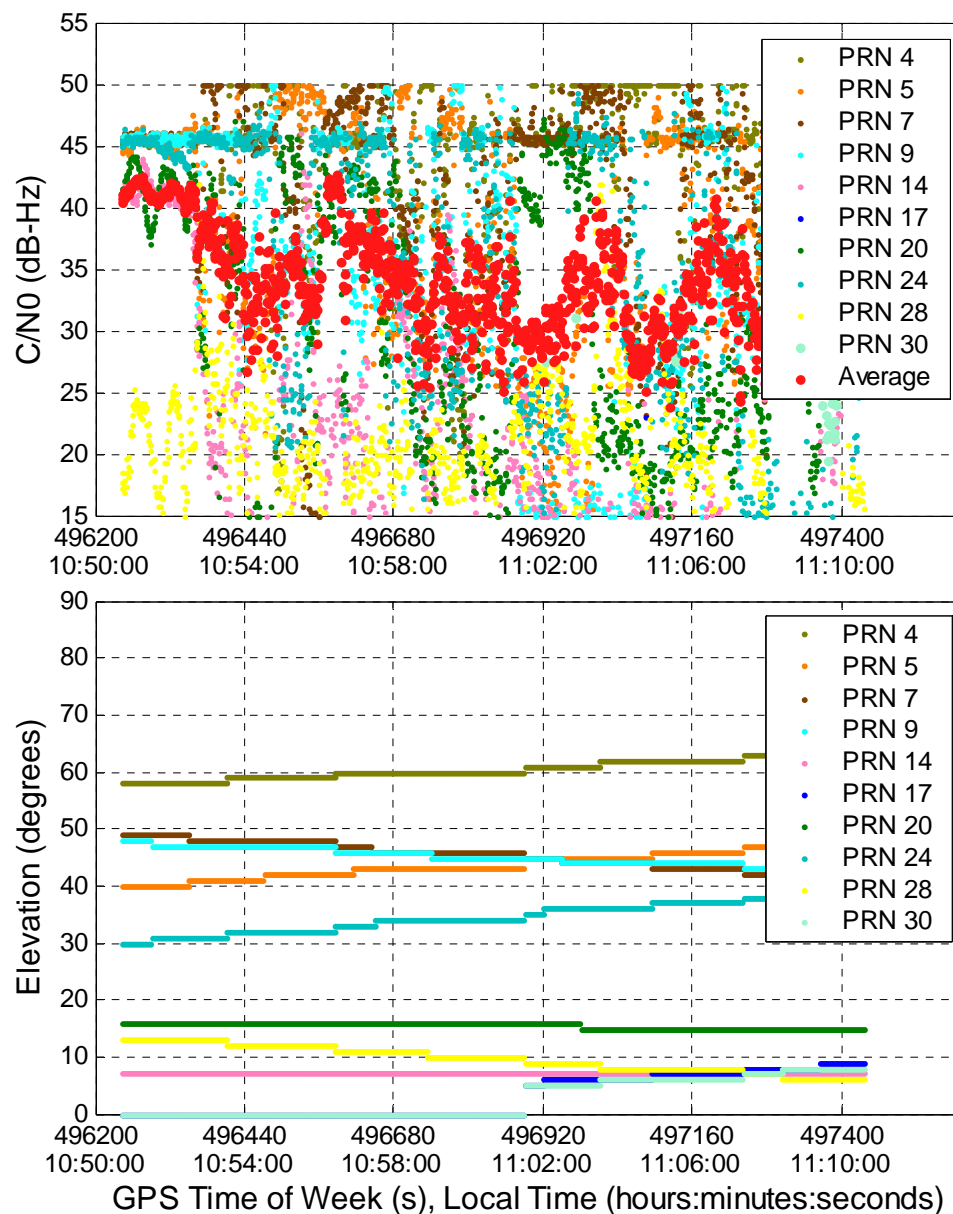


Figure 7-11: C/N₀ and Elevation Angles for All Satellites Tracked, Run #2

The epoch-by epoch Least-Squares solution supplies the system with positions that contain large errors of high frequency. Frequent data gaps indicated by the integrated algorithm do not exceed 10 to 40 seconds in duration (see Table 7-4), so that the position errors of the integrated system in prediction mode do not have time to accumulate.

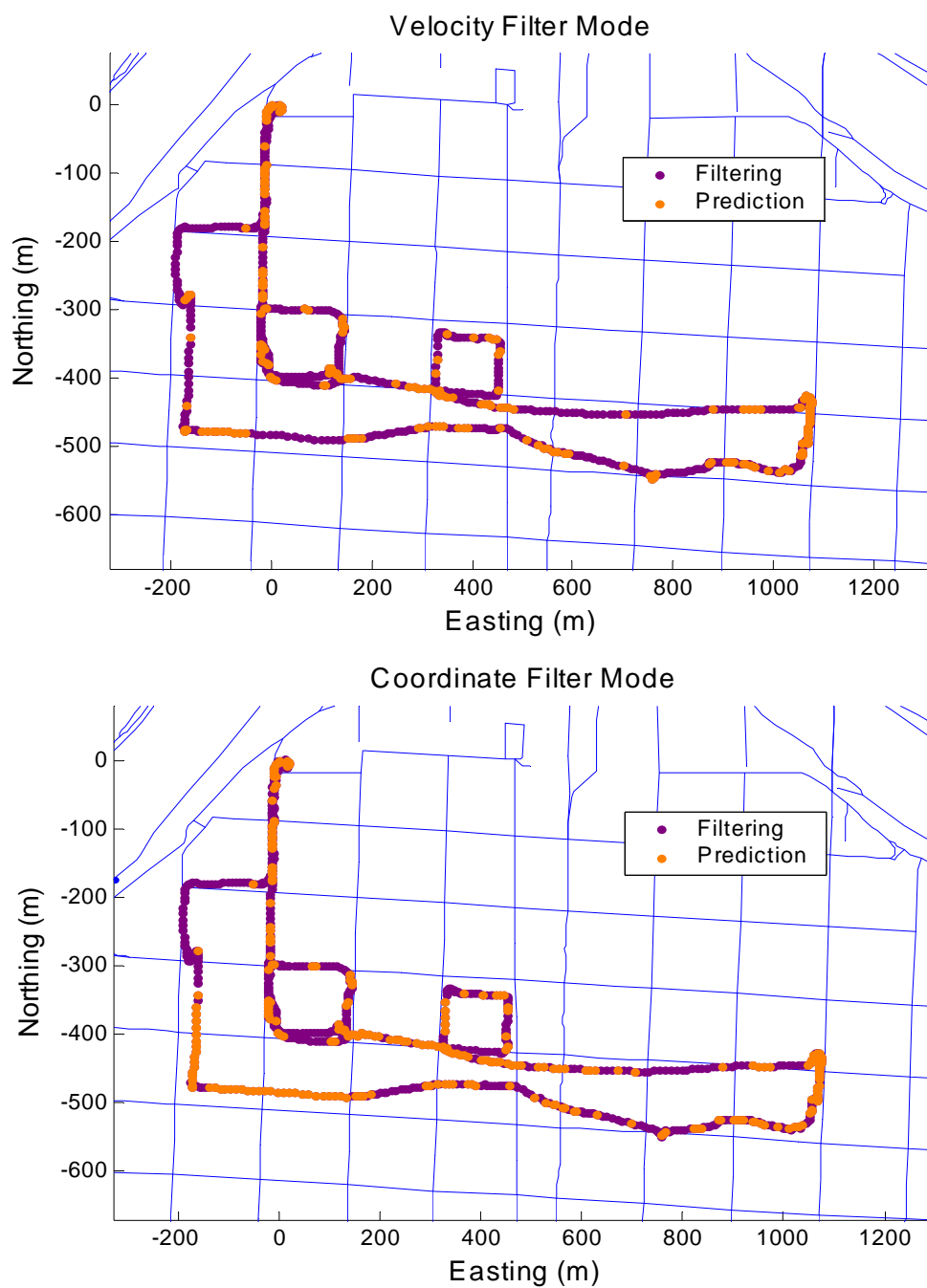


Figure 7-12: Filter Mode for Run #2, The INS/SiRF-Internal Solution

Figure 7-14 shows the PDOP values and a number of satellites used in the solution as an output of the C³NAV²™ software. There are two data outages of two seconds in duration when no solution is obtained. The 3D- and 4D- fix densities of 98% and 96%,

respectively, are very high. These values are not very informative since data gaps are defined not only by measurement availability, but also by the PDOP and differences between GPS and INS-predicted velocities. As a result to the above, prediction intervals for velocity and coordinate filter's operation are much longer than can be expected from the FD and PDOP magnitudes, as illustrated in Figure 7-15.

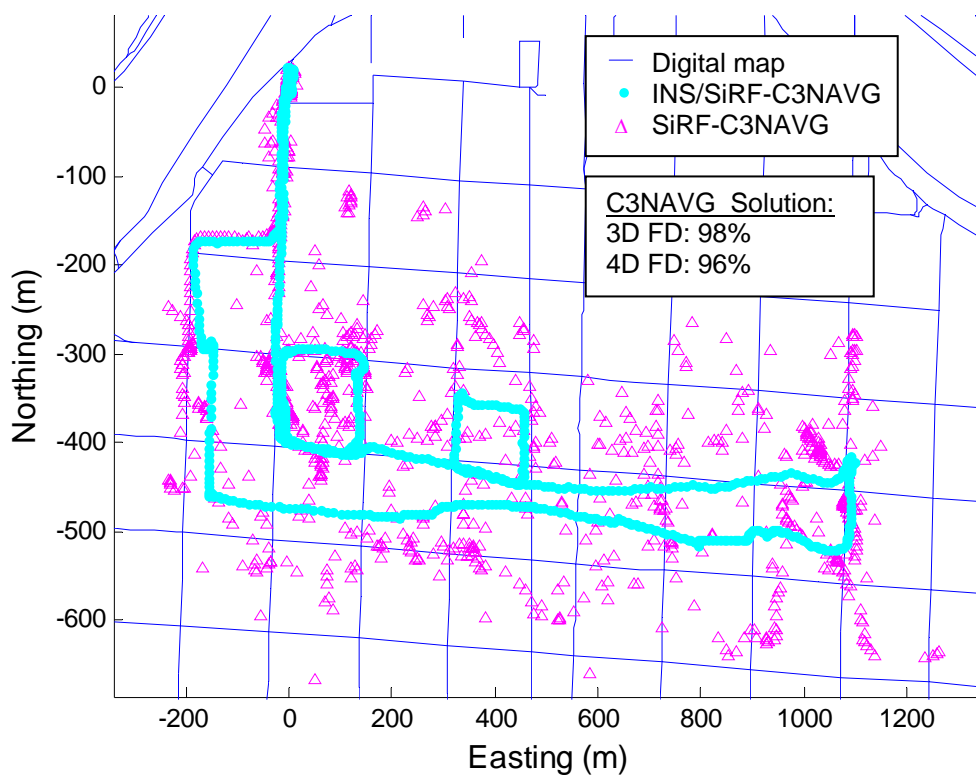
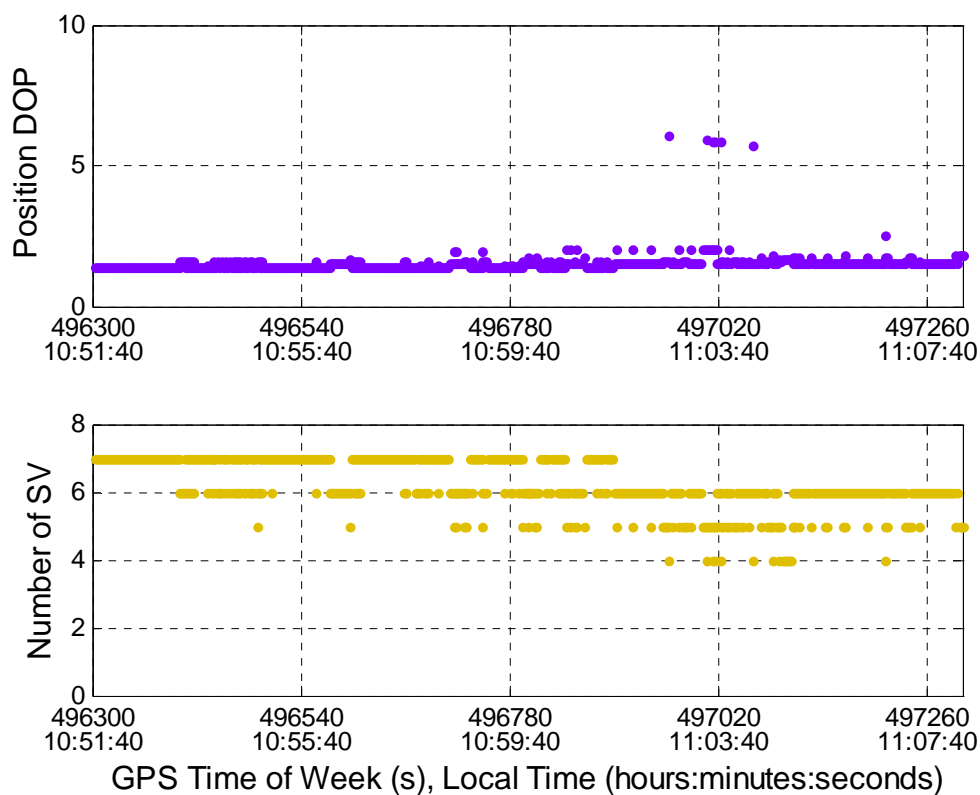


Figure 7-13: Position Output of Integrated System Using The C³NAVG²™ Solution, Run #2 on Trajectory #1

The integrated solution improves the results considerably, as demonstrated in Figure 7-16, which presents the across-track error for Run #2. The stand-alone internal GPS solution has a position accuracy of 30 to 150 metres, while aiding by the INS improves the accuracy to between 10 and 50 metres. C³NAVG²™ produces a position solution of

accuracy in the order of 50 to 150 metres with occasional outliers of 500 to 1000 metres. In this case, the positional accuracy of the integrated system ranges from 20 to 50 metres (see Table 7-2). As seen in Figure 7-16, the integrated system provides positions with across-track error that contains a few jumps varying from 5 to 10 metres. These outliers are result of implementation of the adaptive Kalman filter for position error estimation.



**Figure 7-14: PDOP and Number of Satellites Used in Solution for Run #2,
Based on The C³NAV²™ Output**

Figure 7-17 shows the position output for Run #3 when the internal GPS solution is used. Presumably, the GPS receiver lost lock due to signal masking and could not reacquire satellite signals for this period; meanwhile, the receiver firmware kept propagating the

positions over the prediction interval, resulting in severe accuracy degradation. In this run, the longest prediction interval is more than two minutes long (see Table 7-4).

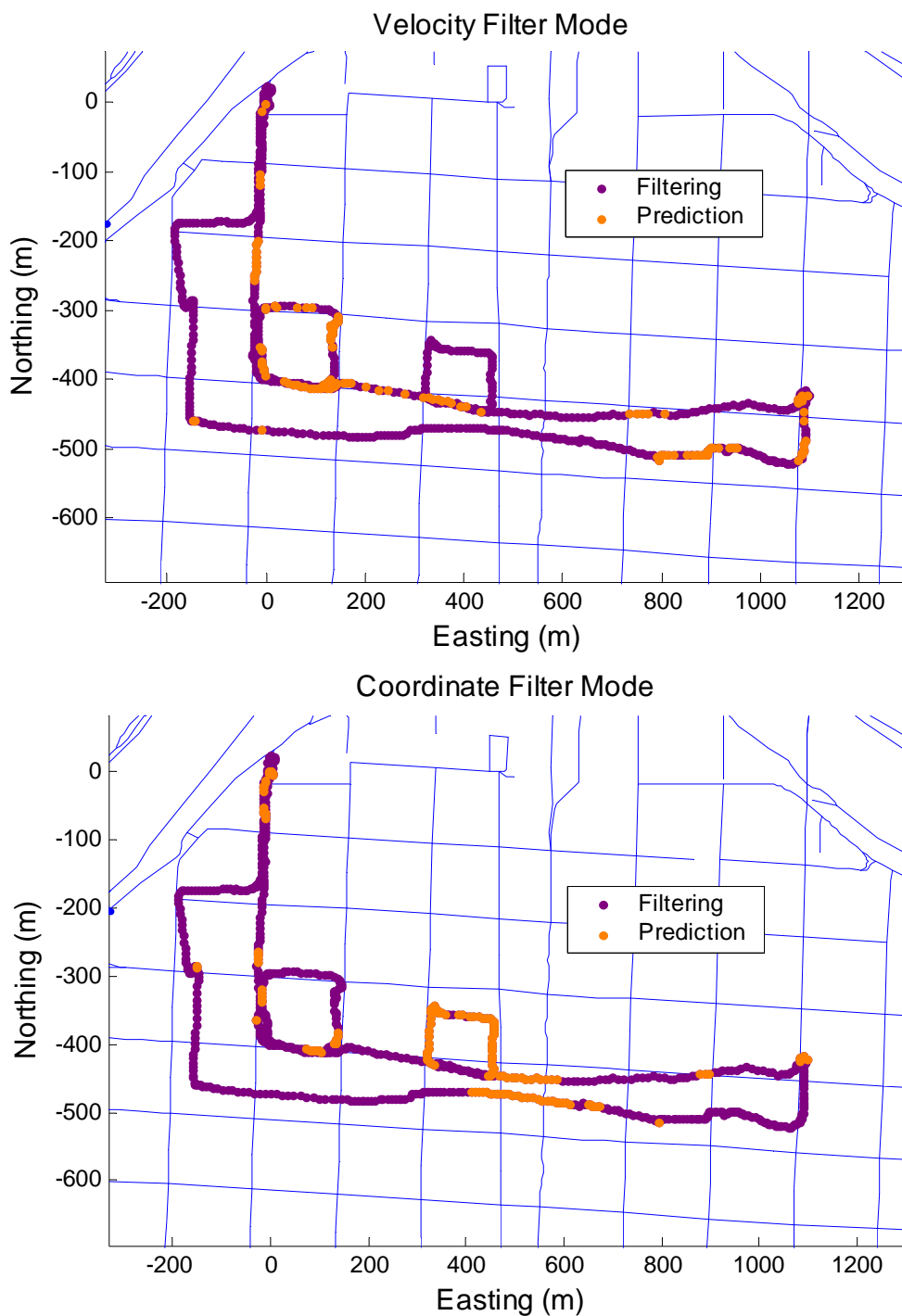


Figure 7-15: Filter Mode for Run #2, The INS/SiRF-C³NAV²™ Solution

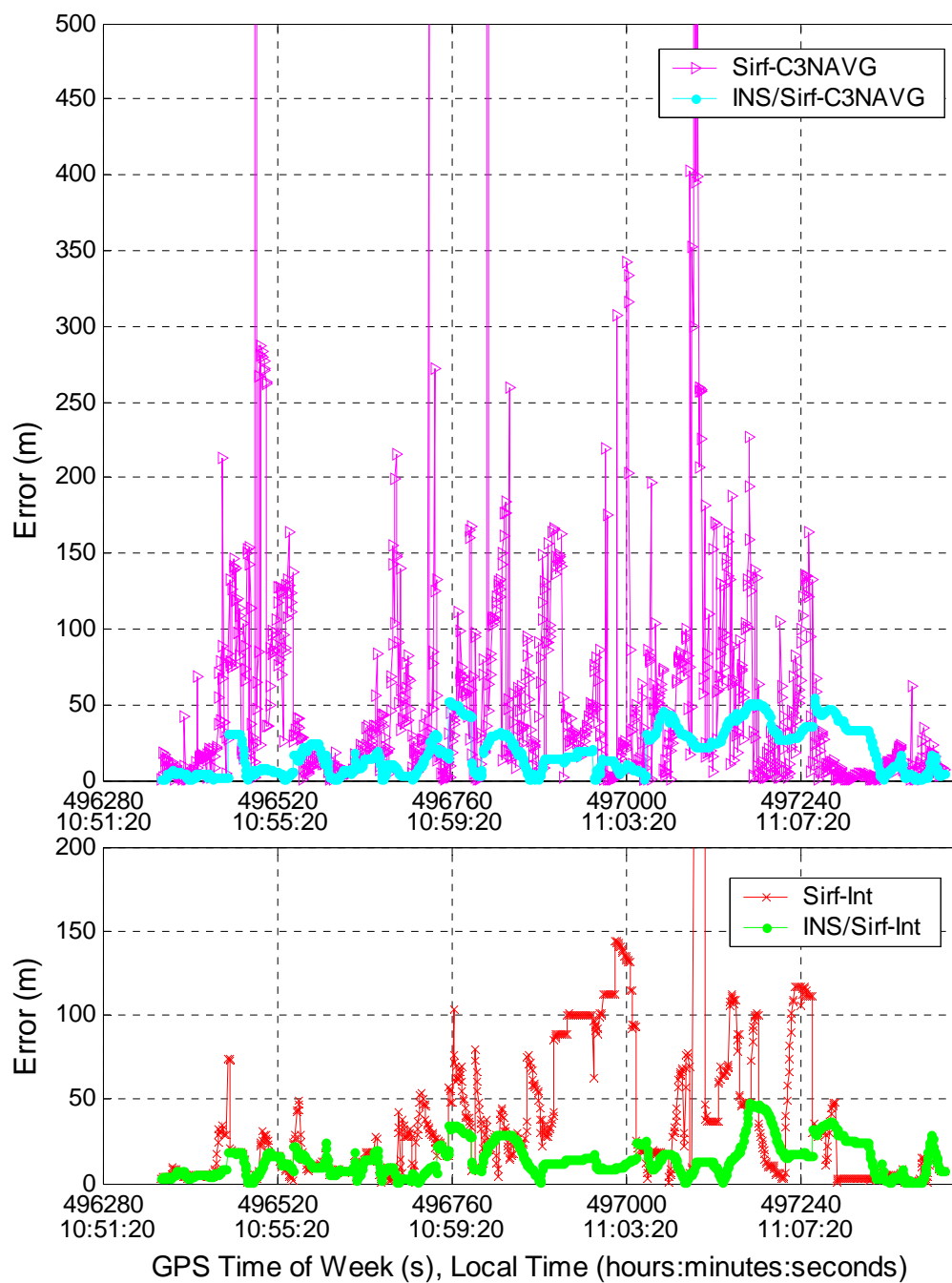


Figure 7-16: Across-track Error, Run #2 on Trajectory #1

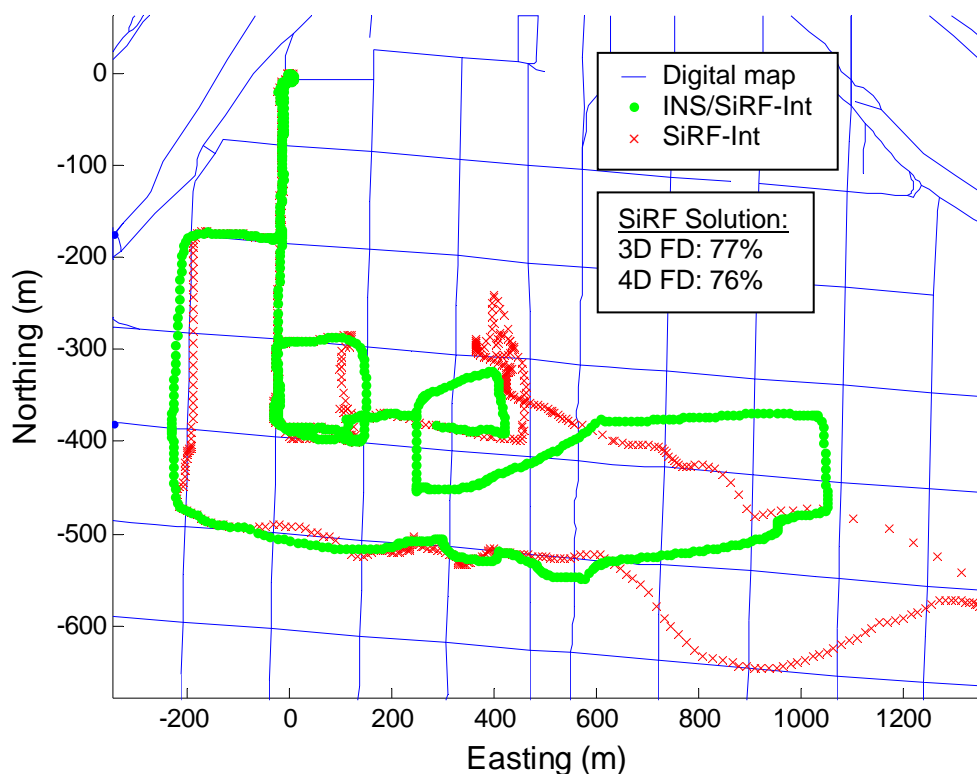


Figure 7-17: Position Output of Integrated System Using The SiRF Internal Solution, Run #3 on Trajectory #1

This is indicated by fix density values of 77% (3D) and 76% (4D). Nevertheless, these numbers are most probably too optimistic, since the SiRF firmware does not provide information about the filtering mode, i.e. the time intervals during which the navigation solution is predicted, remain unknown. It is well illustrated by Figure 7-18, which depicts parts of the test trajectory when the filters in the integrated algorithm and the receiver firmware work in prediction mode. The data outages observed in the internal solution are derived from the number of satellites used in the solution in the respective epoch (highlighted in magenta). These parts of the GPS internally-derived trajectory do not represent the total duration of the gap. The largest errors in GPS internal position were

observed during long-term data gaps on the segments of the trajectory containing curves. During one of these outages, the receiver is updated with measurements for several consecutive epochs before loosing lock again (the right-bottom corner of the plot), however, the SiRF firmware repeatedly interpolated positions in the wrong direction. This can be caused by the adoption of overly optimistic values of the covariance matrix of input noise in the Kalman filter. Too much gain is attributed to the system model, rather than to the measurements.

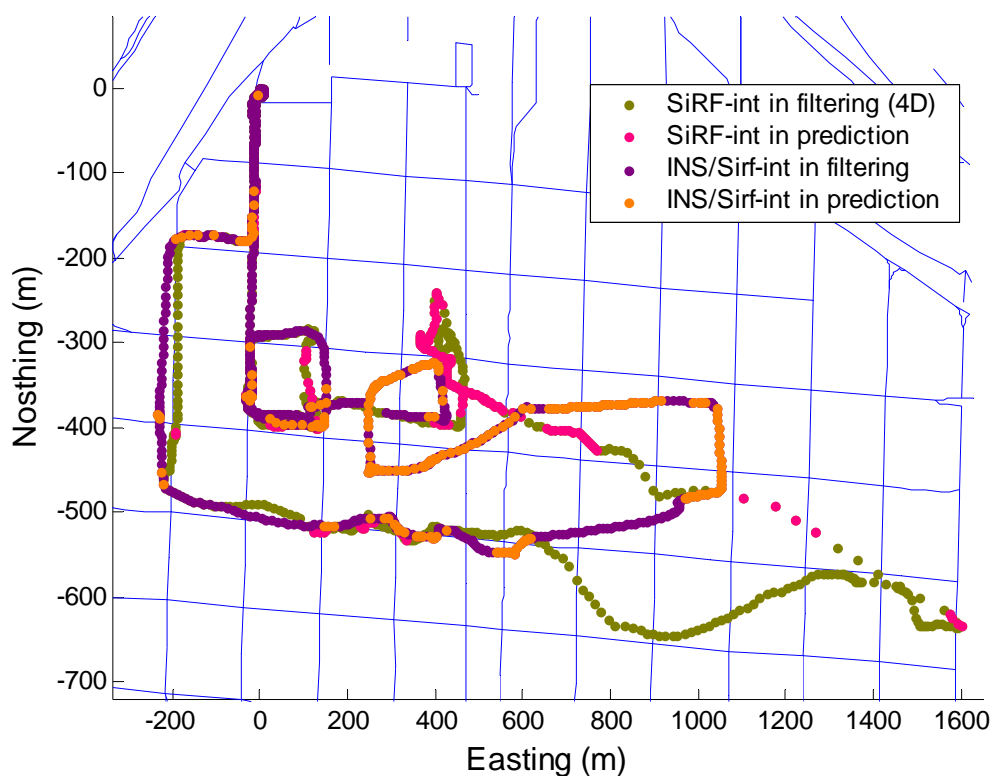


Figure 7-18: Operation Modes of The Coordinate Filters of Integrated System and The SiRF Internal Solution, Run #3

In prediction mode, without external heading information, the stand-alone GPS position solution drifts 150-500 metres away from the test trajectory. Figure 7-19 presents the

C/N_0 and elevation angles for all satellites tracked during Run #3. The results are analogues to the previous two cases.

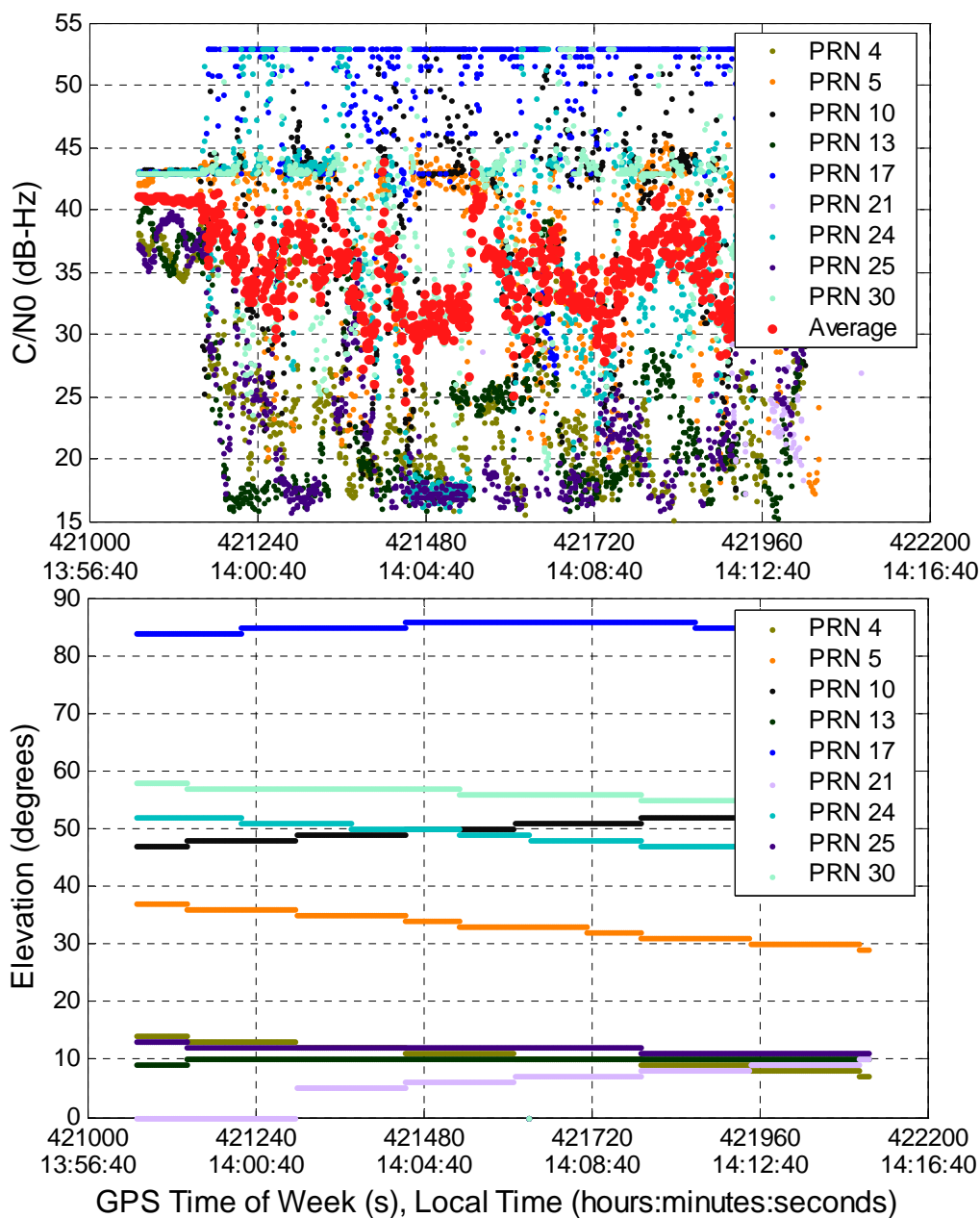


Figure 7-19: C/N_0 and Elevation Angles for All Satellites Tracked, Run #3

The integrated system provides substantial improvement in the positional accuracy. The shape of the trajectory is preserved, and across-track error does not exceed 70 metres.

Similar to the previous run, the filters in the estimation algorithm switch to prediction mode quite often (21% and 36% of the test time for velocity and coordinate filters, respectively, as shown in Figure 7-18).

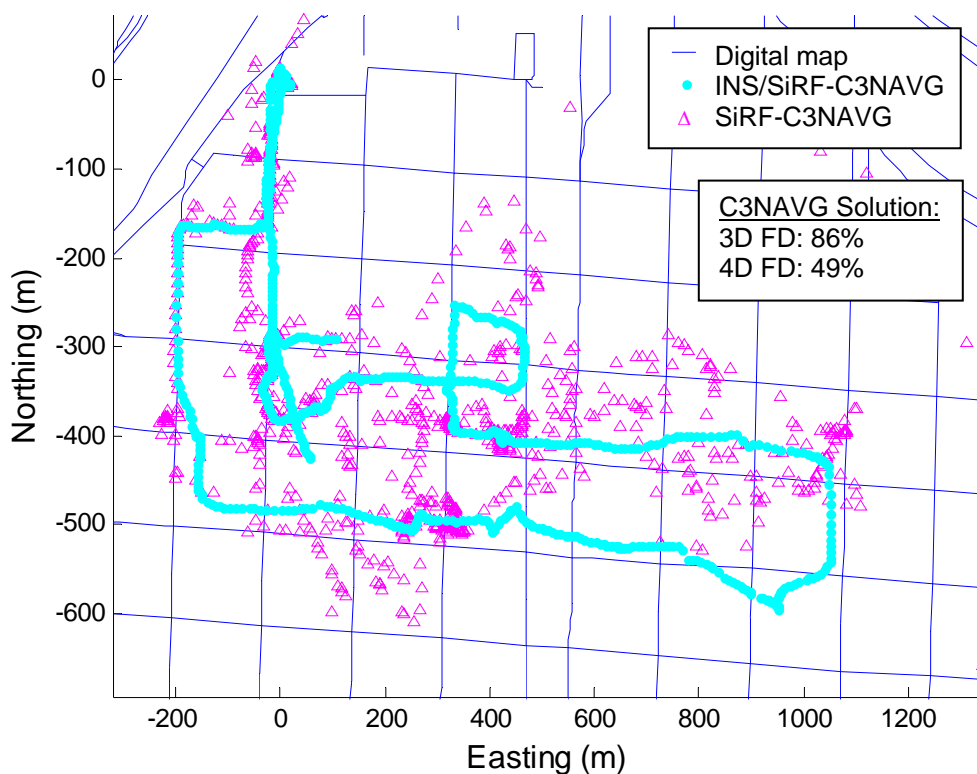
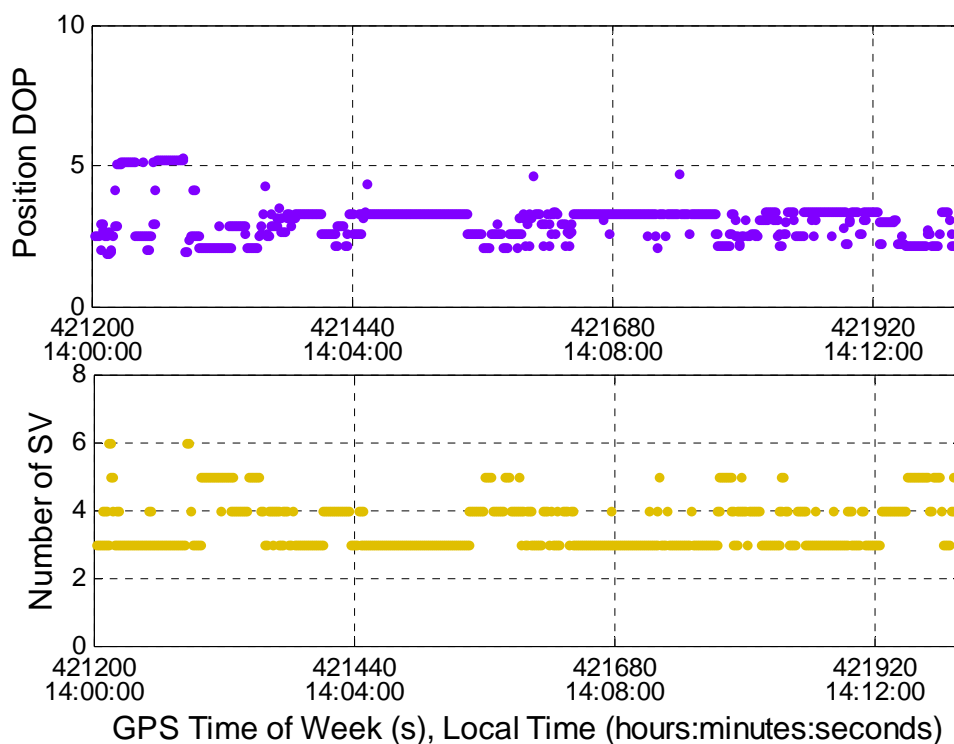


Figure 7-20: Position Output of Integrated System Using The C³NAVG²™ Solution, Run #3 on Trajectory #1

Figure 7-20 presents the position output of the integrated system based on the C³NAVG²™ output. As in the first two runs, the raw GPS solution provides poor position accuracy with large outliers in the order of tens of metres and regular short-term data gaps of 10 to 30 seconds. It is well illustrated by Figure 7-21, which depicts the PDOP magnitudes and the number of satellites used in the solution for Run #3. There are several outages of a few seconds, when no solution is available. The fix densities for Run #3 are:

86% (3D) and 49% (4D). The longest data gap for Run #3 is more than two minutes (this is not reflected in Figure 7-21). The data gaps are defined by the duration of filter operation in prediction mode, while the operational mode criterion is determined not only by the PDOP values and the number of satellites used but also by the difference between the INS and GPS velocities (see Chapter 5).



**Figure 7-21: PDOP and Number of Satellites Used in Solution for Run #3,
Based on The C³NAVG²™ Output**

Analogous to the previous tests, the integrated system improves position accuracy dramatically, which is shown in Figure 7-22. This figure represents the across-track error for Run #3. For this run, utilizing the SiRF firmware output, stand-alone GPS operation produces an across-track error ranging from 50 to 150 metres on average, with outliers of

over 500 metres. The INS, as updated by internal GPS measurements, decreases this error significantly, to between 30 and 70 metres.

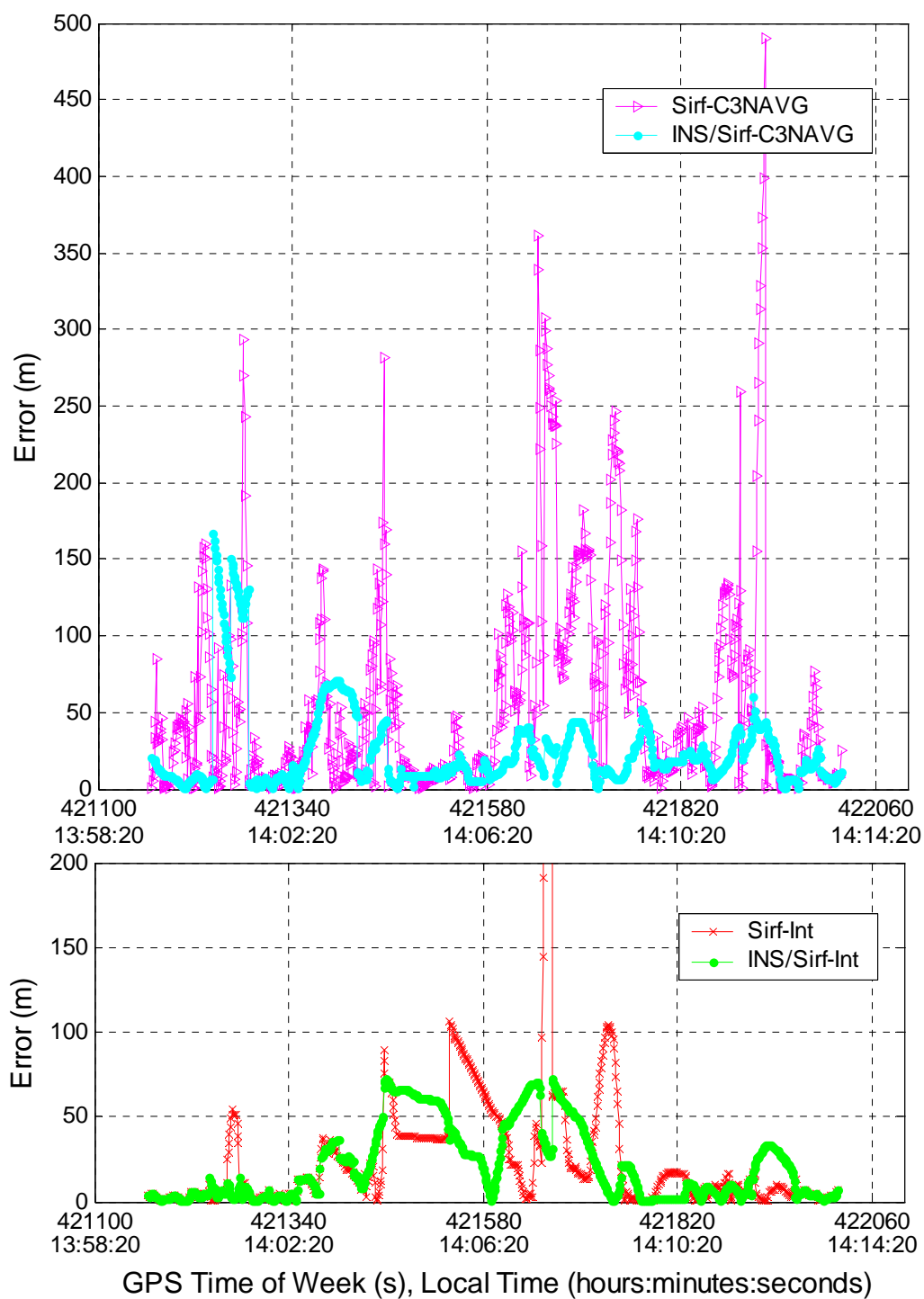


Figure 7-22: Across-track Error, Run #3 on Trajectory #1

The across-track error for the stand-alone C³NAVIG²™ solution varies from 50 to 150 metres with several jumps of 300 to 500 metres. The integrated system improves the resulting accuracy to 50 metres on average; however, the positional accuracy of the integrated solution is degraded to 150 metres in the part of the trajectory containing turns. The origin of this degradation is a rough estimate of INS azimuth misalignment, which degrades the position accuracy of the integrated system considerably. Due to typical GPS data gaps occurring throughout the test (see Figure 7-21), the azimuth error does not have enough time to converge, which leads to a residual error of about 6° to 8°.

Another run in downtown Calgary was conducted on a different trajectory, as shown in Figure 7-23 and is denoted Run #4. A part of this trajectory running along 6th Avenue is characterized by a high density of tall buildings; the remainder is defined by a variegated physical environment. For example, on 9th Avenue, a few skyscrapers along with 3- to 5-storey buildings are located on the north side of the road, while the district south from 9th Avenue is an open sky area.

Figure 7-24 presents the position output of the integrated system using GPS internal positions and velocities for Run #4 on Trajectory #2. On 6th Avenue, the trajectory segment is characterized by a high concentration of buildings, and the stand-alone GPS solution experiences position errors of up to 50 metres due to signal masking and tracking of multipath signals. On the remainder of the trajectory, errors in position do not exceed 10 to 20 metres. The fix densities for this run are quite high: 98% (3D) and 96% (4D).

The loss in measurement availability appears on the trajectory segment characterized by harsh GPS conditions, referred to above. The integrated solution improves the positional accuracy to 25 metres for this part of the test.

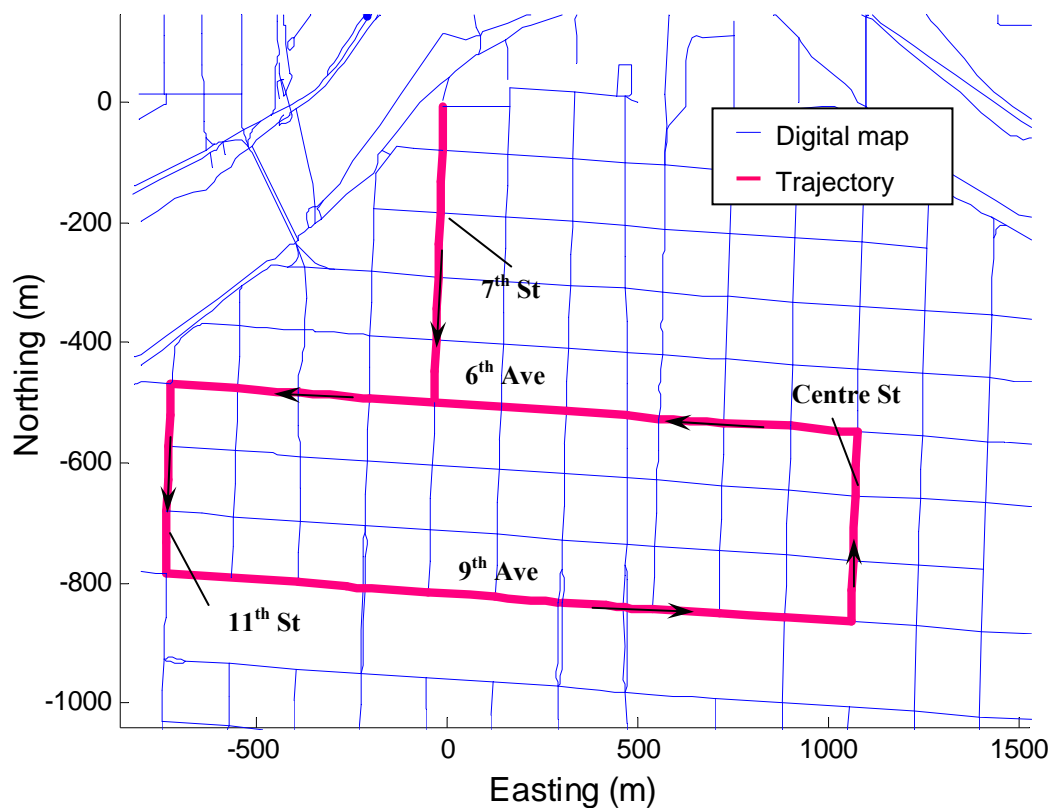


Figure 7-23: Reference Trajectory #2

Figure 7-25 shows the C/N_0 values and elevation angles for all satellites tracked during Run #4. In a similar manner to previous cases, large fluctuations in C/N_0 are observed for some satellites owing to multipath effects and tracking of echo-only signals (for example, possible candidates are PRN 4 and 10). The average position error of stand-alone GPS solutions is in the range of 30 to 100 metres. The GPS solution in Run #4 has only a few

data gaps of several seconds in the part of the trajectory with severe satellite blockage. Figure 7-26 demonstrates the position output for Run #4 using the C³NAV^{G2}™ solution. A few outliers up to 500 to 2000 metres were observed in the C³NAV^{G2}™ positions. The possible error sources are false acquisition of correlation peaks as well as tracking of echo-only signals.

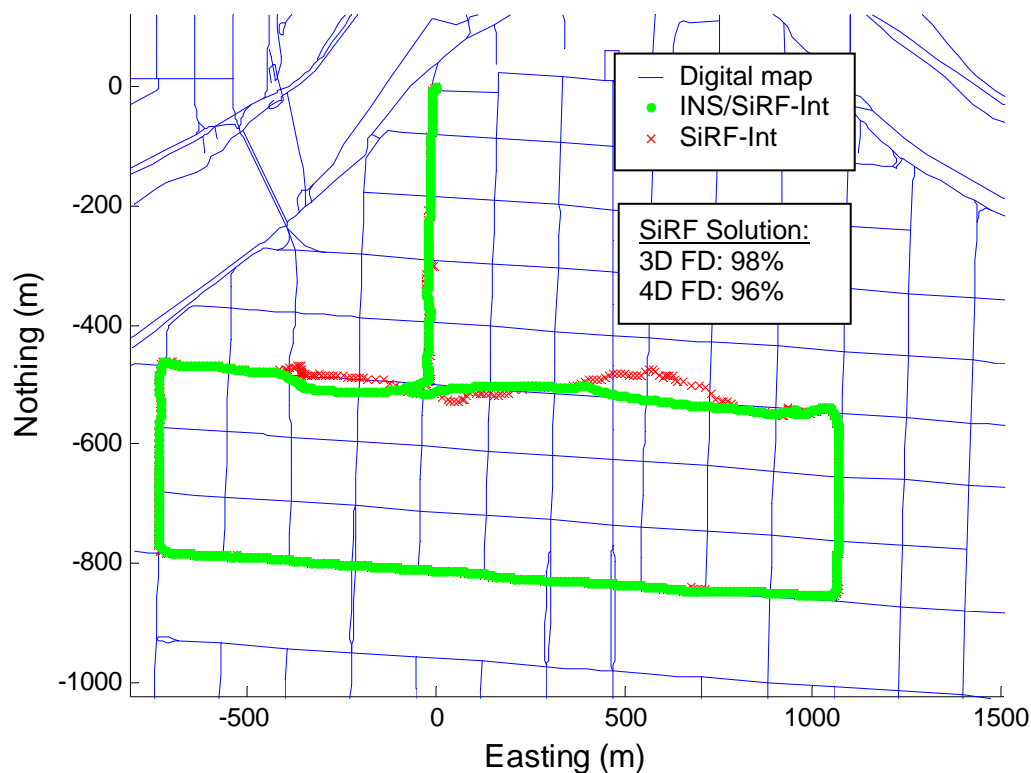


Figure 7-24: Position Output of Integrated System Using The SiRF Internal Solution, Run #4 on Trajectory # 2

Figure 7-27 depicts the PDOP and the number of satellites used in the solution. As seen from the plots, the GPS receiver tracks six satellites throughout the run, except in the portion characterized by challenging GPS conditions, that is also reflected in FD values

(3D FD: 98% and 4D FD: 97%). The PDOP values are also degraded on this part of the trajectory.

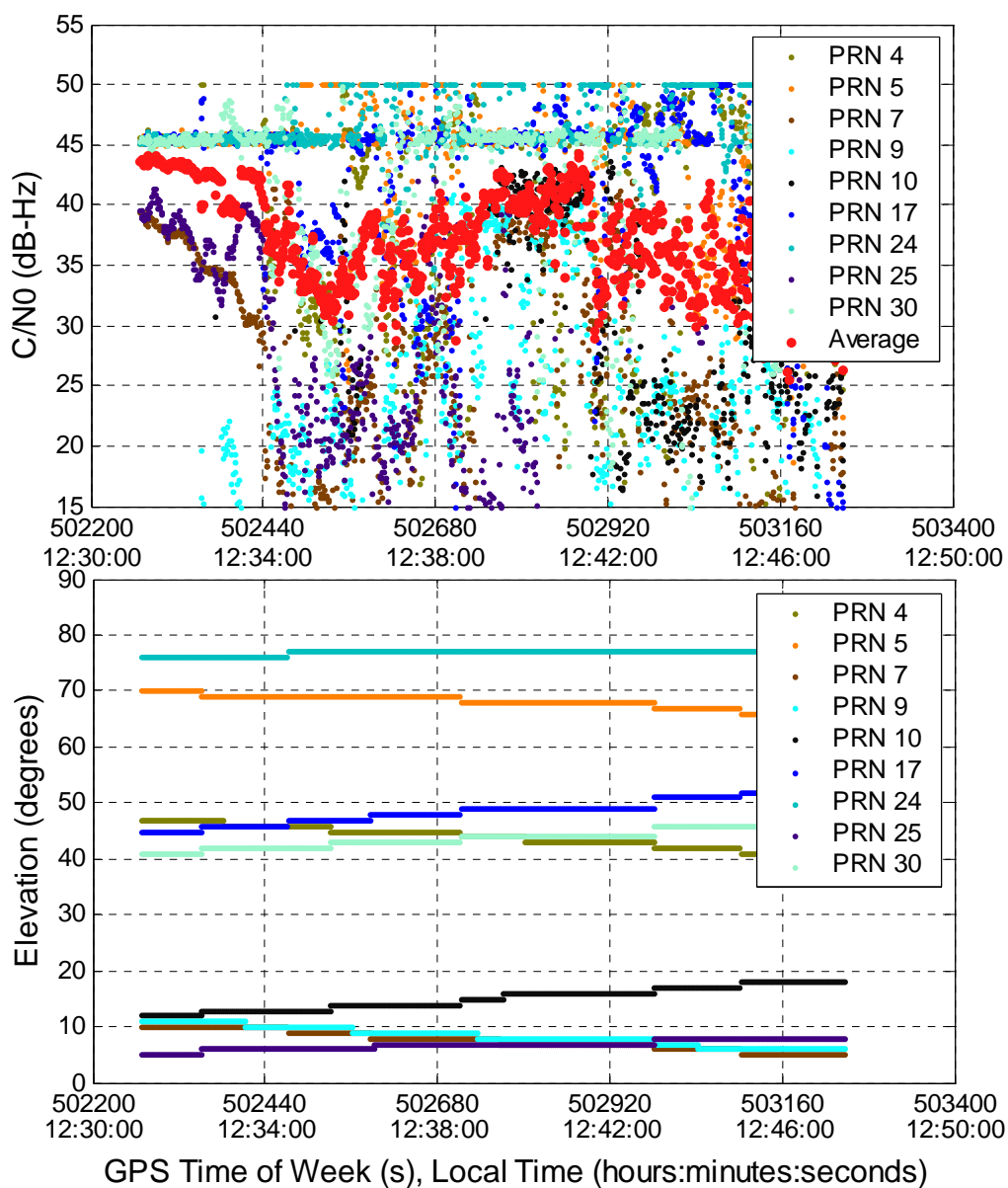


Figure 7-25: C/N₀ and Elevation Angles for All Satellites Tracked, Run #4

The integrated system using C³NAV²™ data recovers the results significantly, so that a level of position accuracy comparable to the integrated internal solution is achieved. The

across-track error for the above two cases is shown in Figure 7-28. The RMS of across-track error for the stand-alone GPS solution is 106 metres, while the integrated solution gives only 9 metres of RMS error.

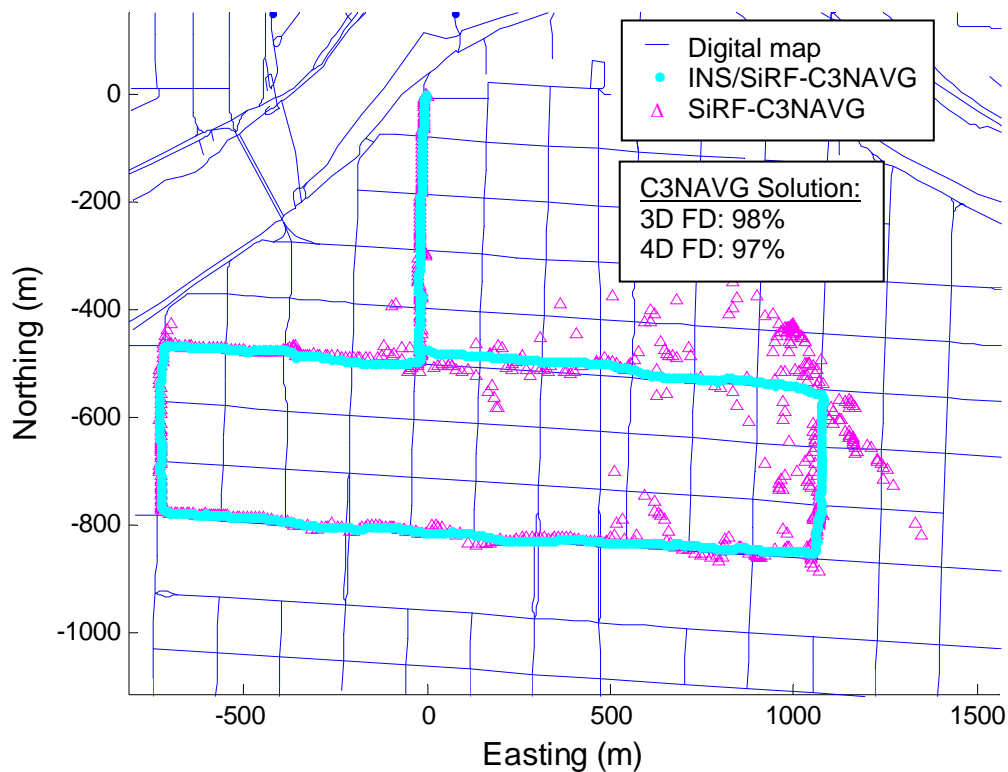


Figure 7-26: Position Output of Integrated System Using The C³NAVG²™ Solution, Run #4 on Trajectory #2

Another three runs were conducted on Trajectory #1. The INS integrated with the GPS internal solution provides test results similar to those considered above. The across-track error of the stand-alone GPS internal solution ranges from 50 to 150 metres, while the integrated system improves the accuracy to between 10 and 40 metres.

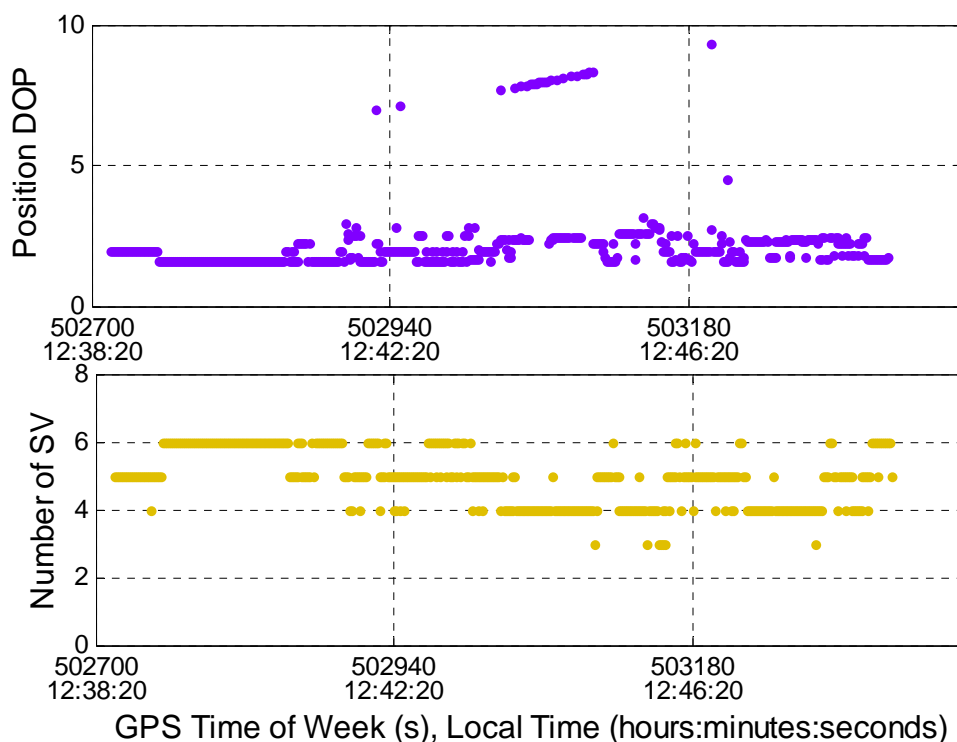


Figure 7-27: PDOP and Number of Satellites Used in Solution for Run #4, Based on The C³NAV²™ Output

For Run #5, the C³NAV²™ solution has frequent data gaps ranging from 40 to 120 seconds. At the beginning of the test, a continuous GPS solution is not available. Without GPS heading updates, the large azimuth error of 8 to 12° could not be corrected and the resulting integrated solution does not improve system performance. The minimum time required for azimuth error convergence is between 100 and 200 seconds, while a consistent GPS solution is available for 20 to 40 seconds. For Run #6 and Run #7, the INS aided by the C³NAV²™ solution produces positions with an accuracy of 20 to 60 metres.

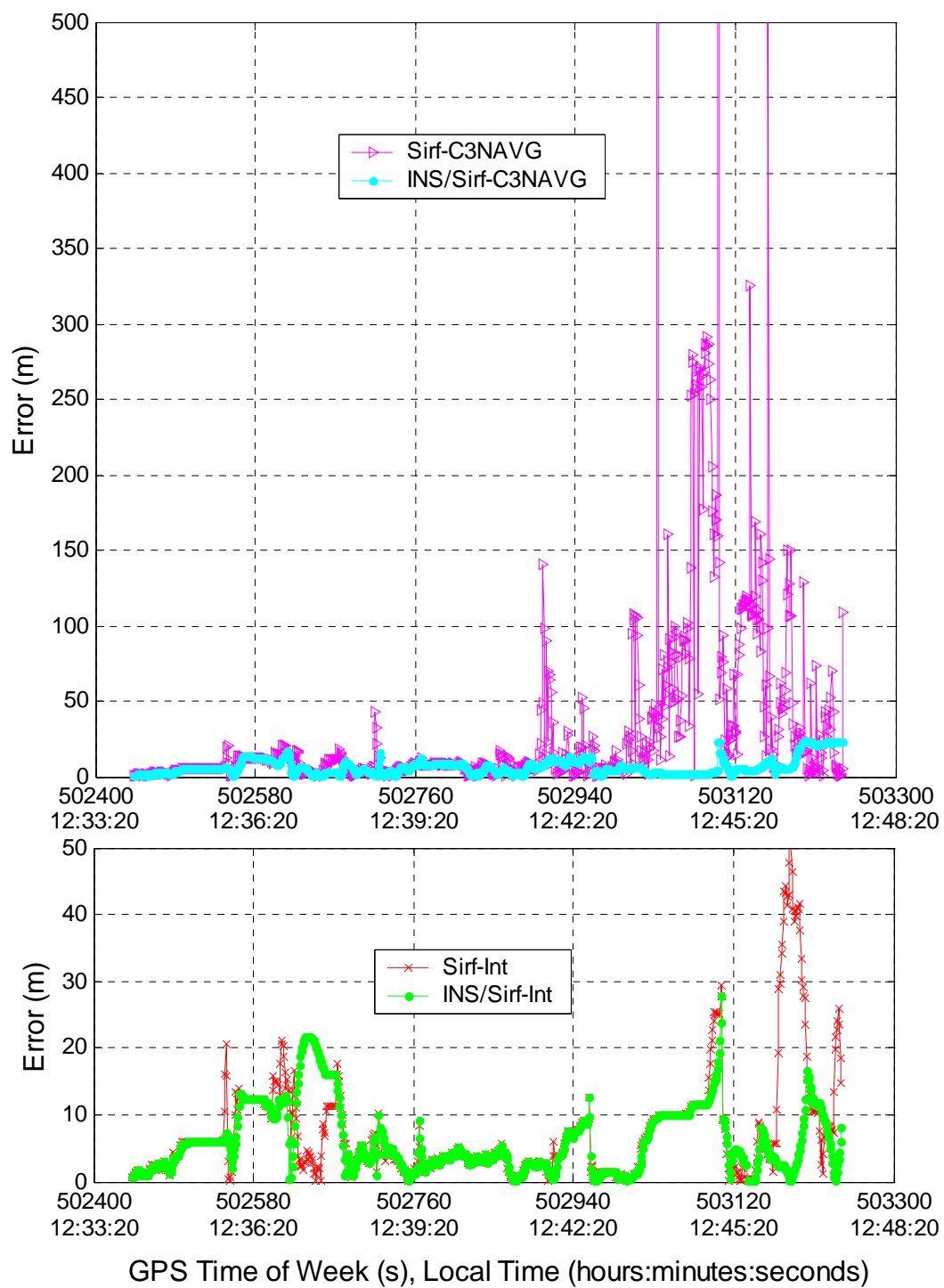


Figure 7-28: Across-track Error for Run #4 on Trajectory 2

The statistics of the across-track errors for all runs are shown in Table 7-2. Table 7-3 presents the percentage of the test time, for velocity and position filters operating in prediction mode. The longest gaps in GPS measurements for all runs, which are defined by the filter prediction intervals, are given in Table 7-4.

Table 7-2: Across-track Error

Across-track error	RMS (m)	Mean (m)	Max (m)
<i>Run #1 on trajectory 1</i>			
C ³ NAV ² TM Solution	68	48	487
INS/GPS – C ³ NAV ² TM Solution	23	18	50
SiRF Internal Solution	14	9	42
INS/GPS - SiRF Internal Solution	12	7	36
<i>Run #2 on trajectory 1</i>			
C ³ NAV ² TM Solution	113	55	1002
INS/GPS – C ³ NAV ² TM Solution	24	19	54
SiRF Internal Solution	61	38	336
INS/GPS - SiRF Internal Solution	18	14	48
<i>Run #3 on trajectory 1</i>			
C ³ NAV ² TM Solution	90	56	490
INS/GPS – C ³ NAV ² TM Solution	38	25	167
SiRF Internal Solution	58	27	520
INS/GPS - SiRF Internal Solution	31	22	72
<i>Run #4 on trajectory 2</i>			
C ³ NAV ² TM Solution	106	34	2110
INS/GPS – C ³ NAV ² TM Solution	9	7	24
SiRF Internal Solution	11	8	54
INS/GPS - SiRF Internal Solution	7	6	27
<i>Average for 7 runs</i>			
C ³ NAV ² TM Solution	86	47	908
INS/GPS – C ³ NAV ² TM Solution	23	17	80
SiRF Internal Solution	37	21	221
INS/GPS - SiRF Internal Solution	21	15	50

Table 7-3: Filter Mode: Percentage of Test Time in Prediction

Filter Mode	INS/SiRF Internal Solution	INS/C³NAVIG²™ Solution
<i>Run #1 on Trajectory 1</i>		
Velocity filters in prediction	4%	41%
Coordinate filters in prediction	19%	54%
<i>Run #2 on Trajectory 1</i>		
Velocity filters in prediction	23%	19%
Coordinate filters in prediction	50%	38%
<i>Run #3 on Trajectory 1</i>		
Velocity filters in prediction	21%	21%
Coordinate filters in prediction	36%	22%
<i>Run #4 on Trajectory 2</i>		
Velocity filters in prediction	8%	10%
Coordinate filters in prediction	24%	37%
<i>Average for 7 runs in downtown</i>		
Velocity filters in prediction	17%	26%
Coordinate filters in prediction	33%	40%

Table 7-4: Longest Gap in GPS Measurements

Longest Gap	SiRF Internal Solution	C³NAVIG²™ Solution
<i>Run #1 on Trajectory 1</i>		
Velocity	4 seconds	34 seconds
Position	15 seconds	40 seconds
<i>Run #2 on Trajectory 1</i>		
Velocity	33 seconds	30 seconds
Position	78 seconds	41 seconds
<i>Run #3 on Trajectory 1</i>		
Velocity	100 seconds	108 seconds
Position	153 seconds	162 seconds
<i>Run #4 on Trajectory 2</i>		
Velocity	14 seconds	14 seconds
Position	57 seconds	57 seconds
<i>Average for 7 runs in downtown</i>		
Velocity	34 seconds	46 seconds
Position	71 seconds	83 seconds

7.3.1 Conclusions

The stand-alone GPS internal solution is characterized by smooth behaviour of position errors, which usually do not exceed 50 metres. The receiver firmware provides continuous position output over the entire run. When the GPS receiver loses lock due to signal masking, positions and velocities are propagated through the duration of an outage. As indicated by the integrated algorithm, long prediction intervals ranging from 30 seconds to 1-3 minutes degrade the accuracy significantly. Position error is observed to increase over the duration of a data gap; on the parts of trajectory containing turns, without heading information, it reaches a level of 300 to 500 metres.

The integrated system, which uses the GPS internal solution, significantly improves the results. Due to reliable GPS updates at the outset of the test, azimuth error is corrected to a level of 1° to 2° ; because of this early correction, even during long prediction intervals of 1 to 2 minutes and more, the integrated system is capable of providing a relatively high positional accuracy of 10 to 50 metres. In filtering mode (i.e. when consistent GPS updates are available) the position errors of the integrated system do not exceed 10 to 20 metres. In downtown canyons, the measurement availability of HS receivers is very high: 4D fix density ranges from 76% to 96% of the total test duration. The velocity and coordinate filters in the estimation algorithm work in prediction mode on average for 17% and 33% of the test time, respectively. This is an indirect indication of the quality of GPS measurements in the time domain. It should be mentioned that coordinate filters switch to prediction mode more frequently than velocity filters. This is due to prediction

mode criteria that oblige the coordinate filters to switch to prediction mode, when the test vehicle is stationary.

In downtown areas, the Least Squares epoch-by-epoch $C^3\text{NAV}G^{2\text{TM}}$ solution is generally poor. It provides positional accuracy of 50 to 100 metres on average with occasional outliers of 500 to 2000 metres. Possible sources of these large errors include signal cross-correlation along with tracking of multipath and echo-only signals caused by strong glassy reflections. It must be pointed out that the stand-alone GPS solution can be improved by implementation of statistical reliability techniques (i.e. Statistical Reliability Testing RAIM); see, for example, descriptions of sequential RAIM implementation using global and local testing (Baarda, 1968; Kuang, 1996; Teunissen et al., 1998), which allow the detection of erroneous measurements and their exclusion from the navigation solution. The $C^3\text{NAV}G^{2\text{TM}}$ solution is defined by noisy error behaviour of high frequency with regular data gaps of 10 to 40 seconds in duration. The measurement availability varies from 49% to 97% 4D FD.

The integration of the $C^3\text{NAV}G^{2\text{TM}}$ solution with inertial data provides a considerable improvement in positional accuracy. The coordinate Kalman filter with adaptive measurement covariance adjusts its parameters properly due to certain behaviour of GPS positions, which was discussed earlier. When the GPS solution is unreliable, the Kalman gain drops down and the estimation algorithm relies upon the system model. The reliability criteria for GPS measurements also work suitably in this case. The filters of the integrated system generally work in prediction mode more often than in the case of

integration with the GPS internal solution. On average, the velocity filters work in prediction mode for 26% of the test time, while coordinate filters operate in prediction mode for 40% of the test time. The positional accuracy of the integration system ranges from 10 to 50 metres on average with irregular outliers of 80 to 150 metres during long GPS data gaps of a few minutes.

7.4 Residential Area Results

Two tests were conducted in a suburban area of Calgary. The reference trajectory was obtained from the GPS double difference carrier phase solution using FLYKIN+TM software, developed by the PLAN group of the University of Calgary (FLYKIN^{TM+}, Liu et al., 2003). The Engineering Building in the University campus was utilized as a reference station; the baseline varied from 100 metres to 8 kilometres during the tests. In the parts of the trajectory with a significant density of roadside trees and buildings, some satellites at lower elevations were periodically blocked and back in view for a few seconds at a time (the elevation cut-off was set to 15°). Because of this, the limited time prevented convergence of the ambiguities to integer values; consequently, the reference trajectory was obtained in the float ambiguity resolution mode. Although the accuracy of the float solution can vary from 0.1 to 1 metres (Lachapelle, 2003), sub-metre level of positional accuracy is considered as sufficient for purposes herein. Because the SiRF internal solution was not tested for suburban applications, only the GPS C³NAVIG^{2TM} positions and velocities were utilized in the integration algorithm.

In suburban environments, signal masking and multipath sources generally occur only at low elevations due to roadside trees and bushes and one- to two-storey buildings. Consequently, these effects can be significantly reduced by an increase in elevation cut-off. It is well illustrated by Figure 7-29, which presents the C/N_0 and elevation angles for all SVs tracked during Run #1 in the residential area. Unlike the downtown area situation, low power signals with large variations in C/N_0 are observed only for satellites at low elevations (for example: PRN 7 with elevation $\sim 10^\circ$; PRN 9 with elevation $\sim 11^\circ$; and PRN 25 with elevation $\sim 7^\circ$). The average C/N_0 of 40 dB-Hz is also higher than for the urban tests and it is closer to the typical for open-sky conditions C/N_0 value of 44 dB-Hz (Ward,1996a; MacGougan, 2003).

The position output of the integrated system for Run #1 is shown in Figure 7-30. The integrated solution is generally constrained to the GPS differential pseudorange solution. The GPS accuracy in residential areas is worse by comparison to open-sky conditions due to degraded geometry caused by a higher elevation mask of 15° , as well as possible tracking of multipath signals at high elevations. The position accuracy of the stand-alone GPS solution ranges from 1 to 20 metres.

As a result of high elevation cut-off, the average number of satellites used in the solution is lower than in open areas, varying from four to six; however, this still provides reasonably good PDOP values that do not exceed two for the majority of test duration, as illustrated in Figure 7-31.

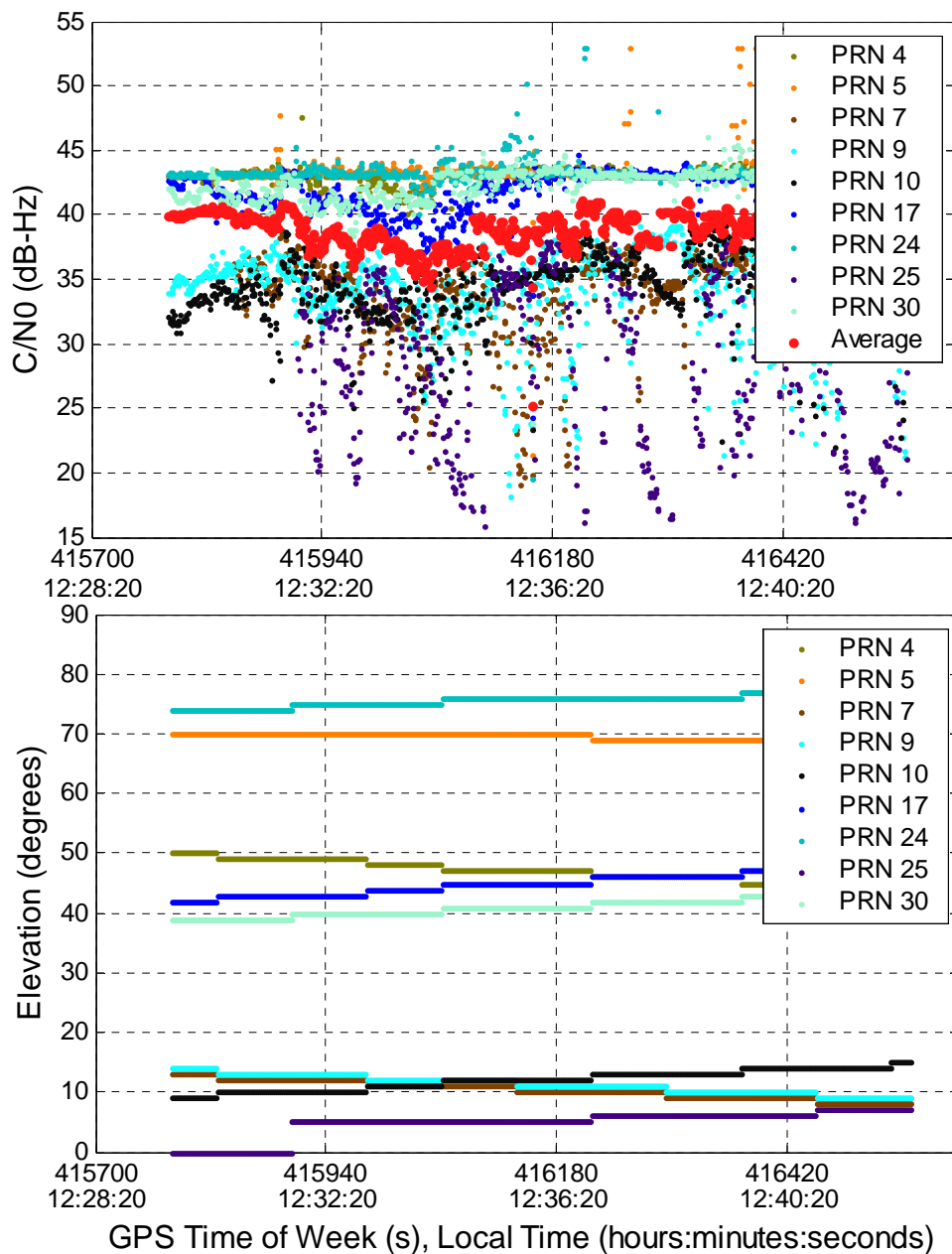


Figure 7-29: C/N₀ and Elevation Angles for All Satellites Tracked, Run #1 in Residential Area

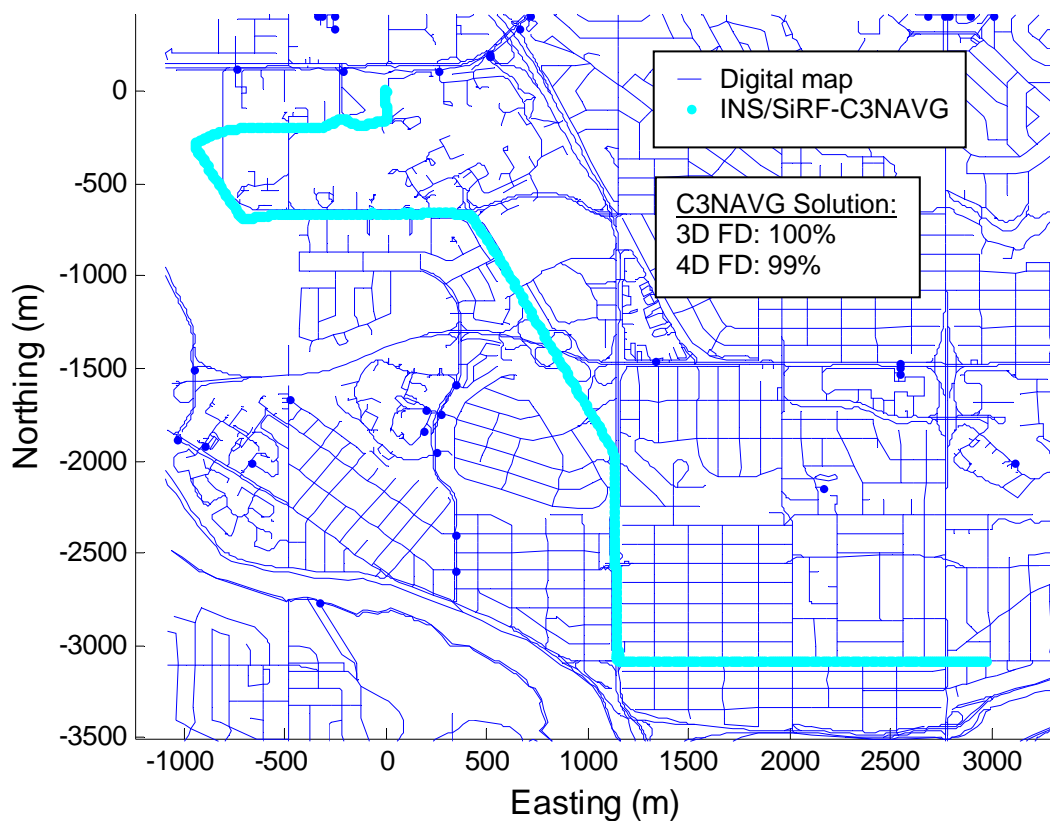


Figure 7-30: Position of Integrated System for Run #1 in Residential Area

These plots show the number of satellites used in the solution and the PDOP values for Run #1. No data gaps were observed in the GPS solution except a gap of one second. The measurement availability is also very good: 100% (3D FD) and 99% (4D FD) of overall test time.

Due to constant GPS updates, the integrated system provides relatively high positional accuracy: the RMS of positional error is in the order of 3 to 4 metres. The statistical parameters of the position errors for both tests are presented in Table 7-5. Because the results obtained are similar to the open area tests, velocity and attitude accuracy analyses are not considered herein.

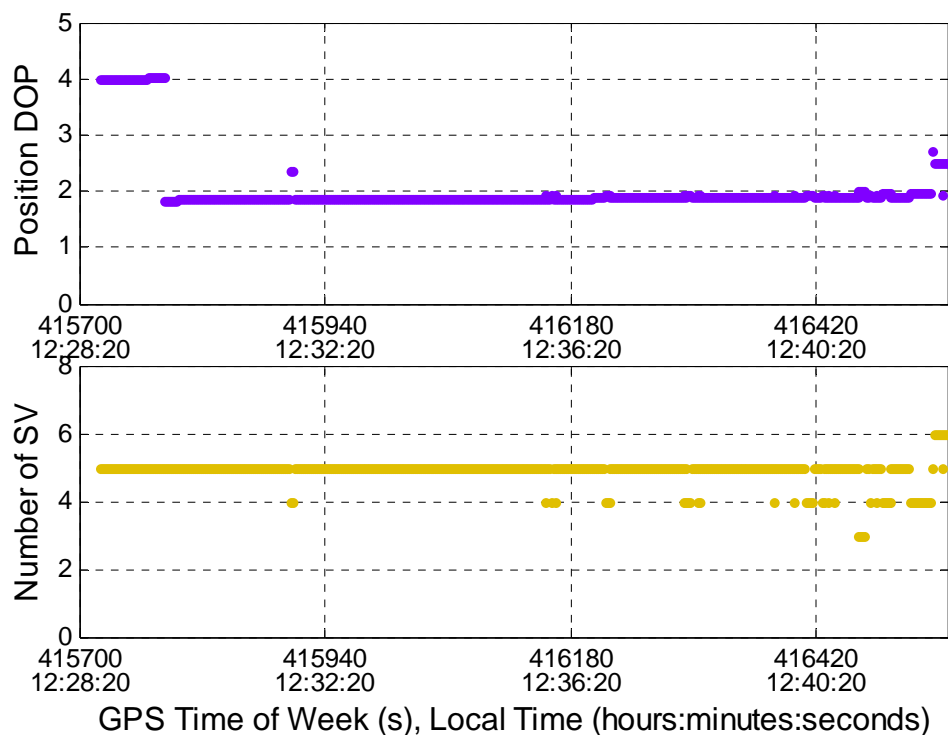


Figure 7-31: PDOP and Number of Satellites Used in Solution, Run #1 in Residential Area

As seen in Table 7-6, due to continuous GPS updates, the filters in the estimation algorithm work in prediction mode quite rarely (0.2% to 2% of test duration). The prediction intervals for the velocity filters occur mostly at the beginning of the tests, during the transition process of the INS azimuth error estimation; meanwhile, the time required for coordinate filter prediction is defined by parts of the tests in static mode. The positioning accuracy of the system is slightly improved due to smoothing of GPS code errors of high frequency (mostly code noise).

Table 7-5: Statistics of Position Errors of Integrated System for Two Runs

Position Error for two runs	RMS (m)	Mean (m)	Max (m)
Northing	3.8	1.9	9.7
Easting	3.1	1.2	8.1

Table 7-6: Filter Mode: Percentage of Test Time in Prediction

Filtering mode	Average for two runs
Velocity filters in prediction	0.2 %
Coordinate filters in prediction	2 %

Chapter 8

Conclusions and Recommendations

This chapter contains a summary of the research presented in this thesis, the conclusions drawn from the test results and analysis, and recommendations for future work in INS/GPS integration.

8.1 Summary

The contribution of this research work is in the development of an algorithm for the integration of a medium-accuracy INS with two types of GPS receivers: conventional and high sensitivity, and the assessment of system performance in various GPS environments, namely in open, residential and urban areas. The system tested used a conventional NovAtel OEM4 GPS receiver, a high sensitivity SiRF Star II Xtrac GPS receiver and a Honeywell HG1700 AG11 IMU. Due to its flexibility and universality for a range of GPS receivers, a cascaded scheme of integration was implemented in the integrated system.

In an effort to optimize the performance of the integrated system under different GPS conditions (reception of satellite signals in open sky districts and challenging environments), two diverse estimation algorithms were developed. A Kalman filter is employed in both strategies. The INS error equations comprise the system model; the measurements, which are fed into the filters, are the differences between INS and GPS positions and velocities.

For open area applications, the estimation scheme utilizes a conventional Kalman filter with a nine-state system model. The INS filter output incorporates the following aspects: position and velocity errors, attitude misalignment errors and gyro drifts. Estimated INS position and velocity errors are compensated in the system output. INS horizontal errors are used to correct the elements of the transformation matrix between the body and navigation frames. The INS azimuth misalignment is compensated independently in the SINS algorithm as a one-step control signal introduced into the quaternion of a small rotation. Estimated gyro drifts are also taken into account in the SINS navigation scheme, in a manner similar to azimuth compensation. Due to the non-stationary property of the INS azimuth misalignment, reliance on traditional estimation approaches for an accurate estimation of this error can be problematic; therefore, a special cascaded procedure was implemented to obtain an accurate estimate of this INS error component. The method takes into consideration the degree of observability associated with the azimuth error. An observability analysis of the INS error equations shows that azimuth misalignment becomes observable during periods of high vehicle dynamics. The filter uses this feature, so that estimation of azimuth misalignment is initialized when a test vehicle experiences large changes in acceleration. In this manner, this INS error component is directly measured, which produces a shortening of the transition period of estimation as well as an overall improvement in estimation accuracy. The compensation of INS azimuth error is performed into two stages, in terms of coarse and fine corrections respectively. To reduce azimuth misalignment after the initial INS alignment, a one-step azimuth

correction is executed using the GPS-derived heading. The residual error is then compensated using the estimate obtained from the Kalman filter.

For applications in dense urban environments containing high-rise buildings, the estimation algorithm is based on the implementation of multiple Kalman filters. The estimation of INS velocity and positional errors, as well as INS azimuth misalignment, are performed separately for the north and east channels in independent Kalman filters with diverse system models. For purposes of velocity error estimation, the system model is defined by simplified INS error equations that describe the Schuler component of the INS errors and include: velocity errors, horizontal misalignment and gyro drifts. Because the velocity filters take vehicle dynamics into account, different gain levels are associated with stationary and in-motion measurements, respectively. As a consequence, the filters work in three modes: 1) filtering with a relatively large Kalman gain matrix for static mode; 2) filtering with a small Kalman gain for kinematic mode; and 3) prediction when GPS measurements are either unreliable or unavailable. The Kalman gain is defined by different covariances of measurement noise. For position error estimation, the system model is a simple dynamic model where velocity is equivalent to white noise. The estimation algorithm herein employs the Kalman filter with adaptive measurement covariance, which is motivated by the high frequency behavior of GPS positional errors. Integrated INS velocities, which are already compensated for the Schuler part of the INS velocity error, are fed into the coordinate filters instead of pure INS positions. In this manner, the size and complexity of the INS position error expansion are reduced. The filters work in two modes: 1) filtering when the GPS solution is accessible; and 2)

prediction during GPS data gaps. The estimation of azimuth misalignment is executed in the autonomous Kalman filter with seven states in the system model; in addition, this error is compensated in the SINS algorithm in a manner similar to the estimation scheme for open area applications. The filter works in prediction mode during GPS outages. The reliability criteria for all filters in the estimation algorithm are defined by the GPS PDOP, the number of satellites used in the GPS solution and the difference between GPS and INS-predicted velocities.

The main difference in the integration strategies for system operation in line-of-sight conditions and harsh GPS environments lies in the distinct feed-back components of the estimated INS errors into the navigation algorithm. In downtown applications, only the estimate of the INS azimuth misalignment is taken into consideration since the estimation accuracy in general is limited owing to error-corrupted GPS measurements. In open areas, the estimated horizontal attitude errors and gyro drifts also are compensated within the SINS scheme.

The following sections highlight the major conclusions found in the course of this research and recommendations for further work toward improvements in system performance.

8.2 Conclusions

The primary objective of this thesis was to develop and test the cascaded scheme of integration and different estimation algorithms for improvement of overall performance

of a medium accuracy IMU integrated with conventional and high sensitivity GPS receivers for application in open areas and downtown canyons respectively. This goal has been met. A SINS mechanization algorithm was designed through the research; the GPS navigation solution was obtained from the existing GPS software C³NAV²™ and the GPS receiver firmware (internal solution). The integrated system was tested in various GPS conditions including open-sky areas, residential districts and urban environments. For open area applications, GPS data gaps were simulated to validate system performance for prediction accuracies. Below, details of the major conclusions of this thesis are summarized in terms of the objectives set out in Chapter 1.

8.2.1 Open Area Applications

1. Test results confirmed the importance of accurate estimation of INS azimuth misalignment. The cascaded Kalman filter decreases the transition period of the azimuth error estimation as well as it improves the estimation accuracy of INS azimuth error in general. A conventional Kalman filter requires at least 300 to 350 seconds for convergence of the azimuth error estimate, while the cascaded scheme reduces this period to between 150 and 200 seconds. The combined azimuth correction using GPS heading and the filter's azimuth misalignment estimate provides better results in comparison to the traditional approach, so that the residual azimuth error ranges from 0.2° to 0.5°.

2. As expected, attitude error compensation in the SINS algorithm improves the overall attitude accuracy of the integrated system, so that roll and pitch are estimated to be accurate to within 0.05° to 0.1° .
3. Due to gyro drift compensation in the SINS algorithm, the large Schuler component of INS velocity error is reduced significantly which, in turn, contributes to the improvement of the overall estimation accuracy of INS errors.
4. The analysis of the results using GPS data with simulated gaps demonstrates that, in prediction mode, accurate estimation of the INS azimuth error becomes essential, especially for long-term GPS outages of 30 to 60 seconds with high vehicle dynamics. Crucial prediction accuracy degradation of 60 to 120 m in position and 3 to 6 m/s in velocity, on average, is observed, if the reduced INS error model is used in the estimation scheme. The conventional Kalman filter with extended system model provides superior positional accuracy of approximately 10 to 30 m and velocity accuracy of 0.5 to 2 m/s for GPS outages of the same duration. The cascaded Kalman filter considered in this thesis improves the above results to 5 to 15 m in position and 0.2 to 0.6 m/s in velocity domains.

8.2.2 Urban and Suburban Area Applications

For this testing, reference information was available in the position domain only, therefore limiting the analysis of positional accuracy in this research. Results in downtown areas illustrated the following aspects:

1. The positional errors of the stand-alone GPS internal solution ranges from 10 to 50 m with occasional outliers of 100 to 500 m. The possible cause of these large errors lies in long-term data outages caused by signal masking effects. Receiver firmware propagates positions through the duration of a gap, resulting in significant error expansion particularly on the parts of the test trajectory containing turns, when absence of heading information becomes critical.
2. The integrated system, which uses the GPS internal solution, significantly improves the results of the stand-alone GPS solution (during long GPS gaps of 30-120 seconds, the integrated system positional accuracy is two to three times better than the stand-alone GPS solution). However, the system accuracy is limited owing to error-corrupted GPS updates and data outages.
 - The small dimensions of the velocity Kalman filters in the estimation scheme result in relatively short transition periods for INS error estimation, producing an INS/GPS integrated solution at the outset of the tests.
 - The unique behaviour of the Schuler component of INS error, which is easy to model and predict, allows its accurate estimation; residual non-stationary errors are relatively small as opposed to stationary ones.
 - The relatively accurate estimation of the azimuth misalignment to 1° to 2° using a Kalman filter with the extended system model is possible due to continuous GPS updates at the beginning of the test; this provides ample time for filter convergence.
 - Due to the smooth behaviour of GPS measurements, the reliability criteria for the filter's operation do not always produce an optimal performance.

- As a consequence to all of the above, a slight improvement of positional accuracy is observed in the filtering mode. Meanwhile, dramatic accuracy enhancement is achieved in prediction mode; i.e. during long-term GPS data gaps. The positional errors of the integrated system range from 10 to 50 m on average.
3. The stand-alone GPS C³NAV²™ solution provides a positional accuracy of 50 to 100 metres on average with occasional outliers of 500 to 2000 metres. Possible sources of these blunders include signal cross-correlation along with tracking of multipath and echo-only signals caused by strong glassy reflections. The C³NAV²™ epoch-by-epoch Least Squares solution can be improved with the implementation of RAIM techniques (Baarda, 1968; Kuang, 1996; Teunissen et al., 1998), which can be used to detect erroneous measurements and, further, to exclude them from the navigation solution. This can improve the results considerably; however, the use of statistical reliability methods is limited by masking effects (since redundant measurements are not always available, and in some cases error corrupted measurements must be used to obtain the navigation solution). The C³NAV²™ solution is defined by regular data gaps of 10 to 40 seconds in duration and by noisy error behaviour of high frequency, stipulated by the epoch-by-epoch least-squares solution.
 4. The INS integrated with the GPS C³NAV²™ solution provides a considerable improvement in positional accuracy (the achieved positional accuracy of the INS/GPS system is on average two to five times better than the stand-alone GPS solution):
 - The coordinate Kalman filter with adaptive measurement covariance adjusts its parameters properly due to certain noisy behaviour characteristics of GPS position

solutions. When the GPS solution is unreliable, the measurement covariance increases, the Kalman gain declines, and the filter relies upon the system model. The reliability criteria for GPS measurements also work properly and the filters in the estimation scheme switch to prediction mode more often than in the case of integration with the GPS internal solution.

- In some runs, regular GPS data gaps occurring at the beginning of the test produce a significant residual azimuth error; this is because the extended Kalman filter is not supplied with the continuous measurement updates that ordinarily facilitate filter convergence. As a consequence, the integrated solution does not significantly improve system accuracy.

The positional accuracy of the integration system ranges from 10 to 50 metres on average with irregular outliers of 80 to 150 metres during long GPS data gaps in the order of a few minutes.

Tests in residential districts produced the following results:

The integrated solution is generally constrained to the GPS differential pseudorange solution. GPS accuracy in residential areas is worse in comparison to open-sky districts owing to degraded geometry caused by a higher elevation mask as well as possible tracking of high elevation multipath signals. Continuous GPS measurements throughout the testing allowed the integrated system to provide relatively high positional accuracy (where RMS of positional error is about 4 metres) as opposed to downtown results. However, the system accuracy is constrained by the uncompensated INS errors, which

are not taken into consideration in the estimation algorithm (namely, the simplified system model and the associated error compensation method).

8.3 Recommendations

The development of an integration scheme for optimal performance in diverse operational environments is problematic. The suggested strategy involves implementing distinct estimation strategies for applications in open-sky areas or harsh GPS conditions. Based on the results and conclusions of this research, the following recommendations for districts with line-of-sight GPS signal reception are proposed:

1. The long-term accuracy of the integrated system can be improved through the use of a more accurate INS error model that contains high-order INS error terms such as gyro and accelerometer installation errors, gyro biases and scale factors as well as accelerometer biases.
2. For high dynamics applications, the non-stationary component of INS error that, in addition to azimuth misalignment, also contains accelerometer scale factors and their non-linearities, can be calibrated *a priori* using ZUPTs; see, for example, [Salychev \(2003\)](#).
3. To achieve improved estimation accuracy of the INS error, velocity damping can be employed. By incorporating velocity error compensation in the SINS algorithm, the magnitude of the total INS velocity error can be reduced significantly which, in turn, affects the estimation accuracy. However, one must consider the possible challenge

- arising from an increase of the natural oscillation frequency of the INS error that surpasses the Schuler frequency (*ibid*).
4. For post-mission analysis, smoothing techniques such as a Kalman filter smoother can be implemented to improve estimation accuracy (*ibid*).
 5. Generally, system accuracy in position and velocity domains is constrained to the GPS solution. A carrier phase GPS solution can be used in the integrated system to achieve centimeter-level positional accuracy. To additionally improve system performance in terms of accuracy and integrity, a tightly-coupled scheme of integration can be implemented. *Petovello (2003)* showed that the tightly-coupled strategy provides generally better results in terms of overall system accuracy during partial or complete GPS outages. INS seeding also simplifiers (i.e. speeds up) ambiguity resolution, thereby providing improvements of 50-70% in comparison to operation in GPS stand-alone mode.

For system operation in urban areas, the following improvements can be considered:

1. The positional accuracy of an INS/GPS integrated system can be improved with the implementation of map-matching techniques such as algorithms based on a geometrical approach combined with vehicle dynamics constrains (*Basnayake and Lachapelle, 2003*) or fuzzy logic (*Syed Qutub and Cannon, 2004*).
2. The stand-alone C³NAVTM solution can be improved by implementation of statistical reliability techniques, which allow detection and further exclusion of erroneous GPS measurements (*Baarda, 1968; Kuang, 1996; Teunissen et al., 1998*). This will improve the overall accuracy of the INS/C³NAV^{2TM} system. However, the

- operational capabilities of such methods are limited due to the challenge of detection of multiple blunders and the lack of redundant observations in general.
3. To improve positional accuracy during long-term GPS gaps, non-holonomic velocity constraints can be used (Shin, 2001).
 4. The testing of a tightly-coupled integration scheme is needed since this integration strategy bolsters system availability; however, fault detection is assumed to be more problematic than for a loosely-coupled integration scheme. To overcome this problem, noise on the pseudorange and Doppler measurements can be characterized in relation to C/N_0 (Wieser and Brunner, 2000).
 5. Only the accuracy analysis in the position domain has been considered in this thesis. Therefore, an investigation of velocity and attitude accuracy of the system using reference from a high accuracy INS is warranted.
 6. The use of HS GPS data was tested in this research; a more comprehensive approach to analysis might also include a comparison with the performance of a conventional GPS receiver (such as the NovAtel OEM4).

References

- Asaoka, N., M. Ooiwa, M. Tanikawara, T. Numajima, Y. Kubo and S. Sugimoto (2003) "*Nonlinear Filtering Methods for INS/DGPS In-Motion Alignment*", Conference proceedings ION GPS 2003, 9-12 September 2003, Portland, OR, pp. 945-956.
- Baarda W. (1968) "*A Testing Procedure for Use in Geodetic Networks*", Netherlands Geodetic Commission, Publication on Geodesy, New Series 2, 5, Delft, Netherlands, 1968, p.97
- Basnayake, C. and G. Lachapelle (2003) "*Accuracy and Reliability Improvement to Standalone High Sensitivity GPS Using Map Matching Techniques*", Conference proceedings, ION AM 2003, 23-25 June 2003, Albuquerque, NM, pp. 209-216.
- Basnayake, C. (2004) "*Automated Traffic Incident Detection Using GPS Based Transit Probe Vehicles*", Ph.D. thesis, UCGE Report # 20196, The Department of Geomatics Engineering, University of Calgary.
- Braasch, M. S. (1995) "*Isolation of GPS Multipath and Receiver tracking Errors*", NAVIGATION: Journal of The Institute of Navigation, 41(4), 415-434.
- Braasch, M. S. (1996) "*Global Positioning System: Theory and Applications*", Volume I, Chapter 14 "Multipath Effects", American Institute of Aeronautics and Astronautics, Inc., Washington D.C., USA, 560 pp.
- Brown, R. G. and Y. C. Hwang (1992) "*Introduction To Random Signals and Applied Kalman Filtering*", John Wiley & Sons Inc., second edition.
- Cannon, M. E. and G. Lachapelle (1992) "*Analysis of a High Performance C/A Code GPS Receiver in Kinematic Mode*", Navigation, Vol. 39, No. 3, The Institute of Navigation, Alexandria, VA, pp. 285-299.
- Cannon, M. E., G. Lachapelle and H. Sun (1999) "*Development and testing of an integrated INS/GPS cross-linked system for sub-meter positioning of a CF-188 jet fighter*", Conference proceedings ION AM 1999, 28-30 June 1999, Cambridge, MA, pp. 463-474.
- Cannon, M. E. (1991) "*Airborne GPS/INS with an Application to Aerotriangulation*", PhD Thesis, UCGE Report #20040, The Department of Geomatics Engineering, University of Calgary.

- Cannon, M. E. (2001) “*Satellite Positioning*”, ENGO 561 Course Lecture notes, The Department of Geomatics Engineering, University of Calgary.
- Chansarkar, M. and L. J. Garin (2000) “*Acquisition of GPS Signals at Very Low Signal to Noise Ratio*”, Conference proceedings ION NTM 2000, 26-28 January 2000, Anaheim, California, pp. 731–737.
- Chiang, K. W. and N. El-Sheimy (2002) “*INS/GPS Integration Using Neural Networks for Land Vehicle Navigation Applications*”, Conference proceedings, ION GPS 2002, 24-27 September 2002, Portland, OR, pp. 535-544.
- Deshpande, S. and M. E. Cannon (2004) “*Interference effects on the GPS signal Acquisition*”, Conference Proceedings, ION NTM 2004, 26-28 January, 2004, San Diego, CA, pp. 1026-1036.
- El-Sheimy, N. (2003) “*Inertial Techniques and INS/DGPS Integration*”, ENGO 623 Lecture notes, The Department of Geomatics Engineering, University of Calgary.
- Engel, P. K. (1996) “*Global Positioning System: Theory And Applications*”, Volume II, Chapter 1, “Differential GPS”, American Institute of Aeronautics and Astronautics, Inc., Washington D.C., USA, 25 pp.
- Engel, P., R. Fan, A. Tiwari, A. Chou, W. Mann, A. Sahai, J. Stone, and B. Roy (2001) “*Improving GPS Coverage and Continuity: Indoors and Downtown*”, Conference Proceedings, ION GPS 2001, 11-14 September 2001, Salt Lake, Utah, pp. 3067–3076.
- Gao, Y. and M. Sideris (2002) “*Data Analysis in Engineering*”, ENGO 563 Course Lecture Notes, The Department of Geomatics Engineering, University of Calgary.
- GCTE (2004) Georgia College of Technical Engineering, Smart Antenna Research group, available at: <http://users.ece.gatech.edu/meta/directory/index.html>
- Gelb, A. (1974) “*Applied Optimal Estimation*”, The Massachusetts Institute of Technology Press, Cambridge, Massachusetts, 374 pp.
- Grejner-Brzezinska, D. A. and J. Wang (1998) “*Gravity Modeling for High Accuracy INS/GPS integration*”, Conference proceedings ION AM 1998, Denver, Colorado, 1-3 June 1998, pp. 425-434.
- Grejner-Brzezinska, D., C. Toth and Y. Yi (2001) “*Bridging GPS Gaps in Urban Canyons: Can ZUPT Really Help?*”, Conference proceedings, ION GPS 2001, 11-14 September, Salt Lake City, UT.

- Hofmann-Wellenhof, B., H. Lichtenegger and J. Collins (1997) *“Global Positioning System: Theory and Practice”*, Fourth Revised Edition, SpringerWienNewYork, Wien 1997, pp. 67-72, 74, 89-126.
- Honeywell (1997) *“Critical Item Development Specification HG1700AG Inertial Measurement Unit”* Document DS34468-01.
- Jekeli, C. (2001) *“Inertial Navigation Systems with Geodetic Applications”*, Walter de Gruyter, New York, pp.51-53, 104-106, 306-318.
- Kalman, R. E. (1960) *“New Approach to Linear Filtering and Prediction Problems”*, Trans. ASME J. Basic Eng. 82, pp. 34-45.
- Kaplan, E. D. (1996) *“Understanding GPS Principles and Applications”*, Artech House, Inc., 685 Canton Street, Norwood, MA 0206, Chapter 1, “Introduction”, pp. 1-4.
- Kaplan, E. D., J. L. Leva and P. Ward (1996) *“Understanding GPS Principles and Applications”*, Artech House, Inc., 685 Canton Street, Norwood, MA 0206.
- Klobuchar, J. A., (1996) *“Global Positioning System: Theory and Applications”*, Volume I, Chapter 12 “Ionospheric Effects on GPS”, American Institute of Aeronautics and Astronautics, Inc., Washington D.C., USA, 504 pp.
- Krakiwsky, E. D. (1990) *“The Method of Least Squares: A Synthesis of Advances”*, ENGO 629 Course Lecture Notes, Department of Geomatics Engineering, University of Calgary.
- Kuang, S. (1996) *“Geodetic Network Analysis and Optimal Design: Concepts and Applications”*, Ann Arbor Press, Inc., 121 South Main Street, Chelsea, Michigan
- Kumagai, H., T. Kindo, Y. Kubo and S. Sugimoto (2000) *“DGPS/INS/VMS Integration for High Accuracy Land-Vehicle Positioning”*, ION GPS 2000, 19-22 September 2000, Salt Lake City, UT, pp.1845-1853.
- Lachapelle, G. (2002) *“GPS Theory and Applications”*, ENGO 625 Course Lecture notes, The Department of Geomatics Engineering, University of Calgary.
- Leick, A. (1995) *“GPS Satellite Surveying”*, John Wiley And Sons Inc., USA.
- Liu, J., M. E. Cannon, D. Chen, and G. Lachapelle (2003) *FLYKIN+™ Operating Manual*, version 1.0, PLAN research group, Department of Geomatics Engineering, The University of Calgary, May 2003.

- MacGougan, G., G. Lachapelle, R. Klukas, K. Siu, L. Garin, J. Shewfelt and G. Cox (2002) "*Degraded GPS Signal Measurements With A Stand-Alone High Sensitivity Receiver*", Conference proceedings, ION GPS 2002, 28-30 January 2002, San Diego, CA, pp.191-204.
- MacGougan, G. D. (2003) "*High Sensitivity GPS Experiments in Degraded Signal Environments*", MSc Thesis. UCGE Report # 20176, The Department of Geomatics Engineering, University of Calgary.
- Mezensev, O., Y. Lu, G. Lachapelle and R. Klukas (2002) "*Vehicular Navigation in Urban Canyons Using A High Sensitivity GPS Receiver Augmented with Low Cost Gyro*", Conference proceedings, ION GPS 2002, September 24-27, Portland, OR, pp. 363-369.
- Misra, P. and P. Enge (2001) "*Global Positioning System: Signals, Measurements, and Performance*", Ganga-Jamuna Press, Lincoln, Massachusetts, pp. 41, 59-61, 125-128, 140-145, 162-165.
- Moeglein, M. and N. Krasner (1998) "*An Introduction to SnapTrackTM Server-Aided GPS Technology*", Conference proceedings, ION GPS 1998, 15-18 September 1998, Nashville, Tennessee), pp. 333–342.
- Mohamed, A. (1999) "*Optimizing the Estimation Procedure in INS/GPS Integration for Kinematic Applications*", PhD Thesis. UCGE Report # 20127, The Department of Geomatics Engineering, University of Calgary.
- Nayak, R. A. (2000) "*Reliable and Continuous Urban Navigation Using Multiple GPS Antennas and a Low Cost IMU*", MSc Thesis. UCGE Report # 20144, The Department of Geomatics Engineering, University of Calgary.
- Park, J. G, J. G. Lee, J. Kim and C. G. Park (2000) "*Observability Analysis of SDINS/GPS In-Flight Alignment*", Conference proceedings, ION GPS 2000, 19-22 September 2000, Salt Lake City, UT.
- Parkinson, B. W. (1996) "*Global Positioning System: Theory And Applications*", Volume I and II, American Institute of Aeronautics and Astronautics, Inc., Washington D.C., USA., Chapter 11 "GPS Error Analysis", pp.469-483
- Peterson, B., D. Bruckner, and S. Heye (1997) "*Measuring GPS Signals Indoors*", Conference Proceedings, ION GPS 1997, 16-19 September 1997, Kansas City, Missouri, pp. 615–624.
- Petovello, M. G., M. E. Cannon, and G. Lachapelle (2000) Combined Code and Carrier for Navigation with GPS and GLONASS, C3NAV²TM, *Operating Manual*, Version 3, The Department of Geomatics Engineering, University of Calgary, May 2000.

- Petovello, M. G (2003) “*Real-time Integration of Tactical-Grade IMU and GPS for High-Accuracy Positioning and Navigation*”, PhD thesis, UCGE Report # 20173, The Department of Geomatics Engineering, University of Calgary.
- Rash, G. D. (1997) “*GPS Jamming In A Laboratory Environment Conference proceedings*”, ION GPS 1997, September 16-19 1997, Kansas City, Missouri, pp. 389-398.
- Ray, J. (2000) “*Mitigation of GPS Code and Carrier Phase Multipath Effects Using a Multi-antenna System*”, PhD Thesis, UCGE Report #20136, The Department of Geomatics Engineering, University of Calgary.
- Ray, J. (2002) “*Advance GPS receiver Technology*”, ENGO 699.73 Course Lecture notes, The Department of Geomatics Engineering, University of Calgary.
- Rhee, I., M. F. Abdel-Hafez and J. L. Speyer (2002) “*On the Observability of an Integrated GPS/INS During Maneuvers*”, Conference Proceedings, ION GPS 2002, 24-27 September 2002, Portland, OR, pp. 1489-1499.
- Rothacher M. and G. Beutler (2002) “*Advanced Aspects of Satellite Positioning*”, Institute for Astronomical, Physical Geodesy Technical University of Munich, Astronomical Institute, University of Berne, ENGO 699.80 Course Lecture notes, The Department of Geomatics Engineering, University of Calgary.
- Salychev, O. S. (1998) “*Inertial Systems in Navigation and Geophysics*” Bauman MSTU Press. pp. 11-98, 118-132, 243-266.
- Salychev O. S., M. E. Cannon, V. V. Voronov, N. Nayak, and G. Lachapelle (2000) “*Low cost INS/GPS integration: Concepts and testing*”, Conference proceedings, ION NTM 2000, Anaheim, CA, pp 98–105.
- Salychev, O. S. (2003) “*Applied Estimation Theory in Geodetic and Navigation Applications*”, Moscow State Technical University, ENGO 699.52 Course Lecture notes, The Department of Geomatics Engineering, University of Calgary.
- Salycheva, A. and M. E. Cannon (2004) “*Kinematic Azimuth Alignment Using GPS Velocity*”, Conference proceedings, ION NTM 2004, January 26-28 2004, San Diego, CA, pp.1103-1113.
- Scherzinger, B. M. (2000) “*Precise Robust Positioning with Inertial/GPS RTK*”, Conference proceedings, ION GPS 2000, Institute of Navigation, Alexandria, VA., pp. 155-162.

- Schwarz, K. P., N. El-Sheimy and Z. Liu (1994) “*Fixing GPS Cycle Slips by INS/GPS*”, Proceedings of the International Symposium on Kinematic Systems in Geodesy, Geomatics and Navigation, pp. 265-275.
- Schwarz, K. P. (1996) “*Fundamentals of Geodesy*”, ENGO 421 Course Lecture Notes, The Department of Geomatics Engineering, University of Calgary.
- Sennott, J. and D. Senffner (1997) “*Robustness of Tightly Coupled Integrations for Real-Time Centimeter GPS Positioning*”, Conference proceedings, ION GPS 1997, 16-19 September 1997, Kansas City, Missouri, pp. 655-663.
- Shin, E. H (2001) “*Accuracy Improvement of Low Cost INS/GPS for Land Applications*”, MSc Thesis. UCGE Report #20156, The Department of Geomatics Engineering, University of Calgary.
- Shin, E. H. and N. El-Sheimy (2002) “*Optimizing Smoothing Computation for Near Real-Time GPS Measurement Gap Filling in NS/GPS Systems*”, Conference proceedings, ION GPS 2002, 24-27 September 2002, Portland, OR, pp. 1434-1441.
- Skaloud, J. (1998) “*Reducing the GPS Ambiguity Search Space By Including Inertial Data*”, Conference proceedings, ION GPS 1998, Alexandria, VA., pp. 2073-2080.
- Skaloud, J. (1999) “*Optimizing Georeferencing of Airborne Survey Systems by INS/DGPS*”, PhD Thesis, UCGE Report # 20127, The Department of Geomatics Engineering, University of Calgary.
- Skone, S. (2003) “*Atmospheric Effects on Satellite Navigation Systems*”, ENGO 633 Course Lecture notes, The Department of Geomatics Engineering, University of Calgary.
- Spenser T. and R. Walker (2004) “*GPS Susceptibility to Multipath and Spoofing Interference*”, Cooperative Research Centre for Satellite System, Queensland University of Technology, power point presentation, available at http://www.eese.bee.qut.edu.au/QUAV/Unrestricted/Postgraduate/GPS%20Interference/Presentations/CRCSS_03.ppt
- Spilker, J. J. and F. D. Natali (1996) “*Global Positioning System: Theory and Applications*”, volume I, Chapter 20 “Interference Effects and Mitigation techniques”, American Institute of Aeronautics and Astronautics, Inc., Washington D.C., USA, pp. 745-752.
- Spilker, J. J., (1996a) “*Global Positioning System: Theory and Applications*”, volume I, Chapter 3 “GPS Signal Structure and Theoretical Performance”. American Institute of Aeronautics and Astronautics, Inc., Washington D.C., USA pp. 73-89.

- Spilker, J. J., (1996b) “*Global Positioning System: Theory and Applications*”, volume I, Chapter 13 “Tropospheric Effects on GPS”, American Institute of Aeronautics and Astronautics, Inc., Washington D.C., USA.
- Sukkarieh, S. (2000) “*Low Cost, High Integrity, Aided Inertial Navigation Systems for Autonomous Land Vehicles*”, Ph.D. Thesis, Australian Centre for Field Robotics, Dept. of Mechanical and Mechatronic Engineering, University of Sydney, Sydney, Australia.
- Syed, S. and M. E. Cannon (2004) “*Fuzzy Logic Based-Map Matching Algorithm for Vehicle Navigation System in Urban Canyons*”, Conference proceedings, ION NTM 2004, January 26-28 2004, San Diego, CA, pp. 982-993.
- Teunissen, P. J. G. and M. A. Salzmann (1998) “*Performance Analysis of Kalman Filters*”, Reports of the Faculty of Geodesy, Delft University of Technology.
- Teunissen P. J. G. and A. Kleusberg (1998) “*Quality Control and GPS*”, Chapter 7, GPS for Geodesy, 2nd Edition, Springer, New York, NY, 1998.
- Titterton, D. and J. L. Weston (1997) “*Strapdown Inertial Navigation Technology*”, Peter Peregrinus Ltd. On behalf of the Institution of Electrical Engineers. 321 pp.
- Townsend, B. and P. Fenton (1994) “*A Practical Approach to the Reduction of Pseudorange Multipath Errors in a LI GPS Receiver*” Conference proceedings, ION GPS 1994, 20-23 September 1994, Salt Lake, Utah, pp.143–148.
- van Dierendonck, A. J. V., P. Fenton, and T. Ford (1992) “*Theory and Performance of Narrow Correlator Spacing in a GPS receiver*”, NAVIGATION: Journal of The Institute of Navigation, 39(3), pp.265–283.
- van Diggelen, F. (2001a) “*Indoor GPS: Wireless Aiding And Low Signal Strength Detection*” NAVTECH Seminar Course Notes, 22 March 2001, San Diego, CA.
- van Diggelen, F. (2001b) “*Global Locate Indoor GPS Chipset & Services*”, Conference proceedings ION GPS 2001, 11-14 September 2001, Salt Lake City, UT, pp. 1515–1521.
- van Nee, R. D. J., J. Sierveld, P. Fenton, and B. Townsend (1994) “*The Multipath Estimating Delay Lock Loop: Approaching Theoretical Accuracy Limits*”, Proceedings IEEE Position, Location and Navigation Symposium, pp.246–251.
- Ward, P. (1996a) “*Understanding GPS Principles and Applications*”, Artech House, Inc., 685 Canton Street, Norwood, MA 0206, Chapter 4, “GPS Satellite Signal Characteristics”, pp.83-116.

- Ward, P. (1996b) "*Understanding GPS Principles and Applications*", Artech House, Inc., 685 Canton Street, Norwood, MA 0206, Chapter 5, "Satellite Signal Acquisition and Tracking", pp.128-207.
- Ward, P. (1996c) "*Understanding GPS Principles and Applications*", Artech House, Inc., 685 Canton Street, Norwood, MA 0206, Chapter 6, "Effects of RF Interference on GPS Satellite Signal Receiver Tracking", pp.209-236.
- Wieser, A. and F. K. Brunner (2000) "*An Extended Weight Model for GPS Phase Observations*", *Earth Planets Space* 52, 2000, pp. 777-782.
- Wolf, R., B. Eissfeller and G. W. Hein (1997) "*A Kalman Filter For the Integration of a Low Cost INS and An Attitude GPS*", *Proceedings of the International Symposium on Kinematic Systems in Geodesy, Geomatics and Navigation*, pp. 143-150.

Appendix A

Strapdown INS Algorithm

The calculation procedure is divided into two major parts: (i) processing of accelerometer data; and (ii) measurement preparation of gyro output. In this thesis, the local-level frame is chosen as the navigation frame.

Factory calibrated velocity increments, $\Delta W_{xb,yb,zb}$, (i.e. initial compensation of the accelerometer biases, scale factors and installation errors) are calculated using the following formula (Salychev, 1998):

$$\Delta W_{xb,yb,zb} = \int_{t_k}^{t_k+T} a_{xb,yb,zb} dt \quad (\text{A-1})$$

where: $a_{xb,yb,zb}$ are the accelerometer indications in the body frame; and T is time sampling of the navigation solution calculation.

An analogous procedure is performed for the gyro measurements. Factory calibrated angle increments, $\Delta \alpha_{xb,yb,zb}$, (after compensation for gyro biases, scale factors and installation errors), are defined:

$$\Delta \alpha_{xb,yb,zb} = \int_{t_k}^{t_k+T} \omega_{xb,yb,zb} dt \quad (\text{A-2})$$

where $\Delta \omega_{xb,yb,zb}$ are gyro outputs in the body frame.

To decrease the data rate, which is usually very high (herein 100 Hz), sculling and coning corrections are typically applied to accelerometer and gyro data, respectively. These procedures take into account the user's motion in-between time samples. However, due to the low intensity of vehicle dynamics in automotive applications as compared to airborne or spaceborne environments, sculling and coning are replaced in this thesis by simple integration (equations (A-1) and (A-2)).

Following the above steps, velocity increments are transformed into the navigation frame:

$$\begin{bmatrix} \Delta W_x \\ \Delta W_y \\ \Delta W_z \end{bmatrix}_b = R_b^N \begin{bmatrix} \Delta W_x \\ \Delta W_y \\ \Delta W_z \end{bmatrix}_N \quad (\text{A-3})$$

where R_b^N is the transformation matrix between the body and navigation frames.

The determination of this matrix is a major goal of the attitude algorithm calculation. It is based on the Poisson formula (3-8) considered in Chapter 3. Due to the simplicity of calculation, this equation is solved in quaternion form (see equation (3-13)). The procedure is divided into two steps (*ibid*). The first step involves calculation of the quaternion between the body and navigation frames, assuming that the n-frame does not move between time samples (considered as an inertial frame during one sample). The transformation from the b-frame to the i-frame has a form:

$$Q_{n+1}^p = Q_n^f \Delta \lambda \quad (\text{A-4})$$

where: Q_{n+1}^p, Q_n^f are rotation quaternions (3-10) on the previous and current steps;

$\Delta\lambda$ is a quaternion of a small rotation of the same form (3-10), which can be represented via the vector of a small rotation, $\Delta\Phi$ (see

$$\text{equation (3-11)): } \Delta\Phi = \begin{bmatrix} \Delta\Phi_{xb} \\ \Delta\Phi_{yb} \\ \Delta\Phi_{zb} \end{bmatrix} = \begin{bmatrix} \sum_i \alpha_{xb}^i \\ \sum_i \alpha_{yb}^i \\ \sum_i \alpha_{zb}^i \end{bmatrix},$$

where $\alpha_{xb}^i, \alpha_{yb}^i, \alpha_{zb}^i$ are the angle increments from (A-2).

The magnitude of this rotation is obtained from gyro measurements at the previous step (A-2). Equation (A-4) can be rewritten in matrix form as:

$$\begin{bmatrix} q_0^p \\ q_1^p \\ q_2^p \\ q_3^p \end{bmatrix}_{n+1} = \begin{bmatrix} \Delta\lambda_0 & -\Delta\lambda_1 & -\Delta\lambda_2 & -\Delta\lambda_3 \\ \Delta\lambda_1 & \Delta\lambda_0 & \Delta\lambda_3 & -\Delta\lambda_2 \\ \Delta\lambda_2 & -\Delta\lambda_3 & \Delta\lambda_0 & \Delta\lambda_1 \\ \Delta\lambda_3 & \Delta\lambda_2 & -\Delta\lambda_1 & -\Delta\lambda_0 \end{bmatrix} \begin{bmatrix} q_0^f \\ q_1^f \\ q_2^f \\ q_3^f \end{bmatrix}_n \quad (\text{A-5})$$

The second step takes into account the motion of the n-frame with respect to the i-frame within the last sample. The quaternion expression for this rotation is the following:

$$Q_{n+1}^f = \Delta m^* * Q_{n+1}^p \quad (\text{A-6})$$

where Δm^* is a quaternion of a small rotation, which is a conjugate of a quaternion (3-10), and it has the form: $\Delta m^* = \Delta m_0 - \Delta m_1 i - \Delta m_2 j - \Delta m_3 k$

This quaternion can be also represented through the rotation vector between the above frames. For slow motion it can be described as (ibid):

$$\Delta m^* = \cos \frac{\omega T}{2} - \frac{\omega_x}{\omega} \sin \frac{\omega T}{2} i - \frac{\omega_y}{\omega} \sin \frac{\omega T}{2} j - \frac{\omega_z}{\omega} \sin \frac{\omega T}{2} k \quad (\text{A-7})$$

where: $\omega_x, \omega_y, \omega_z$ are projections of angular velocity of the n-frame on its axes; end

T is a sampling interval.

Equation (A-6) can be represented in matrix form as:

$$\begin{bmatrix} \mathbf{q}_0^f \\ \mathbf{q}_1^f \\ \mathbf{q}_2^f \\ \mathbf{q}_3^f \end{bmatrix}_{n+1} = \begin{bmatrix} \mathbf{q}_0^p & -\mathbf{q}_1^p & -\mathbf{q}_2^p & -\mathbf{q}_3^p \\ \mathbf{q}_1^p & \mathbf{q}_0^p & \mathbf{q}_3^p & -\mathbf{q}_2^p \\ \mathbf{q}_2^p & -\mathbf{q}_3^p & \mathbf{q}_0^p & \mathbf{q}_1^p \\ \mathbf{q}_3^p & \mathbf{q}_2^p & -\mathbf{q}_1^p & -\mathbf{q}_0^p \end{bmatrix}_{n+1} \begin{bmatrix} \Delta \mathbf{m}_0 \\ \Delta \mathbf{m}_1 \\ \Delta \mathbf{m}_2 \\ \Delta \mathbf{m}_3 \end{bmatrix} \quad (\text{A-8})$$

Splitting the quaternion calculations into two steps is motivated by differences in magnitude and the nature of the rotations. The rotation of the b-frame with respect to inertial space can be considered as fast motion (due to arbitrary angles in-between the above frames). By contrast, rotation of the n-frame with respect to the i-frame comprises a relatively slow motion (due to the Earth's low rotation rate). To avoid calculation errors as a result of the addition of two components with different magnitudes, this cascaded quaternion transformation is appropriate and effective (*ibid*).

Using the property of the quaternion norm (see Chapter 3), the normalization procedure for quaternion transformation is performed as:

$$\text{If } 1 - (\mathbf{q}_0^2 + \mathbf{q}_1^2 + \mathbf{q}_2^2 + \mathbf{q}_3^2) > \Delta, \text{ then } \hat{\mathbf{q}}_{n+1} = \frac{\mathbf{q}_{n+1}}{\sqrt{1 - \Delta}} \cong \mathbf{q}_{n+1} \left(1 + \frac{\Delta}{2}\right)$$

$$\text{Otherwise } \hat{\mathbf{q}}_{n+1} = \mathbf{q}_{n+1} \quad (\text{A-9})$$

The elements $c_{11}, c_{12}, c_{13}, \dots$ of the transformation matrix, R_b^N , are defined utilizing the relationship between the quaternion and direction cosine matrix (3-12).

Vehicle east and north velocities V_E and V_N are defined from the following equation:

$$\begin{aligned}
V_E &= \Delta W_E + \int_{t_k}^{t_k+T} (2V_N U_{up} - V_{up} (\Omega_N + 2U_N)) dt \\
V_N &= \Delta W_N + \int_{t_0}^{t_k+T} (2V_E U_{up} - V_{up} \Omega_E) dt
\end{aligned} \tag{A-10}$$

where: $\Delta W_E, \Delta W_N$ are the projections of integrated velocity increments from (A-3) in the ll-frame;

U_{Nx}, U_{Ny}, U_{Nz} are the projections of Earth rotation onto the ll-frame; and

Ω_E, Ω_N are the projections of relative angular velocity on the ll-frame.

The terms from equation (A-10) can be represented via elements of the transformation matrix between the Earth-fixed and local-level frames, R_e^{ll} (see equation (3-1)). It has the form:

$$R_e^{ll} = \begin{bmatrix} b_{11} & b_{12} & b_{13} \\ b_{21} & b_{22} & b_{23} \\ b_{31} & b_{32} & b_{33} \end{bmatrix}, \text{ where} \tag{A-11}$$

$$\begin{aligned}
b_{11} &= \sin \lambda \\
b_{12} &= \cos \lambda \\
b_{13} &= 0 \\
b_{21} &= -\sin \varphi \cos \lambda \\
b_{22} &= -\sin \varphi \sin \lambda \\
b_{23} &= \cos \varphi \\
b_{31} &= \cos \varphi \cos \lambda \\
b_{32} &= \cos \varphi \sin \lambda \\
b_{33} &= \sin \varphi
\end{aligned}$$

The projections of the relative angular velocity onto the ll-frame, Ω_E and Ω_N , can be expressed as (see equation (3-2)):

$$\begin{aligned}
\Omega_E &= -\frac{V_N}{R + h_\phi} \\
\Omega_N &= \frac{V_N}{R_\lambda + h} \\
\frac{1}{R_\phi} &= \frac{1}{a} \left(1 - e^2 \frac{b_{33}^2}{2} - \frac{h}{a}\right) \\
\frac{1}{R_\lambda} &= \frac{1}{a} \left(1 - e^2 \frac{b_{33}^2}{2} + e^2 b_{23}^2 - \frac{h}{a}\right)
\end{aligned} \tag{A-12}$$

where: e is the eccentricity of the reference ellipsoid;
 a is the semi-major axis of the reference ellipsoid;
 R_ϕ, R_λ are the radii of curvature of the reference ellipsoid in the North-South and East-West directions respectively; and
 h is the vehicle attitude.

The projections of absolute angular velocity of the ll-frame onto their axes have the form (see equation (3-2)):

$$\begin{aligned}
\omega_E &= \Omega_E \\
\omega_N &= \Omega_N + U b_{23} \\
\omega_{up} &= U b_{33}
\end{aligned} \tag{A-13}$$

For coordinate determination instead of direct integration, the Poisson equation in recurrent form is used (*ibid*):

$$\begin{aligned}
b_{12}(N) &= b_{12}(N-1) - \Omega_N b_{32}(N-1)T \\
b_{22}(N) &= b_{22}(N-1) + \Omega_E b_{32}(N-1)T \\
b_{32}(N) &= b_{32}(N-1) + (\Omega_N b_{12}(N-1) - \Omega_E b_{22}(N-1))T \\
b_{13}(N) &= \Omega_N b_{33}(N-1)T \\
b_{23}(N) &= b_{23}(N-1) + \Omega_E b_{33}(N-1)T \\
b_{33}(N) &= b_{33}(N-1) + \Omega_E b_{23}(N-1)T \\
b_{31}(N) &= b_{12}(N) b_{23}(N)
\end{aligned} \tag{A-14}$$

where N is a step number.

After determination of the transformation matrix R_e^N elements, vehicle curvilinear coordinates are defined:

$$\begin{aligned}\varphi &= \arctg \frac{b_{33}}{b_{23}}, [0 \div \pm 90^0] \\ \lambda &= \arctg \frac{b_{32}}{b_{31}}, [0 \pm 180^0]\end{aligned}\tag{A-15}$$

The attitude angles are finally calculated from the elements of the transformation matrix,

R_b^N , (c_{11} , c_{12} , c_{13} ...) as:

$$\begin{aligned}p &= \arctg\left(\frac{c_{32}}{\sqrt{c_{31}^2 + c_{33}^2}}\right), [0 \div 90^0] \\ r &= -\arctg\left(\frac{c_{31}}{c_{33}}\right), [0 \div 180^0] \\ A &= \arctg\left(\frac{c_{12}}{c_{22}}\right), [0 \div 180^0]\end{aligned}\tag{A-16}$$

where: p is pitch;
r is roll; and
A is azimuth.

The calculation scheme of strapdown navigation algorithm is shown in Figure A-1.

A.1 INS Initial Alignment

To start the INS calculation algorithm, the initial parameters of the transformation matrix between the navigation and body frames, R_b^N , must be determined. This procedure, referred to as INS alignment (see Chapter 3), contains the following steps (*ibid*):

1. coarse horizontal alignment;
2. coarse azimuth alignment; and
3. fine alignment.

During INS alignment, the system works in navigation mode; however, to coincide the platform frame with the navigation frame, the additional control signal of the gyro torque should be introduced to the quaternion block (closed-loop alignment).

The additional angular velocities, ω_x^c and ω_y^c , can be introduced as:

$$\begin{aligned}\omega_x^c &= -k_1 \delta V_y \\ \omega_y^c &= k_1 \delta V_x\end{aligned}\tag{A-17}$$

and

$$\begin{aligned}\delta V_x &= \Delta W_x^0 - k_2 \int_0^t \delta V_x dt \\ \delta V_y &= \Delta W_y^0 - k_2 \int_0^t \delta V_y dt\end{aligned}\tag{A-18}$$

where ΔW_x^0 and ΔW_y^0 are the projections of velocity increments in the p-frame, which, for an unmoving vehicle, can be determined as:

$$\begin{aligned}\Delta W_x^0 &= -\int_0^t g \Phi_y dt \\ \Delta W_y^0 &= \int_0^t g \Phi_x dt\end{aligned}\tag{A-19}$$

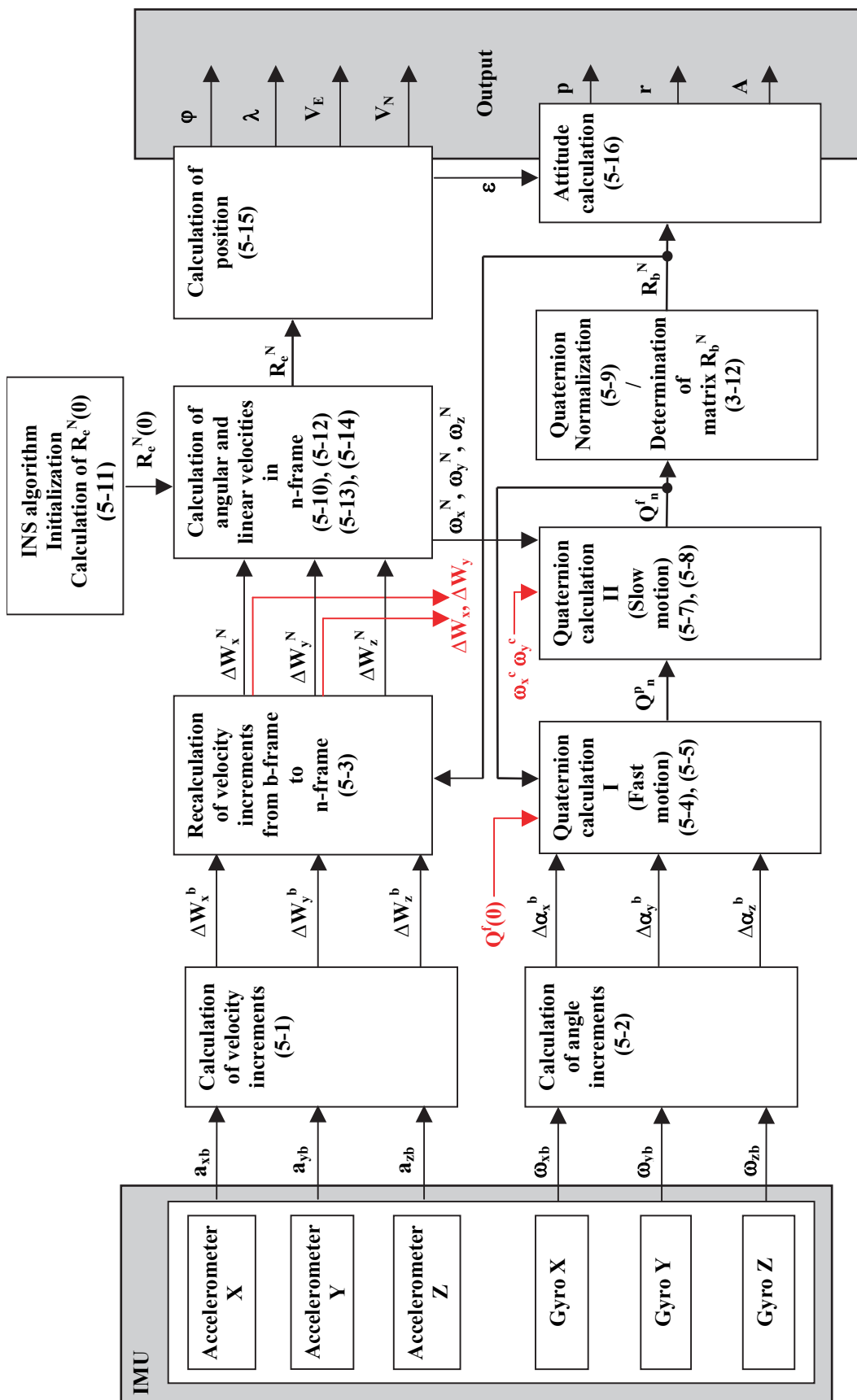


Figure A-1: SINS Calculation Algorithm (ibid)

In the above equations:

t is alignment time;

g is gravity; and

k_1, k_2 are the damping parameters for 2nd order oscillator. It has the form:

$$\begin{aligned}\ddot{\Phi}_x + 2\xi\omega_0\dot{\Phi}_x + \omega_0^2\Phi_x &= \alpha(t) \\ \ddot{\Phi}_y + 2\xi\omega_0\dot{\Phi}_y + \omega_0^2\Phi_y &= \beta(t)\end{aligned}\tag{A-20}$$

where $k_1 = \omega_0^2 / g, k_2 = 2\xi\omega_0$ are chosen so that the horizontal misalignment errors, Φ_x and Φ_y , attenuate within a certain time.

After coarse horizontal alignment, the azimuth error, Φ_z , is estimated:

$$\Phi_z^{\text{coarse}} = \text{arctg} \frac{\omega_x^c}{\omega_y^c + U \cos \varphi}\tag{A-21}$$

The estimated azimuth correction is then introduced to the quaternion of a small rotation, Δm , as additional angular velocity:

$$\omega_z^c = \frac{\Phi_z^{\text{coarse}}}{T}\tag{A-22}$$

After coarse azimuth alignment, using the new quaternion parameters, the fine horizontal and azimuth alignments are initiated. The final azimuth correction thus has the form:

$$\Phi_z^{\text{fine}} = \frac{\omega_x^c}{U \cos \varphi}\tag{A-23}$$

The alignment procedure is shown in red in the INS calculation scheme in Figure A-1.

The overall functional scheme of INS alignment is as follows. Using the initial vehicle position, the initial elements of the matrix R_e^{\parallel} (A-11) are defined. Assuming that the p-frame coincides with the n-frame, the initial quaternion parameters are:

$$q_0 = [1 \ 0 \ 0 \ 0]^T \quad (\text{A-25})$$

In reality, the p-frame has an arbitrary initial position, so that the alignment task is to set misalignment angles to zero. First, the control angular velocity is added to the absolute angular velocity and is introduced into the quaternion of slow motion, Δm , which causes attenuation of horizontal misalignment errors to small magnitudes (also referred to as coarse horizontal alignment). In this case, the quaternion calculation is changed to:

$$\begin{aligned} \Delta m^* = & \cos \frac{\omega + \omega^c}{2} T - \frac{\omega_x + \omega_x^c}{\omega + \omega^c} \sin \frac{(\omega + \omega^c)T}{2} i - \frac{\omega_y + \omega_y^c}{\omega + \omega^c} \sin \frac{(\omega + \omega^c)T}{2} j - \\ & - \frac{\omega_z}{\omega} \sin \frac{(\omega + \omega^c)T}{2} k \end{aligned} \quad (\text{A-26})$$

This step results in convergence of the quaternion parameters to true attitude angles. At this point, control angular velocities are averaged and the rough azimuth misalignment angle is obtained. This azimuth correction is also introduced to the quaternion block, Δm (coarse azimuth alignment). Fine alignment is performed in a similar manner to coarse alignment using new parameters of the quaternions. For more details in the SINS navigation algorithm and alignment a reader is referred to [Salychev \(1998\)](#).